Universidade de Aveiro
2013
Departamento de Engenharia
de Materiais e Cerâmica

Mengistie Leweyehu Debasu

Nanopartículas de Óxidos e Fosfatos de Lantanídeos para Termometria e Imagem Bimodal

Lanthanide Oxide and Phosphate Nanoparticles for Thermometry and Bimodal Imaging

Universidade de Aveiro
2013
Departamento de Engenharia de Materiais e Cerâmica

Mengistie Leweyehu Debasu

Nanopartículas de Óxidos e Fosfatos de Lantanídeos para Termometria e Imagem Bimodal

Lanthanide Oxide and Phosphate Nanoparticles for Thermometry and Bimodal Imaging

"*The whole of science is nothing more than a refinement of every day thinking.*"

— Albert Einstein.
In Physics and reality, *J. Franklin Inst.*, 221(3), 349-382, **1936**.

Universidade de Aveiro
2013

Departamento de Engenharia
de Materiais e Cerâmica

Mengistie Leweyehu Debasu

Nanopartículas de Óxidos e Fosfatos de Lantanídeos para Termometria e Imagem Bimodal

Lanthanide Oxide and Phosphate Nanoparticles for Thermometry and Bimodal Imaging

Tese apresentada à Universidade de Aveiro para cumprimento dos requisitos necessários à obtenção do grau de Doutor em Ciência e Engenharia de Materiais, realizada sob a orientação científica do Doutor Luís António Ferreira Martins Dias Carlos, Professor Catedrático do Departamento de Física da Universidade de Aveiro e do Doutor João Carlos Matias Celestino Gomes da Rocha, Professor Catedrático do Departamento de Química da Universidade de Aveiro.

Apoio financeiro da FCT.
(SFRH/BD/67108/2009)

o júri / the jury

presidente / president

Doutor Casimiro Adrião Pio
Professor Catedrático da Universidade de Aveiro

vogais / examiners committee

Doutor Hugh Douglas Burrows
Professor Catedrático da Faculdade de Ciências e Tecnologia da Universidade de Coimbra

Doutor Rui Manuel Amaral de Almeida
Professor Catedrático do Instituto Superior Técnico da Universidade Técnica de Lisboa

Doutor Carlos Miguel Calisto Baleizão
Investigador Principal do Instituto Superior Técnico da Universidade Técnica de Lisboa

Doutor Joaquim Manuel Vieira
Professor Catedrático da Universidade de Aveiro

Doutor Luís António Martins Dias Carlos
Professor Catedrático da Universidade de Aveiro (orientador)

Doutor João Carlos Matias Celestino Gomes da Rocha
Professor Catedrático da Universidade de Aveiro (orientador)

agradecimentos /
acknowledgements

I thank my supervisors, Prof. Dr. J. Rocha and Prof. Dr. Luís D. Carlos, for offering me a PhD opportunity and their confidence in me to join their research groups. I am deeply indebted to them for their excellent mentorship during the four years in my PhD project; they have taught me how to develop new scientific thoughts, and to organize, write and present good scientific communications. I am grateful to them for respecting my ideas and choices in the development of my PhD. I also thank them for translating this thesis abstract into Portuguese.

I would like to thank Prof. Dr. Luís M. Liz-Marzán and Dr. I. Pastoriza-Santos for allowing me to learn the synthesis of gold nanoparticles and oxide-gold nanocomposites from their Colloid Chemistry Group (Vigo, Spain) in which I have acquired some insight into the preparation and application of plasmonic nanoparticles. I would also like to thank Prof. Dr. Carlos Geraldes, Prof. Dr. M. Sangermano and Prof. Dr. Oscar Malta for their collaborations and contributions to my PhD project. I am indebted to the examiners of this thesis for their time and important questions and comments.

I thank Dr. D. Ananias for his technical help in the experimental works as well as for reading this thesis and providing me constructive comments; I am thankful for his unreserved suggestion over the years. I would also like to extend my gratitude to those who gave me access to the equipments and helped me out with the measurements: Dr. Maria Rute for PL spectroscopy and quantum yield measurements, Dr. R. Soares for powder X-ray diffractometer, M. Ferro for TEM images, and Dr. C. Azevedo for UV-visible and FTIR spectroscopies.

Many thanks to all who helped me on many occasions: Dr. S. Pinho, Dr. P. Lima, Dr. C. Brites, V. Freitas, Dr. P. Brandão, Dr. L. Fu, Dr. P. Silva, Dr. S. M. Bruno, Dr. J. Gonçalves, Dr. F. Castro, Dr. R. Munhá, S. Balabhadra, S. Correia, Mr. F. Reis, Mrs. M. Emília, Abdelgader, Reda, M. Wang, Dr. I. Roppolo, A. Álvarez-Paneque, Ana M. Sánchez-Iglesias and Dr. E. Carbó-Argibay.

My earnest gratitude goes to my wife, Mastie. Without her support I would not have been able to get through all the challenges I faced, and this thesis would not have been completed in its present shape; Mastie, I love you and thank you so much for being with me in such difficult time. My lovely daughter, Hana, I also thank you for giving me much joy. Last but not least, I thank my father and mother for helping me succeed in my studies and siblings for their unlimited love and encouragement; I congratulate them on their productive supports.

Palavras Chave

Fotoluminescência, lantanídeos, nanomateriais, nanotermómetros, nanopartículas de ouro, bioimagem, conversores fotónicos.

Resumo

Nesta tese relatam-se estudos de fotoluminescência de nanopartículas de óxidos e fosfatos dopados com iões trivalentes de lantanídeos, respectivamente, nanobastonetes de $(Gd,Eu)_2O_3$ e $(Gd,Yb,Er)_2O_3$ e nanocristais de $(Gd,Yb,Tb)PO_4$, demonstrando-se também aplicações destes materiais em revestimentos inteligentes, sensores de temperatura e bioimagem.

Estuda-se a transferência de energia entre os sítios de Eu^{3+} C_2 e S_6 dos nanobastonetes Gd_2O_3. A contribuição dos mecanismos de transferência de energia entre sítios para o tempo de subida $^5D_0(C_2)$ é descartada a favor da relaxação directa $^5D_1(C_2)$ $^5D_0(C_2)$ (i.e., transferência de energia entre níveis). O maior tempo de decaimento do nível $^5D_0(C_2)$ nos nanobastonetes, relativamente ao valor medido para o mesmo material na forma de microcristais, é atribuído, quer à existência de espaços livres entre nanobastonetes próximos (factor de enchimento ou fracção volúmica), quer à variação do índice de refracção efectivo do meio em torno dos iões Eu^{3+}.

A dispersão de nanobastonetes de $(Gd,Eu)_2O_3$ em três resinas epoxi comerciais através da cura por UV permite obter nanocompósitos epoxi-$(Gd,Eu)_2O_3$. Relatam-se estudos cinéticos e das propriedades térmicas e de fotoluminescência destes nanocompósitos. Estes, preservam as típicas propriedades de emissão do Eu^{3+}, mostrando o potencial do método de cura por UV para obter revistimentos inteligentes e fotoactivos.

Considera-se um avanço significativo a realização de uma nanoplataforma óptica, incorporando aquecedor e termómetro e capaz de medir uma ampla gama de temperaturas (300-2000 K) à escala nano, baseada em nanobastonetes de $(Gd,Yb,Er)_2O_3$ (termómetros) cuja superfície se encontra revestida com nanopartículas de ouro. A temperature local é calculada usando, quer a distribuição de Boltzmann (300-1050 K) do rácio de intensidades da conversão ascendente $^2H_{11/2}\rightarrow{}^4I_{15/2}/{}^4S_{3/2}\rightarrow{}^4I_{15/2}$, quer a lei de Planck (1200-2000 K) para uma emissão de luz branca atribuída à radiação do corpo negro.

Finalmente, estudam-se as propriedades de fotoluminescência correspondentes às conversões ascendente e descendente de energia em nanocristais de $(Gd,Yb,Tb)PO_4$ sintetizados por via hidrotérmica. A relaxividade (ressonância magnética) do ^1H destes materiais são investigadas, tendo em vista possíveis aplicações em imagem bimodal (luminescência e ressonância magnética nuclear).

Keywords

Photoluminescence, lanthanides, nanomaterials, nanothermometers, gold nanoparticles, bioimaging, up-conversion.

Abstract

This thesis reports photoluminescence studies of trivalent lanthanide-doped oxide and phosphate nanoparticles, respectively, $(Gd,Eu)_2O_3$ and $(Gd,Yb,Er)_2O_3$ nanorods, and $(Gd,Yb,Tb)PO_4$ nanocrystals, and demonstrates applications of these materials in smart coatings, temperature sensing and bioimaging. The emission and excitation spectra, excited-state lifetimes and energy transfer processes of these nanosystems are investigated in detail.

The energy-transfer between the C_2 and S_6 Eu^{3+} sites in Gd_2O_3 nanorods is examined. The contribution of the inter-site energy-transfer mechanisms to the $^5D_0(C_2)$ rise time is ruled out. It is shown that the direct $^5D_1(C_2)$ to $^5D_0(C_2)$ relaxation (i.e., inter-level energy-transfer) is the only path responsible for the rise time effect. The larger $^5D_0(C_2)$ nanorods decay time in air (relatively to decay time of the bulk counterparts) is attributed to both, the small filling factor of the nanorods, and the change in the effective-refractive index of the milieu surrounding the Eu^{3+} ions.

$(Gd,Eu)_2O_3$ nanorods dispersed in three commercially-available photocurable epoxy resins *via* UV-curing afford photoactive epoxy-$(Gd,Eu)_2O_3$ nanocomposites. The polymerization kinetics, thermal and photoluminescence properties of the nanocomposites are studied. The nanocomposites preserve the typical Eu^{3+} emission properties, showing the potential of the UV-curing method to yield photoactive smart coatings.

Considered a breakthrough, a single optical heater-thermometer nanoplatform, able to measure a very wide range temperatures (300 - 2000 K) at the nanoscale, based on $(Gd,Yb,Er)_2O_3$ nanorods (thermometers) surface coated with gold nanoparticles (heaters) is reported. The local temperature is calculated using either the Boltzmann's distribution (300 - 1050 K) of the Er^{3+} up-conversion $^2H_{11/2}\rightarrow{}^4I_{15/2}/{}^4S_{3/2}\rightarrow{}^4I_{15/2}$ intensity ratio, or Planck's law (1200 - 2000 K) for a white-light emission ascribed to blackbody radiation.

Finally, the down-shifting and up-conversion photoluminescence properties of $(Gd,Yb,Tb)PO_4$ nanocrystals synthesized *via* the hydrothermal route are studied. The ^1H magnetic resonance relaxivity properties of these materials are also evaluated, aiming at applications in bimodal (luminescence and nuclear magnetic resonance) imaging.

Table of Contents

List of Figures

List of Tables

List of Acronyms

AuNPs	Gold nanoparticles
CA	Contrast agent
CCD	Charge-coupled device
CE	Cooperative emission
CET	Cooperative energy transfer
CIE	Commission Internationale de l'Eclairage
CR	Cross relaxation
CT	Charge transfer
CUE	Cooperative up-conversion emission
CW	Continuous wave
DGEBA	Bisphenol-A Diglycidyl Ether
DSC	Differential Scanning Calorimetry
ECC	3,4-Epoxycyclohexylmethyl-3',4'-Epoxycyclohexane Carboxylate
ED	Electric dipole
EQ	Electric quadrupole
ESA	Excited state absorption
ET	Energy transfer
ETU	Energy transfer up-conversion
FIR	Fluorescence intensity ratio
FTIR	Fourier transform infrared
GNRs	Gold nanorods
GS	Ground state
GSA	Ground state absorption
HDGE	1,6 Hexanediol Diglycidyl Ether
HS	High spin
ICP-OES	Inductively coupled plasma optical emission spectroscopy
IR	Infrared
IUPAC	International Union of Pure and Applied Chemistry
LASER	Light Amplification by Stimulated Emission of Radiation
LIR	Luminescence intensity ratio
LMCT	Ligand-to-metal charge transfer
Ln	Lanthanide
Ln^{3+}	Trivalent lanthanide ion
LS	Low spin
LSPR	Localized surface plasmon resonance

MD	Magnetic dipole
MLCT	Metal-to-ligand charge transfer
MRI	Magnetic resonance imaging
NPs	Nanoparticles
NRs	Nanorods
NRs-AuNPs	Nanorods-gold nanoparticles
PA	Photon avalanche
PAH	poly(allylaminehydrochloride)
PDF	Powder Diffraction File
PL	Photoluminescence
PMT	Photomultiplier tube
PSS	poly(styrenesulfonate)
PXRD	Powder X-ray diffraction
QE	Quantum efficiency
RE	Rare earth
RF	Radio frequency
rpm	Rotation per minute
SEM	Scanning electron microscope
STEM	Scanning transmission electron microscope
TEM	Transmission electron microscope
UC	Up-conversion
UV	Ultraviolet
UV-Vis-NIR	Ultraviolet-visible-near infrared
XRD	X-ray diffraction

Preface

Motivation and scope of this thesis

In the rapidly developing field of nanotechnology, there is a growing demand to develop multifunctional nanoprobes exhibiting several physical observables for a single external stimulus. As such, trivalent lanthanide ion (Ln^{3+})-doped nanomaterials are among the most promising materials fulfilling current and future demands to fabricate multiplex devices. In particular, the Ln^{3+} luminescent properties are very responsive for various parameters including temperature, pH, gas and analyte concentration providing wide range of potential applications such as sensing and bioimaging. Ln^{3+}-doped materials are thus in the forefront in science and technology of luminescence-based materials, particularly due to the Ln^{3+} sharp emission lines, long excited-state lifetimes, large Stokes and anti-Stokes emissions, and high emission quantum yields. The rich and ladder-like energy level structures of the Ln^{3+} also provide exceptional opportunity to tailor new spectral properties and emission lines ranging from the UV-visible to the infrared region that may be employed in the development of advanced and/or novel luminescent functional materials.

This PhD project was driven by the aforementioned Ln^{3+} luminescent properties and the increasing interest in the design of Ln^{3+}-based multifunctional nanomaterials focusing on the following objectives:

- to explore photoluminescence properties (e.g., emission and excitation spectra, excited-state lifetimes, and energy transfer processes among many others) of Ln^{3+}-doped rare earth oxide and phosphate nanoparticles prepared *via* wet-chemical or hydrothermal routes.

- to demonstrate state-of-the-art applications of the prepared nanoparticles, for instance, for smart coatings, temperature sensing and bioimaging.

Structure of this thesis

As illustrated in Figure 1, this thesis can be divided into four main parts. The first part of the thesis comprises chapters 1 and 2 providing general introductory information including brief history of rare earths, optical properties of Ln^{3+} ions and experimental techniques used for the characterizations of the materials investigated. Chapter 1 discusses terminologies (configuration, state, term and level), free-ion and crystal-field

Hamiltonians, $4f^N \leftrightarrow 4f^N$ and $4f^N \leftrightarrow 4f^{N-1}5d$ transitions, charge-transfer transition, energy transfer and photon up-conversion, radiative and non-radiative transitions, and excited-state lifetimes of Ln^{3+} ions. This chapter is essential to understand the spectroscopic data of Ln^{3+} ions in general and to analyze the results obtained in this thesis in particular. Since photoluminescence (PL) spectroscopy is the principal experimental technique employed in this thesis, Chapter 2 is devoted to PL spectroscopy, and its major components and operating principles.

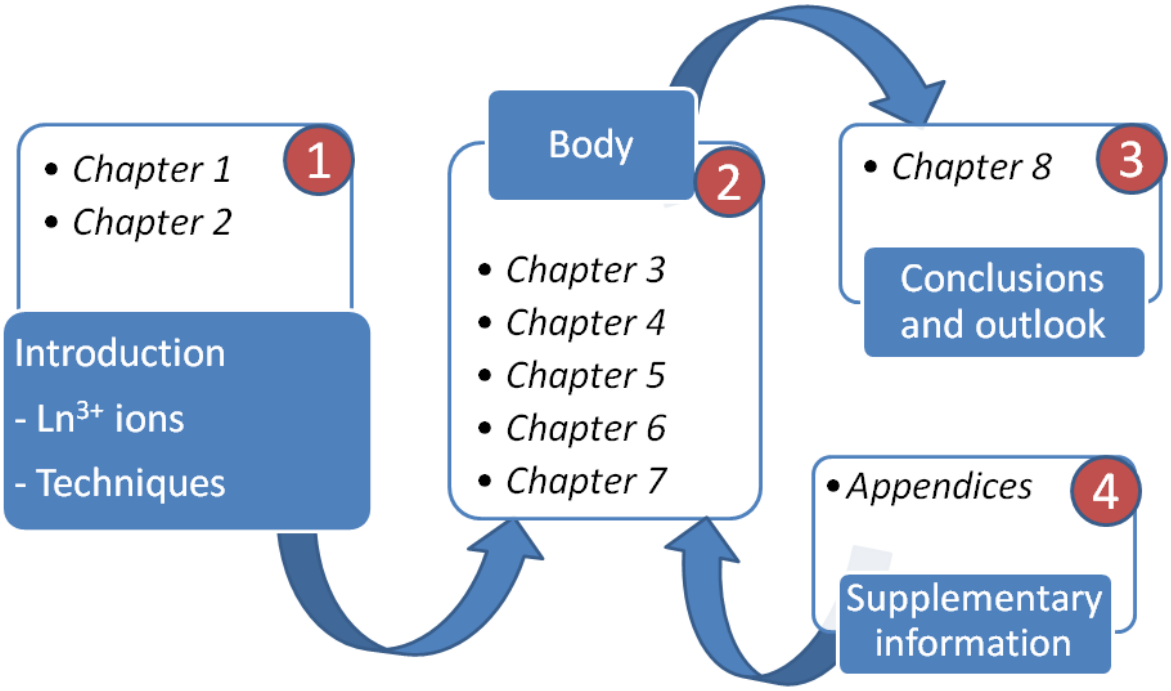

Figure 1: Schematic representation of the structure of this thesis.

The second part of the thesis (Figure 1), covering five chapters 3 - 7, constitutes the scientific contributions obtained during the author's four year PhD project. Chapter 3 reports the detailed analysis of emission decay curves, energy transfer between C_2 and S_6 sites of Eu^{3+} and the effective-refractive index in cubic $(Gd,Eu)_2O_3$ nanorods. One example of applications of $(Gd,Eu)_2O_3$ nanorods is demonstrated in chapter 4 with UV-cured epoxy/$(Gd,Eu)_2O_3$ nanocomposites. In chapter 5, a breakthrough in optical heater-thermometer single nanoplatform based on $(Gd,Yb,Er)_2O_3$ nanorods decorated with gold nanoparticles (AuNPs) is presented. Chapters 6 and 7 deal with the down-shifting PL studies and bimodal imaging applications of $(Gd,Yb,Tb)PO_4$ nanocrystals, respectively.

Conclusions and future outlook based on the findings of this thesis are given in chapter 8, third part of this thesis (Figure 1). When cited, the author recommends the reader to look into the supplementary information given in the appendices representing the final part of the thesis, Figure 1. Complimentary characterization techniques used in the body of the thesis and their experimental conditions are described in appendix A.

TEM images of Ln_2O_3 nanorods/AuNPs composites prepared *via* in situ reduction of the Au precursor on the nanorods, and the synthesis of AuNPs and their attachment to polyelectrolytes modified Ln_2O_3 nanorods are presented in appendices B and C. Appendix D aims at providing a brief introduction to blackbody and blackbody radiation as well as to Plank's law of blackbody radiation. The concepts of color and color coordinates are discussed in appendix E.

List of publications

This thesis is written based on the following papers published in widely read scientific journals:

1. **Debasu, M. L.**; Ananias, D.; Macedo, A. G.; Rocha, J.; Carlos, L. D., Emission-Decay Curves, Energy-Transfer and Effective-Refractive Index in Gd_2O_3:Eu^{3+} Nanorods, *J. Phys. Chem. C*, 2011, 115(31), 15297-15303.

2. Roppolo, I.; **Debasu, M. L.**; Ferreira, R. A. S.; Rocha, J.; Carlos, L. D.; Sangermano, M., Photoluminescent Epoxy/Gd_2O_3:Eu^{3+} UV-cured Nanocomposites, *Macromol. Mater. Eng.*, 2013, 298(2), 181-189.

3. **Debasu, M. L.**; Ananias, D.; Pastoriza-Santos, I.; Liz-Marzán, L. M.; Rocha, J.; Carlos, L. D., All-In-One Optical Heater-Thermometer Nanoplatform Operative From 300 to 2000 K Based on Er^{3+} Emission and Blackbody Radiation, *Adv. Mater.*, 2013, 25(35), 4846-4874, ***Cover of the Issue***.

4. **Debasu, M. L.**; Ananias, D.; Rocha, J.; O. L. Malta; Carlos, L. D., Energy-transfer from Gd(III) to Tb(III) in (Gd,Yb,Tb)PO_4 Nanocrystals, *Phys. Chem. Chem. Phys.*, 2013, 15(37), 25565-15571.

5. **Debasu, M. L.**; Ananias, D.; Pinho, S. L. C.; Geraldes, C. F. G. C.; Carlos, L. D.; Rocha, J., (Gd,Yb,Tb)PO_4 up-conversion nanocrystals for bimodal luminescence-MR imaging, *Nanoscale*, 2012, 4, 5297-15303.

Papers 2, 3, 4 and 5 have the collaborations with the research groups of Prof. M. Sangermano (Torino, Italy), Prof. Luís Liz-Marzán (Vigo, Spain), Prof. Oscar Malta (Recife, Brazil) and Prof. Carlos Geraldes (Coimbra, Portugal), respectively. I have learned the synthesis of gold nanoparticles (AuNPs) and Ln_2O_3/AuNPs nanocomposites from the Colloid Chemistry Group (Vigo) directed by Prof. Luís Liz-Marzán and continued preparing these composites at Aveiro, resulting in the publication of paper 3. The preparation of UV-cured epoxy/$(Gd,Eu)_2O_3$ nanocomposites and their polymerization kinetics and thermal analysis in paper 2 were performed at Torino by the group of Prof. M. Sangermano, and the calculation of energy transfer rates in paper 4 was performed in collaboration with Prof. Oscar Malta. The relaxivity measurements and the corresponding analysis in paper 5 were carried out at Coimbra by the group of Prof. Carlos Geraldes.

Chapter 1

Rare Earths and Optical Transitions of Ln^{3+} ions

1.1 Introduction: Rare earths

According to the IUPAC nomenclature [1], the elements of rare earths (RE) in the periodic table consist of the lanthanide (or lanthanoid) series from lanthanum (atomic number 57) to lutetium (71) along with scandium (21) and yttrium (39). The first discovery of rare earths was made around 1794 by Gadolin for yttrium (Y) from an oxide known as yttria which, in turn, was isolated from the mineral Gadolinite or Ytterbite. Since then, it took more than a century to discover all the remaining rare earth elements until 1947 when promethium (Pm) was the last to be discovered at Oak Ridge National Laboratory [2]. The name "rare earths", however, is misleading since the elements are neither rare in abundance nor "earths". When refereing to the lanthanides (from La to Lu), the etymology of rare earths may be associated with their initial extraction from oxides which, in some ways, resemble calcium, magnesium and aluminum oxides known as common earths [3].

The most common and stable oxidation state of lanthanide ions is +3. In solution, lanthanide ions usually exist in the +3 oxidation state, with a few exceptions e.g., divalent europium (Eu^{2+}) and tetravalent cerium (Ce^{4+}) which are relatively stable in water [3]. An important feature exhibited by the lanthanide series is that the atomic radius decreases with increasing atomic number from ∼103 pm (La^{3+}) to ∼86 pm (Lu^{3+}), known as the *lanthanide contraction*. The *lanthanide contraction* has essential roles on the chemistry of the lanthanide ions.

The fundamental spectroscopic properties of Ln^{3+} ions are indispensable for the photophysical study of Ln^{3+}-doped materials. It is therefore worth discussing the Ln^{3+} optical transitions before presenting the potential applications of Ln^{3+}-based light emitting materials. In this chapter, Ln^{3+} optical transitions necessary for the interpretation of the photoluminescent data reported in the upcoming chapters will be briefly highlighted. These include terminologies (e.g., configuration, states, terms and levels), free-ion and crystal-field Hamiltonians, $4f^N \leftrightarrow 4f^N$ and $4f^N \leftrightarrow 4f^{N-1}5d$ transitions, charge-transfer transitions, energy transfer and photon up-conversion, radiative and non-radiative transitions, and excited-state lifetimes.

1.2 Electron configuration

Electron configuration describes the distribution or population of electrons in an atomic orbital. The ground state electron configuration of Ln^{3+} ions is denoted by $[Xe]4f^N$ ($N = 0 - 14$) in which the $4f^N$ inner shell electrons are shielded by the outer filled $5s^2$ and $5p^6$ shells. Such configuration provides the 4f electrons very little interaction with the field of their surrounding environment (ions and molecules), which is responsible for most of the fascinating spectroscopic properties of Ln^{3+} (e.g., sharp emission lines, long-excited state lifetimes and high emission quantum yields) in various host materials. As shown in Figure 1.1, the expansion of the radial charge density of the $5s^25p^6$ subshells makes the 4f shell inaccessible to the outside environment.

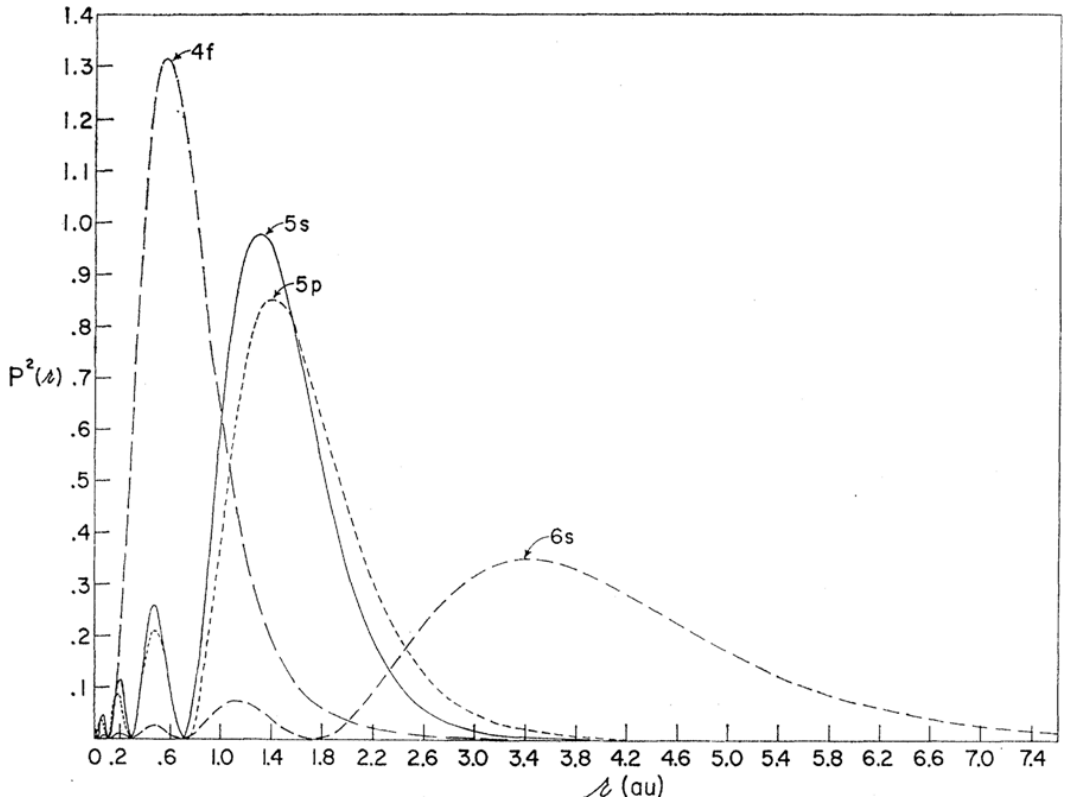

Figure 1.1: Radial charge distribution $P^2(r)$ as a function of r for the 4f, 5s, 5p and 6s orbitals of Gd^{1+} [4].

The electronic state of an atom entirely depends on its unfilled shells/subshells because any combination of closed shells/subshells will result in a total symmetry with a resultant angular momentum equal to zero. Only the N electrons in the 4f orbital are therefore responsible for the Ln^{3+} unique optical properties in solids and solutions. In a particular configuration, electrons may arrange themselves in a number of possible states. The total number of states (multiplicity or degeneracy) of the $[Xe]4f^N$ configuration (Table 1.1), with $2\ell + 1$ orbitals and two possible spin orientations, is given by

the following combinatorial formula:

$$Number\ of\ states = \left(\begin{array}{c} 2(2\ell+1) \\ N \end{array} \right) = \left(\begin{array}{c} 14 \\ N \end{array} \right) = \frac{14!}{N!(14-N)} \tag{1.1}$$

where $\ell = 3$ is the orbital angular momentum quantum number.

The energy states and levels of electrons in atoms and molecules are generally described by the Schrödinger equation:

$$H\Psi = E\Psi \tag{1.2}$$

where H is the Hamiltonian operator, Ψ the wavefunction of the quantum system and E the energy eigenvalue of Ψ. The wavefunction Ψ_{n,ℓ,m_ℓ,m_s}, is defined by four quantum numbers: the principal quantum number n, the orbital angular momentum quantum number l, the magnetic quantum number m_ℓ and the spin quantum number m_s; where n is an integer (1, 2, 3, . . .), ℓ runs 0, 1, 2, . . ., n - 1, m_ℓ (the projection of the vector $\overrightarrow{\ell}$ onto the z axis) varies between -ℓ and +ℓ and m_s (the projection of the vector $\overrightarrow{s}$) takes values of $\pm$ 1/2. Equation 1.2 is analytically solved only for the hydrogen atom (one-electron system) under the assumption that E is time independent and the nucleus is static. For many-electron atoms, the energy level structure is generally determined from the diagonalization of H by the perturbation method using an appropriate coupling scheme [5]. A coupling scheme frequently used is that of Russell-Saunders (LS) coupling [6]. In this coupling scheme the orbital angular momenta of the electrons are vectorially coupled to give a resultant total orbital angular momentum $\overrightarrow{L}$ and the spins of the electrons are coupled to give a total spin $\overrightarrow{S}$. $\overrightarrow{L}$ and $\overrightarrow{S}$ are then coupled to give a total angular momentum $\overrightarrow{J}$. Similarly, the algebraic sums of the values of m_ℓ and m_s for each electron give M_L and M_s, respectively. Mathematically [7]:

$$\begin{aligned} \overrightarrow{L} &= \sum_{i=1}^{N} \overrightarrow{\ell} \\ \overrightarrow{S} &= \sum_{i=1}^{N} \overrightarrow{s} \\ \overrightarrow{J} &= \overrightarrow{L} + \overrightarrow{S} \\ M_L &= \sum_{i=1}^{N} (m_\ell)_i \\ M_S &= \sum_{i=1}^{N} (m_s)_i \end{aligned} \tag{1.3}$$

The combination of a particular quantum number S with a particular L constitutes a spectroscopic *term* denoted by ${}^{2S+1}L$. The quantum number $2S + 1$ is the spin multiplicity of the term. $L = 0, 1, 2, 3, ...$, represents the term code with capital letters S, P, D, F, G, H, I, ..., respectively. Furthermore, the level of the term is defined by the total angular momentum quantum number J and denoted by ${}^{2S+1}L_J$ which is known

as *term symbol*; where J must satisfy $L+S \geq J \geq \mid L-S \mid$. The total number of states (multiplicity) of a term is given by $(2S+1) \times (2L+1)$ and each term symbol may have a $(2J+1)$ multiplicity for a given level. In the absence of spin-orbit coupling all of the various levels of a given term symbol are degenerate. The presence of spin-orbit coupling splits the term symbol into its J levels. The quantum numbers L, S, M_S and M_L generally determine the term symbols. In particular, the ground term symbol with the lowest energy level in an electron configuration can be readily predicted by using these quantum numbers and Hund's rule. Hund's empirical rules, subjected to Pauli's exclusive principle, are as follows (to be applied in the given order):

- **Rule 1**: For a given electron configuration, the ground term (or the term with the lowest energy) will have the maximum spin multiplicity.
- **Rule 2**: For terms with the same spin multiplicity, the ground term (or the term with the lowest energy) will have the largest value of L.
- **Rule 3**: For a given term with the same values of L and $2S+1$, the ground term symbol will have the lowest value of J if the subshell is less than half-filled and the highest value of J if the subshell is more than half-filled. In other words, if $N < (2\ell+1)$, $J = J_{min}$; if $N > (2\ell+1)$, $J = J_{max}$.

Table 1.1: Configurations, States, Terms and Ground levels of free Ln^{3+} ions.

Ln^{3+}	Configuration ($4f^N$)	NO. Sates (Nℓ)	NO. Terms (LS)	NO. Levels (LSJ)	Ground levels ($^{2S+1}L_J$)
La^{3+}, Lu^{3+}	f^0, f^{14}	1	1	1	$^1S_0$, $^1S_0$
Ce^{3+}, Yb^{3+}	f^1, f^{13}	14	1	2	$^2F_{5/2}$,$^2F_{7/2}$
Pr^{3+}, Tm^{3+}	f^2, f^{12}	91	7	13	$^3H_4$, $^3H_6$
Nr^{3+}, Er^{3+}	f^3, f^{11}	364	17	41	$^4I_{9/2}$, $^4I_{15/2}$
Pm^{3+}, Ho^{3+}	f^4, f^{10}	1001	47	107	$^5I_4$, $^5I_8$
Sm^{3+}, Dy^{3+}	f^5, f^9	2002	73	198	$^6H_{5/2}$,$^6H_{15/2}$
Eu^{3+}, Tb^{3+}	f^6, f^8	3003	119	295	$^7F_0$, $^7F_6$
Gd^{3+}	f^7	3432	119	327	$^8S_{7/2}$

For instance, consider Eu^{3+}: it has a $[Xe]4f^6$ electron configuration. The only partially filled subshell of this configuration is $4f^6$ and thus the term symbols and the ground terms can be assigned as follows. The maximum spin multiplicity is 7 for $S = 3$ corresponding to the maximum value of $M_S = 3$ when all the six electrons spin up (according to Pauli's exclusive principle). To obtain the largest orbital multiplicity, the highest M_L must be determined from the largest possible m_ℓ values i.e., + 3, + 2, + 1, 0, - 1 and -2 resulting in $M_L = 3$ which implies $L = 3$. The ground term is therefore ^7F with total number of states $(2S+1) \times (2L+1) = 49$. Furthermore, the spin-orbit coupling splits the ground term into J levels with the condition $L+S \geq J \geq \mid L-S \mid$, i.e., J = 0, 1, 2, 3, 4, 5, 6, each with a $(2J+1)$ multiplicity. Therefore, Eu^{3+} has ground term symbols denoted by $^7F_0$, $^7F_1$, $^7F_2$, $^7F_3$, $^7F_4$, $^7F_5$ and $^7F_6$ with multiplicities 1, 3, 5, 7, 9, 11 and 13, respectively, leading to 49 number of states. In other words,

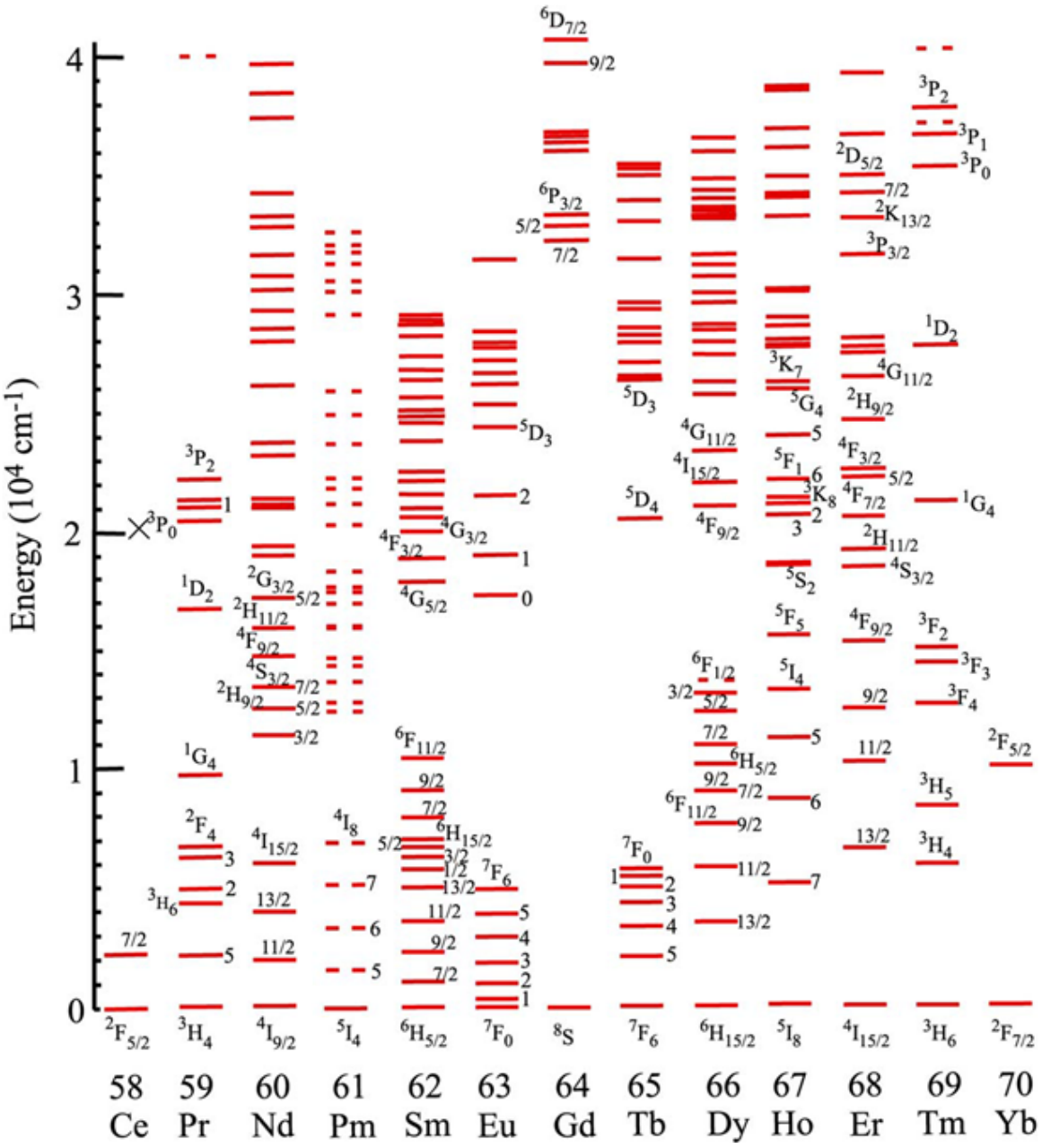

Figure 1.2: Dieke diagram (energy levels of free Ln^{3+} ions, up to 42000 cm^{-1}) [8].

$\sum_J(2J+1) = (2S+1) \times (2L+1) = 49$. Hund's third rule requires $^7F_0$ to be the ground level of Eu^{3+} (Table 1.1). The well-known Dieke diagram for the energy level of Ln^{3+} ions is presented in Figure 1.2. This diagram is important and widely used for the analysis of an unknown spectrum and/or for the spectrum of the Ln^{3+} in novel host materials taking into account that the barycenters of the Ln^{3+} emission lines hardly depend on the host material due to the Ln^{3+} intrinsic electron configuration discussed above.

1.3 Free-ion Hamiltonian

As mentioned, for many-electron system Equation 1.2 may be solved *via* the perturbation method using well-defined coupling (interaction) schemes. The interelectronic (coulomb) repulsion and spin-orbit interactions account for the most relevant part of the energy levels of the Ln^{3+} electron configurations [6, 9]. In this context, the non-relativistic free ion Hamiltonian H_{FI} that determines the energy levels of the 4f electrons is given by:

$$H_{FI} = -\frac{\hbar^2}{2m}\sum_{i=1}^{N}\nabla_i - \sum_{i=1}^{N}\frac{Ze^2}{r_i} + \sum_{i<j}^{N}\frac{e^2}{r_{ij}} + \sum_{i=1}^{N}\zeta(r_i)\overrightarrow{s}_i \cdot \overrightarrow{\ell}_i \tag{1.4}$$

where N = 1, 2, 3, ..., 14 is the number of the 4f electrons, $\hbar = h/2\pi$ the reduced Planck constant, and m the mass of electron. The first and second terms in Equation 1.4 represent the kinetic energy of the 4f electrons and their coulomb interaction with the nucleus, respectively, together denoting the central field Hamiltonian H_O; the third term is the mutual coulomb interaction H_C of the electrons; the last term contains the spin-orbit interaction H_{SO} with $\zeta(r_i)$ representing the spin-orbit coupling function; Ze is the screened charge of the electron, r_i the distance between the i electron, and the nucleus and r_{ij} the distance between the ith and jth electrons.

H_O is spherically symmetric and therefore does not remove any of the degeneracies within the configuration of the 4f electrons. On the other hand, the coulomb and spin-orbit interactions are responsible for the energy level structure of the 4f electrons, giving rise to terms and levels, respectively. The relative size of these two interactions determines the choice of the coupling scheme. For $H_C \gg H_{SO}$, the LS coupling scheme is efficient and the energy level structure is determined from the diagonalization of H_C as L and S are good quantum numbers. On the other hand, when the spin-orbit interaction is much larger than the electrostatic interaction, $H_{SO} \gg H_C$, the so-called jj-coupling scheme is required, which is particularly important for heavy elements or highly excited atoms [5, 6]. In this coupling scheme, the orbital angular momentum of one electron may vectorially couple (interact) with the spin angular momentum of another electron, i.e., $\overrightarrow{\ell}_i$ with $\overrightarrow{s}_j$. In addition, with $H_{SO} \gg H_C$ it is no longer appropriate to consider L and S as good quantum numbers because the respective $\overrightarrow{L}^2$ and $\overrightarrow{S}^2$ operators do not commute with H_{SO} and hence the matrix elements are not diagonal in L and S.

1.4 Crystal-field Hamiltonian

As will be seen in Figure 3.1 of chapter 3, a cation in a crystal is surrounded by a regular matrix of anions. An electric field is induced at the cation site, through which the cation and the anions interact. The effect of such interactions is known as **crystal/ligand field effect** [10]. Consequently, when, for instance, a Ln^{3+} is placed in a crystal field environment, the $(2J + 1)$-fold degeneracy of the free Ln^{3+} energy level

is at least partially lifted by the crystal field interaction that may be introduced as a perturbation in Equation 1.4, giving rise to Stark sublevels. The degree of lifting the degeneracy depends on the Ln^{3+} point group symmetry in the crystal (Table 1.2), the value of J and the magnitude of crystal field interaction. The point group refers to the group of symmetry operation that leaves the crystal invariant, for instance, rotations about particular axes, reflections about planes and inversion about points in the unit cell. Among the 32 crystallographic point groups summarized in Table 1.2, 11 are centrosymmetric (D_{6h}, D_{4h}, D_{3d}, D_{2h}, O_h, S_6, T_h C_{6h}, C_{4h}, C_{2h} and C_i) and the other 21 are noncentrosymmetric (C_{6v}, C_6, C_{3v}, C_{3h}, C_3, C_{4v}, C_4, C_{2v}, C_2, C_s, C_1, D_6, D_{3h}, D_3, D_4, D_{2d}, D_2, S_4, O, T_d and T) [11]. From the knowledge of the point group, the number of levels in which a state of a given J will split into can be predicted [12].

Table 1.2: Splitting of each J levels due to the symmetry point groups, Refs. [6, 11–13].

System	Point group	J (integer)								
		0	1	2	3	4	5	6	7	8
Cubic	O_h, O, T_d, T_h, T	1	1	2	3	4	4	6	6	7
Hexagonal Trigonal	D_{6h}, D_6, C_{6v}, C_{6h}, C_6, D_{3h}, C_{3h} D_{3d}, D_3, C_{3v}, S_6, C_3	1	2	3	5	6	7	9	10	11
Tetragonal	D_{4h}, D_4, C_{4v}, C_{4h}, C_4, D_{2d}, S_4	1	2	4	5	7	8	10	11	13
Triclinic Monoclinic Orthorhombic	S_2 (or C_i), C_1 C_{2h}, C_2, C_s (or C_{1h}) D_{2h}, D_2, C_{2v}	1	3	5	7	9	11	13	15	17
		J (semi-integer)								
		$\frac{1}{2}$	$\frac{3}{2}$	$\frac{5}{2}$	$\frac{7}{2}$	$\frac{9}{2}$	$\frac{11}{2}$	$\frac{13}{2}$	$\frac{15}{2}$	
Cubic		1	1	2	3	3	4	5	5	
Other local symmetry		1	2	3	4	5	6	7	8	

The magnitude of the crystal field effect on the Ln^{3+} energy levels is determined from Equation 1.4, for example, by treating the crystal field interaction as a point charge perturbation on the free ion Hamiltonian [6]. Hence, the Hamiltonian H for an ion in a crystal field potential is given by $H = H_{FI} + H_{CF}$, where H_{FI} is the free ion Hamiltonian as defined before, and H_{CF} is the crystal field Hamiltonian. Since the eigenfunctions of the free ion energy states have spherical symmetry (spherical harmonic functions), the perturbing crystal field can be expanded into a series of spherical harmonics or tensor operators that transform like spherical harmonics. Accordingly, H_{CF} is expanded in terms of the tensor operators C_q^k [14, 15]:

$$H_{CF} = \sum_{k,q,i} B_q^k (\mathbf{C}_q^{(k)})_i \tag{1.5}$$

where the summation involving i is over all the equivalent electrons of the open shell of the ion of interest; the B_q^k are crystal field parameters (coefficients of expansion); for 4f electrons, $k = 0, 2, 4, 6$ and $q \leq k$ [2]; the $\mathbf{C}_q^{(k)}$ are components of the tensor operators

$\mathbf{C}^{(k)}$ that transform like spherical harmonics. The values of k and q are limited by the local point symmetry of the ion while the B_q^k depend on both the ion-ligand distance and the point symmetry.

Combining Equations 1.4 and 1.5 yields the total Hamiltonian H for a Ln^{3+} in a crystal field can be given by:

$$H = \underbrace{-\frac{\hbar^2}{2m}\sum_{i=1}^{N}\nabla_i - \sum_{i=1}^{N}\frac{Ze^2}{r_i}}_{H_O} + \underbrace{\sum_{i<j}^{N}\frac{e^2}{r_{ij}}}_{H_C} + \underbrace{\sum_{i=1}^{N}\zeta(r_i)\overrightarrow{s}_i\cdot\overrightarrow{\ell}_i}_{H_{SO}} + \underbrace{\sum_{k,q,i}B_q^k(\mathbf{C}_q^{(k)})_i}_{H_{CF}} \tag{1.6}$$

Finally, the order of magnitude of the interaction Hamiltonians for the $4f^N$ configuration is summarized as $H_{FI} > H_C$, $H_{SO} > H_{CF}$: LS-coupling for $H_C > H_{SO}$, intermediate coupling $H_C \approx H_{SO}$ and jj-coupling $H_{SO} > H_C$ [2].

1.5 Intra- and inter-configurational transitions

1.5.1 $4f^N \leftrightarrow 4f^N$ transitions and selection rules

In quantum mechanics, not all electron transitions between two quantum levels are permitted leading to the notion of selection rules that determine whether a transition is *forbidden* (very low probability) or *allowed* (high probability). An electron transition between two quantum levels with initial state i and final state f is allowed if the matrix element M_{fi} of the transition probability is non-zero [10, 11]:

$$M_{fi} =< f|H'|i >= \int \Psi_f(\mathbf{r})^* H' \Psi_i(\mathbf{r}) d^3\mathbf{r} \neq 0 \tag{1.7}$$

where H' is the perturbation, $\mathbf{r}$ the position vector of the electron, and $\Psi_i(\mathbf{r})$ and $\Psi_f(\mathbf{r})$ the wavefunctions of the initial and final states. The perturbation H' is mainly induced by the electromagnetic radiation and consists of the transition operators. Accordingly, there are three major transition operators known as the odd-parity electric dipole (ED) operator $\overrightarrow{P}$, even-parity magnetic dipole (MD) operator $\overrightarrow{M}$, and odd-parity electric quadrupole (EQ) operator $\overrightarrow{Q}$ [2, 7]:

$$\begin{aligned}
\overrightarrow{P} &= -e\sum_{i=1}^{N}\overrightarrow{r}_i \\
\overrightarrow{M} &= -e\frac{\hbar}{2mc}\sum_{i=1}^{N}(\overrightarrow{\ell}_i - 2\overrightarrow{s}_i) \\
\overrightarrow{Q} &= \frac{1}{2}\sum_{i=1}^{N}(\overrightarrow{k}_i\cdot\overrightarrow{r}_i)\cdot\overrightarrow{r}_i
\end{aligned} \tag{1.8}$$

where e is the electron charge, and $\overrightarrow{k}$ is the wave vector. ED transitions are caused by the interaction of the electrons with the electric field component of the light wave through an electric dipole while MD transitions are caused by interaction of the electrons with the magnetic field component of the light wave through a magnetic dipole. EQ transitions arise from charge displacement with quadrupolar nature (four point charges with overall zero charge and zero dipole moment).

The selection rules for ED, MD and EQ transitions in free ions are summarized in Table 1.3. According to parity selection rules, *allowed* transitions require a change of parity of the electronic states while *forbidden* transitions occur without the change of parity of the states [16]. ED transitions are allowed since they occur between states of opposite parity, Table 1.3. MD and EQ transitions only occur between states of the same parity (Table 1.3); hence, they are forbidden. Referring to parity selection rules, the intra-configurational $4f^N \leftrightarrow 4f^N$ transitions are therefore forbidden and cannot be connected by the operator $\overrightarrow{P}$. However, these selection rules may be broken by spin-orbit, crystal field and/or vibrational interactions. For instance, when a Ln^{3+} is under the influence of a crystal field, *noncentrosymmetric* interactions or vibrational states allow the mixing of electronic states with different parity into the $4f^N$ wavefunctions, resulting in partially allowed transition known as an induced (or forced) ED transition [7]. The mixing of states of different J values (J-mixing), due to the interaction with the crystal field tensor operator is another reason for allowing induced ED transitions. Consequently, the observed $4f^N \leftrightarrow 4f^N$ transitions for Ln^{3+} ions are induced/forced ED and/or parity forbidden transitions. As can be seen in Table 1.3, all transitions (ED, MD and EQ) with $\Delta S = 0$ are spin allowed and those with $\Delta S \neq 0$ are forbidden. On the other hand, the selection rules for angular momenta may depend on the type of transitions (Table 1.3).

Table 1.3: Selection rules for atomic transitions in free atoms or ions [16, 17].

Electric Dipole	**Magnetic Dipole**	**Electric Quadrupole**
$\Delta J = 0, \pm 1$	$\Delta J = 0, \pm 1$	$\Delta J = 0, \pm 1, \pm 2$
$0 \nleftrightarrow 0$	$0 \nleftrightarrow 0$	$0 \nleftrightarrow 0, 1$ or $\frac{1}{2} \nleftrightarrow \frac{1}{2}$
$\Delta M = 0, \pm 1$	$\Delta M = 0, \pm 1$	$\Delta M = 0, \pm 1, \pm 2$
Parity change	No parity change	No parity change
$\Delta \ell = \pm 1$	$\Delta \ell = 0$	$\Delta \ell = 0, \pm 2$
	$\Delta n = 0$	
$\Delta S = 0$	$\Delta S = 0$	$\Delta S = 0$
$\Delta L = 0, \pm 1$	$\Delta L = 0$	$\Delta L = 0, \pm 1, \pm 2$
$0 \nleftrightarrow 0$	$0 \nleftrightarrow 0$	$0 \nleftrightarrow 0, 1$

1.5.2 $4f^N \leftrightarrow 4f^{N-1}5d$ transitions

The inter-configurational $4f^N \leftrightarrow 4f^{N-1}5d$ (f-d) transitions are allowed by the parity selection rule for electric dipole radiation and possess broadband characteristic when compared to the intra-$4f^N \leftrightarrow 4f^N$ transitions [18]. Furthermore, unlike the $4f^N \leftrightarrow 4f^N$ transitions, the f-d transitions may be strongly influenced by the crystal field environment since the 5d orbitals are exterior and more sensitive to the crystal field interactions. In this case, the magnitude of the crystal field interaction is higher than that of the spin-orbit interaction, at least in the first order. Most of the f-d transitions of Ln^{3+} lie on the vacuum ultraviolet (VUV) region shorter than 200 nm [18–20]. One good example of f-d transition is the excitation spectrum of Tb^{3+} in $LiYF_4$ shown in Figure 1.3, reported by Wegh and Meijerink [19], clearly showing a high spin (HS) state and a low spin (LS) state of f-d transitions. The ground state (GS) configuration of $4f^8$ has 6 unpaired parallel spins with $S = 3 \Rightarrow 2S + 1 = 7$. The $4f^7 5d$ configuration can have

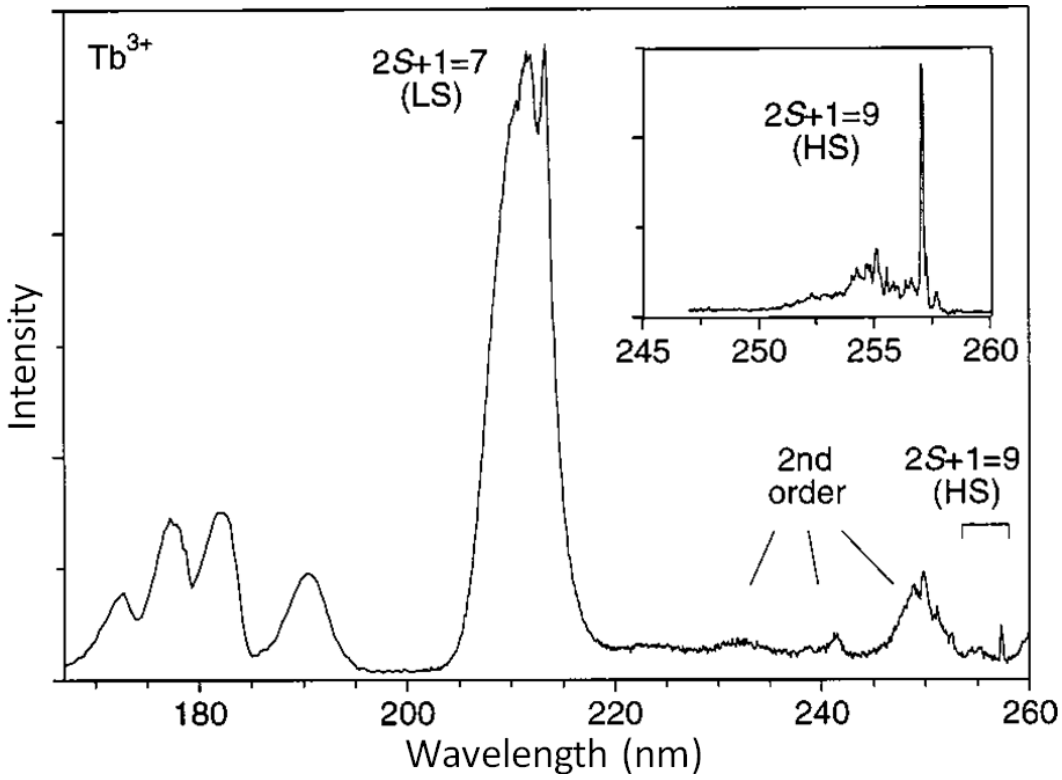

Figure 1.3: Excitation spectrum of $LiYF_4$:Tb^{3+} 1% monitoring $4f^8(^5D_4 \rightarrow {}^7F_5)$ emission (545 nm) at 10 K. Inset: high-resolution excitation spectrum monitoring $4f^8(^5D_4 \rightarrow {}^7F_5)$ emission (545 nm) at 10 K, recorded with a tunable laser setup [19].

two possible states because the electron in the 5d shell can orient its spin (i) parallel to the 7 remaining 4f electrons, giving rise to a HS state with $S = 4 \Rightarrow 2S + 1 = 9$ or (ii) antiparallel, yielding a LS state with $S = 3 \Rightarrow 2S + 1 = 7$. According to Hund's rule stated before, the HS state will be lower than the LS one in energy. Furthermore, referring to the spin selection rules (Table 1.3) the transition from the GS to the HS state is spin forbidden as ($\Delta S = 1 \neq 0$) and its intensity is relatively weak when com-

pared to that of GS to LS transition, which is spin allowed ($\Delta S = 0$), Figure 1.3. As a result, all the strong excitation bands in the shorter-wavelength side below 220 nm in Figure 1.3 were assigned to the spin-allowed GS to LS transitions of Tb^{3+}. Several weak excitation bands were also observed at the longer-wavelength side of the band at 211 nm, assigned to the second order bands of the Tb^{3+} LS excitations at 125, 120, and 116 nm. However, the sharp line at 257 nm and the weak band around 255 nm were assigned to the zero-phonon line and the vibronic sideband of the spin-forbidden HS transition, respectively. Similarly, *f-d* transitions for Dy^{3+}, Ho^{3+}, Er^{3+} and Tm^{3+} in $LiYF_4$ were reported by the authors [19].

1.6 Charge-transfer transition

Besides the intra- and inter-configurational transitions discussed above, other optical transitions include charge transfer (CT) (ligand-to-metal, LMCT or metal-to-ligand, MLCT) transitions [21–23].

The CT energy mainly depends on the optical electronegativities of the Ln^{3+} ions, which are related to the strength of the binding energy for the electron transferred from the ligand ions to the Ln^{3+} $4f^N$ shell [24]. Theoretical and experimental results

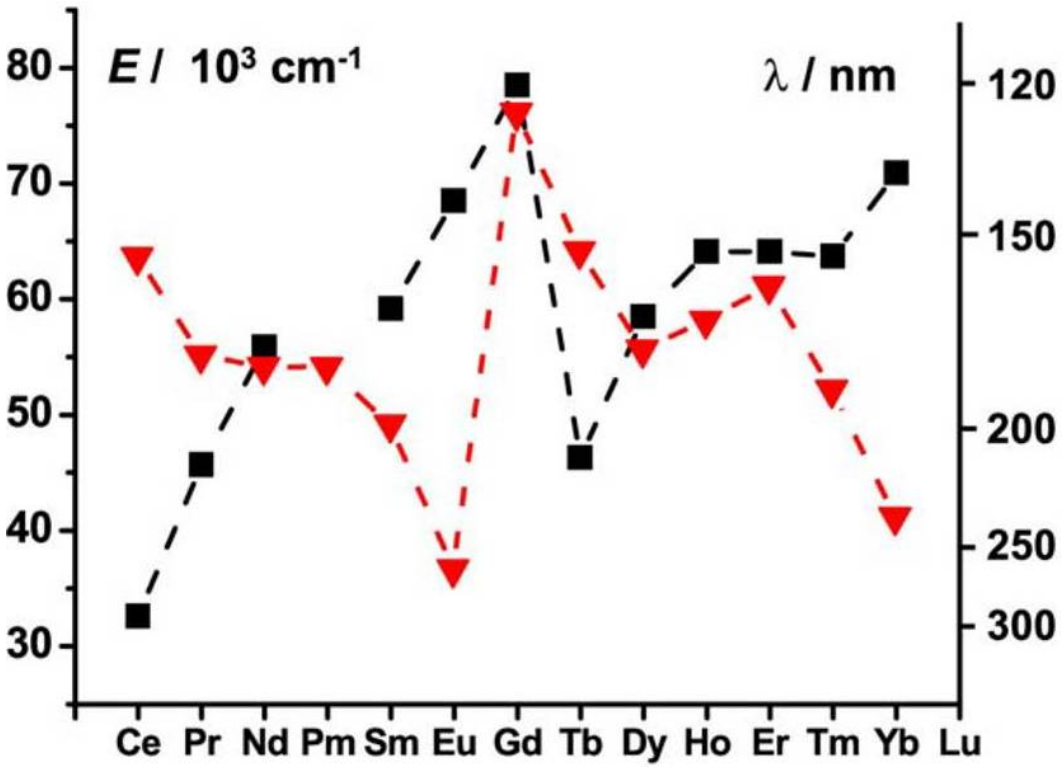

Figure 1.4: Energy of the 4f-5d transitions in Ln^{3+}:CaF_2 (squares) and of the 2p (O)-4f LMCT transitions (triangles), Ref. [7, 25] and references therein.

for the *f-d* and CT transition energies have been reported for Ln^{3+} ions in different

inorganic hosts [21, 26–29]. The studies showed that CT transition bands of Ln^{3+} in inorganic hosts have energies in the UV-region (Figure 1.4) and are relatively broad. For instance, the CT band in the excitation spectra monitoring the red emission of Eu^{3+} in oxides may be observed at energies between 4 and 6 eV, with 0.6 - 0.8 eV full-width-at-half-maxima, depending on the host material [21, 26]. It was proposed that CT occurs when an electron transfers from the oxygen ligand (2p orbital of O^{2-}) to the $4f^6$ orbital of Eu^{3+} resulting in an excited CT band where Eu^{3+} is in its excited $4f^6$ state, i.e., the ground $4f^7$ state of Eu^{2+}. In this case, however, the transferred electron should be still bound by the Coulomb potential of O^{2-} or of the hole in the valance band.

1.7 Energy transfer and photon up-conversion

1.7.1 Energy transfer

Energy transfer (ET) from a donor/sensitizer (D) ion to an acceptor/activator (A) one may occur between ions of identical species or of a different nature. Since the principles of ET are independent of the ion species (Ln^{3+} or any other type), we shall briefly describe here the most common ET processes [13, 30], which are also useful for the discussions in the forthcoming chapters. In photoluminescence spectroscopy the presence of ET can be detected by the emission and excitation spectra and/or the excited-state lifetimes. For instance, if ET from D to A exists the excitation spectrum obtained by monitoring the emission of A may show excitation peaks that belong to D or emission from A may be observed upon excitation in the absorption energy of D. Figure 1.5 is a schematic illustration of the different ET processes in a system consisting of a sensitizer and an activator [13].

i. Resonance energy transfer (Figure 1.5a). In this process, ion D goes from its excited state D* to its ground state D and thereby excites another ion A to its excited state A*; energy is fully conserved, i.e., D→D transition and A*→A transition have the same energy.

ii. Phonon-assisted energy transfer (Figure 1.5b). In this process, there is energy mismatch between the activator and the sensitizer; the A*→A transition occurs with the emission (for larger D*→D energy transition) or with the absorption (for smaller D*→D energy transition) of a phonon to conserve energy. This process is temperature dependent.

iii. Up-conversion (Figure 1.5c). In this process, two (or more) successive transitions in the donor system excite one acceptor ion to an energy level approximately twice (or more) the donor excited state energy level. For instance, the first photon of the D* state excites ion A to its excited state A* and a second photon excites A* to another excited state B*. The A*→B* transition may involve resonant and/or phonon-assisted energy transfer processes. The photon energy of the B*→A emission is larger than (approximately twice) the excitation energy of the

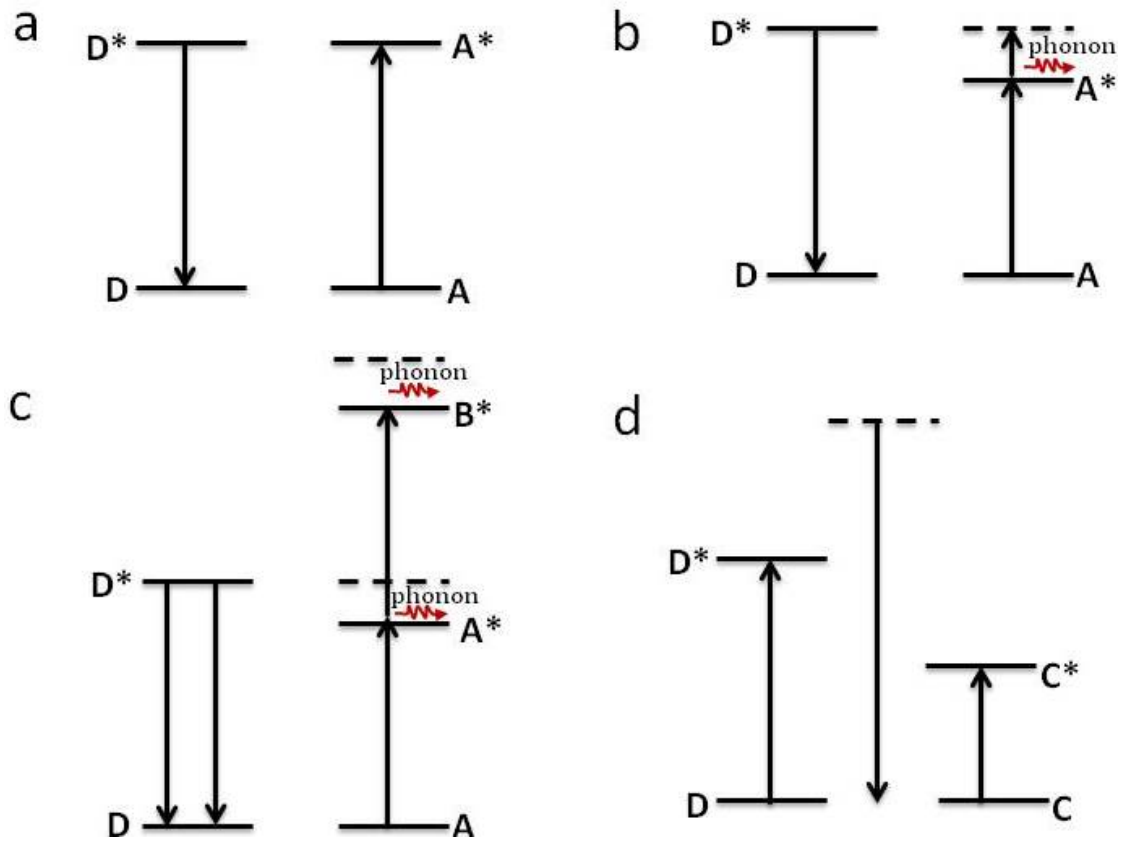

Figure 1.5: Schematic diagram for the various energy transfer processes: a) resonance energy transfer, b) phonon-assisted energy transfer with emission of a phonon, c) stepwise up-conversion by phonon-assisted energy transfer and d) two-ion emission. Adapted from Ref. [13].

D→D* transition, hence the name up-conversion. Indeed, there are several types of mechanisms for up-conversion processes which will be discussed later.

iv. Two-ion emission and absorption (Figure 1.5d). In a two-ion emission processes, two ions D and C decay simultaneously from their excited states D* and C*, thereby emitting a photon with energy equal to the sum of the excited state energies of the two ions; the reverse of this is a two-ion absorption processes whereby a photon is absorbed by D and C resulting in an excited state with energy equal to the sum of the excited state energies D* and C*. These processes are usually known as cooperative (emission or absorption) process and cooperative energy transfer when the sum of the excited state energy is transferred to another state (Figure 1.5c,d).

Energy transfer rate

Energy transfer rate from a donor to an acceptor may be determined using Fermi's golden rule [13, 30, 31]. This approach is, however, more appropriate for *resonance energy*

transfer because of the good spectral overlap between the emission band of the donor and the absorption band of the acceptor in which the overlap integral is non-vanishing. The overlap integral contains the emission and absorption spectral functions of the donor and the acceptor and may vanish when energy mismatch between the acceptor and the donor states exists [32], e.g., for phonon-assisted ET.

The interaction mechanisms responsible for resonance ET between the donor and acceptor ions can be of three types: electric multipole interaction (dipole-dipole, dipole-quadrupole or quadrupole-quadrupole), exchange interaction and virtual phonon exchange interaction [13]. Förster [33, 34] developed the first ET model based on the electric dipole-dipole interaction, which was later generalized and extended by Dexter [35, 36] who included exchange and higher-order multipolar interactions. The electric dipole-dipole and electron-exchange interactions have been extensively explored in the literature. The major difference between the Förster's and Dexter's models relies on the donor-acceptor distance R over which the interactions can occur. Förster resonance ET through electric dipole-dipole interaction takes place within R in the range of 5 - 100 Å, with the transfer probability proportional to R^{-6} [37]. On the other hand, ET by Dexter's electron-exchange interaction can take place (and is only efficient) over shorter values of $R < 5$ Å, whereby the transfer probability varying roughly exponentially with R.

1.7.2 Photon up-conversion

Photon up-conversion is a nonlinear optical process in which low-energy (e.g., infrared) photon is converted into high-energy (e.g., visible) photon *via* the successive absorption of two or more low-energy incident photons. The output intensity (I) of the emitted photon is proportional to the n^{th} power of the excitation power (P) of the incident photon, i.e., $I \propto P^n$, where n is the number of absorbed photons in the process [30], in contrast to the conventional down-shifting (fundamental) process which is independent of the intensity of the excitation photon. For comparison, the main differences among photon up-conversion, down-conversion and down-shifting processes are illustrated in Figure 1.6; the latter analogous to quantum-cutting process [38, 39] is indeed the inverse of the former. Associated with its nonlinearity, the major drawback of photon up-conversion is that it is efficient at relatively high excitation power of the incident photon [30]. Furthermore, the phonon energy of the host material significantly determines the up-conversion efficiency since the process is mostly phonon-assisted. Therefore, the choice of an appropriate host material, sensitizer and activator is crucial for efficient up-conversion emission. In this regard, in addition to their long excited-states, the Ln^{3+} ions provide excellent combinations of energy levels for the various energy transfer mechanisms leading to efficient photon up-conversion. As shown in Figure 1.7, up-conversion emissions occur *via* several mechanisms. The most common and relatively efficient up-conversion mechanisms are excited state absorption (ESA) and energy transfer up-conversion (ETU) [30, 40]. In a simple ESA, a photon is excited from the ground state to the excited state within a single ion through a ground state absorption (GSA) process and a second incident photon excites the previously excited

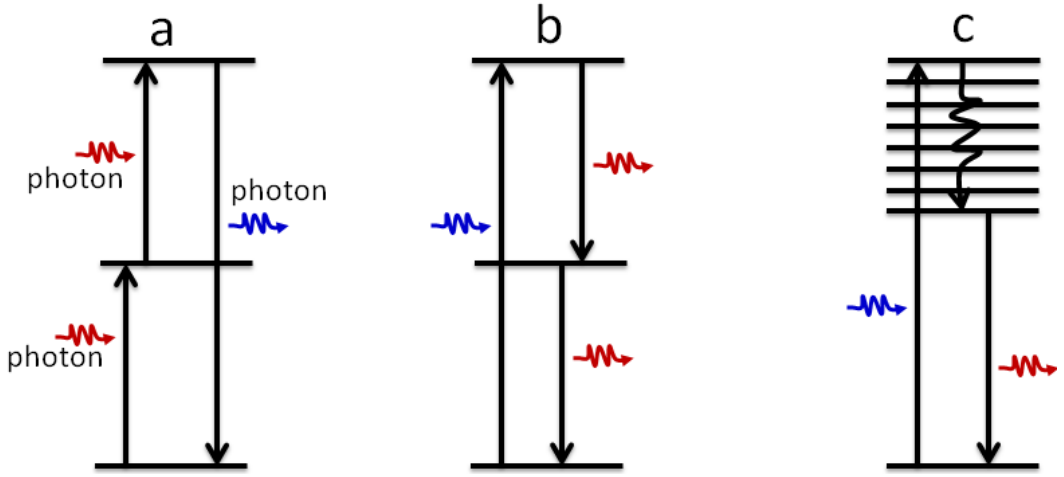

Figure 1.6: Schematic diagram for photophysical mechanisms: a) photon up-conversion, b) down-conversion and c) down-shifting.

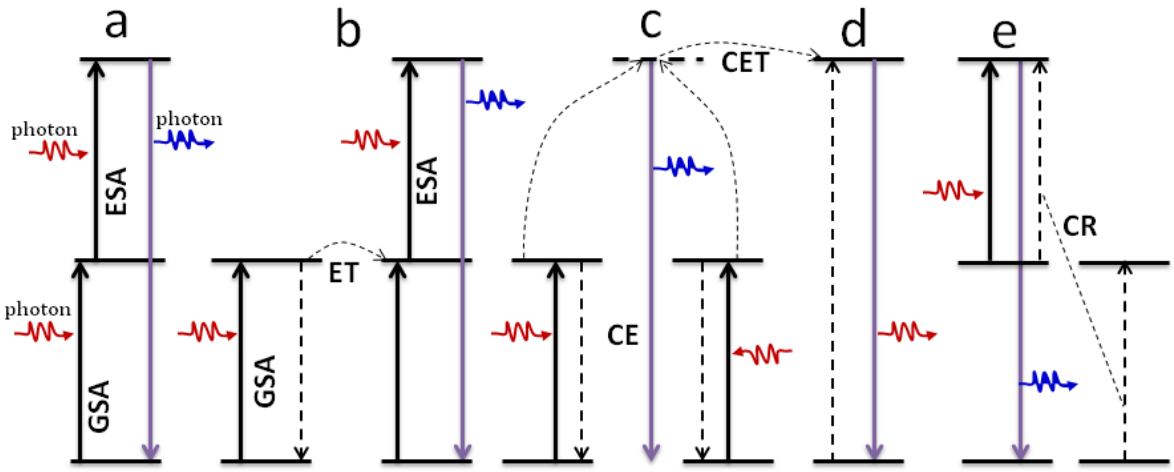

Figure 1.7: Schematic diagram for photon up-conversion processes: a) ground state absorption (GSA) followed by excited state absorption (ESA), b) GSA followed by energy transfer (ET) and ESA, known as energy transfer up-conversion (ETU), c) cooperative emission (CE), d) cooperative energy transfer (CET), e) photon avalanche process assisted with cross-relaxation (CR). Adapted from Refs. [30, 40]

.

photon into another higher excited state of the same ion, Figure 1.7a. In ETU, both the donor and accepter ions (e.g., Yb^{3+}/Er^{3+} system) may be present. The donor ion is excited *via* GSA and it may transfer its energy to an excited state of the nearby acceptor ion which, in turn, is then promoted into a higher excited state by e.g., ESA and another ET, Figure 1.7b. Other higher order and low efficient up-conversion processes include cooperative energy transfer (CET) and cooperative up-conversion emission (CUE). CET means two excited donor ions simultaneously transfer their energies to an excited state of the acceptor ion, Figure 1.7d. Alternatively, in CUE two excited ions

emit a photon with energy equal to the sum of the excited state energy of the ions, Figure 1.7c. Another photon up-conversion mechanism is a photon avalanche (PA) process which may be modeled by a simplified three-level system [40, 41], as shown in Figure 1.7e. It mainly exhibits the following typical features: i) the excitation photon energy is resonance with the energy gap between a metastable state and the next upper emitting state, ii) critical threshold pump power for photon emission and iii) time delay at threshold [30, 41]. The metastable state of the acceptor ion can be populated by an efficient cross-relaxation process from an excited-state of a donor and/or by a nonresonance GSA of the acceptor itself, Figure 1.7e. A subsequent incident photon further increases the population of the metastable state and eventually emission from the upper emitting state may be triggered at a certain threshold excitation power, Figure 1.7e.

1.8 Radiative/non-radiative transitions and lifetimes

The Einstein coefficient of spontaneous emission rate $A_{JJ'}$ between two manifolds J and J' within the $4f^N$ configuration is given by [9, 13, 15]:

$$A_{JJ'} = \frac{64\pi^4\nu^3}{3hc^3(2J+1)}[\frac{n(n^2+2)^2}{9}S_{ED} - n^3 S_{MD}] \tag{1.9}$$

where h is the Planck constant, c the speed of light, ν the frequency of the transition, n the refractive index of the medium, S_{ED} the electric dipole line strength and S_{MD} the magnetic dipole line strength. The dipole line strengths are determined by the matrix element of the respective transition operators. According to the Judd-Ofelt theory, S_{ED} and S_{MD} of a transition between two states Ψ and Ψ' are given by [9, 25]:

$$\begin{aligned} S_{ED} &= |<\Psi'|\overrightarrow{P}|\Psi>|^2 = -e^2 \sum_{\lambda=2,4,6} \Omega_\lambda |((4f^N)\Psi' J'\|U^\lambda\|(4f^N)\Psi J)|^2 \\ S_{MD} &= |<\Psi'|\overrightarrow{M}|\Psi>|^2 = \mu_B^2 |((4f^N)\Psi' J'\|\overrightarrow{L} + 2\overrightarrow{S}\|(4f^N)\Psi J)|^2 \end{aligned} \tag{1.10}$$

where $\overrightarrow{P}$ is the electric dipole operator, e the electron charge, Ω_λ the Judd-Ofelt intensity parameters ($\lambda = 2, 4, 6$), U^λ the irreducible unit tensor operator, $\overrightarrow{M}$ the magnetic dipole operator, μ_B the Bohr magneton, and $\overrightarrow{L} + 2\overrightarrow{S}$ the spin-orbit operator.

The inverse of the radiative lifetime τ_R of a given initial state is given by the sum of each $A_{JJ'}$ over all possible final states:

$$\tau_R^{-1} = \sum A_{JJ'} \tag{1.11}$$

However, the spontaneous emission of a certain energy level may also be accompanied by a non-radiative process characterized by a particular non-radiative transition rate W_{NR}. In this case, the total (observed) lifetime τ is expressed as:

$$\tau^{-1} = \sum (A_{JJ'} + W_{NR}) \tag{1.12}$$

Here, the contribution of the non-radiative transition to the total lifetime is strongly dependent on the energy separation between the upper emitting level and the next lower levels as well as the temperature of the sample. As was discussed, this is because a non-radiative process is mainly assisted by vibrational phonon or multiphonon absorption/emission processes. The theory of multiphonon emission predicts W_{NR} as a function of temperature [13]:

$$W_{NR}(T) = W_{NR}(T=0)(1 - exp(\frac{\hbar\omega}{kT}))^{-n} \tag{1.13}$$

where $\hbar\omega$ is the average phonon energy of the system under investigation, n the number of phonons emitted, k the Boltzmann constant and T the absolute temperature. This implies increasing the magnitude of the energy separation ΔE between which a transition takes place, increases the number of phonons required to bridge the separation, i.e., $n = \Delta E/\hbar\omega$, yielding a higher order multiphonon process. Therefore, a transition between two energy levels may be considered as a purely radiative only for large energy separation between the levels and at cryogenic temperatures. Under such conditions the calculated lifetime is roughly equal to the measured lifetime.

The radiative lifetime induced by either an electric dipole process or a magnetic dipole process may be determined using the following expressions [42]:

$$\begin{aligned} \tau_R &= \frac{1.5 \times 10^4 \ (s \ m^{-2})}{f_{ED}} \frac{\lambda_o^2 \ (m^2)}{(\frac{(n^2+2)^2}{9})n} \\ \tau_R &= \frac{1.5 \times 10^4 \ (s \ m^{-2})}{f_{MD}} \frac{\lambda_o^2 \ (m^2)}{n^3} \end{aligned} \tag{1.14}$$

where λ_o is the transition wavelength of light in vacuum, f_{ED} the electric-dipole oscillator strength of the transition and f_{MD} the magnetic dipole oscillator strength.

1.9 Summary

A brief history and etymology of rare earths and lanthanides are presented. The fundamental properties of Ln^{3+} optical transitions discussed in this chapter such as $4f^N \leftrightarrow 4f^N$ and $4f^N \leftrightarrow 4f^{N-1}5d$ transitions, charge-transfer transition, energy transfer and photon up-conversion, radiative and non-radiative transitions, and excited-state lifetimes are essential to understand and analyze the photoluminescent properties of the materials studied in the forthcoming chapters.

Chapter 2

Experimental Techniques

2.1 Introduction: Luminescence

The term *luminescence* was first introduced in the literature by Eilhard Wiedemann in 1888. Luminescence is defined as the emission of light from a substance not connected to heating or increasing of temperature. It can be induced by several mechanisms such as photon energy, electrical energy, X-ray and electron beams, and chemical and biological reactions. In this case, a descriptive prefix of the activating energy is usually added before the word luminescence. For instance, *photoluminescence* is the emission of light after excitation with photons; *cathodoluminescence* is when the light emission occurs under excitation with an electron beam; *radioluminescence* is due to excitation by high-energy electromagnetic radiation such as X-rays, γ-rays, α-rays or β-rays; *triboluminescence* is induced by a mechanical disturbance such as rubbing and fracture; *chemiluminescence* is as a result of a chemical reaction; *bioluminescence* is produced by chemical reactions inside an organism and so on [32, 43–45].

This chapter deals with photoluminescence (PL) and PL spectroscopy as it is the central characterization technique used in this thesis. An optical spectroscopy generally consists of excitation (light) sources, monochromators, detectors and data analyzer/collector. Hence, these components will be discussed in next sections. Other complimentary characterization techniques used in this thesis and their experimental conditions are described in appendix A.

2.2 Excitation light sources

Light (in the range of UV-visible to infrared spectral region) is essential for the study of optical properties of materials. For this purpose, different types of light sources may be used. Here, excitation sources widely employed in luminescence spectroscopy [45–48] such as incandescent lamps, gas or arc-discharge lamps and lasers are briefly discussed as follows.

2.2.1 Incandescent lamps

Incandescent lamps may be used as excitation sources in visible and infrared spectral regions [47]. These types of lamps are indeed widely used in household and commercial

lighting such as table lamps, car headlamps and flashlights. They operate based on an electrically-heated filament. The heated filament emits light with a continuous spectrum that depends on the filament temperature similar to that of blackbody radiation. For instance, in a typical tungsten filament lamp, the filament inside a glass envelope filled with an inert gas (argon or nitrogen) is electrically heated until it glows, which turns white-hot at temperature nearly 2800 K [44]. Incandescent lamps are, however, poor UV light generators and much of the power they consumed (over 90%) is wasted as heat rather than being emitted as light (photons) [46, 49]. They are used as color standards for other lamps. Halogen incandescent lamps use a much smaller quartz envelope and are more efficient than standard incandescent lamps.

2.2.2 Gas/arc-discharge lamps

In a gas-discharge lamp, an electric current passes through an ionized gas thereby electrons are excited to higher energy sates due to the collisions with gas and metal atoms in the lamp tube. Light in the infrared, visible, or ultraviolet region is emitted when the electron decay to their lower states. Fluorescent lamps are among gas-discharge lamps. The visible light in these lamps is obtained by converting the UV emission using a fluorescent coating on the inside wall of the glass tube of the lamp. The spectral feature of the emitted light from a gas-discharge lamp generally depends on the gas pressure; for instance, low-pressure lamps have sharp emission lines with typical characteristics of the gas atoms while high-pressure lamps have broad spectral features.

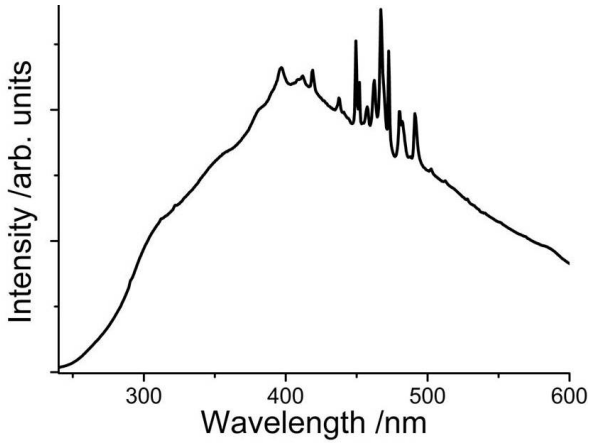

Figure 2.1: Typical emission spectrum of a 450 W Xe-arc lamp used in our lab.

Arc lamps also operate in a similar principle for gas-discharge lamps but the gas is ionized in an electric arc between two electrodes. A common example of arc lamps used in PL spectroscopy as an excitation source is a xenon arc lamp which produces light in the range of UV-visible to infrared region. Figure 2.1 shows typical spectral profile of a 450 W xenon-arc lamp used as steady-state excitation source in one of the Fluorologs installed at the University of Aveiro, CICECO (Figure 2.6). Other discharge lamps include hydrogen or deuterium, mercury, argon, neon and krypton. It is important to

note that a pulsed light can also be obtained from gas-discharge lamps but the output power is usually much lower than the one obtained from a laser [47].

2.2.3 Lasers

The term *laser* is an acronym for *Light Amplification by Stimulated Emission of Radiation*. Lasers are important sources of artificial light and have tremendous applications in the field of optical spectroscopy. In particular, light from a laser is notable for its high degree of spatial and temporal coherence characterized by high spectral density of excitation power, small divergence of the radiation beam, and polarized beam at a single frequency with longer coherent length. A laser beam may be radiated in continuous and/or (ultra fast) pulsed modes. Depending on the operating principle and/or the type of materials used, several types of lasers are available such as semiconductor lasers, solid-state lasers, gas lasers, photonic crystal lasers, fiber lasers and dye lasers [49]. The former type is used in this thesis.

2.3 Monochromator

A monochromator is an essential element of many optical spectroscopic techniques [44, 47]. Figure 2.2 shows a typical diffraction-grating monochromator with a Czerny-Turner configuration. This type of monochromator design consists of an entrance slit for polychromatic light, the collimator mirror (a concave mirror) for making parallel beams of the polychromatic light, the grating for the collimated light, the focusing mirror for the diffracted light (another concave mirror) and an exit slit. At the exit slit, a monochromatic wavelength of interest can be selected/scanned by adjusting the angle of the rotating grating with respect to the direction of the incident light.

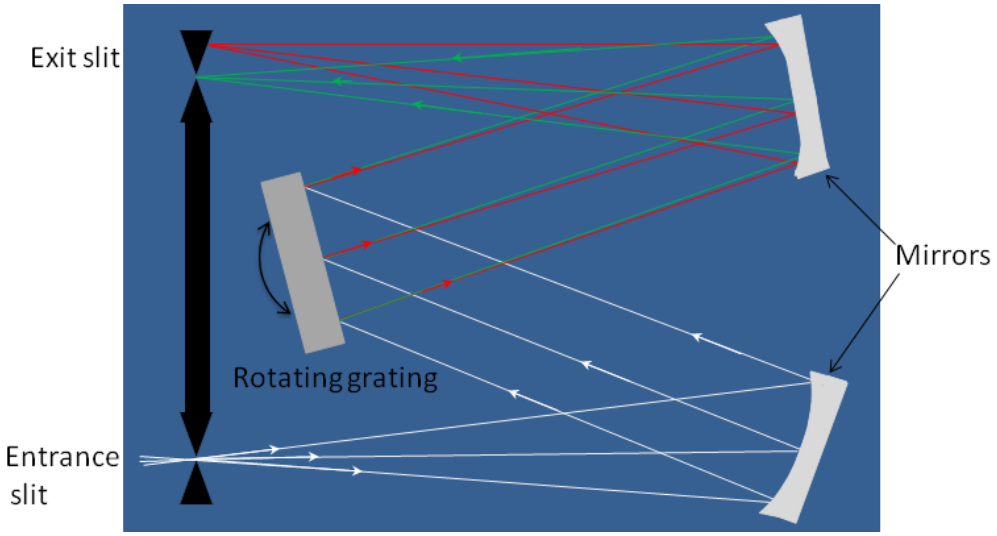

Figure 2.2: Schematic representation of a monochromator in a Czerny-Turner configuration.

2.3.1 Diffraction grating

A diffraction grating consists of a number of grooves that may depend on the spectral region of the light to be diffracted [50, 51]. Gratings are manufactured to operate with maximum efficiency at a designated angle known as *blaze angle* θ, the direction in which maximum grating efficiency is achieved (Figure 2.3). Similarly, the blaze wavelength is defined as the wavelength at which the grating operates with its highest efficiency. Diffraction of light with a grating may be explained using an echelette-type planar diffraction grating shown in Figure 2.3 [47]. Such a grating has a saw-tooth shape. The blaze angle θ is the angle between the grating plane and the saw-tooth plane. The grating constant d is defined as the pitch of the grooves. The incident angle and the diffraction angle with respect to the line normal to the grating plane are denoted by α and β, respectively. Constructive interference of the light occurs when the following geometrical relation is satisfied [47, 50]:

$$m\lambda = d(\sin\alpha + \sin\beta), \qquad (m = 0, \pm1, \pm2, \pm3, ...) \tag{2.1}$$

where m is called the diffraction order and λ is the wavelength of incident light. Zero-order diffraction occurs for $m = 0$ corresponding $\alpha = -\beta$, $m = \pm1$ the first-order, $m = \pm2$ the second-order and so on.

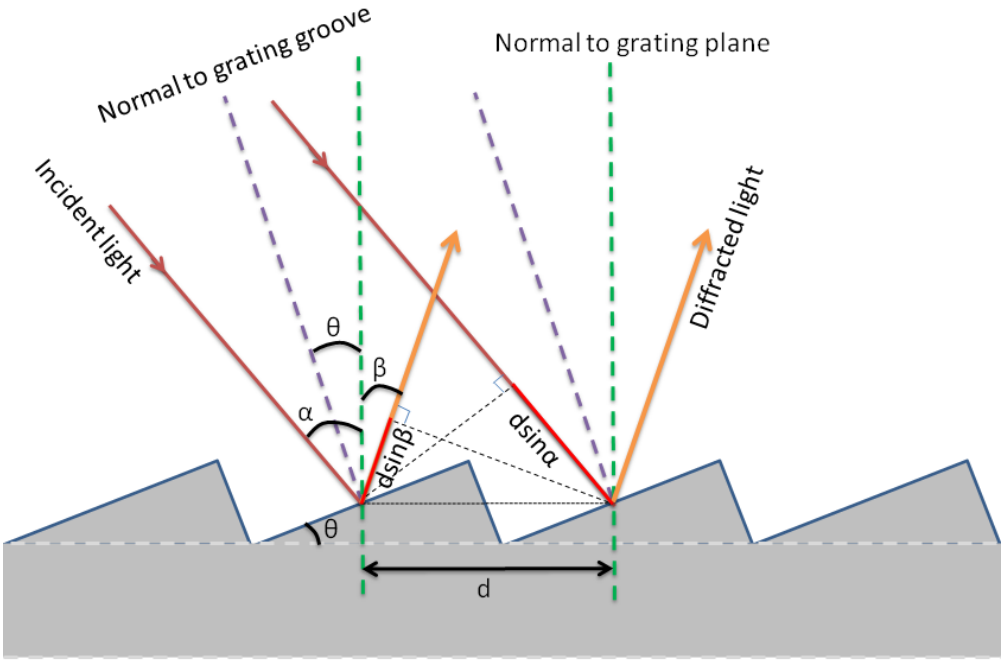

Figure 2.3: Schematic representation of a echelette-type planar diffraction grating.

For the Littrow configuration, in which the light is diffracted back toward the direction from which it came (i.e., $\alpha = \beta$) and the beams are perpendicular to the plane of the grating grooves (i.e., $\alpha = \beta = \theta$), Equation 2.1 is expressed as [46]:

$$m\lambda = 2d\sin\theta \tag{2.2}$$

Therefore, first-order diffracted light is maximized at $m\lambda = 2d\sin\theta$, which is called the blaze wavelength. From equation 2.2, it is evident that $m\lambda =$ *constant* for a grating of given α, β, and d. This implies that if the diffraction order m is doubled, λ is halved, m is tripled, λ one-third etc. For instance, if a light source emits a continuum of wavelengths from 20 nm to 1000 nm, then at the physical location of 800 nm in first order, wavelengths of 400, 266.6 and 200 nm will also be available to the same detector [51]. Therefore, in order to monitor only light at 800 nm, filters must be used to eliminate the higher orders.

The major parameters of a grating or a spectroscopic system include the **bandpass**, **dispersion** and **resolving power** [46, 50, 51]. A purely monochromatic beam with line profile may appear to have a finite width profile by analyzing it with a monochromator (a spectrometer), attributed to the instrumental line profile. The bandpass is then defined as the full-width-at-half-maximum (fwhm) of the output beam assuming monochromatic light. The relationship between the recorded spectrum $F(\lambda)$, the instrumental line profile $P(\lambda)$ and the real spectrum of the source $B(\lambda)$ is given by [51]:

$$F(\lambda) = B(\lambda) \cdot P(\lambda) \tag{2.3}$$

As was mentioned, a polychromatic light incident on a grating will be separated into its component wavelengths through diffraction. Linear (or angular) dispersion of the grating is thus a measure of the separation between the diffracted light of different wavelengths. The angular dispersion D of the grating can be obtained by differentiating Equation 2.1 with respect to the diffraction angle β [46, 47, 51]:

$$D = \frac{d\beta}{d\lambda} = \frac{mk}{\cos\beta}, \qquad (rad \cdot nm^{-1}) \tag{2.4}$$

where k is the groove density (grooves/mm) of the grating.

Similarly, the linear dispersion of a monochromator refers to the ability of the monochromator to resolve fine spectral detail at the exits slit. For instance, the dispersion of 0.1 nm spectral segment at the exit slit over 1 mm. In this case, the linear dispersion is the product of the angular dispersion D of the grating and the effective focal length f of the monochromator [50]. Accordingly, if two spectral lines separated by $d\lambda$ (nm) at the exit slit are separated by a spatial distance of dx (mm) across the slit, the reciprocal linear dispersion perpendicular to the diffracted beam at a central wavelength, λ, is given by [46]:

$$\frac{d\lambda}{dx} = \frac{1}{f}\frac{d\lambda}{d\beta} = \frac{1}{fD} = \frac{1}{f}\frac{\cos\beta}{mk}, \qquad (nm \cdot mm^{-1}) \tag{2.5}$$

For example, a grating with 1200 grooves/mm in first-order would have an angular dispersion of 1.2×10^{-3} rad/nm and a reciprocal linear dispersion of $\sim$0.8 nm/mm for a 1 m monochromator, taking into account $\cos\beta \approx 1$. Unlike reciprocal linear dispersion, angular dispersion is independent of the size of the monochromator, i.e.,

focal length.
Another important parameter is resolving power (or resolution power) of the grating [50]. The resolving power is the ability of the grating to separate two adjacent spectral lines of central wavelength λ. Two peaks are considered resolved if the distance between them is such that the maximum of one falls on the first minimum of the other, which is called the Rayleigh's criterion [46, 51]. If the minimum spectral distance between two spectral lines of equal intensity in the vicinity of the central wavelength λ (nm) that can be resolved by the grating is $d\lambda$ (nm), the theoretical resolving power R is then given by [46, 50]:

$$R = \frac{\lambda}{d\lambda} = mkW_g = mN \tag{2.6}$$

where W_g is the illumination width of the grating and N is the total number of grooves on the grating. R is a dimensionless quantity. Using $mk = \frac{(\sin\alpha + \sin\beta)}{\lambda}$ and $|\sin\alpha + \sin\beta| < 2$, the maximum attainable resolving power R_{max} is:

$$R_{max} = \frac{2W_g}{\lambda} \tag{2.7}$$

Gratings with high groove density (300 - 2000 grooves/mm) provide high resolution and low dispersion and are commonly used in the UV-visible region. Low groove density gratings (10 - 200 grooves/mm) provide low resolution and high dispersion, and they are usually used in the infrared region [52].

2.4 Light detectors

Light sources and dispersion of a polychromatic light into a monochromatic beam were briefly discussed. In this section we will described a few examples of light detecting devices. Light detectors commonly used for spectroscopic purpose include photomultiplier tubes (PMTs), solid-state photodiodes and charge-coupled devices (CCDs). These devices operate with the same basic principle to detect light in which the light energy is first converted into electrical energy (photoelectrons) as illustrated in Figure 2.4. PMTs and solid-state photodiode are classified as single-channel detectors. A single-channel detector has a single light-detecting element and the detector should be placed in front of the exit slit of a monochromator to measure the light intensity at a given wavelength. CCDs are typical examples of a multichannel detector, which has multiple light-detecting elements arranged linearly or in two dimensions, with each element operating individually [47]. The width and height of each light-detecting element are equivalent to the width and height of the exit slit in a monochromator. Thus, a multichannel detector can be placed at the focal plane of the light exit of a monochromator with the exit slit removed and it can measure a wide spectral range at a time. Here, we shall describe in detail the operating principle of a PMT detecor and its components.

2.4.1 Photomultiplier tubes (PMTs)

PMTs are expensive detectors. Yet, they are widely used in PL spectroscopy because of their high sensitivity and stability [44, 46]. A schematic diagram of a side-on type PMT is shown in Figure 2.4. The photon to be detected passes through an optical glass or quartz window that covers a photosensitive surface called a photocathode, which generates electrons due to the absorption of incident photons. These initial electrons are accelerated and multiplied many fold by a chain of electrodes known as metal channel dynodes. Finally, all the amplified electrons arrive at an anode or collection electrode where the output electrical signal may be measured by an external current meter. The aforementioned components of a PMT tube are sealed in a vacuum tube. An external power supply is also applied, which produces an electric field between the photocathode and first dynode, between the dynodes, and between the last dynode and the anode. The voltage between the dynodes is divided by external resistors. The detected current depends on the number of electrons ejected from the photocathode and the gain of the PMT. The gain (current amplification) is defined as the number of electrons collected at the anode relative to the number of electrons ejected from the photocathode. Therefore, the gain of a PMT depends on the electron multiplication factor of each dynode and the total number of dynodes of the PMT. For instance, if the multiplication factor is 2 and the number of dynodes is 8, then the gain of the PMT will be 2^8. The gain is also strongly dependent on the external applied voltage, which may increase the acceleration filed of the electrons when the voltage is raised which, in turn, may increase the multiplication factor. Gain in the range of 10^5 - 10^8 can be obtained for PMTs [48].

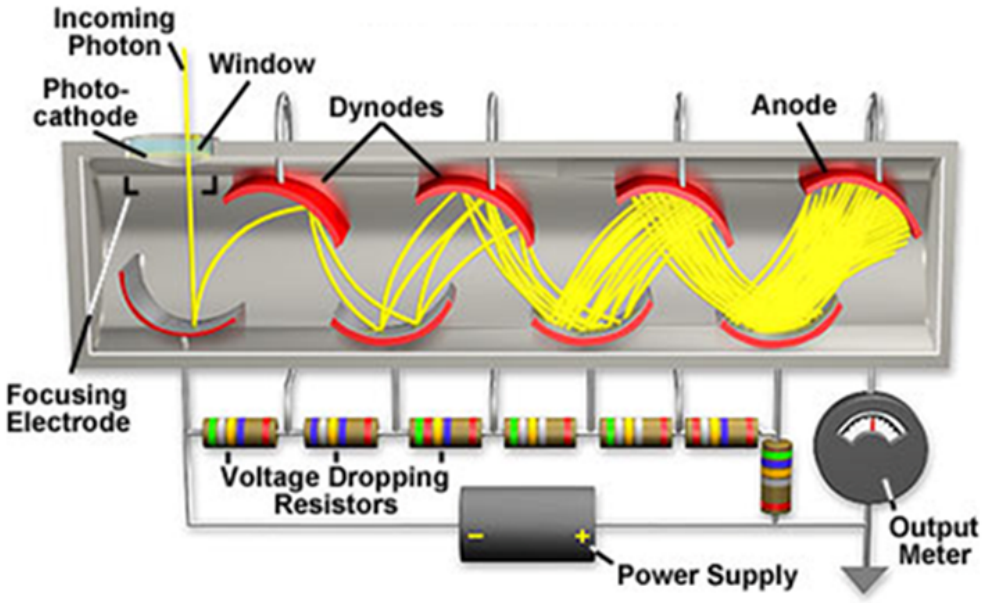

Figure 2.4: Schematic representation of a side-on type photomultiplier tube (PMT) [53].

The major parameters of a PMT includes the spectral response, cathode radiant sensitivity (S) and quantum efficiency (QE), which are determined by the composition of

the photocathode of the PMT. QE (usually expressed in %) is defined as the ratio of the number of photoelectrons emitted by the photocathode to the number of incident photon. S (A/W) is the photocathode current produced in response to an incident light power. Both the QE and S are dependent on the wavelength of the incident photons, known as the spectral response characteristic [54], related by:

$$QE(\%) = \frac{1240 \times S(A/W)}{\lambda(nm)} \times 100\% \tag{2.8}$$

Figure 2.5 shows a typical spectral response (185 to 900 nm) of a R928 PMT used in our lab. As can be seen from the graph, both the QE and S significantly decrease above 800 nm. The maximum QE is 25.42% at 260 nm.

A PMT may generate current even without the absorption of light, which is known as dark current originating from thermionic emission of the PMT. Thus, dark current may be reduced by decreasing the temperature of the PMT. The sensitivity and quantum efficiency of the PMTs drop to zero above 900 nm, Figure 2.5. In this case, suitable detectors for the infrared region, e.g., photodiodes, may be used.

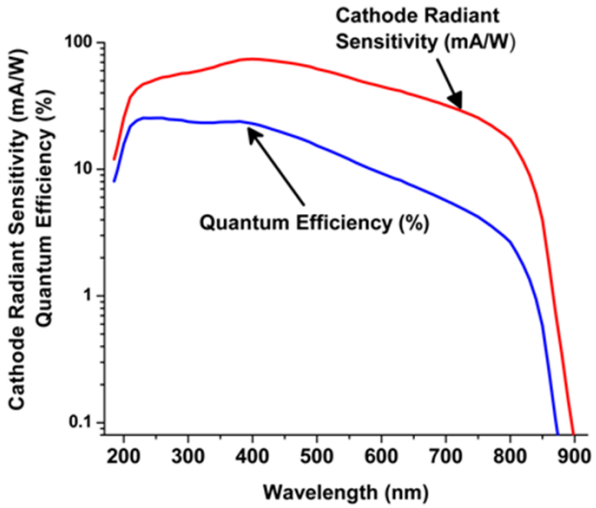

Figure 2.5: Typical spectral response of a side-on R928 PMT used in our lab.

2.5 Photoluminescence spectroscopy: Experimental setup

This section presents the experimental setup for the PL measurements used in this thesis and the measurement principles. Figure 2.6 shows a schematic representation of one of the PL spectroscopes installed in the Department of Physics, University of Aveiro, CICECO. The major components in this spectroscopy have been discussed in the previous sections. Briefly, the spectroscopy is a Fluorolog®-3 Model FL3-2T

with double excitation monochromator and single emission monochromator (Triax 320) fitted with gratings used in UV-Vis and NIR regions. The double excitation monochromator has a Czerny-Turner configuration (Figure 2.6c), fitted with 1200 grooves/mm ruled gratings blazed at wavelength 330 nm, band pass from 0 to 5 nm, dispersion 2.1 nm/mm, and 3 slits. The single emission monochromator (Figure 2.6e) also has Czerny-Turner configuration fitted with a 1200 grooves/mm grating blazed at 500 nm, dispersion 2.6 nm/mm, and band pass from 0 to 18.5 nm for the UV-Vis region and a 600 grooves/mm grating blazed at 1 μm, dispersion 5.2 nm/mm and band pass from 0 to 37 nm for the NIR region; the three slits are from 0 to 7 mm and the two gratings are on an automated turret. PMT R928 detector (Figure 2.6f) in the UV-Vis range, 200 - 900 nm, and PMT H9170-75 detector (Figure 2.6g) in the NIR range, 950 - 1700 nm, are used for steady-state and phosphorescence spectral acquisitions. The

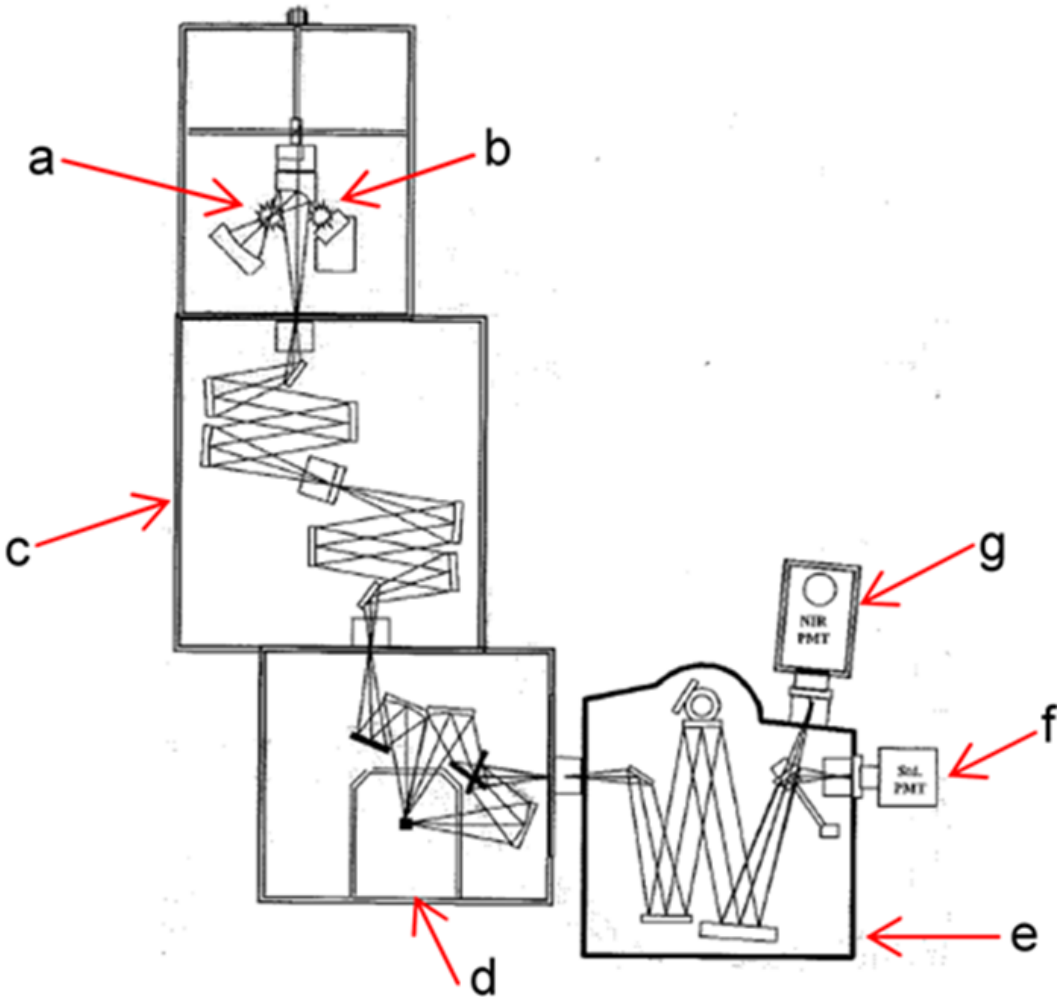

Figure 2.6: Schematic diagram for the PL spectroscopy: a) 450 W xenon-arc lamp, b) xenon-mercury pulsed lamp, c) double excitation monochromator, d) sample compartment and cryostat, e) single emission monochromator, f) UV-Vis emission detector, and g) near infrared (NIR) emission detector. Adapted from Ref. [55].

excitation sources (Figures 2.6a,b) are a 450 W high pressure xenon-arc lamp (con-

tinuous emission) and xenon-mercury pulsed lamp (6 μs pulse) for steady state and phosphorescence measurements, respectively. External excitation sources for instance, a continuous laser beam can also be used as an excitation source. A helium closed-cycle cryostat with a vacuum system composed by rotary and diffusion pumps (from Edwards Company) is used to carry out measurements at low temperature up to 11 K and at pressure in the range of $10^{-5}-10^{-6}$ mbar. A Lakeshore 330 auto tuning temperature controller and a resistance heater at the cold end of the cryostat allow controlled variation of temperature. Acquisition of the PL data requires little or no sample preparation. The sample can be solution, solid, film or powder form. Powder samples are usually mounted on a solid sample holder.

2.5.1 Steady-state photoluminescence

A steady-state emission spectrum of a phosphor is measured by continuously exciting the phosphor at a fixed excitation wavelength which may correspond to one of the peaks in the excitation spectrum of the phosphor. The emission monochromator scans in a range of wavelengths and the spectral data may contain the emission intensity as a function of the wavelength. In this case, if the excitation source is a continuous lamp, e.g., xenon-arc lamp (Figure 2.1), an excitation monochromator must be used to select a single excitation wavelength. To measure a steady-state excitation spectrum of the phosphor, the emission monochromator is fixed at a particular emission wavelength (usually corresponding to one of the emission peaks of the phosphor if known) while the emission intensity of the fixed wavelength is recorded as a function of the excitation wavelength. An excitation spectrum reveals the energy levels (or bands) that are involved in the emission of the fixed wavelength.

2.5.2 Time-resolved photoluminescence

As the name indicates, the main difference between steady-state and time-resolved measurements is the excitation mode of the light source. In the former, a continuous excitation source is required while in the later a pulsed excitation coupled with time sensitive detecting system is employed. Time-resolved (lifetime) measurement is essential and routinely utilized for analyzing the excited-state dynamics of phosphors that may contain multiple emitting centers.

Figure 2.7 depicts the principle of time-resolved photoluminescence measurement with some of the important parameters such as excitation pulse, delay time and measurement time [56]. To acquire time-resolved spectra, the intensity of the emission/excitation spectra is recorded as a function of wavelength after an appropriate delay time is enforced. Only those emission/excitation intensities with lifetime longer than the delay time are thus captured. For a phosphor with several emitting centers, this approach is particularly suited for precise measurements of long-lived emission intensities which are coexisting with those of short-lived background (or unwanted) intensities. In other words, for a phosphor composed of multiple emitting centers, the short-lived background (or unwanted) emission may be eliminated right before measuring the long-lived

emission by applying an appropriate delay time.

The lifetime (or emission decay curve) of an emitting level is measured after the applied delay time is completed and the emission intensity is recorded as a function of time (with a series of delay increment). The selection of the delay time, the pulse width of the excitation light and the measurement time are therefore the very important parameters that should be taken into account during time-resolved (lifetime) measurement. For instance, if the delay time is too long, the emission intensity of the desired emitting center may decrease to the background noise level.

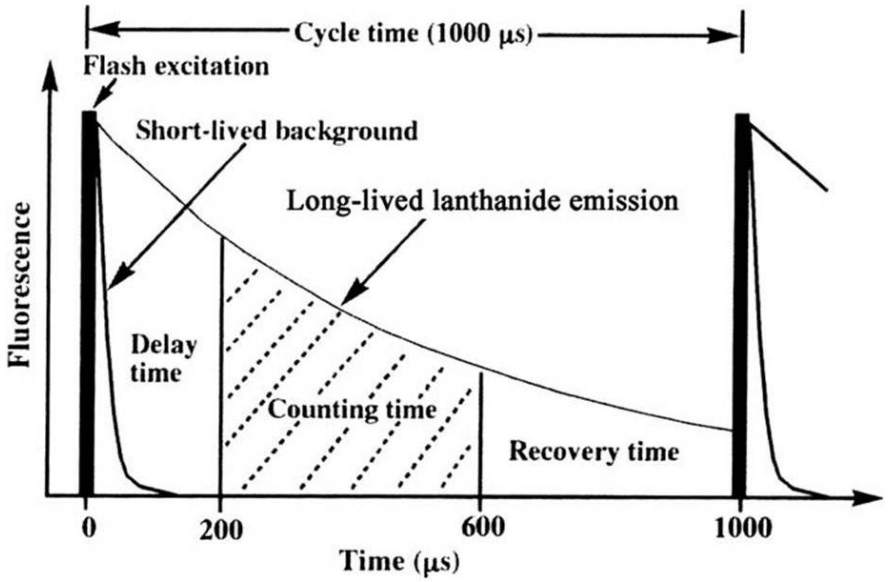

Figure 2.7: Principle of time-resolved spectroscopy with delay time of 200 μs, counting time of 400 μs, and cycle time of 1000 μs [56].

For a simple two-level energy system, the emission decay curves essentially possess exponential nature and the rate equation is given by:

$$\begin{aligned} \frac{dN(t)}{dt} &= (A_R + W_{NR})N(t) \\ N(t) &= N(0)exp(\frac{t}{(A_R + W_{NR})}) = N(0)exp(\frac{t}{\tau}) \end{aligned} \tag{2.9}$$

where $N(t)$ and $N(0)$ are the populations of the emitting level at time t and $t = 0$, respectively, A_R the radiative rate, W_{NR} the non-radiative rate, τ the lifetime. However, the measurable parameter is the emission intensity I. The intensity I can substitute for N in Equation 2.9 since N is proportional to I. The lifetime of emission from a particular energy level is thus readily calculated by fitting the experimental data with Equation 2.9. In general, the emission decay curve may not follow a single-exponential. It may rather be characterized by two or more exponentials or may have a more complicated relations with time, for instance, depending on the nature of the emitting centers and energy levels.

2.6 Summary

This chapter provides a brief introduction to the different types of luminescence with emphasis on photoluminescence which is induced by photon excitation. The basic components including light sources, monochromators, and detectors, and the operating principles of photoluminescence spectroscopy, the main experimental techniques used for the characterization of materials presented in next chapters, are discussed. Photoluminescence spectroscopy is important to study steady-state (time-resolved) emission and excitation spectra, and excited-state lifetimes of light-emitting materials upon photon excitation.

Chapter 3

Emission-decay Curves, Energy-transfer, and Effective-refractive Index in $(Gd,Eu)_2O_3$ Nanorods

3.1 Introduction

The study[1] presented in this chapter was broached by the intriguing photoluminescence properties of $(Gd,Eu)_2O_3$ nanotubes observed by the former PhD student [57], such as the anomalous thermalization of the $^7F_1 \rightarrow {}^5D_1$ transition and the longer $^5D_0$ decay time of Eu^{3+} associated with the reduction in size of the host nanocrystal.

As will be discussed in the next section, cubic Gd_2O_3 contains two non-equivalent cation sites, C_2 (*noncentrosymmetric*) and S_6 (*centrosymmetric*), in a 3:1 ratio. The Eu^{3+} energy levels in the two sites are, thus, quite different and energy-transfer occurs between them. The emission and excitation spectra of Eu^{3+} in cubic Gd_2O_3 are well-documented in the literature [58–61]. In this system, however, no analysis of Eu^{3+} $^5D_1(C_2)$ and $^5D_0(S_6)$ emission-decay curves and energy-transfer mechanisms responsible for the rise-time component of the $^5D_0(C_2)$ emission-decay curve is available [61–67]. In particular, evidence for the $^5D_0(C_2)$ rise time of $(Gd,Eu)_2O_3$ nanostructures (including nanotubes and nanorods) is missing.

Herein, the $^5D_0(C_2)$ and $^5D_1(C_2)$ emission-decay curves, the $^5D_1(C_2)$ to $^5D_0(C_2)$ inter-level relaxation (or inter-level energy transfer), and the inter-site energy-transfer pathways feeding the $^5D_0(C_2)$ level of Eu^{3+} in cubic Gd_2O_3 nanorods are investigated. The path responsible for the observed rise time in the $^5D_0(C_2)$ emission-decay curve is identified. The effect of the Eu^{3+} concentration (0.30, 1.01, 2.78 and 4.60 mol%) and temperature on the $^5D_1(C_2)$ and $^5D_0(C_2)$ lifetimes are analyzed. It is shown that the $^5D_0(C_2)$ lifetime is easily tuned by varying the dispersion/compactness of the nanorods in air, and this is attributed to the size of the nanorods and the effective-refractive index of the medium surrounding Eu^{3+} ions.

[1] **M. L. Debasu**, D. Ananias, A. G. Macedo, J. Rocha, L. D. Carlos, Emission-decay curves, energy-transfer and effective-refractive index in Gd_2O_3:Eu^{3+} nanorods. *J. Phys. Chem. C* 115, 15297-15303, 2011.

3.2 Rare earth sesquioxides

Rare earth sesquioxides (RE_2O_3), are among the most thermally stable materials with melting point in the range of 2200 - 2500 ^oC [68]. They are usually formed by calcination (in air) of the RE precursors such as oxalates, carbonates, nitrates and hydroxides [69]. For instance, cubic Gd_2O_3 nanocrystals can be obtained after calcination of the hexagonal $Gd(OH)_3$ structure at 700 ^oC in air. In general, sesquioxides exhibit five polymorphisms depending on temperature and/or pressure. The three structural types designated as the A-type (hexagonal, space group P-3m1), B-type (monoclinic, C/2m), and C-type (cubic, Ia-3) are commonly reported at lower temperatures below 2000 ^oC and at ambient pressure [68,70]. Other polymorphisms include H-type (hexagonal, $P6_3/mmc$) and X-type (cubic, Im-3m) formed at elevated temperatures above 2000 ^oC. It is important to note that such polymorphism also strongly depends on the type (size) of the RE metal and pressure [71]. For example, an irreversible structural transformations from the cubic phase (7.0 GPa) to a hexagonal high-pressure phase (15.0 GPa) which, in turn, transformed to a monoclinic structure after release of pressure was reported for Gd_2O_3 [70]. For further information, the reader is recommended comprehensive reviews of RE sesquioxides in Refs. [68, 69].

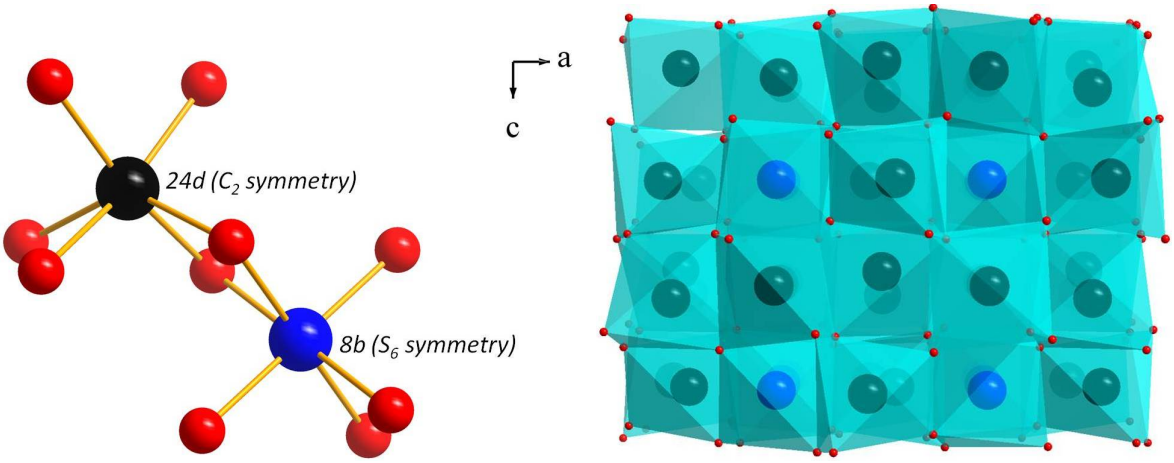

Figure 3.1: Cubic C-type structure of Gd_2O_3: (Left) coordination geometry of the 24d (C_2 symmetry) and 8b (S_6 symmetry) sites of Gd^{3+} and (Right) polyhedral representation. Black and blue balls stand for the 24d and 8b sites of Gd atoms, respectively, and red balls represent O atom.

Emphasis shall be given to cubic C-type structure as it is more relevant to the present chapter. This type of structure is of the cubic bixbyite type, mineral of $(Fe,Mn)_2O_3$ [69,72]. It can be described as a doubled-edge fluorite, CaF_2, structure with one-fourth of the metal atoms having oxygens missing across the body-diagonal and three-fourths having oxygens missing across the face-diagonal. This arrangement constitutes two non-equivalent cation sites known as 8b (S_6 symmetry) and 24d (C_2 symmetry), with three times as many of 24d sites as 8b sites. As illustrated in Figure 3.1 (left panel), both 8b and 24d sites are in six-fold coordination [73]. The former is octahedrally coordinated with the six oxygen atoms located at the same bond distance *ca.* 2.3283

Å from the metal center, forming three pairs of oxygen-metal-oxygen angle *ca.* 180^o. The latter, however, has an irregular coordination with all oxygen-metal-oxygen angles different from 180^o and three distinct pairs of metal-oxygen bond distance ca. 2.2933, 2.3058, and 2.3837 Å. Consequently, such coordination induces lack of inversion symmetry about the metallic center for C_2 site (*noncentrosymmetric*) while S_6 site is *centrosymmetric*. The photoluminescence properties of emitting cations residing in the two sites are thus quite different which will be presented in detail in this chapter. The polyhedral representation of C-type cubic Gd_2O_3 is shown along [010] direction in Figure 3.1 (right panel).

RE_2O_3 nanoparticles have received much attention in the last decade due to their potential applications in wide range of areas including bioimaging and temperature sensing. For instance, $(Gd,Eu)_2O_3$ nanoparticles as reporters in optical imaging of antibody micropatterns and fluorescent labels were first reported by Nichkova et al. [74, 75]. Bimodal contrast agents of $(Gd,Ln)_2O_3$ (Ln = Tb and Yb,Er) nanorods for optical and magnetic resonance imaging were demonstrated by Das et al. [76]. Hemmer et al. [77,78] evaluated the *in vitro/in vivo* bioimaging potential of $(Gd,Yb,Er)_2O_3$ nanostructures, along with cytotoxic analysis. Liu and co-authors [79] showed a multimodal nanoprobe based on $(Gd,Yb,Er)_2O_3$ up-conversion nanorods combining optical, magnetic resonance and X-ray computed tomography imaging. In a similar study, the *in vitro/in vivo* optical and magnetic resonance imaging as well cytotoxicity test were assessed using $(Gd,Yb,Er)_2O_3$ and $(Gd,Yb,Tm)_2O_3$ up-conversion nanoparticles [80].

This chapter aimed at both understanding how in Ln^{3+}-containing nanostructures (interlevel and intersite) energy transfers that feed a given (emitting) energy level determine its lifetime and confirming that the latter depends on the effective-refractive index and polarizability of the milieu surrounding the ions. The control of the lifetime values is an important factor in the development of many applications of Ln^{3+}-doped nanostructures, for instance, immunoassay purposes.

3.3 Synthesis of Ln^{3+}-doped Gd_2O_3 nanorods

Eu^{3+}-doped cubic Gd_2O_3 nanorods were prepared *via* wet-chemical route following a modified procedure described in Ref. [66]. The procedure is schematically illustrated in Figure 3.2. In a typical synthesis of $(Gd_{0.97}Eu_{0.03})_2O_3$ nanorods, aqueous solutions of $Gd(NO_3)_3$ (9.00 mL, 0.4 M), and $Eu(NO_3)_3$ (0.56 mL, 0.2 M) were mixed with distilled water (40 mL) in a 250 mL round-bottom flask. Aqueous NH_3 (30 mL, 25 wt%) was added to the mixture under magnetic stirring at room temperature. The resulting white solution was put in an ultrasonic water bath for 3 minutes and then vigorously stirred again for 10 minutes at room temperature. The solution was then heated to 70 ^{o}C under continuous magnetic stirring for 16 hours. After 16 hours, the temperature was turned off and the solution was allowed to cool down to room temperature. The resulting

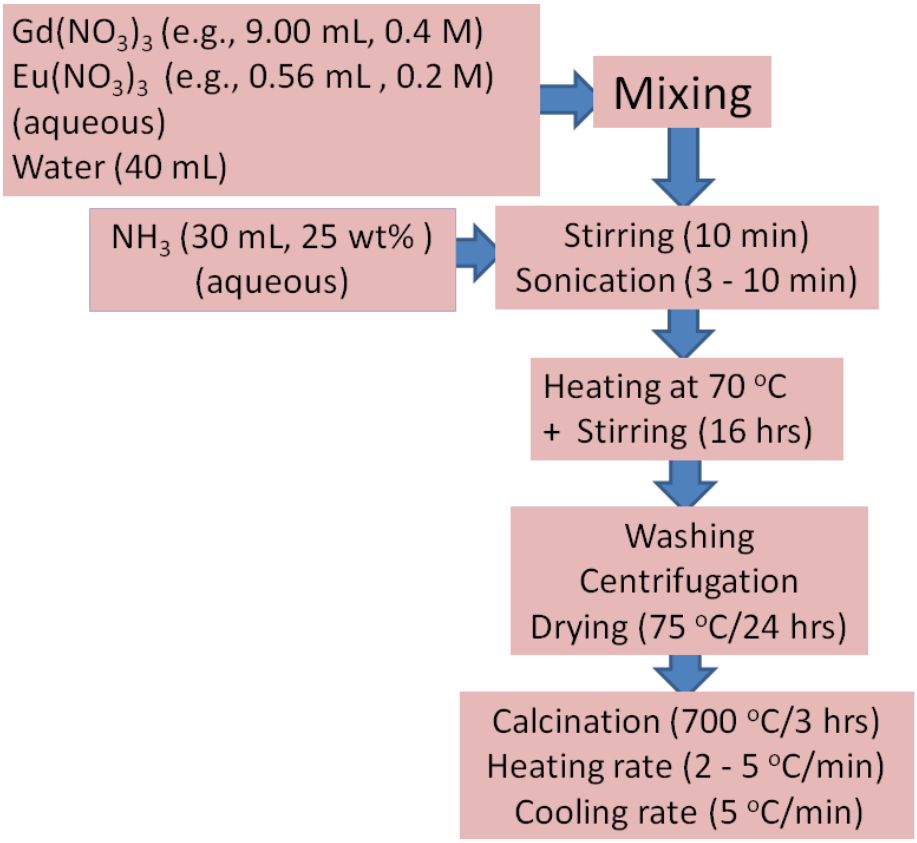

Figure 3.2: Schematic representation of wet-chemical synthesis of Eu^{3+}-doped Gd_2O_3 nanorods.

white precipitate was washed several times with distilled water, once with ethanol and finally centrifuged and dried in air at 75 ^{o}C for 24 hours, yielding $(Gd_{0.97}Eu_{0.03})(OH)_3$ powder. This powder was ground in an agate mortar and pestle to obtain relatively fine powder a few milligrams of which were then calcined at 700 ^{o}C for 3 hours, with heating and cooling rates of 5 ^{o}C/min, affording $(Gd_{0.97}Eu_{0.03})_2O_3$ powder, Figure 3.2. Gd_2O_3 nanorods with Eu^{3+} concentrations 0.30, 1.00 and 5.00 mol% were synthesized in a similar procedure. It should be noted that this synthesis procedure is suitable for

the preparation of other Ln^{3+} ions-doped Gd_2O_3 nanorods, e.g., $(Gd,Yb,Er)_2O_3$, which will be discussed in chapter 5.

3.4 Composition, structure and morphology

Elemental analysis

Inductively coupled plasma optical emission spectroscopy (ICP-OES-Activa-M, Horiba Jobin Yvon) revealed that the nominal concentrations of 0.30, 1.00, 3.00 and 5.00 mol% Eu^{3+} relative to Gd^{3+} in the starting materials were 0.30, 1.01, 2.78 and 4.60 mol% Eu^{3+}, respectively, in the final $(Gd,Eu)_2O_3$ nanorods.

Powder X-ray diffraction (PXRD)

The crystal structures of the as-synthesized and calcined nanorods were identified with PXRD. As presented in Figure 3.3a, PXRD patterns of samples before calcination are indexed into the pure hexagonal $Gd(OH)_3$ phase (according to the Powder Diffraction File (PDF) database: PDF-01-083-2037). Figure 3.3b shows the diffraction patterns of nanorods obtained after calcination of the parent hexagonal phase at 700 ^oC for 3 hours. All calcined samples correspond to the pure Gd_2O_3 cubic phase, PDF-04-010-3292.

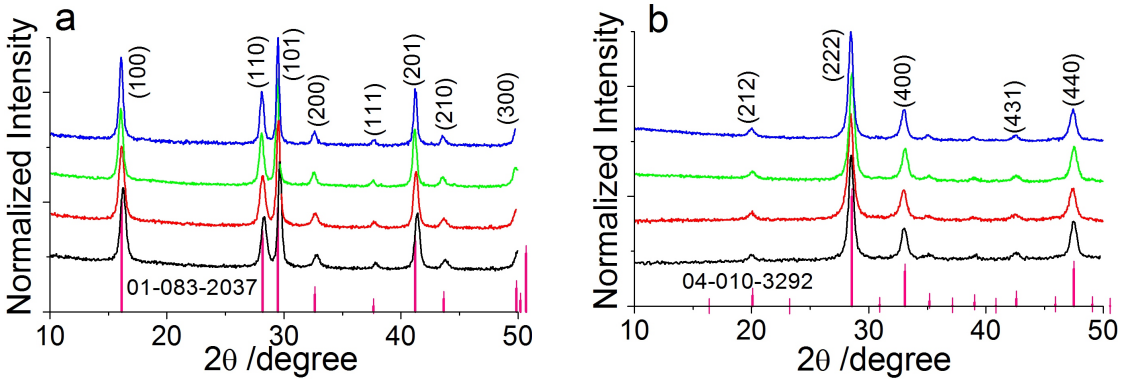

Figure 3.3: PXRD patterns: a) as-synthesized hexagonal $(Gd,Eu)(OH)_3$ nanorods, and b) cubic $(Gd,Eu)_2O_3$ nanorods obtained after calcination of the as-synthesized one at 700 ^oC/3 hrs; Eu^{3+} concentrations 0.30 mol% (black line), 1.01 mol% (red), 2.78 mol% (green), and 4.60 mol% (blue). The vertical pink lines are the reference powder diffraction files.

Transmission electron microscopy (TEM)

Representative TEM images of nanorods are given in Figure 3.4. TEM images show that the nanorods are relatively uniform in size, while the electron diffraction patterns

indicate that they are polycrystalline (inset in Figure 3.4). The size distribution calculated for 105 nanorods shows an average diameter of *ca.* 14.00 ± 3.22 nm (Figure 3.4, right panel). In general, nanorods with diameter between 10 and 25 nm and length smaller than 180 nm can be obtained following the synthesis protocol described in Figure 3.2. In this synthesis procedure, the major determining factor for the formation of nanorods instead of other shapes such as spherical nanoparticles may be due to the surface energy effects at the nucleation and growth stages. In particular, the (001) plane of hexagonal $Gd(OH)_3$ has the lowest surface energy and it is expected that the fastest growth rate is along the [001] direction leading to one dimensional anisotropic growth of $Gd(OH)_3$ nanorods. The length of the nanorods is much larger than their diameter and thus any size effect observed on the photoluminescence properties of the nanorods may be associated with the size of the diameter.

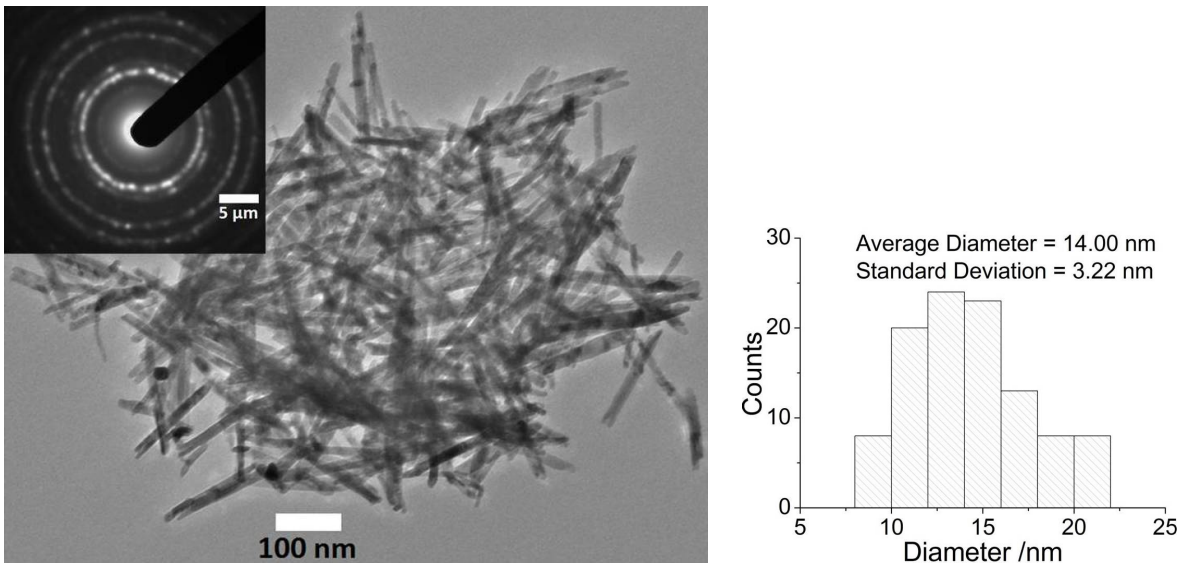

Figure 3.4: Representative TEM image of Gd_2O_3:2.78% Eu^{3+} nanorods synthesized *via* wet-chemical route; the inset is the electron diffraction pattern, and the graph on the right is the size distribution of the corresponding nanorods.

Discussion

3.5 $^5D_{0,1}(C_2)$ rise time and decay time

As mentioned, emission and excitation spectra of Eu^{3+} in cubic Gd_2O_3 have been discussed elsewhere [58, 60], and thus only the spectral features and electronic-energy levels relevant to the study of the rise time, decay time and energy-transfer processes are presented in the coming sections. For the purpose of the present discussions, the emission and excitation spectra of $(Gd,Eu)_2O_3$ nanorods (NRs) are given in Figure 3.5. The emission-decay curves of the $^5D_0(C_2)$ and $^5D_1(C_2)$ levels were recorded

after a 0.01 ms initial delay of the excitation pulse by monitoring the Eu^{3+} emission within the $^5D_0 \rightarrow {}^7F_2(C_2)$ transition at 610.7 nm and the $^5D_1 \rightarrow {}^7F_1(C_2)$ transition at 534 nm, respectively, exciting at 260 nm (within the ligand-to-metal charge-transfer, LMCT, band [58]). Figure 3.6 shows a schematic representation of the $^5D_1(C_2)$ to

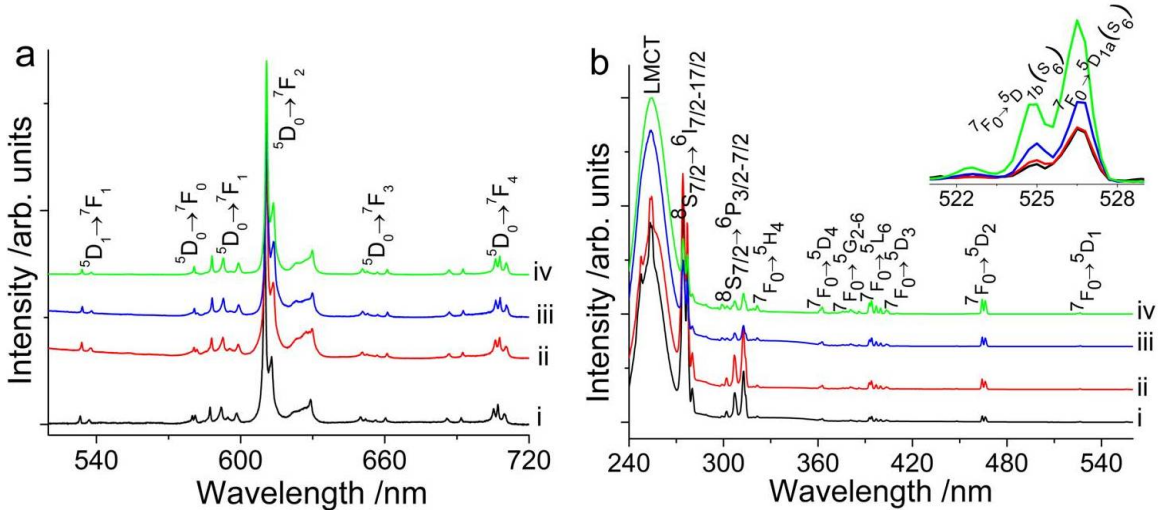

Figure 3.5: a) Emission spectra of $(Gd,Eu)_2O_3$ NRs at 11 K acquired under excitation within the LMCT band at 260 nm and b) excitation spectra at 11 K monitoring the emission within the $^5D_0 \rightarrow {}^7F_2(C_2)$ emission at 610.7 nm, Eu^{3+} concentrations: i) 0.30% ii) 1.01%, iii) 2.78% and iv) 4.60%. The inset in (b) shows the $^7F_0 \rightarrow {}^5D_{1a,b}(S_6)$ transition lines.

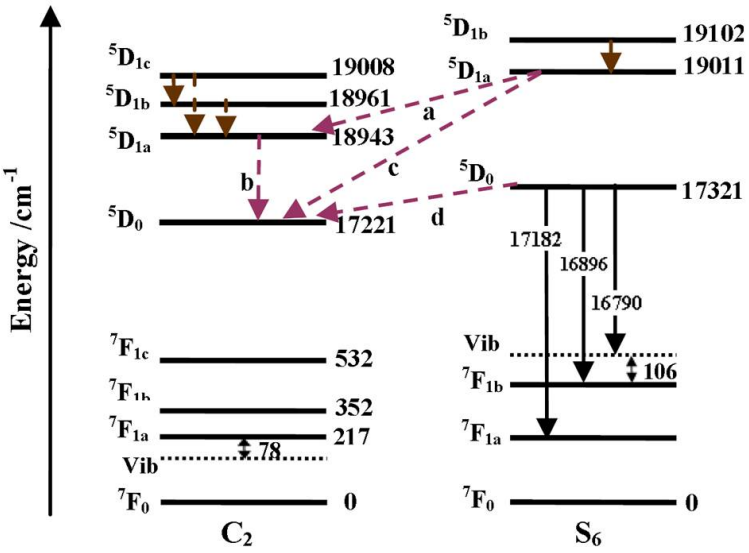

Figure 3.6: Partial Eu^{3+} energy-level diagram for the C_2 and S_6 sites in cubic $(Gd,Eu)_2O_3$ nanotubes/nanorods (error *ca.* 10 cm^{-1}) [58]. Transitions *a*, *c* and *d* represent inter-site energy-transfer, whereas transition *b* stands for inter-level relaxation [81, 82].

$^5D_1(C_2)$ inter-level and $^5D_{1,0}(S_6)$ to $^5D_{1,0}(C_2)$ inter-site energy-transfer processes in cu-

bic $(Gd,Eu)_2O_3$. Under 260 nm excitation, electrons from the C_2 and S_6 ground states are excited to higher-energy states, including the $^5D_1$ and $^5D_0$ levels. There are several energy-transfer channels that populate the lower $^5D_0(C_2)$ levels, Figure 3.6. Four energy-transfer pathways feeding the $^5D_0(C_2)$ and/or $^5D_1(C_2)$ levels were considered to analyze the $^5D_0(C_2)$ and $^5D_1(C_2)$ emission-decay curves.

For all $(Gd,Eu)_2O_3$ NRs with 0.30 - 4.60 mol% Eu^{3+}, the $^5D_1(C_2)$ emission-decay curves (Figure 3.7) measured at 11 and 300 K are well described by a single exponential:

$$i = i_0 exp(\frac{-t}{\tau_d}) + i_c \tag{3.1}$$

where i and i_0 are the intensities of the emitting $^5D_1(C_2)$ level at time t and $t = 0$, respectively, τ_d is the $^5D_1(C_2)$ decay time, and i_c is the background constant. Figure 3.7 shows typical emission-decay curves of the $^5D_1(C_2)$ level at 11 K. The estimated decay times are collected in Table 3.1. The single-exponential character of the $^5D_1 \rightarrow {}^7F_1(C_2)$ emission for Eu^{3+} in Y_2O_3 nanotubes/nanowires was also noted by Bai et al. [83]. The

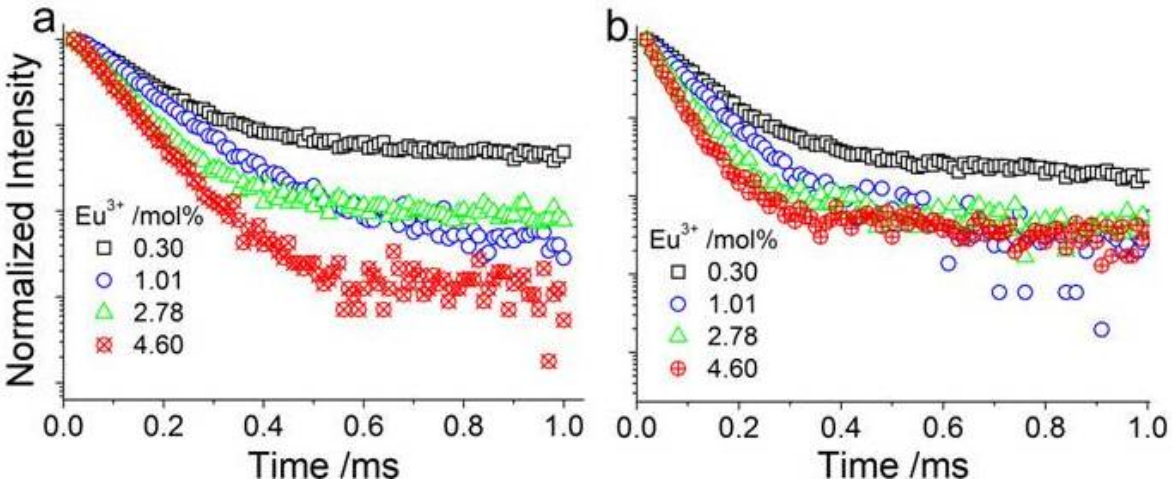

Figure 3.7: $^5D_1(C_2)$ emission-decay curves of $(Gd,Eu)_2O_3$ NRs measured at a) 11 K and b) 300 K, monitoring the emission at 534 nm and exciting at 260 nm.

behavior of the $^5D_1(C_2)$ emission-decay curve confirms that all the inter-level and inter-site energy-transfers feeding the $^5D_1(C_2)$ level are much faster than the $^5D_1(C_2)$ decay time. The presence of a relatively long-lived feeding level would cause the $^5D_1(C_2)$ emission-decay curve to have a rising component [84]. In fact, the energy-transfer from the $^5D_1(S_6)$ to the $^5D_{1,0}(C_2)$ levels, achieved along path a and/or c in Figure 3.6, is witnessed by the appearance of the $^7F_0 \rightarrow {}^5D_{1a,b}(S_6)$ transitions at 11 and 300 K in the steady-state excitation spectra acquired by monitoring the $^5D_0 \rightarrow {}^7F_2(C_2)$ emission at 610.7 nm (inset in Figure 3.5b). Therefore, as the $^5D_1(C_2)$ emission-decay curve exhibits no rising component within the experimental time range, the observed energy-transfer to the $^5D_1(C_1)$ level along path a is much faster than the $^5D_1(C_2)$ decay time.

Table 3.1: $^5D_{0,1}(C_2)$ lifetimes and filling factors for $(Gd,Eu)_2O_3$ NRs in air.

	$^5D_0(C_2)$				$^5D_1(C_2)$		
Eu^{3+}	11 K	300 K	11 K	300 K	11 K	300 K	Filling
(mol%)	τ_d (ms)	τ_d (ms)	τ_r (μs)	τ_r (μs)	τ_d (μs)	τ_d (μs)	factor
0.30	1.40±0.015	1.42±0.008	85±1.81	66±0.84	116±1.30	84±0.71	0.78
1.01	1.73±0.015	1.75±0.013	70±1.46	46±1.09	102±2.49	67±0.61	0.67
2.78	1.41±0.009	1.56±0.009	58±1.30	31±0.89	73±1.40	45±0.40	0.78
4.60	1.35±0.007	1.46±0.009	49±1.33	20±0.98	64±1.35	35±0.21	0.80

To clarify the nature of energy-transfer along paths *b*, *c* and *d* we now discuss the behavior of the $^5D_0(C_2)$ emission-decay curve, Figure 3.8. This curve exhibits a rising part before decaying (insets in Figure 3.8), indicating that there is a decaying source feeding this level. The $^5D_0(C_2)$ decay curve is well described by a simplified model equation [82]:

$$I = [I_0 + I_1(1 - exp(\frac{-t}{\tau_r}))]exp(\frac{-t}{\tau_d}) + I_c \tag{3.2}$$

where I and I_0 are, respectively, the intensities of the emitting lower-level ($^5D_0(C_2)$) at time t and $t = 0$; I_1 is the intensity at $t = 0$ of the upper level feeding the emitting lower-level; τ_r and τ_d are, respectively, the rise time and $^5D_0(C_2)$ decay time; I_c is the background constant.

For all the samples, the $^5D_0(C_2)$ emission-decay curves (Figure 3.8) acquired at 11 and 300 K were fitted using Equation 3.2 and the obtained lifetimes are collected in Table 3.1.

3.6 Effects of concentration and temperature

The estimated $^5D_1(C_2)$ decay time and the $^5D_0(C_2)$ rise time extracted from the rising component of the $^5D_0(C_2)$ emission-decay curve using Equation 3.2 strongly depend on the Eu^{3+} concentration and temperature, Figure 3.9. Several interaction mechanisms including dipole-dipole, dipole-quadrupole, and exchange interactions, which depend on temperature, concentration and distance between the ions, were widely investigated [60, 81, 85]. The effect of the Eu^{3+} concentration on the lifetimes could be explained in terms of these interactions. At a given temperature, increasing the Eu^{3+} concentration shortens the $^5D_1(C_2)$ decay time and the $^5D_0(C_2)$ rise time (Figure 3.9), which implies a back-energy transfer from the $^5D_1(C_2)$ to $^5D_0(S_6)$ and/or an energy-transfer from the $^5D_1(C_2)$ level to the quenching centers. Even though it cannot be confirmed from the excitation spectra as no emission can be monitored for the $^5D_1(S_6)$ level, the former hardly occurs at 11 K. The latter is, however, likely to happen at relatively high ($> 0.1\%$) Eu^{3+} concentrations [60] due to the presence of quenching centers, such as surface defects of the NRs [83, 86, 87]. As the Eu^{3+} concentration increases, the probability of energy migration from the Eu^{3+} ions in the C_2 sub-lattice to the quenching centers increases [60, 85], thereby shortening the $^5D_1(C_2)$ decay time. Considering the

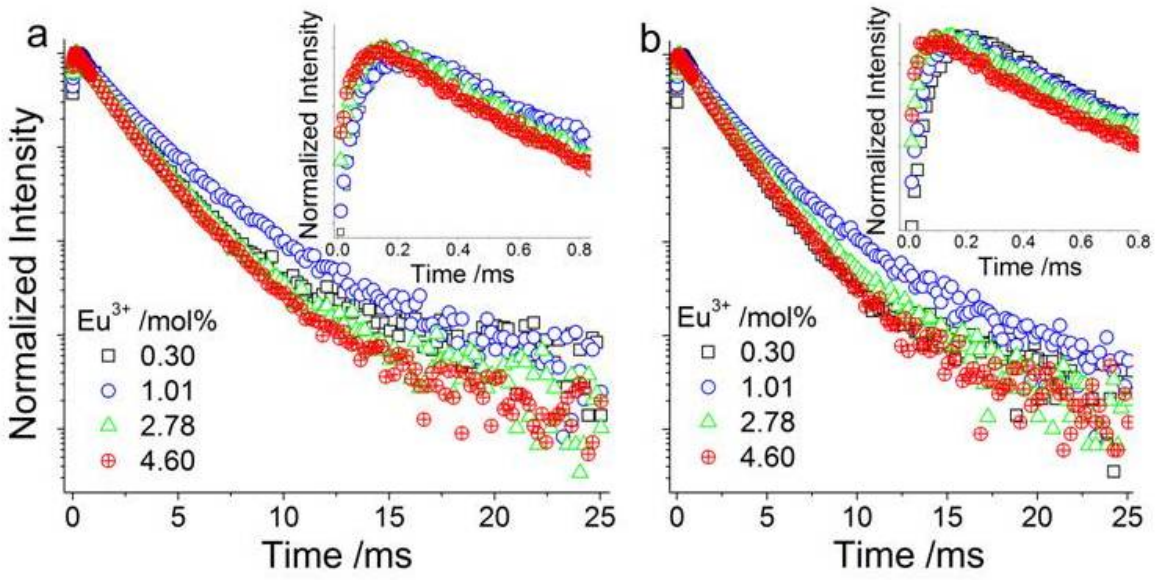

Figure 3.8: $^5D_0(C_2)$ emission-decay curves of $(Gd,Eu)_2O_3$ NRs measured at a) 11 K and b) 300 K, monitoring the emission at 610.7 nm and exciting at 260 nm. The insets show the rising components.

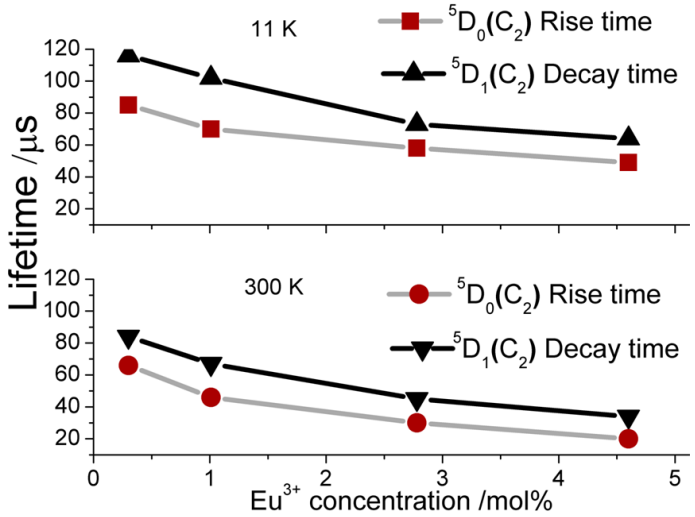

Figure 3.9: $^5D_0(C_2)$ rise time and $^5D_1(C_2)$ decay time of $(Gd,Eu)_2O_3$ NRs as a function of the Eu^{3+} concentration.

3:1 population ratio of the Eu^{3+} ions in the two sites, such energy migration over the C_2 sub-lattice is dominant [60]. The relative intensities of the $^5D_1 \rightarrow {}^7F_1(C_2)$ emissions support such energy migration. As will be seen later (Figure 3.11), the intensity of the $^5D_1 \rightarrow {}^7F_1(C_2)$ emission at 11 and 300 K decreases with increasing Eu^{3+} concentration, suggesting that energy migration due to concentration effect is the most likely mechanism responsible for shortening the $^5D_1(C_2)$ decay time. At higher Eu^{3+} concentration,

the $^5D_0(C_2)$ rise time also shortens, and there is a stronger quenching of the rising intensity in the $^5D_0(C_2)$ emission-decay curve (Figure 3.8). Moreover, the $^5D_1(C_2)$ decay time at 11 K is 116 μs for 0.30% and 64 μs for 4.60% Eu^{3+} concentration (Table 3.1). A similar observation of a decrease in the $^5D_1(C_2)$ decay time from 134 μs, for 0.02% Eu^{3+}, to 66 μs, for 5% Eu^{3+}, in bulk Y_2O_3 crystals was reported by Buijs et al. [60].

For a given Eu^{3+} concentration (Figure 3.9), the decrease in the $^5D_0(C_2)$ rise time and the $^5D_1(C_2)$ decay time from 11 to 300 K shows that they are also sensitive to temperature. According to the theory of multiphonon relaxation, as the energy gap between an emitting upper level and the next lower level becomes smaller the decay time from the upper to the lower level decreases due to the involvement of phonon emissions [88, 89]. Considering the maximum phonon energy in bulk Gd_2O_3 *ca.* 600 cm^{-1} [61], nearly three phonons are emitted from the $^5D_1(C_2)$ to $^5D_0(C_2)$ level due to lattice vibrations at high temperature, thus shortening the $^5D_1(C_2)$ decay time. The $^5D_1(C_2)$ decay time at 300 K may also be shortened by energy migration [85], which increases with temperature, from the C_2 sub-lattice to the quenching centers. It should be noted that the $^5D_0(C_2)$ rise time is also influenced by temperature. Accordingly, the $^5D_1(C_2)$ decay times for Gd_2O_3:4.60% Eu^{3+} NRs decrease from 64 μs, at 11 K, to 34 μs, at 300 K. These values are similar to those reported by Liu et al. [61] for 5% Eu^{3+} in Gd_2O_3 NRs (65 μs, at 10 K, and 37 μs at 295 K). The Eu^{3+} concentration seems to have no influence on the $^5D_0(C_2)$ decay time measured at a given temperature, that is, the effect of concentration quenching on the $^5D_0(C_2)$) decay time is negligible. Indeed, the energy gap between the $^5D_0$ and the $^7F_{0-6}$ levels is relatively large (> 12000 cm^{-1}), which is not easily overcome by nonradiative processes induced by temperature and/or ion-ion interactions. The absence of a significant concentration effect on the $^5D_0(C_2)$ decay time was previously reported by Pires et al. [64] for 1 - 5% Eu^{3+} concentration in spherical Gd_2O_3 nanoparticles (although the rise time was not presented).

The $^5D_0(C_2)$ decay time of Gd_2O_3:1.01% Eu^{3+} NRs was measured at temperatures in the range from 11 to 300 K and, as expected, the decay time hardly changed (Figure 3.10). The most pronounced effect on the $^5D_0(C_2)$ decay time is observed due to the change in the effective-refractive index (filling factor), which may be easily modified by changing the dispersion of the NRs in air. A change in the dispersion of the nanorods in air during the measurement resulted in a significant variation of the $^5D_0(C_2)$ decay time. In general, the $^5D_0(C_2)$ decay times of all samples are longer than that of the bulk counterparts, 1.00 and 0.94 ms reported by Andreia et al. [58] and Liu et al. [61], respectively, and agree with those previously reported results for analogous materials [58, 62, 64, 67, 83, 86]. The increase in the $^5D_0(C_2)$ decay time is attributed to the modification of the effective-refractive index of the medium surrounding the Eu^{3+} ions due to the reduction in the size of the nanorods.

Under excitation at 394 nm, the rise-time phenomena were also noticed in the Gd_2O_3:Eu^{3+} nanocrystals prepared through a hydrothermal method by Andreia et al. [58]. For comparison with the present samples, the $^5D_0(C_2)$ lifetimes of Gd_2O_3:1.00% Eu^{3+} nanotubes [58] were measured with excitation in the ligand-metal charge transfer band. The $^5D_0(C_2)$ rise time (77 μs at 11 K and 47 μs at 300 K) and the $^5D_0(C_2)$ decay

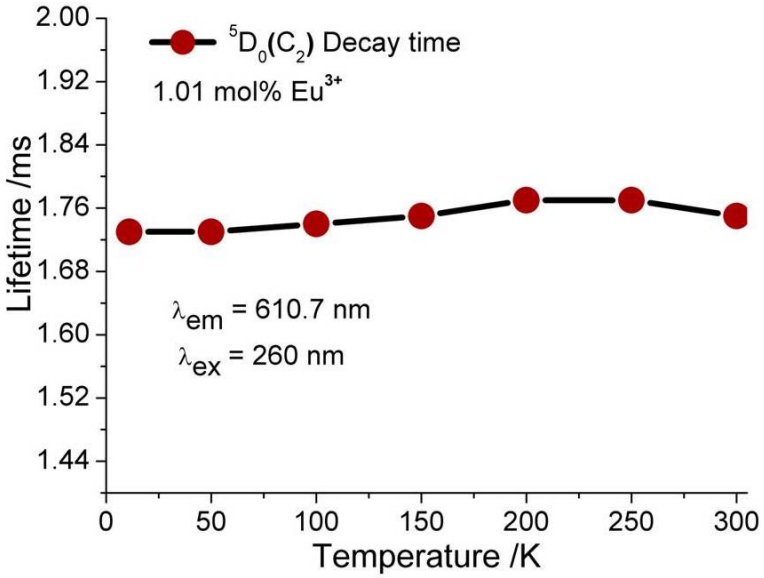

Figure 3.10: $^5D_0(C_2)$ decay time of $(Gd,Eu)_2O_3$ NRs as a function of temperature.

time (1.41 ms at 11 K and 1.57 ms at 300 K) are in agreement with the corresponding lifetimes measured for 1.01% Eu^{3+} in the NRs (Table 3.1). As was mentioned, the small differences in the $^5D_0(C_2)$) decay times, however, may be associated with the differences in the dispersion of the nanotubes and NRs in air.

3.7 Energy-transfer and rationalization of the rise time

In this section, (inter-level and inter-site) energy-transfer along paths *b*, *c* and *d* in Figure 3.6 are defined and the rise time is rationalized. First, the contribution of energy-transfer along path *d* to the rise time can be clearly identified from the emission and excitation spectra. In the steady-state emission spectra acquired under excitation at 260 nm, energy-transfer from the $^5D_0(S_6)$ to $^5D_0(C_2)$ level induced by Eu^{3+} concentration was detected at 11 and 300 K, Figure 3.11).

At high Eu^{3+} concentration, the $^5D_0 \rightarrow {}^7F_{1a}(S_6)$ emission intensity decreases whereas that of the $^5D_0 \rightarrow {}^7F_0(C_2)$ emission increases at the expenses of the $^5D_0 \rightarrow {}^7F_{1a}(S_6)$ emission (Figure 3.11). In other words, a relatively efficient energy-transfer from the $^5D_0(S_6)$ to $^5D_0(C_2)$ level occurs at 11 K over an energy gap of ca. 100 cm^{-1} for the sample with the highest Eu^{3+} concentration. These results are similar to those reported by Zych for Lu_2O_3:Eu^{3+} [90] and in agreement with Heber's et al. [81] empirical function for the dependence of the energy-transfer probability, $W_t \approx (1 - exp(\frac{-m}{m_0}))$, between the two sites, where m and m_0 are the molar concentrations of Eu^{3+}. No back energy-transfer from the $^5D_0(C_2)$ to $^5D_0(S_6)$ level was, however, observed as confirmed from the excitation spectra obtained by monitoring the $^5D_0 \rightarrow {}^7F_{1a}(S_6)$ emission

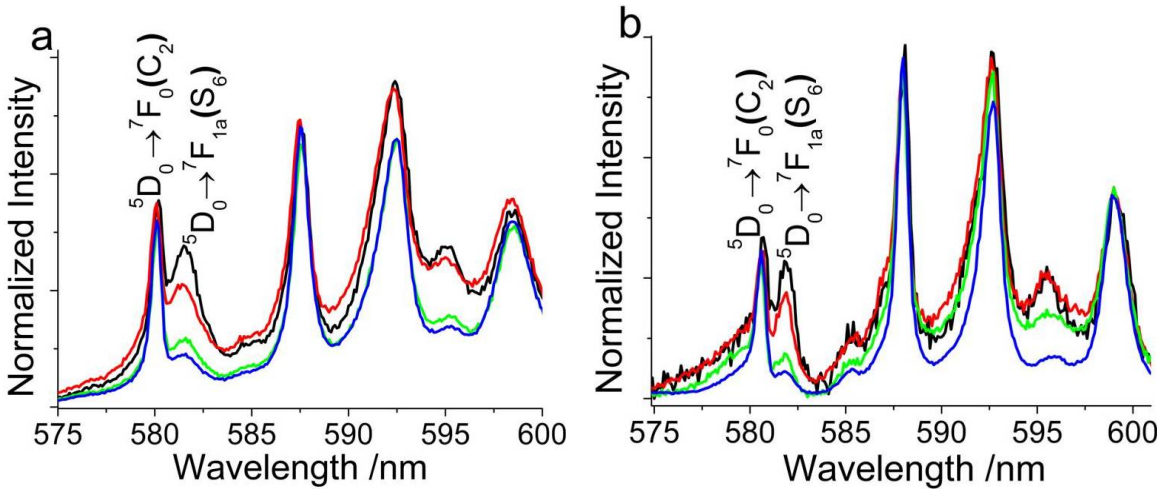

Figure 3.11: Emission spectra, normalized to the $^5D_0 \rightarrow {}^7F_2(C_2)$ transition lines, of $(Gd,Eu)_2O_3$ NRs at a) 300 K and b) 11 K in the range of 575 to 600 nm, acquired under excitation at 260 nm; Eu^{3+} concentration 0.30% (black line), 1.01% (red), 2.78% (green) and 4.60% (blue). The relative intensity of the $^5D_0 \rightarrow {}^7F_0(C_2)$ and $^5D_0 \rightarrow {}^7F_{1a}(S_6)$ emissions changes with the Eu^{3+} content, showing an efficient inter-site energy transfer from the $^5D_0(S_6)$ to $^5D_0(C_2)$ level at high Eu^{3+} concentration.

at 581.5 nm [61]. Therefore, if the rise time is due to an efficient energy-transfer from the $^5D_0(S_6)$ to $^5D_0(C_2)$ level, it must be relatively long for the sample having high Eu^{3+} content. This is, however, in contrast with Figure 3.9, which clearly shows a decrease in the rise time on increasing the Eu^{3+} concentration both at 11 and 300 K. The result proves that the $^5D_0(C_2)$ rise time does not arise due to the inter-site energy-transfer from the $^5D_0(S_6)$ to $^5D_0(C_2)$ level, i.e., along path *d*, leading to the conclusion that the energy-transfer along path *d* is much faster than the $^5D_0(C_2)$ rise time, as the energy-transfer along path *a* was found to be too fast compared to the $^5D_1(C_2)$ decay time. Moreover, the energy-transfer along path *c* is obviously ruled out if one considers the small energy gap between the $^5D_1(S_6)$ and $^5D_1(C_2)$ levels (compared to that between the $^5D_1(S_6)$ and $^5D_0(C_2)$ levels). This implies that the observed energy-transfers from the $^5D_1(S_6)$ to $^5D_{1,0}(C_2)$ levels are preferably achieved only along path *a*, Figure 3.6. Additionally, the increase in the energy-transfer from the $^5D_1(S_6)$ to $^5D_{0,1}(C_2)$ levels on increasing Eu^{3+} concentration (Figure 3.11) shows that the energy-transfer along path *c* is not responsible for the rise time, since the rise time shortens at high Eu^{3+} concentration (Figure 3.9). Finally, the inter-level relaxation along path *b* is the only route to slowly feed the $^5D_0(C_2)$ level. This can be deduced from the behaviors of the $^5D_1(C_2)$ decay time and the $^5D_0(C_2)$ rise time. The relatively long-lived emission of the $^5D_1(C_2)$ level suggests that the inter-level energy-transfer along path *b* may cause a rise time in the $^5D_0(C_2)$ emission-decay curve. As discussed above, the $^5D_0(C_2)$ rise time and $^5D_1(C_2)$ decay time follow a similar dependence as a function of the Eu^{3+} concentration and temperature (Figure 3.9 and Table 3.1). Furthermore, the $^5D_1(C_2)$ decay time matches the corresponding rise time component of the $^5D_0(C_2)$ emission-decay curve. The conclusion is that the main energy-transfer path responsible for the rise time in the $^5D_0(C_2)$ emission-decay curve is a direct relaxation from the $^5D_1(C_2)$

to the $^5D_0(C_2)$ level, path *b* in Figure 3.6. This is, however, in disagreement with the Ranson's et al. [82] discussion of the rise time for the Y_2O_3:Eu^{3+} phosphor, in which energy-transfer along paths *a*, *b* and *d* were considered to be too fast (< 5 μs) compared to the energy-transfer along path *c*, which was hold responsible for the rise time. In fact, the 5 μs rise time in the $^5D_0(C_2)$ emission decay curve for the Y_2O_3:Eu^{3+} phosphor was observed at a particular excitation wavelength (528.2 nm) by Hunt et al. [91] At 527.5 nm excitation wavelength, for instance, Hunt et al. [91] have also observed 200 μs $^5D_0(C_2)$ rise time for the same phosphor and they have pointed out that the emission-decay curves were strongly dependent on the excitation wavelengths.

3.8 Effective-refractive index and filling factor

As the average size of the NRs (*ca.* 14 nm in diameter) is smaller than the irradiation wavelength, it is expected that the effective-refractive index and the polarizability of the medium surrounding the Eu^{3+} ions will be modified [92–95], thereby changing the radiative lifetime. A suitable theoretical model should be employed to describe this physical effect. Here, the virtual-cavity model was chosen because of its previous successful application to Ln^{3+}-doped oxide nanocrystals [61,63,92,96]. By introducing a local-field correction factor according to the virtual-cavity model, the radiative lifetime, τ_R, of the emitting ion embedded in a medium with an effective-refractive index, n_{eff}, is given by [92, 96]:

$$\tau_R \approx \frac{\lambda_0^2}{f_{ED}(\frac{1}{3}(n_{eff}^2+2))^2 n_{eff}} \tag{3.3}$$

where λ_0 is the transition wavelength in vacuum; f_{ED} is the electric-dipole oscillator strength of the transition and $n_{eff} = \chi n_{Gd_2O_3} + (1-\chi)n_{med}$; χ is the fraction of sample space occupied by the NRs; $n_{Gd_2O_3}$ and n_{med} are the refractive indices of gadolinium oxide and the medium, respectively; $n_{Gd_2O_3} = 1.976$ [59, 63] and $n_{med} = 1.0$.

The filling factor gives the fraction of sample volume occupied by the NRs. Therefore, the larger the filling factor is the greater is the volume of sample occupied by the NRs. In other words, in the limit $\chi = 1$, the effective-refractive index is that of the gadolinium oxide and the radiative lifetime of the NRs will be close to that of the bulk counterparts. We noticed that the filling factor strongly depends on the compactness and dispersion of NRs in air during the measurement and variation of the $^5D_0(C_2)$ decay time from 1.40 to 2.10 ms has been observed by simply changing the compactness and the dispersion of NRs in air. For this purpose, e.g., 10 and 200 mg of Gd_2O_3:0.30% Eu^{3+} NRs were prepared in the form of pellets with a hydraulic press under 2 and 7 tons, respectively, while keeping the other experimental conditions unchanged. The $^5D_0(C_2)$ decay time was 1.94 ms for the relatively thin pellet prepared at low pressure press, and 1.45 ms for the thick and highly compacted pellet (Table 3.2). However, no significant change was observed in the $^5D_0(C_2)$ rise time, Table 3.2. Even though further experimental studies are required, this effect may be qualitatively explained in terms of the filling factor of the NRs and the change in the effective-refractive index, as pointed out by Meltzer et al. [92]. Under high pressure

press, the NRs are obviously highly compacted (no space between them and thus have high filling factor) and any local-field effect due to the reduction in size is lost. Instead, a highly compacted powder of NRs behaves as the bulk counterpart [94]. On increasing the thickness and compactness of the powder pellet, the majority of the Eu^{3+} ions will be fully immersed in Gd_2O_3 and, hence, the effective-refractive index of the medium surrounding the emitters will be close to that of the Gd_2O_3, leading to a shorter decay time. In addition, aggregates of NRs larger than the wavelength of light do not show the local-field effect and the $^5D_0(C_2)$ decay time measured may become shorter than expected [94, 96]. This may explain why the filling factor (the $^5D_0(C_2)$ decay time) of the Gd_2O_3:0.30% Eu^{3+} nanotubes was the same as that of the NRs in ref. [61] while the nanotubes were smaller in size.

Assuming that the $^5D_0 \rightarrow {}^7F_2(C_2)$ transition is purely radiative, the filling factors of the NRs from each sample were estimated using Equation 3.3 and the results are summarized in Tables 3.1 and 3.2. As discussed, the filling factor depends on the dispersion of the NRs in air. It ranges from 0.57 (for 2.10 ms) to 0.80 (for 1.35 ms). The result shows that the $^5D_0(C_2)$ decay time depends mainly on the dispersion of the NRs in air and it is generally longer than that of the bulk counterpart. For analogous materials, Liu et al. [61, 63] have also observed a longer $^5D_0(C_2)$ decay time (2.20 ms) with a smaller estimated filling factor in air, 0.55, for Gd_2O_3:5% Eu^{3+} NRs of 30 - 40 nm in diameter and 70 - 80 nm in length. Similarly, for Gd_2O_3:Eu^{3+} nanotubes of 40 nm in diameter and 200 - 300 nm in length [66], a 2.173 ms decay time was reported for the $^5D_0(C_2)$ level (with no rise time observed). In order to compare experimental results, it is therefore essential to describe the dispersion/suspension of the nanocrystals in a medium whenever the lifetime, effective-refractive index and filling factor are to be reported for nanocrystals smaller than the wavelength of light.

Table 3.2: $^5D_0(C_2)$ decay and rise times, and filling factors for pellets of $(Gd,Eu)_2O_3$ nanorods in air at 300 K.

Eu^{3+} (mol%)	Powder amount (mg)	Hydraulic press (ton)	$^5D_0(C_2)$		Filling factor
			τ_d (ms)	τ_r (μs)	
0.30	200	7	1.45±0.003	61±0.67	0.76
	20	2	1.94±0.006	65±0.85	0.61
	10	1	2.10±0.005	64±1.08	0.57

3.9 Summary and conclusion

Cubic $(Gd,Eu)_2O_3$ NRs, with Eu^{3+} concentrations, 0.30, 1.01, 2.78 and 4.60 mol%, were prepared by a simple wet-chemical route at mild temperature and ambient pressure. The samples were characterized by PXRD, ICP-AES, TEM and PL spectroscopy. The $^5D_1(C_2)$ and $^5D_0(C_2)$ emission-decay curves were investigated in detail. The $^5D_1(C_2)$ emission-decay curve is described by a single exponential, whereas the $^5D_0(C_2)$ emission-decay curve comprises an initial rising component followed by an exponential tail. The $^5D_1(C_2)$ decay times match the corresponding rise times measured from the rising component of the $^5D_0(C_2)$ emission-decay curve. Furthermore, the $^5D_1(C_2)$ decay time and the $^5D_0(C_2)$ rise time show similar behaviors upon changing the temperature and Eu^{3+} concentration. The $^5D_{1,0}(S_6))$ to $^5D_{1,0}(C_2)$ inter-site energy-transfer is much faster than the $^5D_1(C_2)$ decay time and the $^5D_0(C_2)$ rise time. The contribution of the inter-site energy-transfer mechanisms to the $^5D_0(C_2)$ rise time is ruled out, being the direct $^5D_1(C_2)$ to $^5D_0(C_2)$ relaxation (inter-level energy transfer) the only responsible path for the rise time effect. The longer $^5D_0(C_2)$ decay time observed for the NRs (relatively to the bulk decay time) in air is mainly due to the small filling factor of the NRs and the change in the effective-refractive index of the milieu surrounding the Eu^{3+} ions.

Chapter 4

UV-cured Epoxy/$(Gd,Eu)_2O_3$ Nanocomposites

4.1 Introduction

Dispersing Ln^{3+} containing inorganic nanocrystals in polymeric matrices may provide interesting functional properties combining the good processability and mechanical properties as well as the transparency of the polymeric matrices and the unique Ln^{3+} luminescence. In this chapter, we discus the photopolymerization kinetics, thermal and photoluminescence (PL) properties of epoxy/$(Gd,Eu)_2O_3$ nanocomposites prepared *via* UV-curing of pre-made $(Gd_{0.96}Eu_{0.04})_2O_3$ nanorods dispersed in three different commercially-available photo-curable epoxy resins. The composite materials present original PL properties and demonstrate the potential of UV-curing to develop smart photoactive coatings[1].

The preparation of the nanocomposites and their kinetics and thermal analysis presented in this chapter were performed at Torino by Dr. I. Roppolo in collaboration with Prof. M. Sangermano. The synthesis of $(Gd,Eu)_2O_3$ nanorods, and PL measurements and analyses for the prepared composites were done by the author of this thesis.

4.2 Preparation of the nanocomposites

The preparation of UV-cured epoxy/$(Gd,Eu)_2O_3$ nanocomposites was performed in two steps as follows.

i. Nanorods

$(Gd_{0.96}Eu_{0.04})_2O_3$ nanorods were prepared through a microwave-assisted hydrothermal method [97, 98] described as follows. In a typical synthesis of $(Gd_{0.96}Eu_{0.04})_2O_3$ nanorods at 150 ^{o}C, aqueous solutions of $Gd(NO_3)_3$ (38.4 mL, 0.4 M) and $Eu(NO_3)_3$

[1] I. Roppolo, **M. L. Debasu**, R. A. S. Ferreira, J. Rocha, L. D. Carlos, M. Sangermano, Photoluminescent Epoxy/Gd_2O_3:Eu^{3+} UV-cured Nanocomposites. *Macromol. Mater. Eng.* 298, 181-189, 2013.

(3.2 mL, 0.2 M) were mixed in distilled water (45 mL), Figure 4.1a. Then, aqueous solution of NaOH (20 mL, 1 M) was added to the mixture under magnetic stirring. The solution was then equally divided into four parts (*ca.* 27 mL each) and transferred to autoclaves. The solution in one of the autoclaves was set as a control with pH $\sim$ 11.50 while the pH's of the solutions in the other three autoclaves were adjusted to 10.06, 11.04 and 12.81 with aqueous NaOH. The final volume of the solution in each autoclave was the same (*ca.* 29 mL each). After 1 hour magnetic stirring at room temperature, the autoclaves were transferred to the microwave oven set to operate at 1200 watt and 150 ^{o}C for 9 hours. After 9 hours, the autoclaves were cooled down to room temperature. The white precipitate from each autoclave was independently washed several times with distilled water, once with ethanol and finally centrifuged and dried in air at 75 ^{o}C for 24 hours, which gives $(Gd_{0.94}Eu_{0.04})(OH)_3$ powder. For further characterization, the dried $(Gd_{0.94}Eu_{0.04})(OH)_3$ powder was ground in an agate mortar and pestle to obtain a relatively fine powder. The fine powder was calcined at 700 ^{o}C for 3 hours with cooling and heating rates of 5 ^{o}C/min and $(Gd_{0.96}Eu_{0.04})_2O_3$ nanorods were obtained. The sizes of the nanorods were greatly dependent on the pH. For the purpose of embedding in polymer matrices, the sample synthesized at pH = 12.81 was considered as it was relatively small, *ca.* 13.5 nm in diameter, (Figure 4.1b). Furthermore, it should be noted powder X-ray diffraction revealed that the obtained $(Gd_{0.94}Eu_{0.04})(OH)_3$ and $(Gd_{0.96}Eu_{0.04})_2O_3$ samples have hexagonal and cubic phases, respectively.

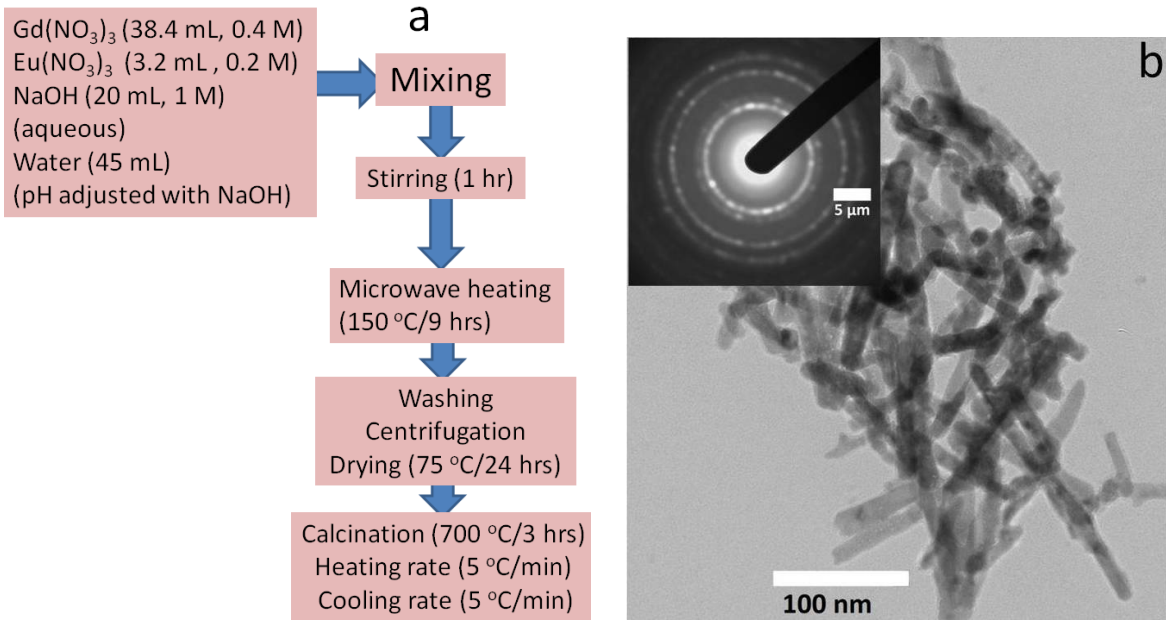

Figure 4.1: a) Schematic representations of microwave-assisted hydrothermal synthesis of $(Gd,Eu)_2O_3$ NRs. b) a representative TEM image of $(Gd_{0.96}Eu_{0.04})_2O_3$ nanorods obtained at pH = 12.8; the insets show the electron diffraction patterns of the corresponding image.

ii. Nanocomposites

Epoxy/$(Gd,Eu)_2O_3$ nanocomposites were prepared by dispersing $(Gd_{0.96}Eu_{0.04})_2O_3$ nanorods (Figure 4.2) into three different commercially-available photo-curable epoxy resins, namely, 1,6 Hexanediol Diglycidyl Ether (HDGE), Bisphenol-A Diglycidyl Ether (DGEBA) and 3,4-Epoxycyclohexylmethyl-3',4'-Epoxycyclohexane Carboxylate (ECC). Each formulation containing the nanorods and the epoxy resin was sonicated for 1 hour and afterwards 2 wt% of the cationic photo-initiator (triarylsolfonium exafluoroantimonate salt) was added. The mixture was coated on a glass slide *via* spin-coating (three steps of spinning: 500 rpm, 1000 rpm and 2000 rpm, 10 seconds each) and cured with UV-light (a Italquartz Hg medium pressure lamp) in air for 3 minutes; the homogeneity of the nanorod distribution in the coated samples can be deduced from the Eu^{3+} emission in the polymer matrices upon UV-light excitation as shown in Figure 4.2. The light intensity on the surface of the samples was 50 mW cm^{-2} (measured with EIT instrument). The kinetics of the photopolymerization was determined by realtime fourier-transform infrared (FTIR) spectroscopy (a Thermo-Nicolet 5700). The formulations were coated onto a silicon wafer with a wire wound bar (nominal thickness 25 μm). The sample was exposed simultaneously to the UV beam, which induces the polymerization, and to the IR beam, which analyses in situ the extent of the reaction.

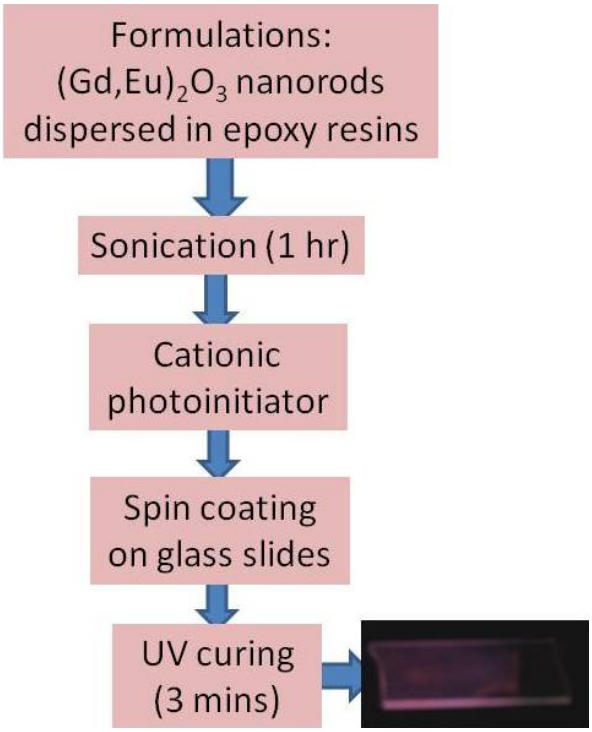

Figure 4.2: a) Schematic representations of the preparation of epoxy/$(Gd,Eu)_2O_3$ nanocomposites; digital photograph of HDGE with 10 wt% of $(Gd,Eu)_2O_3$ nanorods under UV irradiation at room temperature is shown in the right bottom. The pink color is due to the Eu^{3+}; the uncoated part of the glass slide is visible.

A medium pressure mercury lamp (Hamamatsu LC8) equipped with an optical guide was used to induce the photopolymerization (light intensity on the surface of the sample was 25 mW cm^{-2}). Because the IR absorbance is proportional to the monomer concentration, conversion versus irradiation time profiles may be obtained. To this aim, the epoxy ring opening mechanism was followed by monitoring the decrease in the absorbance of the peak centered at 910 cm^{-1}. IR spectra were collected with the same equipment. Differential scanning calorimetry (DSC) measurements were performed in the range between -80 °C and 60 °C with a heating rate of 20 °C/min for the samples in HDGE matrix and in the range between 50 °C and 250 °C with a heating rate of 20°C/min for the samples in DGEBA and ECC matrices. The gel content was determined on the cured films by measuring the weight loss after 24 hours extraction with chloroform at room temperature according to the standard test method (ASTM D2765-84).

4.3 Polymerization kinetics and thermal analysis

In order to understand effects of the photoactive fillers, i.e., the nanorods (NRs), on the UV-curing process, the photopolymerization kinetics of samples containing different amount of NRs in HDGE matrix was investigated by using realtime FTIR analysis, following the decrease of the intensity of the band centered at 910 cm^{-1} attributable to the opening of the epoxy ring. Epoxy ring opening conversion as a function of irradiation time is presented in Figure 4.3a. The presence of the photoactive filler strongly influences the photo-curing mechanism leading to an important decrease of the photo-curing rate and final epoxy group conversion upon increasing the fillers content. This effect may be attributed to: (i) a competition between the photo-initiator and the $(Gd_{0.96}Eu_{0.04})_2O_3$ fillers for the absorption of the UV radiation, with the consequent decrease of the number of the photoacids generated during UV-irradiation and, thus, the number of initiating species and (ii) an increase of the viscosity induced by the filler dispersion, reducing the overall mobility of the reactive groups. The UV-curing conversion curves for the three pristine epoxy resins (HDGE, ECC and DGEBA) and the respective composites formed by adding 10 wt% of $(Gd_{0.96}Eu_{0.04})_2O_3$ NRs to each of the epoxy resins were also compared as shown in Figure 4.3b. Here, it is important to note that an optimum amount of 10 wt% of $(Gd_{0.96}Eu_{0.04})_2O_3$ NRs was chosen for further analysis by considering a filler limit above which the photo-curing process is strongly affected (Figure 4.3a and Table 4.1) as well as based on the photoluminescence properties which will be discussed later. As expected, a decrease in the final conversion with the composites when compared to their relative pristine matrices was observed. Due to the intrinsic characteristics of the resins, such as reactivity and viscosity, the conversion trends of the three epoxy resins and their relative composites are similar but the compared reactivity and final epoxy-group conversions are quite different.

DSC measurements were performed on photo-cured films in order to evaluate the effect of the $(Gd_{0.96}Eu_{0.04})_2O_3$ NRs on the thermal properties of the polymer networks as presented in Table 4.1. All the cured films present a high gel content (nearly all higher than 90%, Table 4.1) indicating the absence of significant amounts of extractable

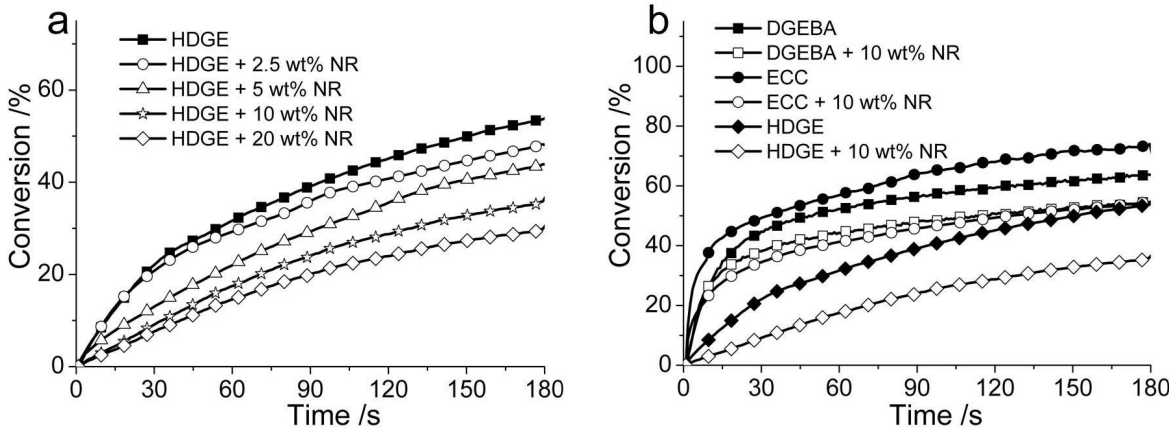

Figure 4.3: Epoxy ring opening conversion as a function of the irradiation time: a) comparison between pristine HDGE resin (filled symbols) and the corresponding formulations containing increasing amounts of $(Gd_{0.96}Eu_{0.04})_2O_3$ NRs (open symbols), and b) comparison between the three pristine resins DGEBA, ECC and HDGE (filled symbols) and the corresponding matrices containing 10 wt% of $(Gd_{0.96}Eu_{0.04})_2O_3$ NRs (open symbols). In both cases, the film thickness was 25 μm, and the light intensity was 25 mW cm^{-2}.

oligomers or monomers. Introducing 10 wt% of NRs to the resin films gives only a slight increase of the glass transition temperature (T_g) for the composites with DGEBA and ECC matrices (which have higher Tg), while a stronger effect on Tg is observed for the composite with HDGE matrix of lower Tg, Table 4.1. The increase of T_g may be due to a hindering effect of the NRs on the polymer chain mobility, increasing the stiffness and therefore the Tg. In the case of HDGE matrix, the stiffness effect is proportional to the amount of NRs, Table 4.1, with a linear increase in Tg on increasing the content of NRs in the photo-curable formulation. This indicates that the hindering effect should play an important role since one observes an increase of Tg notwithstanding a decrease of epoxy-group conversion and therefore of cross linking density.

4.4 Photoluminescence

4.4.1 Emission and excitation spectra

Figures 4.4a,b presents the room-temperature emission spectra of photo-cured HDGE films containing NRs excited at 260 nm. Two relatively broad emission bands with a full-width-at-half-maximum, fwhm, of *ca.* 40 nm centered, respectively, at 320 and 360 nm were observed for the pristine HDGE matrix (Figure 4.4a), similar to the previous emission reported for DGEBA matrix that was attributed to bisphenol groups [99]. Similar emission broad bands are also detected for the other NRs-polymer composites (Figures 4.5a-c), in addition to the typical $^5D_{0,1}\rightarrow{}^7F_{0-4}$ Eu^{3+} transition lines between 570 and 720 nm. The composite samples with the lowest amount of NRs exhibit the weakest intensity of $^5D_0\rightarrow{}^7F_2$ (C_2) transition at 610.5 nm, with intensities similar to that of the broad band from the polymers, Figure 4.4a. Moreover, increasing the

Table 4.1: Glass transition temperature (T_g) and gel content for UV-cured films of pristine HDGE, ECC and DGEBA and the corresponding matrices containing $(Gd_{0.96}Eu_{0.04})_2O_3$ nanorods (NR).

Materials	T_g [a] (^{o}C)	Gel content[b] (%)
HDGE	-26	93
HDGE + 2.5 wt% NR	-25	92
HDGE + 5 wt% NR	-23	92
HDGE + 10 wt% NR	-19	90
HDGE + 20 wt% NR	-15	85
DGEBA	153	98
DGEBA + 10 wt% NR	155	94
ECC	156	97
ECC + 10 wt% NR	159	95

[a]Determined on photopolymerized films by DSC.
[b]Determined after 24 hrs extraction in chloroform according to ASTM D2765-84.

amount of NRs in the resins increases the emission intensity of the $^5D_0 \rightarrow {}^7F_{0-4}$ Eu^{3+} transitions, which dominates the broad emission band of the polymer at the optimal value of 10 wt% NRs. Varying the amount of NRs in the polymer matrix does not change the position of the emission bands and relative intensity of the Eu^{3+} intra $4f^6$-$4f^6$ electronic transition as shown in Figure 4.4b, indicating that the dispersion of $(Gd_{0.96}Eu_{0.04})_2O_3$ NRs in the polymeric matrix does not affect the emission properties of the Eu^{3+}. The excitation spectra of HDGE matrix containing different amount of $(Gd_{0.96}Eu_{0.04})_2O_3$ NRs were recorded at room temperature monitoring the $^5D_0 \rightarrow {}^7F_2$ (C_2) emission at 610.5 nm, Figure 4.4c. A broad band centered at 250 nm was observed, attributed to the O-Eu LMCT band [100]. Moreover, the excitation spectra of the pure NRs and HDGE-NR composites (Figure 4.4c) display the intra-$4f^6$-$4f^6$ transitions of Eu^{3+} ($^7F_{0,1} \rightarrow {}^5D_{0-4}, {}^5L_6, {}^5G_{2-6}$) and the Gd^{3+} intra-$4f^7$-$4f^7$ lines ($^8S_{7/2} \rightarrow {}^6I_{7/2-17/2}$, $^6P_{3/2-7/2}$), in agreement with previous reports for analogous oxide materials [58–61]. For the HDGE matrix with $(Gd_{0.96}Eu_{0.04})_2O_3$ NRs, a progressive blue-shift of the LMCT band was observed on increasing the amount of NRs, (Figure 4.4c). This could be explained in terms of the size of the NRs. Previously, it was shown that reduction of particle size in Y_2O_3:Eu^{3+} crystals resulted in lattice distortion and increase in the ionic character of the Eu-O bond (shorter Eu-O bond length), leading to a blue shift of the LMCT band [29]. Such blue shift has also been noted in the excitation spectra of Gd_2O_3:Eu^{3+} nanotubes and NRs, relatively to those of the microcrystals [58]. In the present case, after the incorporation of the NRs in the polymer and during the dispersion and UV-curing processes some NRs may presumably be broken into shorter pieces and/or be transformed into nanoparticles. The reduction of particle size causes lattice distortion (larger lattice constant) with the corresponding increase in the ionic character of the Eu-O bonds leading to the shifting of the LMCT band towards the high energy side (Table 4.2). The increase of this blue shift with increasing the content of NRs in the films may indicate the presence of shorter Eu-O bond lengths due to the increasing number of particles with much smaller size. Furthermore, as shown in Figure

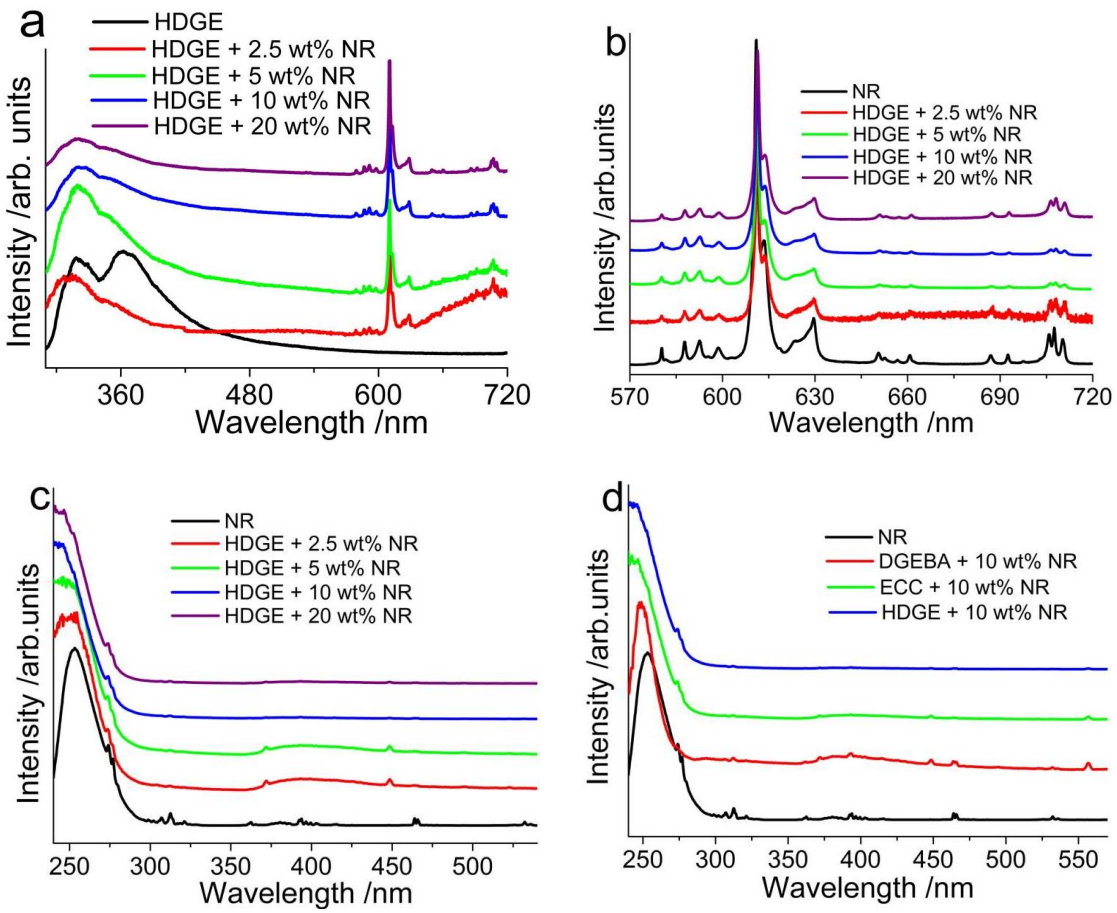

Figure 4.4: a) Room-temperature emission spectra of pristine HDGE and HDGE-$(Gd_{0.96}Eu_{0.04})_2O_3$ nanocomposites excited at 260 nm, b) comparison of the emission spectra of HDGE-$(Gd_{0.96}Eu_{0.04})_2O_3$ nanocomposites and pure $(Gd_{0.96}Eu_{0.04})_2O_3$ NRs in the 570-720 nm spectral region, c) excitation spectra of Eu^{3+} in pure Gd_2O_3 NRs and in HDGE-$(Gd_{0.96}Eu_{0.04})_2O_3$ composites monitoring the emission at 610.5 nm, and d) excitation spectra of Eu^{3+} in pure Gd_2O_3 NRs and in the three polymeric matrices monitoring the emission at 610.5 nm.

4.4c there is a decrease on the relative intensity of all the intra-$4f^6$-$4f^6$ transitions of Eu^{3+} in the composites, when compared to the intra-$4f^6$-$4f^6$ transitions of Eu^{3+} in the pure NRs, indicating that direct excitation of Eu^{3+} in the composites is less efficient than in the Gd_2O_3 host. On the other hand, excitation through the LMCT band of the composites efficiently sensitizes the Eu^{3+}.

As was mentioned, 10 wt% of $(Gd_{0.96}Eu_{0.04})_2O_3$ NRs in the HDGE matrix is the optimal amount to have a measurable Eu^{3+} emission intensity, while preserving the emission features of the pristine matrix. Furthermore, 10 wt% of NRs is the maximum amount which has no significant effect on the photo-curable process. Thus, the effect of the host matrix on the excitation and emission properties of the NRs were also studied by introducing 10 wt% of $(Gd_{0.96}Eu_{0.04})_2O_3$ NRs into two other epoxy resins (DGE-BA and ECC), Figures 4.5a-c. Figure 4.4d shows the room-temperature excitation

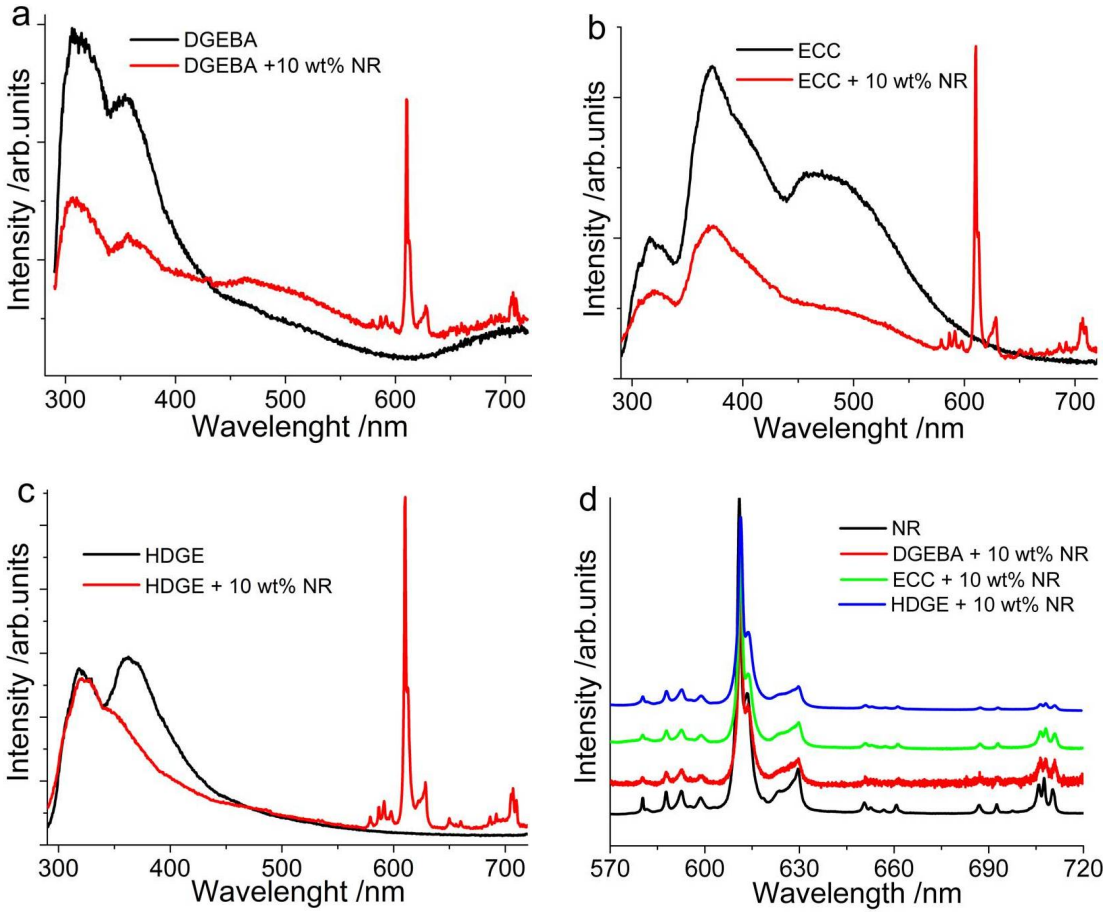

Figure 4.5: a-c) Comparison of the room-temperature emission spectra of pristine polymer matrices and their related composites containing 10 wt% of $(Gd_{0.96}Eu_{0.04})_2O_3$ NRs and d) emission spectra of Eu^{3+} in the three polymer matrices compared with the emission spectra of Eu^{3+} in pure Gd_2O_3 NRs; the excitation wavelength was at 260 nm.

spectra of the $(Gd_{0.96}Eu_{0.04})_2O_3$ NRs and the NR-polymeric composites, monitoring the $^5D_0 \rightarrow {}^7F_2(C_2)$ emission at 610.5 nm. Similar to the HDGE-$(Gd_{0.96}Eu_{0.04})_2O_3$-NRs composite (Figure 4.4c), it is evident that a blue-shift and a broadening of the LMC-T are observed, relatively to the values measured for the pure $(Gd_{0.96}Eu_{0.04})_2O_3$ NRs (Table 4.2). Thus, the blue shift may be associated with the reduction of particle size of the NRs in the composite (relatively to the pure NRs) resulted in lattice distortion and increase in the ionic character of the Eu-O bonds (shorter Eu-O bond length) [29].

The room-temperature emission spectra of pristine polymer matrices and their corresponding composites with 10 wt% NRs are compared and presented in Figure 4.5a-c. Dominant broad emission bands in the UV-visible region are observed for the polymer matrices without the NRs. The spectral range of these bands and their peak positions depends on type of the polymer matrix. The incorporation of 10 wt% NRs into each polymer, however, results in a dominant red emission of the $^5D_0 \rightarrow {}^7F_2(C_2)$ line centered at 610.5 nm. The influence of the different polymer matrices on the Eu^{3+} emission lines is also shown in Figure 4.5d. There is no significant difference in the energy of the e-

Table 4.2: LMCT band peak position, E_{LMCT} (cm^{-1}), in the nanocomposites, its peak shift, ΔE_{LMCT} (cm^{-1}), relatively to that of pure $(Gd_{0.96}Eu_{0.04})_2O_3$ nanorods, $^5D_0(C_2)$ decay time, τ_d (ms), of Eu^{3+} in the NRs and in the nanocomposites, and thickness (μm), measured by perfilometer, of the nanocomposite films.

Materials	E_{LMCT}, ΔE_{LMCT} (cm^{-1})	τ_d (ms)	Thickness (μm)
Nanorods (NR)	39216, 0	1.97±0.004	....
HDGE + 2.5 wt% NR	40650, 1434	.....	11.2
HDGE + 5 wt% NR	40733, 1517	1.18±0.012	10.6
HDGE + 10 wt% NR	41322, 2106	1.14±0.013	11.9
HDGE + 20 wt% NR	41494, 2278	1.18±0.012	7.9
DGEBA + 10 wt% NR	40000, 784	0.98±0.027	10.2
ECC + 10 wt% NR	41237, 2021	1.15±0.016	7.9

mission peaks or in the number of Stark components, indicating that the change of the host polymeric matrix has little effect on the dispersion of the $(Gd_{0.96}Eu_{0.04})_2O_3$ NRs. As mentioned, the choice of the matrix strongly influences the matrix-to-Eu^{3+} emission intensity ratio, Figure 4.5d. Indeed, the intensity depends on the number of photons emitted from the upper excited states and, thus, the presence of non-radiative channels will significantly reduce the emission intensity of the $4f^6$-$4f^6$ transition lines. In the polymeric materials the presence of various high vibration frequency bonds (e.g., C-H and O-H bonds), obviously leads to a non-radiative energy transfer from the photoactive filler (in this case energy levels of Eu^{3+}) to the matrix, resulting in a decrease in the intensity and/or quenching of the metal emission) [101].

4.4.2 $^5D_0(C_2)$ decay time

Among the intra-$4f^6$-$4f^6$ transitions of Eu^{3+} in cubic Gd_2O_3, the $^5D_0 \rightarrow {}^7F_2(C_2)$ emission line dominates the spectral intensity with relatively long lifetime upon excitation in the LMCT band [58–61]. In the present composite materials, the $^5D_0 \rightarrow {}^7F_2(C_2)$ transition is also shown to be the dominant emission of Eu^{3+} (Figure 4.5) and the study of its lifetime in these types of systems may be useful. Figure 4.6 shows the room-temperature emission decay curves of the $^5D_0(C_2)$ level recorded by monitoring the $^5D_0 \rightarrow {}^7F_2(C_2)$ transition at 610.5 nm and exciting at 260 nm (LMCT band). All the $^5D_0(C_2)$ emission-decay curves of Eu^{3+} in the different composites (Figure 4.6) are monoexponential, $i = i_0 exp(-t/\tau_d)$, where i and i_0 are the emission intensity of the $^5D_0$ level at time t and $t = 0$, respectively, and τ_d is the $^5D_0$ decay time. The composites exhibit τ_d values (Table 4.2) shorter than the pure $(Gd_{0.96}Eu_{0.04})_2O_3$ NRs. As discussed above, this may be attributed to the presence of high-frequency vibration modes in the polymer matrices, which quench the radiative energy from the emitting level. In contrast, no effects on the decay time were observed by changing the amount of NRs in HDGE (Figure 4.6c and Table 4.2).

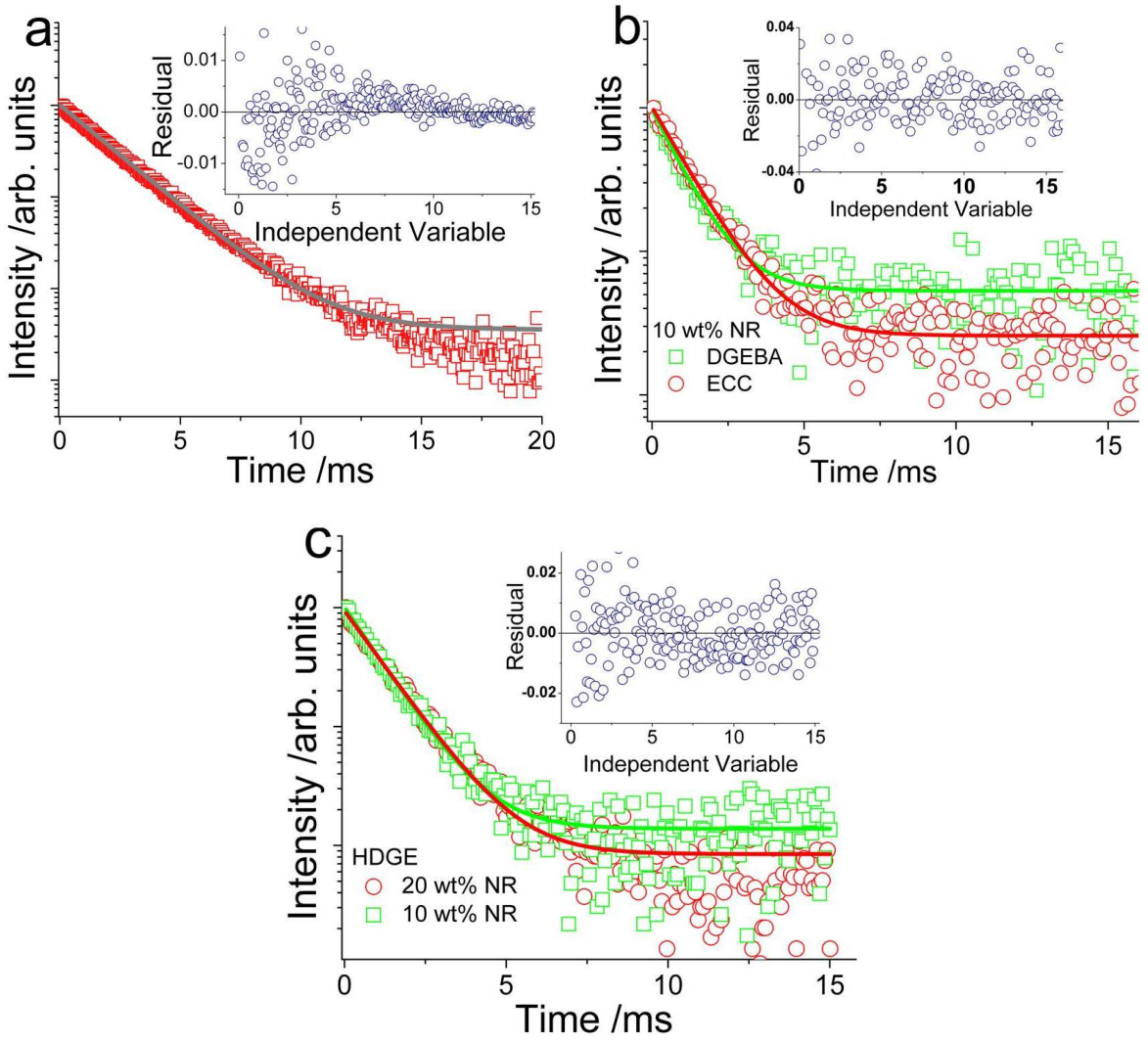

Figure 4.6: Room-temperature $^5D_0(C_2)$ emission decay curves, exciting at 260 nm and monitoring the emission at 610.5 nm: a) pure $(Gd_{0.96}Eu_{0.04})_2O_3$ NRs, b) 10 wt% $(Gd_{0.96}Eu_{0.04})_2O_3$ NRs in ECC and DGEBA matrices and c) 10 and 20 wt% NRs in HDGE matrix. The solid lines represent the fitting curves while the open squares and circles are the experimental data; the inset in each graph shows the residual *vs.* independent variable as an indication for the goodness of fit parameter.

4.5 Summary and conclusion

Light-emitting epoxy/$(Gd_{0.96}Eu_{0.04})_2O_3$ nanocomposite materials were produced by embedding $(Gd_{0.96}Eu_{0.04})_2O_3$ NRs in different epoxy matrices *via* UV-curing process. The effect of the $(Gd_{0.96}Eu_{0.04})_2O_3$ NRs incorporation on the kinetics of the photo polymerization mechanism and on the thermal properties of the coatings was evaluated. The epoxy-ring conversion decreases proportionally to the amount of the NRs in the mixtures associated with the competition between the photo-initiator and NRs for absorbing the irradiating UV light. The high value of insoluble fraction measured by chloroform extraction indicates that the lower conversion does not affect much the

properties of the materials up to 10 wt% of NRs embedded in the polymeric matrix. Finally, DSC measurements performed on the photo-cured films evidenced a slight increase of the glass transition temperature due to the hindering effect of the NRs on the chain mobility. The three composite films preserved the emission characteristics of Eu^{3+}, with only a variation in the relative intensity between the Eu^{3+} emission and the broad band emission of the polymer matrix. The $^5D_0 \rightarrow {}^7F_2(C_2)$ lifetimes of NRs and composites were measured from the monoexponential decay curves. Due to the presence of non-radiative channels in the polymer matrix, the composites decay time is shorter than that of pure NRs. The excitation spectra measured monitoring the $^5D_0 \rightarrow {}^7F_2(C_2)$ transition of the polymer matrices revealed the presence of efficient energy transfer from the LMCT band and the Gd^{3+} $4f^7$ levels to the Eu^{3+} energy levels. This study demonstrates the potential of UV-curing to obtain photoactive smart coatings.

Chapter 5

All-In-One Optical Heater-Thermometer Nanoplatform Operative from 300 to 2000 K Based on Er^{3+} Emission and Blackbody Radiation

5.1 Introduction

The use of plasmonic nanoparticles as sources of heat attracted much interest in the last decade. Ratiometric nanothermometers with high-spatial resolution, in turn, emerged only in the last couple of years as a very active field of research. Suitable nanoplatforms integrating heaters and thermometers, however, have not yet been realized, despite their great potential in nanophotonics and biomedicine. In this chapter, we demonstrate a step forward towards assessing the local temperature of laser-excited gold nanostructures using an all-in-one nanoplatform comprising $(Gd,Yb,Er)_2O_3$ nanorods (thermometers) that were surface-decorated with gold nanoparticles (heaters)[1]. This study aims at (i) improving the local temperature measurement of laser-excited gold nanostructures, whereby the photoluminescent thermometer size was reduced to the scale of the Au nanoheaters, (ii) increasing the span of sensed temperature and (iii) demonstrating a simple and all-in-one nanoplatform for laser-induced heat generation that leads to white-light emission upon increasing AuNPs concentration and for temperature sensing. The local temperature is calculated using either Boltzmann's distribution (300 - 1050 K) of the Er^{3+} up-conversion $^2H_{11/2} \rightarrow {}^4I_{15/2}/{}^4S_{3/2} \rightarrow {}^4I_{15/2}$ intensity ratio or Planck's law (1200 - 2000 K) for white-light emission ascribed to the blackbody radiation. The surface temperature increase of the $(Gd,Yb,Er)_2O_3$ nanorods and the operating range of the nanothermometers can be tuned *via* the amount of AuNPs. An outstanding result of this study is the unambiguous attribution of the white-light emission to an incandescence process, which settles the existing controversy on the subject. The synthesis and plasmonic resonance characterization of the nanoplatforms have collaboration with Prof. L. M. Liz-Marzán (Vigo and Bilbao, Spain).

[1] **M. L. Debasu**, D. Ananias, I. Pastoriza-Santos, L. M. Liz-Marzán, J. Rocha, L. D. Carlos, All-In-One Optical Heater-Thermometer Nanoplatform Operative From 300 to 2000 K Based on Er^{3+} Emission and Blackbody Radiation, *Adv. Mater.*, 25(35), 4868-4874, 2013, ***Cover of the Issue***.

5.2 State of the art in temperature sensing

Temperature is a fundamental thermodynamic variable whose knowledge and quantification is absolutely essential in numerous areas. Measuring the temperature at the nanoscale with high spatial (1 μm) and temperature (0.1 degree) resolution is, however, very challenging and an exciting field of research (e.g., in intracellular temperature fluctuations and temperature mapping of microcircuits) [102–104]. In order to overcome this challenge, a considerable effort has been made towards developing non-contact, self-referenced and non-invasive optical temperature sensors based on Ln^{3+}-doped materials as a new class of thermometers [105–108]. In these materials, sensing is achieved using temperature-sensitive emission properties of the Ln^{3+}, e.g., excited-state lifetimes [109], relative emission intensities [102,110], or spectra line shifts [108,111]. In particular, the Ln^{3+} (e.g., Er^{3+} and Nd^{3+}) may exhibit at least two distinct emission bands originating from two closely-spaced energy states that respond differently to induced temperature changes. This can be illustrated by a simplified energy level diagram with a three-level state in which the energy separation between the ground level 0 and the upper levels 1 and 2 is much larger than the thermal energy kT, where T is the absolute temperature and k the Boltzmann constant. The two closely-spaced energy levels 1 and 2 with energy separation ΔE_{21} can be populated from the ground level 0 by photon excitation. When ΔE_{21} is close enough to kT, level 2 can also be populated from level 1

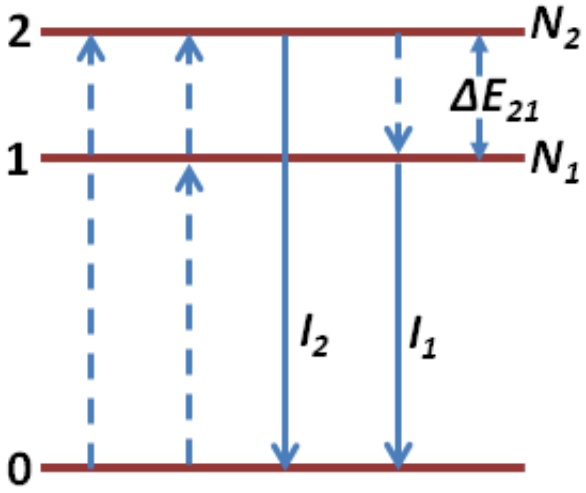

Figure 5.1: Schematic diagram for a three-level energy state.

by the thermal excitation. According to the Boltzmann distribution, the ratio of the populations N_2 and N_1 in levels 2 and 1 at equilibrium is given by:

$$\frac{N_2}{N_1} = exp(\frac{-\Delta E_{21}}{kT}) \tag{5.1}$$

Here, appropriate measurable parameters that can be directly related to the populations N_2 and N_1 of the upper levels are the corresponding emission intensities I_2 and I_1 due to the depopulation of these levels to the common lower/ground level 0 (Figure

5.1). The intensities are directly proportional to the populations:

$$\begin{aligned} I_1 &= \varphi_1 N_1 \\ I_2 &= \varphi_2 N_2 \end{aligned} \tag{5.2}$$

where φ_1 and φ_2 are constants. These constants depend on geometrical factors and intrinsic properties of the emitting levels (such as degeneracies, branching ratios and luminescence quantum efficiency) [108]. Then, using Equation 5.1 the ratio between I_2 and I_1 can be given by:

$$\frac{I_2}{I_1} = \frac{\varphi_2}{\varphi_1}\frac{N_2}{N_1} = Bexp(\frac{-\Delta E_{21}}{kT}) \tag{5.3}$$

where B is a constant to be determined.

Equation 5.3 constitutes the so-called fluorescence (or luminescence) intensity ratio, FIR (LIR), method which enables a self-referenced optical readout of absolute temperature at the nanoscale. Such ratiometric method was indeed proposed as early as 1976 by Kusama et al. [111] to measure the internal temperature of Y_2O_2S:Eu phosphor based on the Eu^{3+} emission. Recently, several ratiometric thermometers based on Ln^{3+}-doped inorganic nanophosphors have emerged [106–108]. Singh et al. [112], for instance, reported an optical nanothermometer using Gd_2O_3:Yb^{3+}/Er^{3+} nanocrystals. The authors use the FIR of two thermally coupled excited states of Er^{3+}, $^2H_{11/2}$ and $^4S_{3/2}$ centered at 523 and 548 nm, described by Boltzmann's distribution (Equation 5.3) in the temperature range between 300 and 900 K. The first attempt to determine the internal temperature of a living cell was performed by Vetrone and co-workers [110] based on $NaYF_4$:Er^{3+}/Yb^{3+} nanoparticles (Figures 5.2a-c). In this study, the internal temperature of the living cell was measured in the range of 25 to 45 ^{o}C (Figure 5.2d), based on the FIR of the green emission bands of Er^{3+} ($^2H_{11/2}\rightarrow{}^4I_{15/2}$ and $^4S_{3/2}\rightarrow{}^4I_{15/2}$), Figure 5.2b.

In the emerging field of plasmonics [113], there is a growing interest to develop plasmonic-induced nanoheaters [114, 115] for applications in e.g., nanomedicine [116–118]. Plasmonic structures as heat nanosources (so-called thermo- or molecular-plasmonics) exploit the small size and large optical cross-section of the metal nanostructure to induce large temperature variations within a small volume, but we presently lack a full understanding of the effects that such large temperature gradients may have on these systems [119]. Moreover, the precise measurement of the surface-temperature increments of nanoheaters (for example in hyperthermia) caused by thermo-plasmonics is crucial to regulate the heat released to the surrounding medium, thereby permitting the adjustment of the irradiation parameters and guiding the therapy [114, 120]. The local temperature increase avoids the need for macroscopic heating, with the concomitant attenuation of collateral effects arising from heating of healthy tissues. Until recently, the FIR method has been the most promising approach for accurate control of the local temperature in these systems.

To image the temperature profile in the vicinity of gold nanostructures excited with a

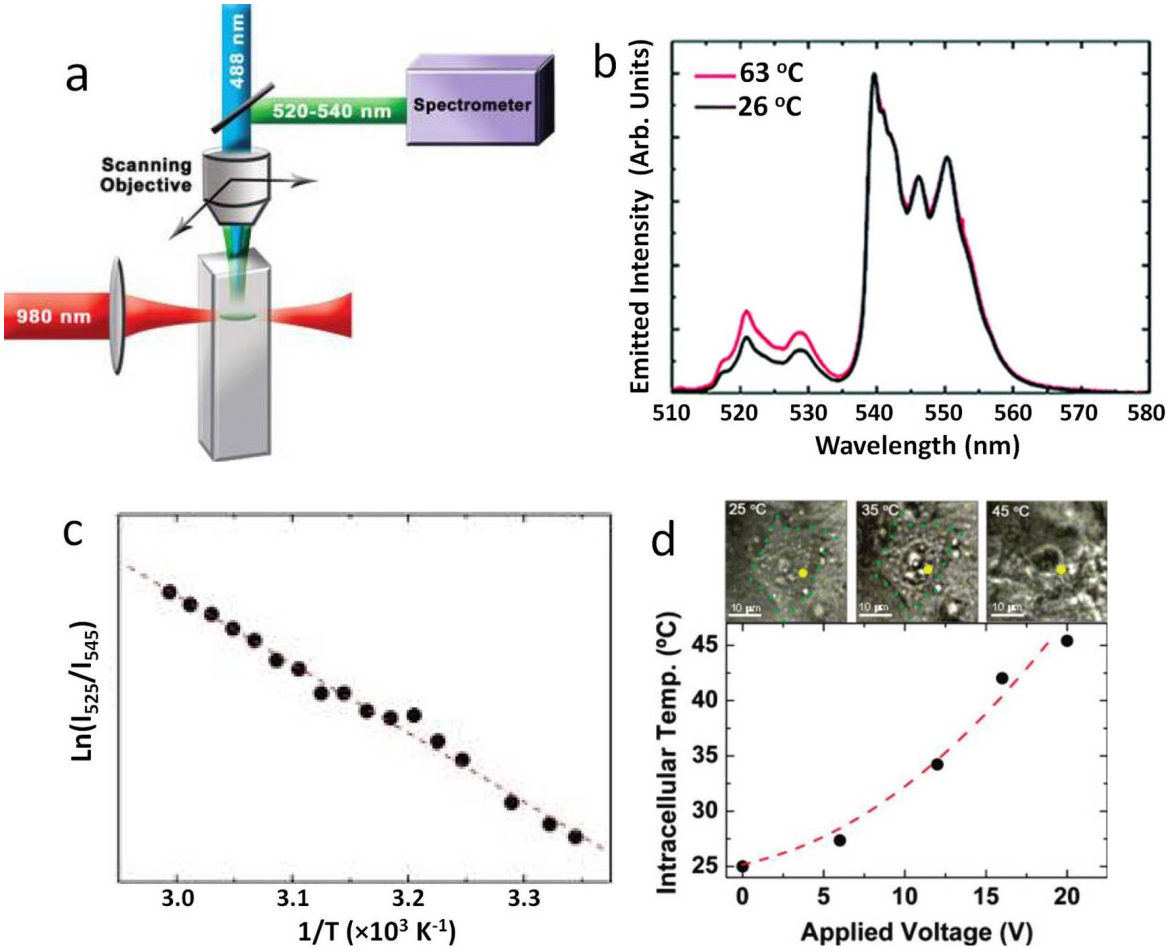

Figure 5.2: a) Schematic of the pump-probe setup used to measure the temperature profile created by heating a colloidal solution of $NaYF_4$:Er^{3+},Yb^{3+} NPs in water with a 980 nm diode laser (pump beam) and subsequently scanned with a 488 nm Ar-laser (probe beam). b) Up-conversion emission spectra obtained at two different cuvette temperatures. c) a plot of $ln(I_{525}/I_{545})$ *vs.* $1/T$ to calibrate the thermometric scale for the water-dispersible $NaYF_4$:Er^{3+},Yb^{3+} NPs. d) (Top) Optical transmission images of an individual HeLa cell at three inner temperatures. Cell death is observed at 45 ^{o}C. (Bottom) Temperature of the HeLa cell determined by the Er^{3+} emission in the $NaYF_4$:Er^{3+},Yb^{3+} NPs as a function of the applied voltage [110].

532 nm continuous wave (CW) laser (0.2 - 6×10^{10} W cm^{-2}) Carlson and co-workers used a photoluminescent thin film of Er^{3+}-doped $Al_{0.94}Ga_{0.06}N$ [119, 121, 122], Figure 5.3a. The thin-film luminescent sensor was calibrated to determine the local temperature of either a single 40 nm gold nanoparticle (AuNP) or a single lithographically-prepared gold nanodot by comparing the measured temperature change of the former to the theoretical temperature change calculated from the absorption cross-section. This calibration (a factor of 12.8, Figure 5.3b) was necessary because of the insufficient spatial resolution of the optical system used: the real image size of the NP temperature profile was much smaller than the light-detection aperture (500 nm diameter) and, thus, the measured temperature was an average value weighted over all Er^{3+} ions in the sample

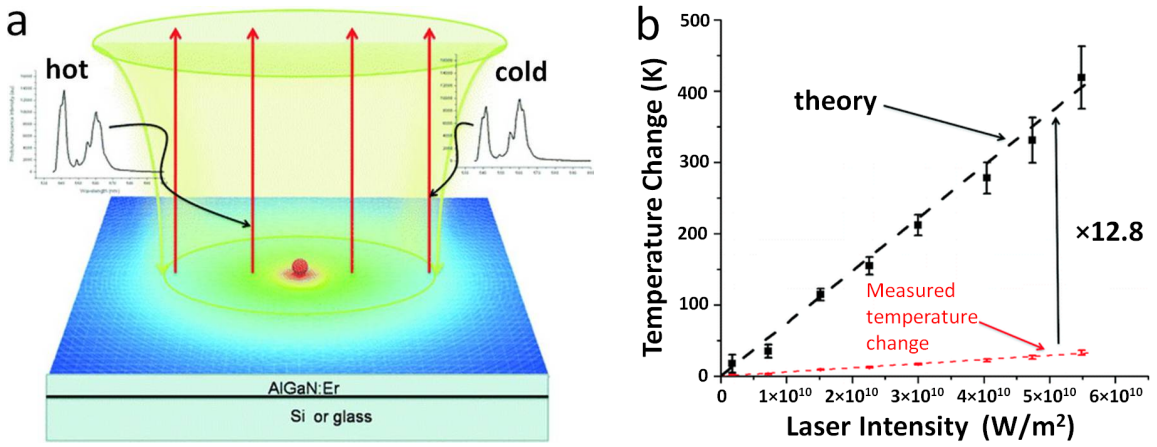

Figure 5.3: a) Diagram illustrating the properties of the thermal sensor. Excitation of a gold nanostructure with 532 nm light produces a hot spot whose temperature falls off as one over the distance. The photoluminescence spectrum from Er^{3+} embedded in the thin film changes with temperature. Hotter temperatures increase the photoluminescence intensity of the higher energy peak at 540 nm relative to the lower energy peak at 565 nm. b) Temperature change (measured using from Er^{3+}) of the 40 nm gold NP (red dashes) as a function of laser intensity. This data is scaled by 12.8 to give the data (black symbols) that fits theory (black dashes), using Equation 5.4, for the thermal behavior of a 40 nm gold NP [121].

volume. This approach has other limitations, since the theoretically calculated surface temperature change strongly relies on the precise estimation of the sample's absorption cross-section, effective-refractive index and thermal conductivity, as well as on the laser power density according to the relation [119]:

$$\Delta T_{max} = \frac{C_{abs} P}{4\pi k_{eff} R} \tag{5.4}$$

where ΔT_{max} is the steady-state maximum local temperature change (K) at the nanoparticle surface, C_{abs} the absorption cross-section (m^2) of the nanoparticle, P the pump power density (W m^{-2}) of the excitation laser on the particle, k_{eff} the effective thermal conductivity (W m^{-1} K^{-1}) of the medium and R the radius (m) of the nanoparticle. Setoura et al. [123] circumvented some of the referred limitations, in particular the particle temperature was not affected by the spatial resolution of the optical setup. Indeed, these authors have demonstrated a straightforward way of estimating the particle temperature based on the measurement of the scattering spectral peak shifts caused by a 488 nm CW laser irradiation ($< 7{\times}10^5$ W cm^{-2}) of a single AuNP supported on a glass substrate. Yet, the temperature could only be determined with an accuracy of $\pm$ 20 K over the range 300 - 700 K. Moreover, the method requires parameters such as the Au temperature-dependent dielectric function and effective-refractive index of the medium.

In an effort to bring together the sizes of the nanothermometer and the nanoheater, Rocha et al. [124] used Nd-doped LaF_3 nanoparticles and gold nanorods (GNRs) to measure sub-tissue temperature in a single-beam plasmonic-mediated heating experi-

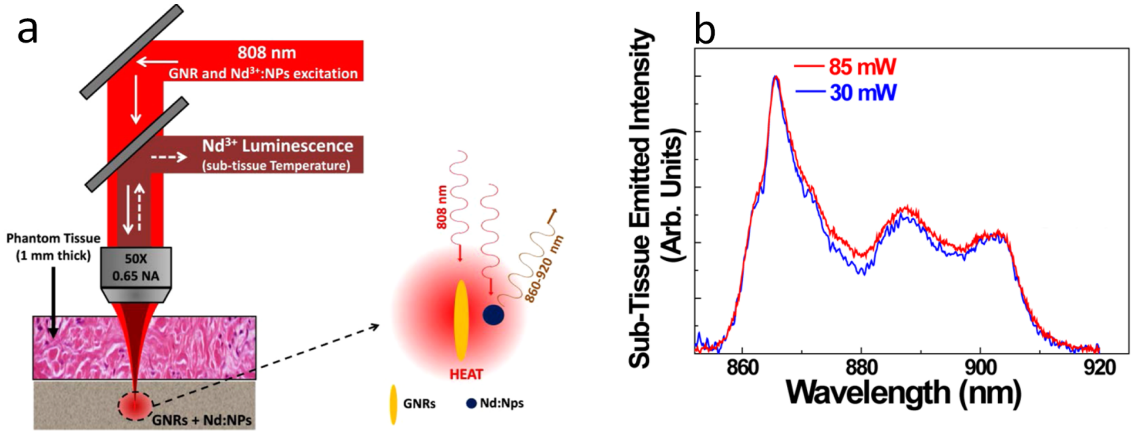

Figure 5.4: a) Schematic representation of the experimental setup developed by Rocha and co-workers for single-beam sub-tissue-controlled hyperthermia. A 808 nm laser beam is focused into an aqueous solution containing GNRs (nanoheaters) and Nd^{3+}:LaF_3 nanoparticless (thermometers). The solution was placed under a 1 mm thick phantom tissue. The luminescence of Nd^{3+}:LaF_3 nanoparticles was collected by using the same objective, and the sub-tissue temperature was extracted from its spectral analysis. Diagram at the right reflects the fact that both GNRs and Nd^{3+}:LaF_3 NPs were simultaneously excited by the 808 nm radiation. b) Subtissue normalized emission spectra generated by Nd^{3+}:LaF_3 nanoparticles as obtained for two different 808 nm laser powers (30 and 85 mW) [124].

ment, Figure 5.4a. The authors were able to measure sub-tissue temperature changes (10 - 60 ^{o}C) induced by laser-excited GNRs (heaters) using the Nd-doped particles as thermometers, based on the FIR of Nd^{3+} emissions band centered at 863 and 885 nm (Figures 5.4b). The GNR heaters and the nanothermometer particles are separated in space and do not constitute a single integrating nanoplatform (Figure 5.4a). Only an average temperature (not the absolute local temperature) of the sample volume under irradiation is measured, however, as the emission intensity includes the contribution of the Nd-doped LaF_3 particles that are away from the heaters.

Our approach constitutes a step forward towards (i) improving the local temperature measurement of laser-excited gold nanostructures, whereby the photoluminescent thermometer size was reduced to the (nano) scale of the Au nanoheaters, (ii) increasing the span of sensed temperature and (iii) demonstrating a simple and all-in-one nanoplatform for laser induced heat generation that leads to white-light emission upon increasing AuNPs concentration and for temperature sensing. The nanocomposites consist of $(Gd,Yb,Er)_2O_3$ NRs whose surface was decorated with AuNPs and, thus, there is only a small dispersion in the heater-thermometer distances, i.e., in the sensed temperature. The local temperature is calculated using: (i) Boltzmann's distribution (300 - 1050 K with resolution of 0.3 - 2.0 K and under several pump power cycles) for the Er^{3+} up-conversion $^2H_{11/2}\rightarrow{}^4I_{15/2}/{}^4S_{3/2}\rightarrow{}^4I_{15/2}$ intensity ratio and (ii) Planck's law (1200 - 2000 K with resolution of 4.13 K and under a single pump power cycle) for the observed white-light emission. No other parameters are required. The increase of the surface temperature of the $(Gd,Yb,Er)_2O_3$ NRs and, thus, the operating range of the nanothermometers is easily adjusted by controlling the amount of AuNPs. Anal-

ogous white-light emission upon CW laser excitation has been reported for disparate materials, such as lanthanide oxides [125–127], $LiYbP_4O_{12}$ [128], YVO_4:Yb^{3+}/Er^{3+} nanoparticles [129], carbon nanotubes [130] and Si and SiC nanoparticles [131] but its origin is still contentious. A remarkable result of the present study is the unambiguous attribution of this white-light emission to an incandescence process, hence settling the controversy.

5.3 Synthesis of $(Gd,Yb,Er)_2O_3$ NRs-AuNPs-C

$(Gd_{0.95}Yb_{0.03}Er_{0.02})_2O_3$ NRs were synthesized *via* the wet-chemical route as described in chapter 3, (Figure 3.2), using aqueous solutions of $Gd(NO_3)_3$ (9.50 mL, 0.4 M), $Yb(NO_3)_3$ (0.3 mL, 0.4 M) and $Er(NO_3)_3$ (0.40 mL, 0.2 M). AuNPs were adsorbed on the NRs by the in situ reduction of $HAuCl_4{\cdot}3H_2O$ with $NaBH_4$ in an aqueous dispersion of the NRs (Figure 5.5). In a typical procedure illustrated in Figure 5.5, NRs powder (25 mg) was dispersed in distilled water (40 mL) under sonication for 15 minutes. An aqueous solution of $HAuCl_4{\cdot}3H_2O$ (0.25 mL, 0.01 M) was then added to the dispersion and the solution was stirred for 2 hours. Freshly prepared aqueous $NaBH_4$ solution (0.32 mL, 0.1 M) was quickly added to this solution under strong magnetic stirring. The solution immediately turned dark red and stirring was continued for 20 minutes,

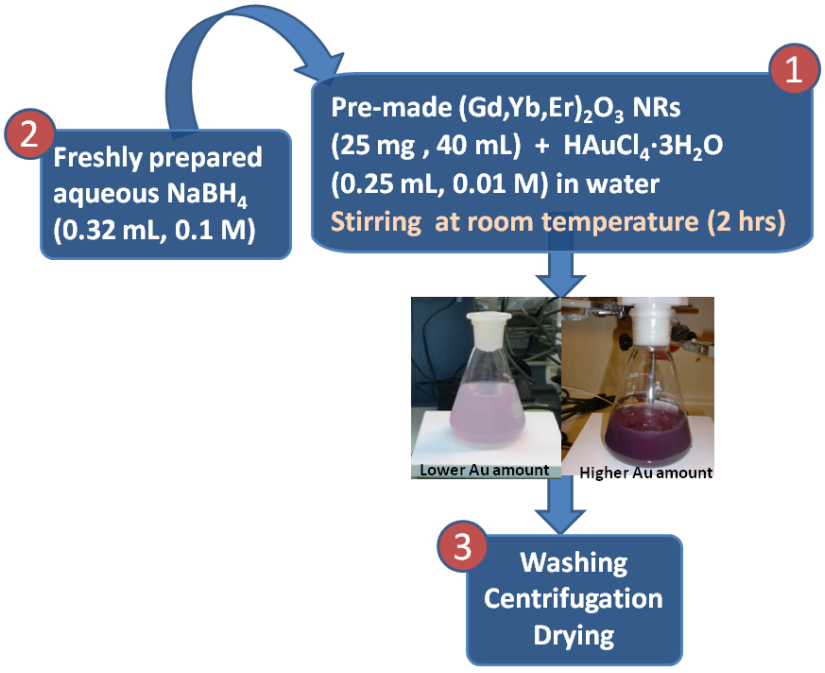

Figure 5.5: Schematic representation of the synthesis of $(Gd,Yb,Er)_2O_3$ NRs-AuNPs nanocomposite.

after which a dark-red precipitate was formed. The latter was washed several times under sonication, redispersed in water and centrifuged at 6000 rpm for 10 minutes. Finally, the precipitate was dried in air at 348 K affording $(Gd_{0.95}Yb_{0.03}Er_{0.02})_2O_3$

NRs-AuNPs-C, where C = 2.5 stands for the nominal Au amount (expressed in μmoles of gold metal). A similar synthesis procedure was employed for preparing samples with different C values (1.25, 5.0, 12.5, 25.0 and 37.5) by changing the $HAuCl_4 \cdot 3H_2O$ and $NaBH_4$ concentrations but keeping ratio the same.

Powder X-ray diffraction (PXRD)

PXRD patterns of bare $(Gd_{0.95}Yb_{0.03}Er_{0.02})_2O_3$ NRs and NRs-AuNPs-C, with C = 1.25 to 250.0, were analyzed. As expected, the diffraction patterns of NRs-AuNPs-C showed the presence of cubic Gd_2O_3 and cubic gold phases (PDF-04-002-1170) for C up to 37.5, Figure 5.6. Increasing the values of C increases the relative intensity of Au diffraction peaks and eventually gives only the cubic gold phase, e.g., for C = 250.0 (Figure 5.6, orange line).

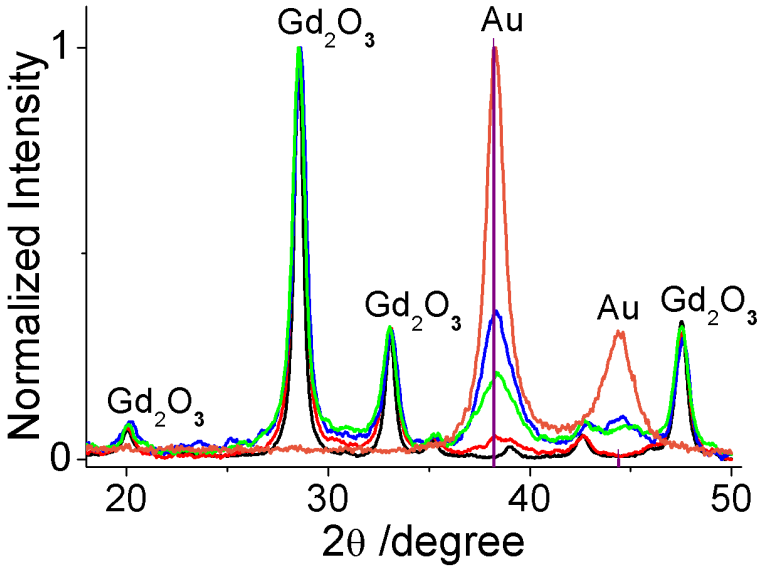

Figure 5.6: PXRD patterns: a) bare $(Gd_{0.95}Yb_{0.03}Er_{0.02})_2O_3$ NRs and NRs-AuNPs-C: bare NRs (black line), C = 5.0 (red), 25.0 (green), 37.5 (blue) and 250.0 (orange). The vertical violet lines are taken from the PDF database.

Transmission electron microscopy (TEM)

Figure 5.7 shows representative TEM images of $(Gd_{0.95}Yb_{0.03}Er_{0.02})_2O_3$ NRs decorated with AuNPs. The AuNPs are formed *via* reduction of the chloroaurate adsorbed on the NRs by $NaBH_4$. The surface defects on NRs may have important contribution to the nucleation and growth of AuNPs. The number of AuNPs decorating NRs may be easily tuned by changing the precursor concentration (Figure 5.7). As expected, the lower the amount of Au precursor, the fewer the number of AuNPs supported on

the NRs. Few AuNPs were found away from the surface of the NRs. The interplanar distances between adjacent planes for the NRs and AuNPs were determined from the high resolution TEM images along with the identification of the corresponding orientations of the crystallographic planes indexed from PXRD patterns (Figures 5.7a,b). It was noted that as the amount of Au precursor and $NaBH_4$ raised some of the NRs were broken into pieces and/or their shape was completely destroyed, e.g., for C = 250.0 (appendix B, Figure B.2f), in agreement with the PXRD evidence. Hence, only samples with C up to 37.5 shall be studied in this chapter. In general, TEM images indicate that the size of the AuNPs that can be grown on the NRs ranges from 5 nm to 15 nm, Figure 5.7 and Figures B.2a-f.

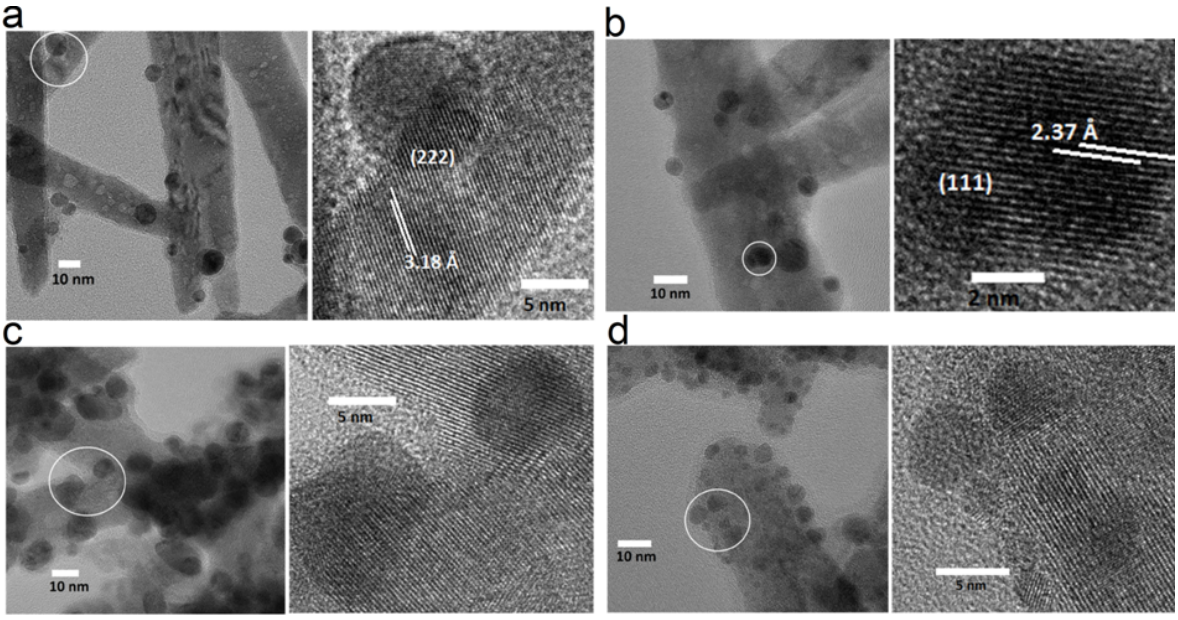

Figure 5.7: TEM images of NRs-AuNPs-C. a) C = 1.25. b) C = 2.5. c) C = 12.5. d) C = 25.0. The images on the right side zoom in the regions depicted by the white circles on left. The crystallographic planes and interplanar distances for NRs (a) and AuNPs (b) are presented on the right side.

UV-Vis-NIR absorption

UV-Vis-NIR absorption spectra for aqueous suspensions of bare NRs and as-prepared NRs-AuNPs-C are presented in Figure 5.8. As expected, the localized surface plasmon resonance (LSPR) bands ascribed to AuNPs are observed. The LSPR bands show different intensities and are centered at 535 - 550 nm depending on the value of C (Figure 5.8). The LSPR band is more evident for samples with larger C content, in agreement with the intensity of PXRD peaks corresponding to Au, Figure 5.8. The differences in the peak positions of LSPR band with C are attributed not only to the average size of AuNPs but also to the interparticle distances between the particles.

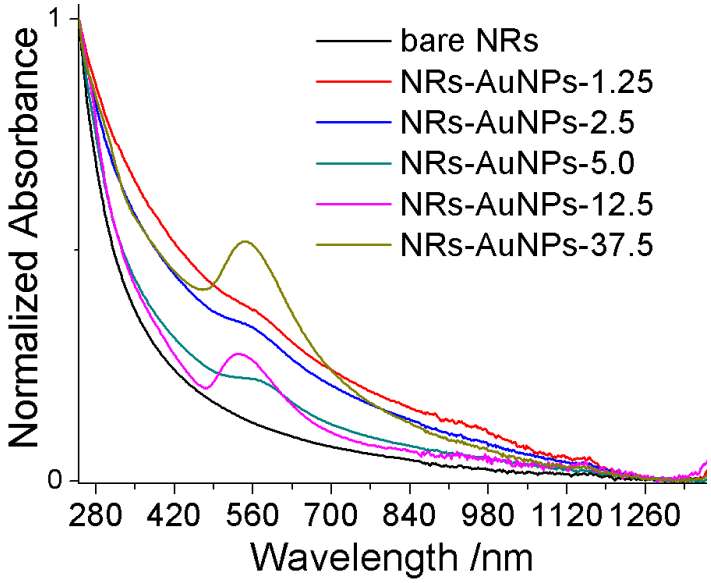

Figure 5.8: UV-Vis-NIR absorption spectra of aqueous suspensions of bare $(Gd,Yb,Er)_2O_3$ NRs and NRs-AuNPs-C.

Discussion

The emission properties of $(Gd_{0.95}Yb_{0.03}Er_{0.02})_2O_3$ NRs-AuNPs-C strongly depend on the value of C providing two different emission properties: Er^{3+} emission for C $\leqslant$ 5.0 and white-light emission ascribed to blackbody radiation for higher C values. In what follows, we discuss these distinct emission features and demonstrate the measurement of absolute local temperature based on the emission spectra in both cases.

5.4 Er^{3+} Emission: Boltzmann's Law

Figures 5.9a,b show the Er^{3+} up-conversion $^2H_{11/2}$,$^4S_{3/2}\rightarrow$ $^4I_{15/2}$ (510 - 565 nm) and $^4F_{9/2}\rightarrow^4I_{15/2}$ (620 - 670 nm) transitions of bare $(Gd_{0.95}Yb_{0.03}Er_{0.02})_2O_3$ NRs and NRs-AuNPs-1.25 excited at pump power up to 600 W cm^{-2}. It is evident that the presence of AuNPs strongly influences the relative emission intensity of the $^2H_{11/2}\rightarrow^4I_{15/2}$ and $^4S_{3/2}\rightarrow^4I_{15/2}$ transitions at a particular pump power, Figures 5.9a,b. The up-conversion mechanism for the red and green emission bands can be deduced from the power law relation [30, 132]:

$$\begin{aligned} I_{uc} &\propto P^n \\ \Rightarrow \log(I_{uc}) &\propto n\log(P) \end{aligned} \tag{5.5}$$

where I_{uc} is the integrated up-conversion emission intensity, P is the pump power and n is the number of absorbed photons for the emission. Accordingly, the well-known two-photon absorption process [30] is responsible for the red and green emissions (Figures 5.9)c,d.

Consider the spectral range 510 - 565 nm (Figures 5.9a,b): for bare NRs, the $^4S_{3/2}\rightarrow{}^4I_{15/2}$ transition dominates, while NRs-AuNPs-1.25 exhibits a prominent $^2H_{11/2}\rightarrow{}^4I_{15/2}$ emission. In addition, the integrated fluorescence intensity ratio FIR of the $^2H_{11/2}\rightarrow{}^4I_{15/2}$ to $^4S_{3/2}\rightarrow{}^4I_{15/2}$ bands increases with increasing pump power and, for a given pump power, with increasing concentration of AuNPs on the NRs (Figure 5.10a). The FIR

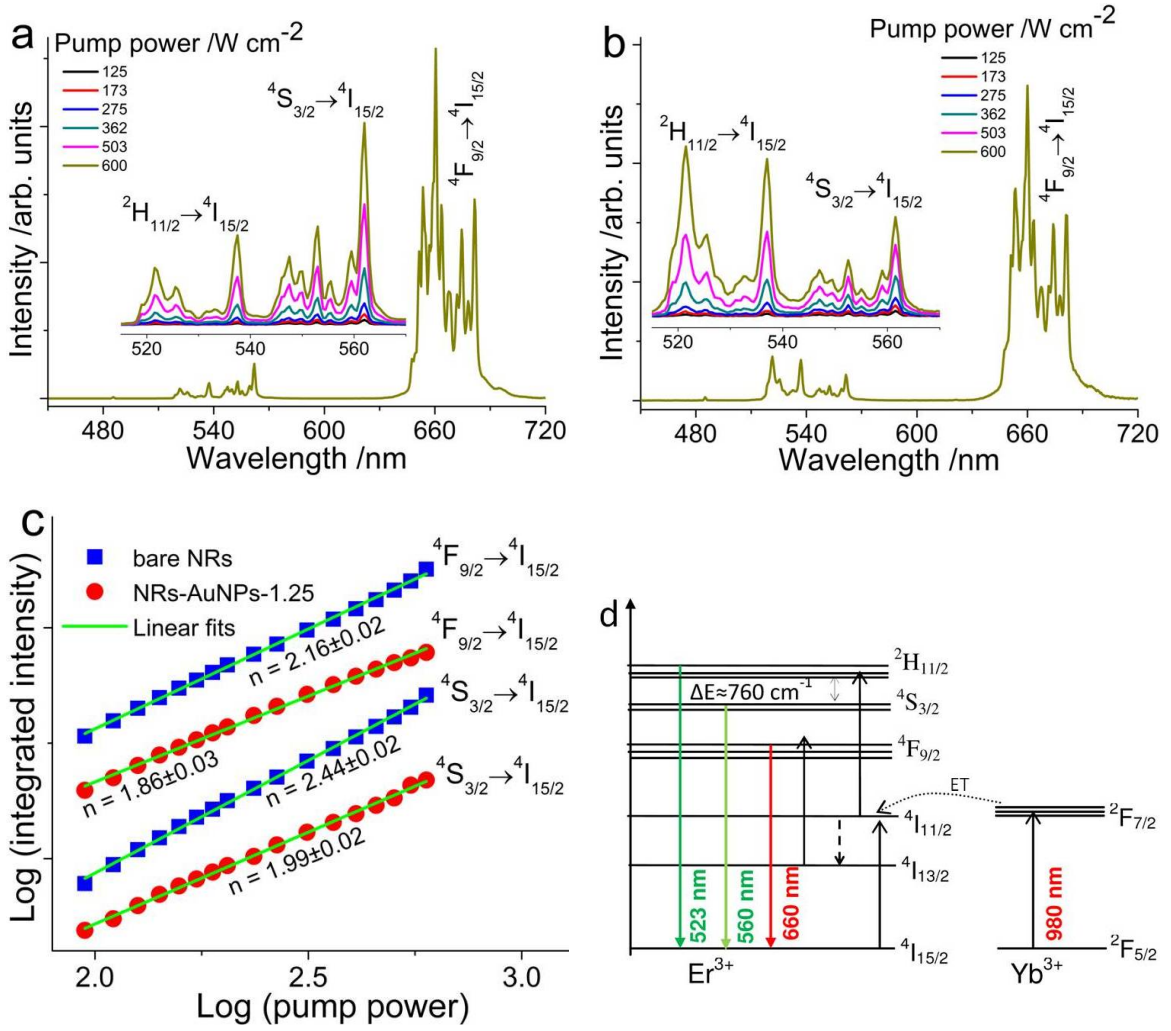

Figure 5.9: Evolution of the up-conversion emission spectra with pump power under excitation with a 980 nm CW laser diode: a) bare NRs and b) NRs-AuNPs-1.25; the insets zoom in the $^2H_{11/2}$,$^4S_{3/2}\rightarrow{}^4I_{15/2}$ transition regions. c) Double-log plots of pump power *vs.* up-conversion emission intensity for bare NRs and NRs-AuNPs-1.25. d) scheme of Yb^{3+}/Er^{3+} partial energy level diagrams showing the most probable Yb^{3+}-Er^{3+} energy transfer pathway.

variations observed for NRs covered with AuNPs are ascribed to the increase of the local temperature. UV-Vis-NIR absorption spectra of NRs-AuNPs-C (Figure 5.8) show that although the absorbance is stronger in the UV-Vis regions it is significant at 980 nm, thus allowing the heating of the AuNPs and increasing the temperature at the surface of the insulating oxide NRs. It has been previously observed that off-resonance plasmon excitation of gold nanoparticles may result in efficient heat generation [133, 134]. The details of the heating process are not yet clear and deserve further investigation.

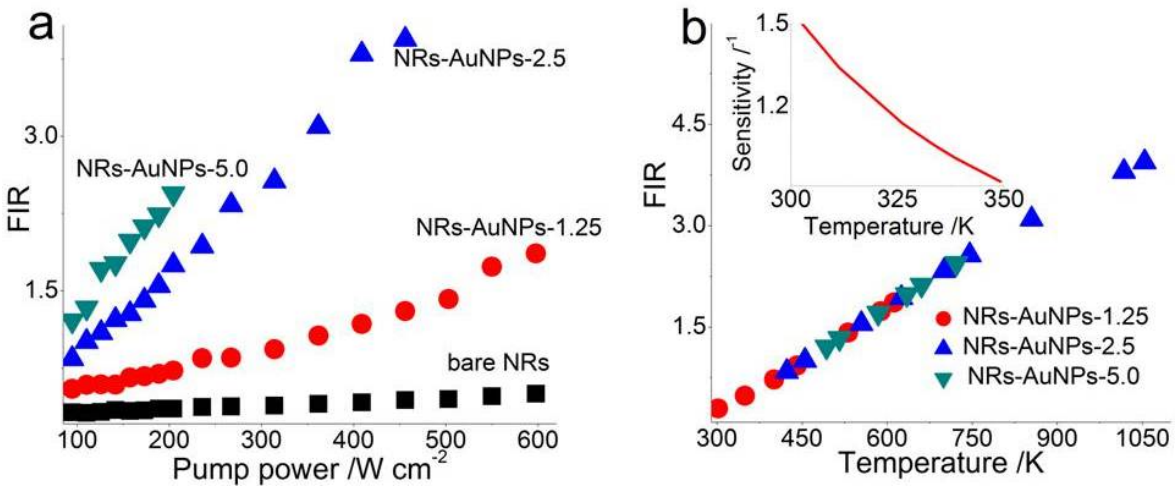

Figure 5.10: a) *FIR* plot of the $^2H_{11/2} \rightarrow {}^4I_{15/2}$ to $^4S_{3/2} \rightarrow {}^4I_{15/2}$ transitions *vs.* pump power for NRs-AuNPs-C, with C = 0.0 - 5.0) and b) *FIR vs.* absolute local temperature for NRs-AuNPs-1.25, NRs-AuNPs-2.5 and NRs-AuNPs-5.0 under excitation with a 980 nm CW laser diode with pump power in the ranges of 32 - 600 W cm^{-2}, 95 - 455 W cm^{-2} and 95 - 205 W cm^{-2}, respectively; the inset shows the temperature sensitivity curve for NRs-AuNPs-1.25 in the temperature range of physiological interest.

At this point, we have evidence for direct (980 nm) and multi-photon absorption, probably involving interband transitions of Au. Another possible mechanism may involve the AuNPs-absorption of part of the Er^{3+} visible emission (particularly the green band 510 - 565 nm), which is in good resonance with the LSPR band (Figure 5.8). The fact that the FIR value increases with increasing AuNPs coverage of NRs (Figure 5.10a) for a particular pump power is in agreement with previous results showing that the heat generated increases with the concentration of metal nanoparticles [117, 135, 136]. For comparison, the variation of the FIR with the pump power for the bare NRs is also shown in Figure 5.10a.

The increasing of the temperature at the NRs surface, in turn, induces the thermally-driven population increase of the $^2H_{11/2}$ energy level Figure 5.9b, at the expense of the lower-energy $^4S_{3/2}$ level. Using Equation 5.3:

$$\begin{aligned} FIR &= \frac{I(^2H_{11/2} \rightarrow {}^4\ I_{15/2})}{I(^4S_{3/2} \rightarrow {}^4\ I_{15/2})} = Bexp(\frac{-\Delta E}{kT}) \\ \Rightarrow \quad \ln(FIR) &= \ln(B) + (\frac{-\Delta E}{kT}) = \ln(B) + (\frac{-C}{T}) \end{aligned} \tag{5.6}$$

where B and C are constants to be determined. The energy separation ΔE between the two-closely spaced upper energy levels *ca.* 760 cm^{-1} is obtained from the emission spectrum (inset in Figure 5.11a) which gives C = 1094 K (for k = 0.6950 K^{-1} cm^{-1}). The value of $ln(B)$ is determined from the plot of the FIR *vs.* pump power (Figure 5.11a) by extrapolating the linear curve to the limit of no laser excitation power (FIR *ca.* 0.29) that corresponds to 300 K [121, 137]. Plugging these two values (FIR

= 0.29 and T = 300 K) into Equation 5.6 gives $ln(B) = 2.41$, which is in agreement with previously reported range ($1.5 \leq ln(B) \leq 2.5$) for this constant [138–141].

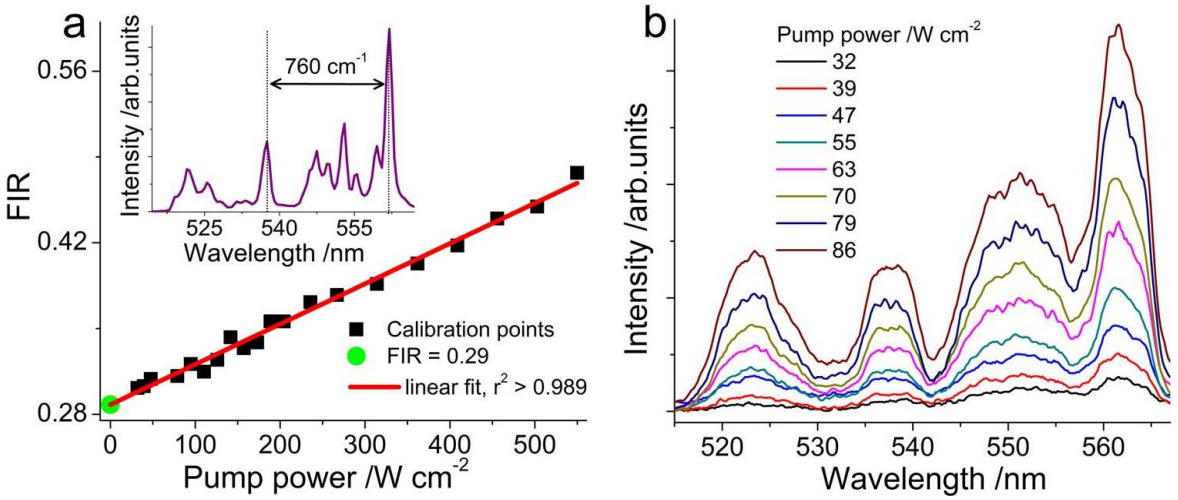

Figure 5.11: a) Calibration curve FIR vs. pump power; the green symbol is the FIR value at the limit of no laser excitation and the inset shows the energy gap ΔE between the $^2H_{11/2}$ and $^4S_{3/2}$ levels (vertical dotted lines). b) Evolution of the Er^{3+} ($^2H_{11/2}$, $^4S_{3/2}$) emission intensity for NRs-AuNPs-1.25 under low-power excitations (32 - 86 W cm^{-2}) corresponding to the temperature range of 301 - 350 K.

Using Equation 5.6, T is readily determined and the result is displayed in Figure 5.10b. By varying the pump power and the AuNPs coverage of NRs, it is possible to sense a wide range of temperatures (*ca.* 300 to 1050 K), Figure 5.10b. In particular, for NRs-AuNPs-1.25, and using low excitation power (32 - 86 W cm^{-2}), temperatures in the physiological range of interest, *ca.* 301 - 350 K, are measured (inset in Figure 5.10b and Figure. 5.11b).

5.5 White-light emission and its origin: Planck's Law

It is important to note that a reversible Er^{3+} emission for repeated cycles of laser irradiation is only observed for NRs-AuNPs-C, with C = 1.25, 2.5 and 5.0. For C $\geq$ 2.5, however, an intense white-light emission (Figure 5.12a) is observed in the first cycle of laser irradiation with a pump power above a certain threshold, which depends on the AuNPs coverage of NRs: C = 2.5 (threshold 500 W cm^{-2}), 5.0 (240 W cm^{-2}) and 12.5 - 37.5 (110 W cm^{-2}). Figure 5.12 shows the emission spectra of NRs-AuNPs-C in the first cycle of irradiation for selected laser excitation powers. This white-light emission undergoes photo-bleaching under continuous irradiation at a fixed pump power (with a 165 W cm^{-2} pump power it drops 83% after 30 hours, Figure 5.12b).

The white-light emission extends from the visible to infrared range and is well described by Planck's law of blackbody radiation (fitting blue curves in Figure 5.13a)

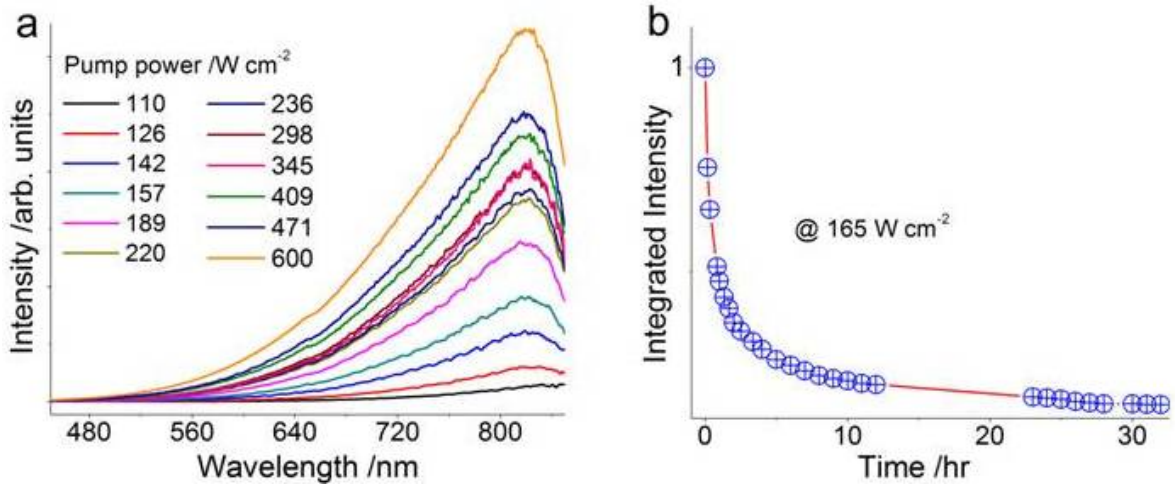

Figure 5.12: a) White-light emission spectra of NRs-AuNPs-12.5 under ambient pressure in the first cycle of irradiation with a 980 nm CW laser diode. b) Integrated emission intensity vs. irradiation time at a fixed pump power *ca.* 165 W cm^{-2}. The red line is guide to the eye and the symbols $\oplus$ are experimental data.

yielding an absolute temperature value T:

$$I(\lambda, T) = \frac{2\pi hc^2}{\lambda^5(exp^{(\frac{hc}{\lambda kT})} - 1)} \tag{5.7}$$

where I is the spectral radiance proportional to the intensity of radiation, λ the wavelength, T the absolute temperature, h Planck's constant, c the speed of light and k Boltzmann constant, appendix D. In fact, other evidences also favor a blackbody origin for the white-light emission. Firstly, according to Planck's law, as the temperature increases the intensity of the blackbody emission increases and the maximum intensity shifts to the blue. Indeed, on increasing the pump power, a progressive blue shift from ca. 845 to 820 nm and an intensity increase were observed (Figure 5.12a), in excellent agreement with Planck's law. Secondly, the calculated 1960 (u,v) Commission Internationale de l'Eclairage (CIE) uniform scale chromaticity color coordinates (appendix E) obtained under different pump powers exactly follow the chromaticity diagram of the Planckian (blackbody) locus (Figure 5.13b). Thirdly, the integrated intensity of the white-light emission is supralinear with the pump power P according to Equation 5.5, yielding n up to ~10 (Figure 5.14a). Such a high-order supralinear optical process cannot be ascribed to the Au interband electronic transition or to the plasmonic-induced photoluminescence of AuNPs because these processes are two-photon excitations under the infrared photon irradiation [142–145].

The presence or absence of a thermally conducting medium, able to dissipate the heat generated by the laser-excited AuNPs, determines, as expected, the observation of the white-light emission. For example, no white-light emission was observed for aqueous dispersions of NRs-AuNPs-C (under the same excitation conditions used for same powder samples). Furthermore, in vacuum (20 Pa) and at 300 K the white-light e-

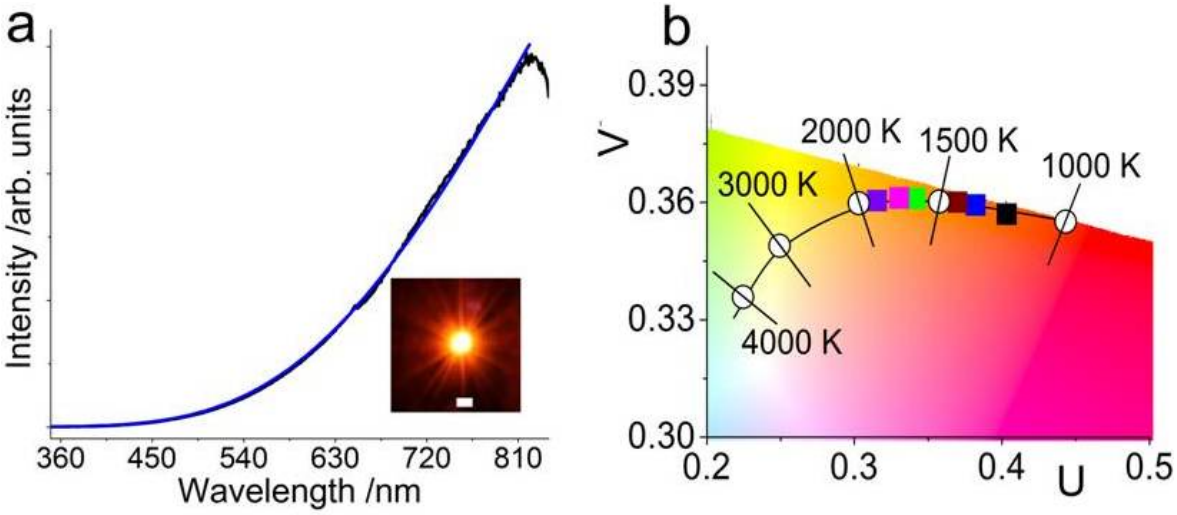

Figure 5.13: a) White-light emission spectrum of as-prepared NRs-AuNPs-12.5 excited at 600 W cm^{-2} with a 980 nm CW laser diode. b) CIE 1960 (u,v) uniform chromaticity diagram of the emission at different pump powers, 142 W cm^{-2} (black square), 187 W cm^{-2} (blue), 235 W cm^{-2} (wine), 267 W cm^{-2} (green), 314 W cm^{-2} (magenta) and 600 W cm^{-2} (purple), compared to the Planckian locus (curved line with circles). The blue line in (a) is fit using Planck's law (Equation 5.7) while the inset photo is a digital photograph of the corresponding white-light emission, scale bar 2 mm.

mission was observed at a very low threshold pump power, e.g., 10 W cm^{-2} for C = 12.5 (*cf.* 110 W cm^{-2} in air), Figure 5.14b. This is due to the fact that certain heat-dissipation mechanisms, such as convection, are strongly limited in vacuum. Increasing the pressure, for instance to 1000 Pa, quenches the emission, which can be restored to its original intensity by decreasing the pressure. Cooling the sample to 100 K quenches the emission, though the pressure is much lower at this temperature. As will be discussed later, white-light emission was also observed for other host/supporting nanostructures and the profiles of the emission spectra are similar for all supporting materials (NRs and NPs). Only the threshold pump power yielding the white-light emission, and the photostability, depend on the supporting materials, presumably due to differences in the thermal conductivity. NRs supporting silver nanoparticles (AgNPs) also showed similar white-light emission. The aforementioned results clearly indicate that the white-light emission is not associated with any specific electronic transitions of the constituting atoms, depending only on the local temperature, thus confirming that it is indeed ascribed to a blackbody emission (appendix D).

The origin of a laser-induced white-light emission in various materials has been the subject of much controversy. For instance, a broadband visible emission ascribed to a two-photon absorption process has been previously observed for AgNPs embedded in polymer matrices [143], gold cusp structures [144], rough gold films [142] and AuNRs [145], but only under pulsed laser irradiations with high pump powers up to e.g., 1×108 W cm^{-2} [142]. No emission was detected when a CW laser with the same pump power was used [142–145]. Onuta et al. [144] also observed the broadband e-

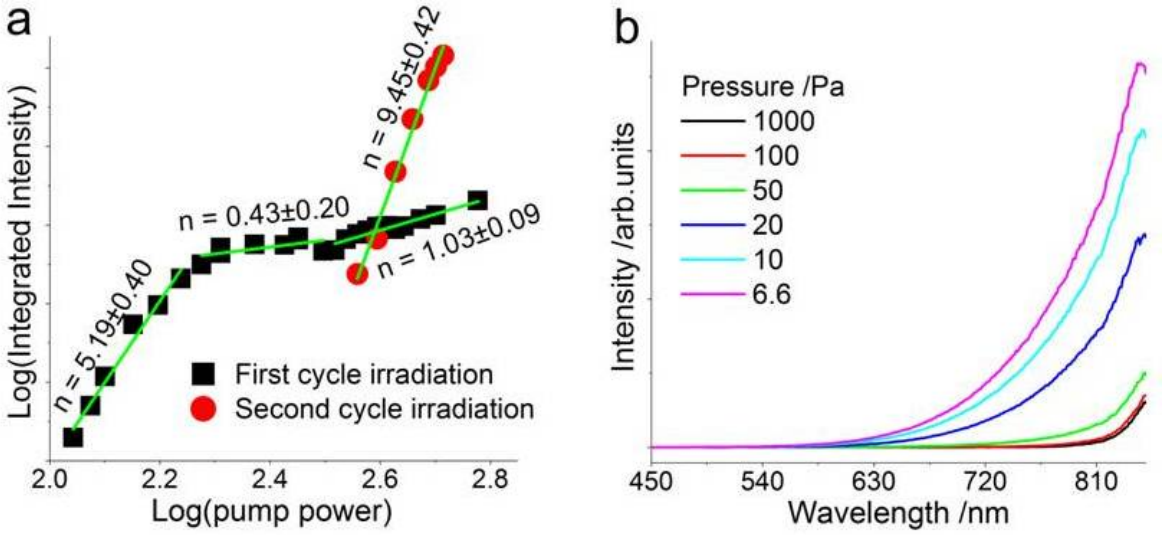

Figure 5.14: a) Double-log plot of pump power vs. integrated intensity of the white-light emission of NRs-AuNPs-12.5 in the first and second cycles of irradiation under ambient pressure; the solid green lines are linear fits using Equation 5.5. b) White-light emission spectra of NRs-AuNPs-12.5 recorded under vacuum (different pressures) at a fixed laser excitation power (15 W cm^{-2}).

mission for cusp antennas made from Al film and pointed out that other mechanisms besides the two-photon absorption process may contribute to its emission. In addition to two-photon photoluminescence in the arms of gold dipole antennas, white-light supercontinuum (attributed to a fourth-order nonlinear optical process) was generated in the antenna feed gap under irradiation with picosecond pulsed lasers [146]. A similar broadband visible emission has been reported for lanthanide oxides [125–127], $LiYbP_4O_{12}$ [128], YVO_4:Yb^{3+}/Er^{3+} nanoparticles [129], carbon nanotubes [130], and Si and SiC nonoparticles [131], upon CW laser excitations but its origin is still contentious: it has been ascribed to incandescent/blackbody emission [125, 126, 130, 131], photon up-conversion emission induced by a thermal avalanche process [127], defect emissions [129] and anti-Stokes emissions [128]. In references [127] and [131] the emissions were observed only in vacuum. On the other hand, the strong infrared emission part from the rough gold film in ref. [142] was supposed to be generated by intraband transitions enhanced by the localized surface plasmons. Cerrutiet et al. [136], however, attributed an infrared emission of AuNPs and silica-coated AuNPs to blackbody radiation, used as thermographic labels for DNA detection.

Using Equation 5.7, absolute temperature in the range of 1200 - 2000 K is calculated for samples with C $\geq$ 12.5 upon excitation with a 980 nm CW laser diode (Figure 5.13, Table 5.1, and Figure B.4).

5.6 Temperature sensitivity and resolution

The relative sensitivity S of the temperature T is defined by [106]:

$$S = \frac{(\frac{\partial \Delta}{\partial T})}{\Delta} \tag{5.8}$$

where Δ is the thermometric parameter which corresponds to: i) the FIR when Boltzmann's law (Equation 5.6) is used and ii) the integrated intensity of the white-light emission when Planck's law (Equation 5.7) is employed. The relative sensitivity curves for the samples studied here are shown in Figure 5.15 and the results are summarized in Table 5.1 along with previously reported data for Er^{3+}-based analogous sensor materials. In using Equation 5.8, the Δ values were first calculated by fitting the experimental data to a polynomial interpolation or to a function that best fits the experimental data so that the distance between two adjacent points is small enough as well as sufficiently large data points can be obtained to perform an accurate derivation. Besides sensitivity, another important parameter of a temperature sensor is its temperature resolution. Accordingly, the temperature resolution δT of the sensors is determined from $\frac{\delta \Delta}{S_a}$, where $\delta \Delta$ is the resolution of Δ calculated from the standard deviation of the residuals in the interpolation/fit and S_a is the absolute sensitivity defined by $S_a = \frac{\partial \Delta}{\partial T}$ [106]. Temperature resolution may also be estimated from the sensitivity of the detection system and the calculated sensitivity [147, 148]. Hence, considering the minimum sensitivity (0.58%) of the detector used in the precision of the luminescence intensity within the corrected spectral region and the obtained maximum relative sensitivities of the sensors (0.58 - 1.51% K^{-1}) the minimum temperature that can be detected is (or the minimum resolution of the sensor should be within) *ca.* 0.38 - 1.00 K, which is compatible with the temperature resolutions (between 0.3 and 13.0 K, Table 5.1) determined from the relation $\delta T = \frac{\delta \Delta}{S_a}$. Table 5.1 presents the temperature sensing parameters of Er^{3+}-based analogous sensing materials. It should be noted that the response time of the

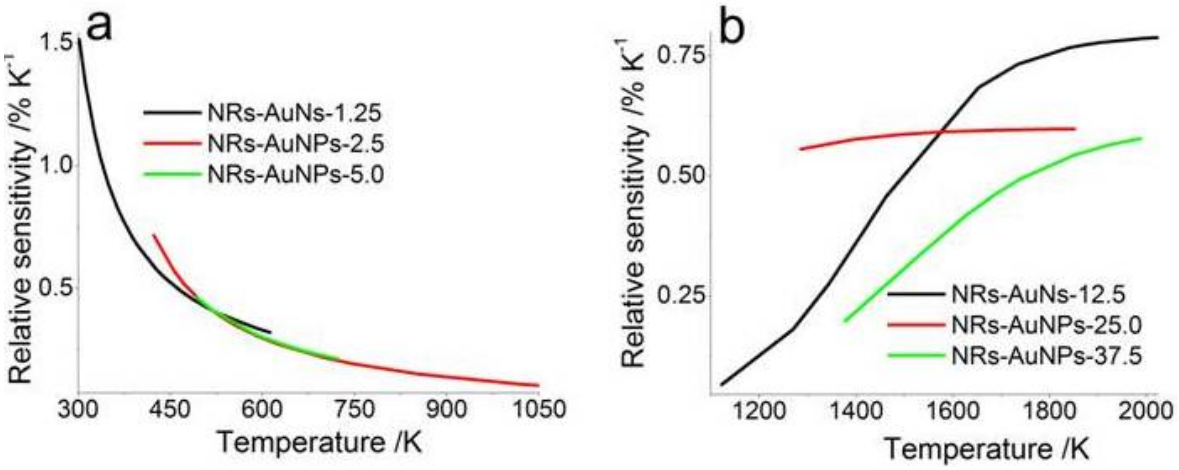

Figure 5.15: Temperature sensitivity curves for NRs-AuNPs-C: a) samples with C $\leq$ 5.0 and b) C $\geq$ 12.5 in the first cycle of irradiation.

NRs-AuNPs-C is generally fast enough to the laser excitation input though it requires quantification.

Table 5.1: Comparison of temperature sensing parameters for Er^{3+}-based up-conversion materials under excitation at or near 980 nm of a laser beam: temperature range ΔT (K), pump power range ΔP (W cm^{-2}) @ excitation wavelength λ (nm), maximum relative sensitivity S_{max} (% K^{-1}) @ temperature T (K), and temperature resolution σT (K).

Materials	ΔT (K)	ΔP @ λ (W cm^{-1} @ nm)	S_{max} @ T (% K^{-1} @ K)	σT (K)	Ref.
NRs-AuNPs-1.25	301 - 615	32 - 600 @ 980	1.51 @ 302	1.0	[a]
NRs-AuNPs-2.5	423 - 1050	95 - 455 @ 980	0.72 @ 423	2.0	[a]
NRs-AuNPs-5.0	493 - 720	95 - 205 @ 980	0.46 @ 493	3.0	[a]
NRs-AuNPs-12.5[b]	1122 - 2024	110 - 600 @ 980	0.79 @ 2000	4.0	[a]
NRs-AuNPs-25.0[b]	1286 - 1852	110 - 600 @ 980	0.60 @ 1852	8.0	[a]
NRs-AuNPs-37.5[b]	1376 - 1988	110 - 600 @ 980	0.58 @ 1988	13.0	[a]
Gd_2O_3:Yb^{3+}/Er^{3+}	300 - 900	— @ 976	0.73 @ 300	—	[112]
Gd_2O_3:2%Yb^{3+}/1%Er^{3+}	270 - 357	42 - 488 @ 978	1.06 @ 270	—	[137]
Gd_2O_3:10%Yb^{3+}/1%Er^{3+}	324 - 612	42 - 488 @ 978	0.70 @ 324	—	[137]
$NaYF_4$:Er^{3+}/Yb^{3+}	298 - 318	< 500 @ 920	1.00 @ 298	—	[110]
$Yb_3Al_5O_{12}$:Mo/Er	295 - 973	— @ 976	0.62 @ 295	0.3	[149]
Al_2O_3:Yb^{3+}/Er^{3+}	295 - 973	175 @ 978	1.93 @ 295	0.3	[150]
ZnO:Er^{3+}	273 - 573	2750 - 5100 @ 978	0.60 @ 273	—	[141]
PbF_2:Yb^{3+}/Er^{3+}	315 - 415	— @ 975	1.0 @ 345	5.0	[151]
$BaTiO_3$:Er^{3+}[c]	345 - 480	2000 @ 980	0.67 @ 346	—	[152]

[a] This work.
[b] In the first cycle irradiation.
[c] Sample C in the reference.

5.7 Er^{3+} emission in the second cycle irradiation for $C \geq 12.5$

The local temperature (1200 - 1350 K) estimated using Planck's law at the threshold pump power is close to the melting point of bulk gold (1343 K) [117, 121]. Consequently, samples of NRs-AuNPs-C with $C \geq 12.5$ that do not exhibit, initially, any Er^{3+} up-conversion emission do so after subsequent laser (second cycle) irradiation (Figure 5.16). The reason for this behavior may be two-fold. Firstly, the AuNPs size increases upon particle coalescence, thereby red-shifting the LSPR band (Table 5.2) and favoring the absorption of the incoming 980 nm photons by the Yb^{3+} ions in the NRs followed by Er^{3+} emission. Secondly, AuNPs coalescence results in the NRs surface being less densely covered by gold and thus providing 'windows' for the excitation photons to hit the Yb^{3+} ions, leading to the Er^{3+} up-conversion emissions similar to those observed for samples with $C \leq 5$ (Figure 5.17). Increasing the pump power in

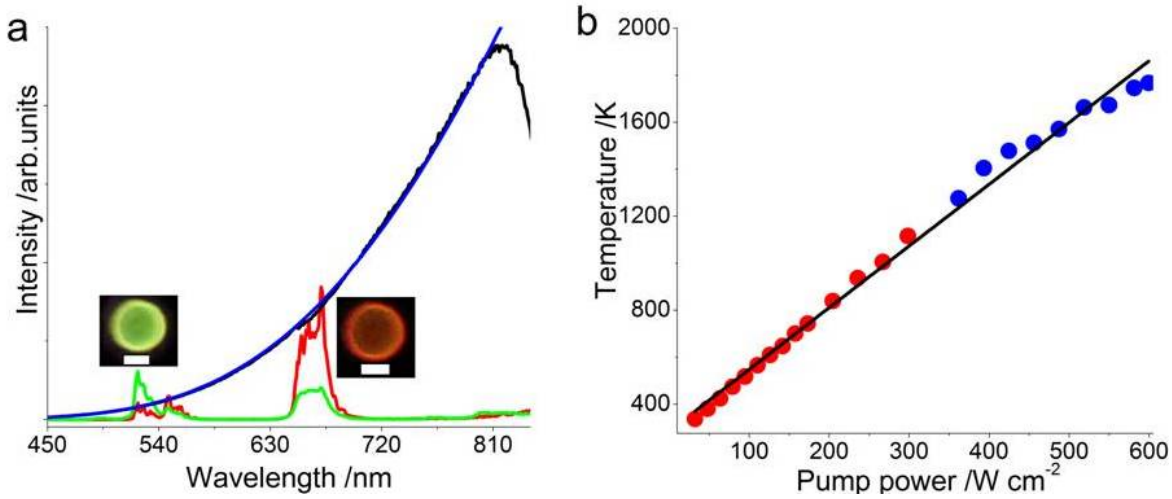

Figure 5.16: a) Emission spectra of NRs-AuNPs-12.5 in the second cycle irradiation at different pump powers: 47 W cm^{-2} (red line) and 236 W cm^{-2} (green line), Er^{3+} up-conversion; 600 W cm^{-2} (black line), white-light emission. b) Calculated local temperature *vs.* pump power in the second cycle of irradiation. The temperatures calculated using Boltzmann's law (red) and Planck's law (blue) in (b) show a linear trend (solid line is a linear fit with $r^2 > 0.99$). The blue line in (a) is fit using Planck's law (Equation 5.7) while the inset photos are digital photographs of the corresponding Er^{3+} emissions, scale bar 0.5 mm.

the second irradiation cycle brings back the blackbody emission (Figure 5.16a). As will be shown in the next section, PXRD, absorption spectroscopy and TEM reveal that the pump power that onsets the blackbody emission indeed leads to coalescence of the AuNPs, whose average particle size increases (Figures 5.18-5.20 and Table 5.2). Both Boltzmann's and Planck's laws were used to determine the temperatures between 300 and 2000 K as there are Er^{3+} emission and white-light emission from the same spot of an irradiated sample volume, Figure 5.16b. The temperature values obtained from the two independent laws follow the same linear trend with pump power (Figure 5.16b), lending support to the incandescence nature of the white-light emission and may also

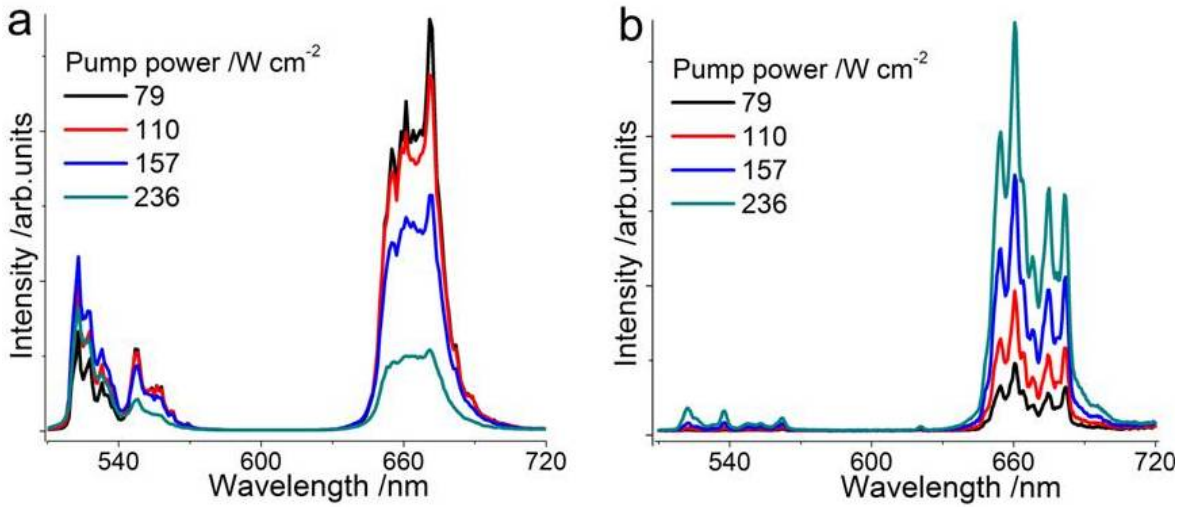

Figure 5.17: Emission spectra of a) NRs-AuNPs-12.5 in the second cycle irradiation and b) NRs-AuNPs-2.5 in the first cycle irradiation.

indicate the reliability of the models employed here for the absolute temperature determination at the nanoscale.

Here, it is also important to point out that although the Er^{3+} emission is observed in the second cycle of irradiation for C $\geq$ 12.5, the red and green emission lines are quite different from those observed in bare NRs and NRs-AuNPs-C (C $\leq$ 5.0), Figure 5.17. Such difference in the Er^{3+} red and green emission lines may not be associated with structural changes in the nanocomposites because the structure and the emission spectra of bare NRs do not change after calcination at 1373 K, which is indeed higher than the temperature (980 K) extracted from Boltzmann's law for NRs-AuNPs-12.5 at 236 W cm^{-2}. In other words, the mechanisms for the Er^{3+} emission dynamics with pump power as well as with AuNPs concentration (Figure 5.17) is not clear and needs further investigation.

5.8 Effect of laser irradiation

It was shown that for C $\geq$ 12.5 NRs-AuNPs-C exhibit two distinct emission properties (the appearance of the white-light and Er^{3+} emissions) that depend on the laser irradiation. Therefore, in order to better understand the effects of laser irradiation on the structure, morphology, LSPR property and surface charge of NRs-AuNPs-C, a 50 mg powder of NRs-AuNPs-12.5 was irradiated at selected pump powers (47, 126, 236 and 600 W cm^{-2}) for about 20 minutes by regularly stirring the powder on a glass support and the sample was then analyzed and results are discussed as follows.

Figure 5.18 shows the room temperature Vis-NIR absorption spectra of aqueous dispersion of NRs-AuNPs-12.5 before and after laser irradiations. The as-prepared sample shows a LSPR band centered at 535 nm. However, irradiating the sample with pump

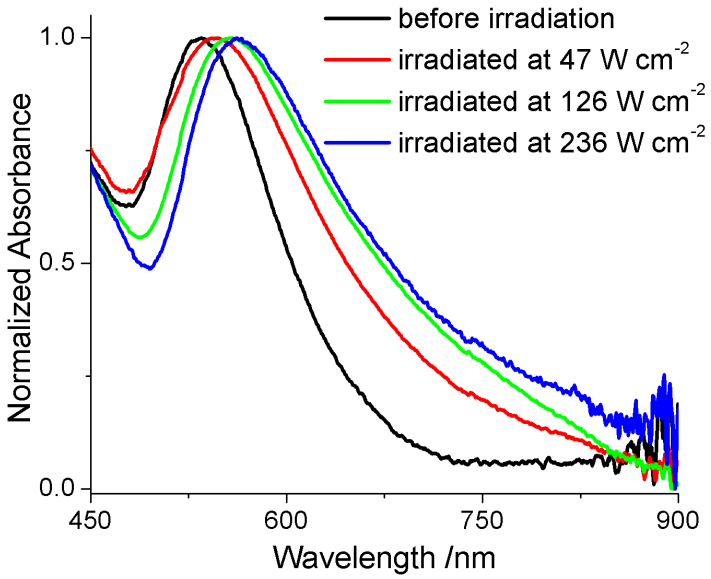

Figure 5.18: Vis-NIR absorption spectra of NRs-AuNPs-12.5: effect of laser irradiation on the LSPR band.

powers at 47, 126 and 236 W cm^{-2} results in red-shifting of the LSPR peaks observed at 547, 558 and 562 nm, respectively, showing that the average particle size of AuNPs increased on increasing the laser excitation power, which supports the PXRD results (Table 5.2 and Figure 5.19). Such shift is generally in accord with the well-known properties of LSPR band of AuNPs, exhibiting a red-shift on increasing particle size. However, it was noted that the sample irradiated at high pump power (600 W cm^{-2}) was less stable in aqueous dispersion (which was further confirmed from the zeta potential measurement, Table 5.2) and found precipitating a lot before the the absorption measurement was completed. This may be because of the increased particle size (and/or strong laser induced surface changes) and thus only the smaller particles remaining in the suspension may account for the blue-shifted LSPR band, i.e., at 554 nm when compared to the one obtained by irradiating at lower pump powers (126 and 236 W cm^{-2}), which is in contrast to the PXRD results (Figure 5.19 and Table 5.2). As presented in Table 5.2, results from zeta potential measurement clearly indicate that the surface charge of the NRs-AuNPs-12.5 was significantly changed because of the laser irradiation, which gives as low as +14.5 mV.

Furthermore, no structural (phase) change of the NRs and AuNPs was detected after irradiation of NRs-AuNPs-12.5 at different pump powers, Figure 5.19. However, the irradiation has strong effect on the broadening of the diffraction peaks of AuNPs where a progressive sharpening at $2\theta = 38.20$ and 44.40 was detected upon increasing the irradiation pump power, clearly indicating that the size of AuNPs changes due to the laser irradiation. The Scherrer equation using the most intense peak at $2\theta = 38.20$, yields average particle sizes of 15, 20, 40 and 57 nm before laser irradiation, after irradiation at 47, 126 and 600 W cm^{-2}, respectively, (Table 5.2). TEM images also reveal that the laser irradiation results in the aggregation and growth of AuNPs

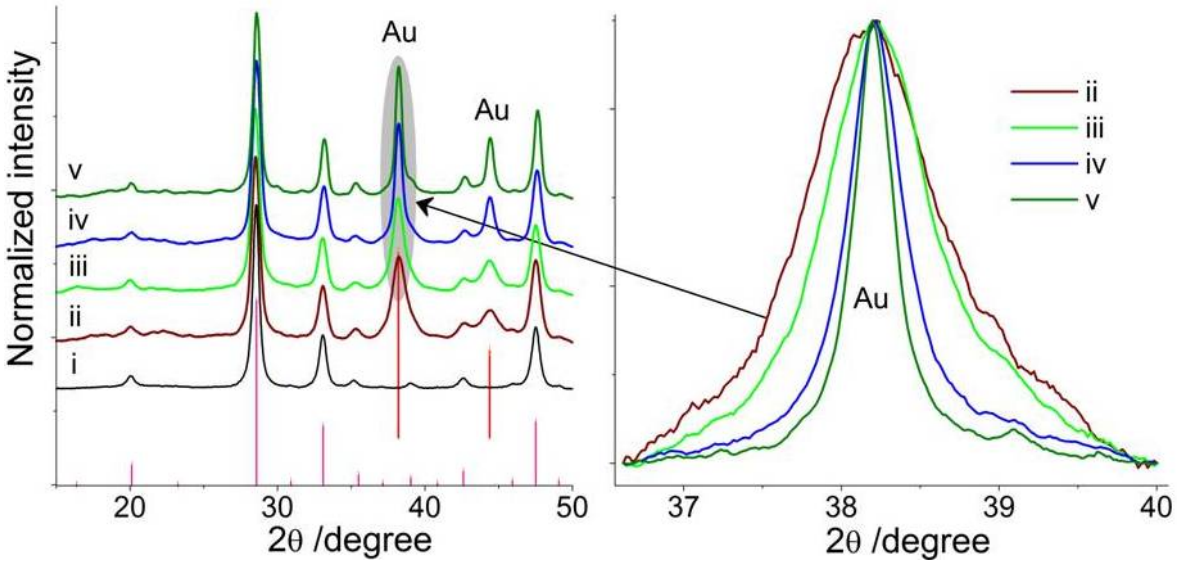

Figure 5.19: Effect of laser irradiation on PXRD patterns of bare NRs and NRs-AuNPs-12.5 (left-side): before laser irradiation for bare NRs (i) and NRs-AuNPs-12.5 (ii); after laser irradiation for NRs-AuNPs-12.5 at 47 W cm^{-2} (iii), 126 W cm^{-2} (iv) and 600 W cm^{-2} (v). Normalized diffraction peaks at $2\theta = 38.20$, ascribed to AuNPs (right-side); the peak sharpens on increasing the pump power indicating the increase in particle size): 15 nm at 0 W cm^{-2} (ii), 20 nm at 47 W cm^{-2} (iii), 40 nm at 126 W cm^{-2} (iv) and 57 nm at 600 W cm^{-2} (v); the sizes are estimated using Scherrer's equation. The pink and red vertical lines stand for PDF-04-015-1513 and PDF-04-002-1170 databases for cubic Gd_2O_3 and gold phases, respectively.

(Figure 5.20).

Table 5.2: Effect of laser irradiation on zeta potential (mV), LSPR peak (nm) and average AuNPs size (nm) measured for NRs-AuNPs-12.5 after laser irradiation at selected pump powers (W cm^{-2}).

Pump power (W cm^{-1})	Zeta potential (mV)	LSPR peak (nm)	AuNP size (nm)
0	28.2	535	15
47	22.3	547	20
126	15.2	558	40
236	14.5	562	55
600	24.1	554	57

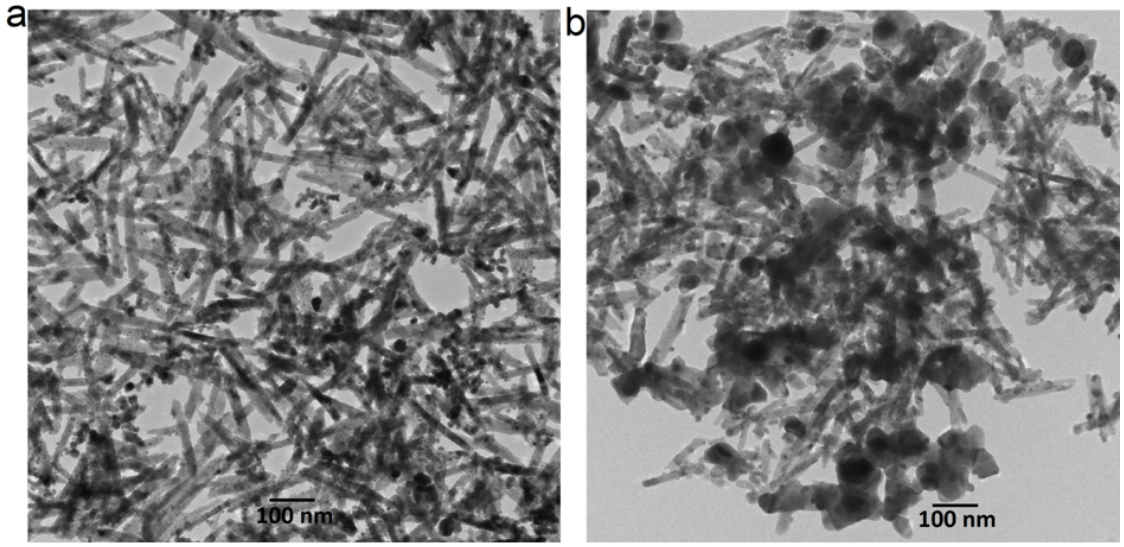

Figure 5.20: TEM images of $(Gd,Yb,Er)_2O_3$ NRs-AuNPs-12.5 a) before irradiation and b) after irradiation at 600 W cm^{-2}.

5.9 Dependence of the white-light emission on the laser focus

Besides the concentration of AuNPs on the NRs, one important parameter to observe white-light emission at ambient pressure (samples with C $\geq$ 2.5) or to detect significant heating *via* the Er^{3+} emission (samples with lower C values) is the focus of the laser beam on the sample. We noted that a slight deviation from the well-focused region at a specific pump power may result in a complete loss of the white-light emission or a relative decrease in the emission intensity and in the calculated local temperature. Figure 5.21 is a schematic demonstration for the optimal distance between the laser diode and the sample in order to observe the white-light emission in an open atmosphere.
Sample Position 1 located at *ca.* 2 cm is the optimal distance in which the white-light emission was observed under ambient pressure, Figure 5.21. At this position, the laser beam is well-focused (the spot area is smaller, diameter *ca.* 0.406 mm); the threshold pump power for the emission is *ca.* 110 W cm^{-2}. On the other hand, at sample Position 2 located at *ca.* 4 cm from the laser diode, the laser beam is not well-focused and its spot area is larger, diameter *ca.* 1.312 mm. As a result, irrespective of the value of C, no white-light emission is detected under ambient pressure over the whole range of pump power used in this study. In this case, the white-light was observed only in vacuum ($<$ 1000 Pa) at a threshold pump power *ca.* 10 W cm^{-2}, about one order of magnitude smaller than the one required under ambient pressure at a distance of 2 cm. In general, under low pressure (vacuum) the white-light emission intensity is much stronger; the threshold pump power is lower; and the laser beam is not necessarily focused. Moreover, at this position, the emission is reversible for reversed pressure changes.

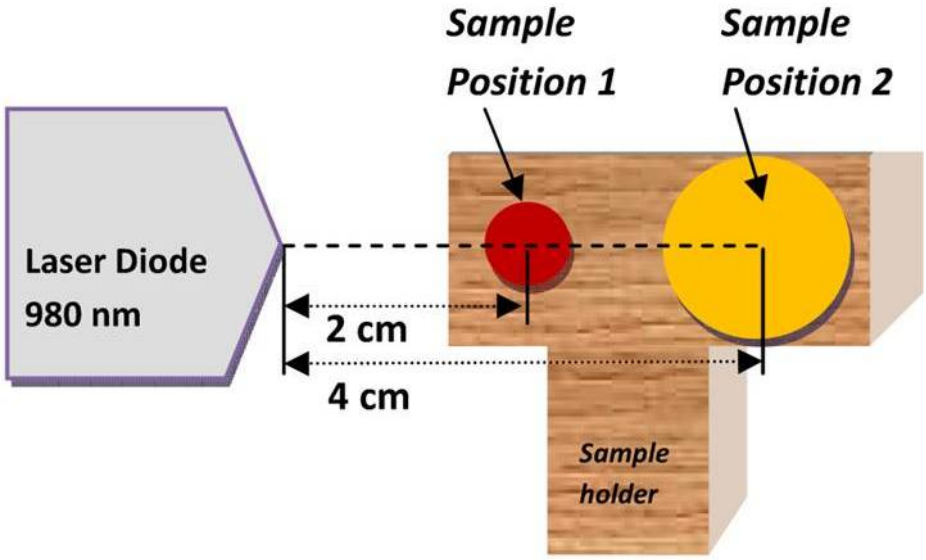

Figure 5.21: Schematic representation of the optimal distance between the laser diode and the sample to observe the white-light emission under ambient atmosphere (Position 1) otherwise vacuum is required (e.g., at Position 2).

5.10 White-light emission in other host materials

For the purposes of studying the nature of the heat generation and origin of the white-light emission, AuNPs and AgNPs were also supported on different host materials including $(Gd,Eu)_2O_3$, $(Gd,Yb,Tm)_2O_3$, Y_2O_3, $(Gd,Eu)_2O_3$@SiO_2, $(Gd,Eu)_2O_3$@ PSS@PAH, $(Gd,Yb,Er)_2O_3$@PSS@PAH, and $(Gd,Yb,Tb)PO_4$ nanostructures (nanorods and nanoparticles). The preparation of spherical AuNPs and their attachment to the NRs is described in appendix C, along with representative TEM images of AuNPs, $(Gd,Eu)_2O_3$ NRs@PSS@PAH@AuNPs, $(Gd,Yb,Er)_2O_3$NRs@PSS@PAH@ AuNPs, (Gd, $Eu)_2O_3$ NRs-AuNPs, and $(Gd,Yb,Tm)_2O_3$-NRs-AuNPs. In general, the profile of the white-light emission spectrum is independent of the host material, shape of the host material, the preparation method and the type of the metal nanoparticle (e.g., AuNPs and AgNPs) and the spectra are superposeable as shown in Figure 5.22a, supporting the incandescent nature of the white-light emission as was discussed before. Figure 5.22b shows the emission spectra of $(Gd,Yb,Er)_2O_3$ NRs@PSS@PAH@AuNPs in the first cycle irradiation. For this sample, Er^{3+} emission was also observed in the second cycle of irradiation (Figure 5.22c).

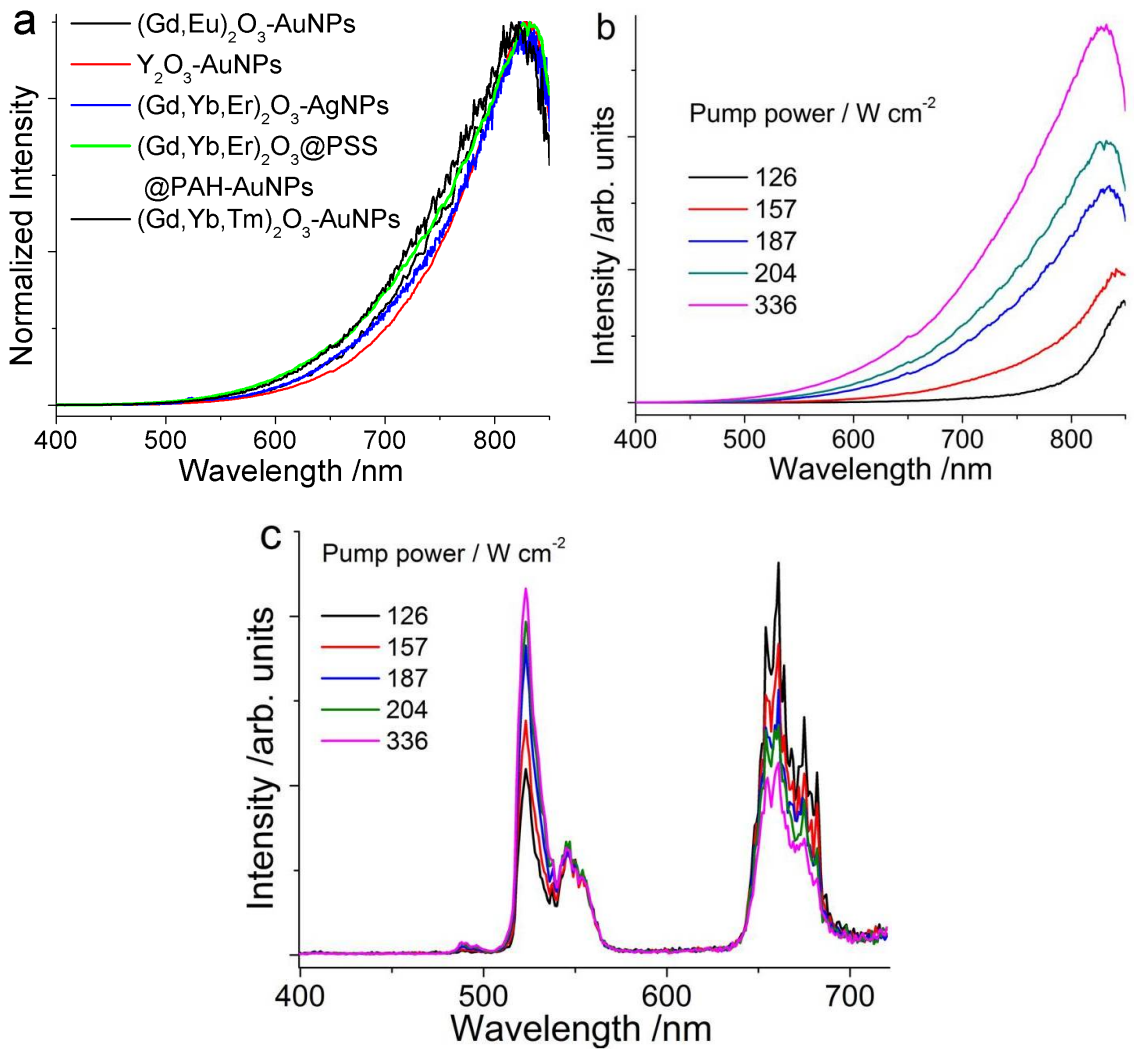

Figure 5.22: a) Typical emission spectra of different materials supporting AuNPs and AgNPs under irradiation with a 980 nm CW laser diode; b) white-light emission spectra of $(Gd,Yb,Er)_2O_3$ NRs@PSS@PAH@AuNPs (in the first cycle irradiation) and c) Er^{3+} emission spectra of $(Gd,Yb,Er)_2O_3$ NRs@PSS@PAH@AuNPs (in the second cycle of irradiation, i.e., after irradiation at 600 W cm^{-1}).

5.11 Summary and conclusion

$(Gd_{0.95}Yb_{0.03}Er_{0.02})_2O_3$ nanorods (synthesized *via* a wet-chemical route) are decorated with gold nanoparticles (AuNPs) through the reduction of $HAuCl_4 \cdot 3H_2O$ precursor by $NaBH_4$ at room temperature, denoted by NRs-AuNPs-C with C = 1.25 - 37.5. The amount of AuNPs decorating the NRs is controlled by adjusting the nominal amount, i.e., C, of the gold metal in the precursor. The nanocomposites are analyzed by TEM, PXRD, absorption spectroscopy and photoluminescence spectroscopy. The photoluminescence spectroscopy reveals that the present materials are potential candidates for the state-of-the-art application in the local temperature determination of laser-excited metal nanostructures, irrespective of their shapes. It is demonstrated

that the nanoplatform integrating heaters and thermometers studied in this thesis is a step change towards local-temperature sensing with a simple approach for laser-induced heat generation and increased span of sensed temperature, consisting of $(Gd,Yb,Er)_2O_3$ NRs, acting as thermometers, with a surface decorated with AuNPs, the heaters. The local temperature is ascertained from the Boltzmann's distribution of the Er^{3+} up-conversion $^2H_{11/2} \rightarrow {}^4I_{15/2}/{}^4S_{3/2} \rightarrow {}^4I_{15/2}$ intensity ratio, in the range 300 - 1050 K with resolution of 0.3 - 2.0 K, and from the Planck's law for a white-light emission between 1200 and 2000 K with resolution of 4 - 13 K. Increasing the amount of AuNPs increases the surface temperature of the $(Gd,Yb,Er)_2O_3$ NRs and the operating range of the nanothermometers. A remarkable result is the unambiguous attribution of the white-light emission to an incandescence process. A maximum relative sensitivity up to 1.51% K^{-1} (resolution 1 K) in the temperature range of physiological interest (301 - 350 K) is demonstrated with NRs-AuNPs-1.25 under low-power (32 - 86 W cm^{-2}) near-infrared light (980 nm) excitation in the therapeutic window. This offers much potential for biological applications in laser-induced controlled hyperthermia and in deep-tissue optical bioimaging, while avoiding thermal damage of the surrounding healthy tissues as well as background fluorescence.

Chapter 6

Energy-transfer from Gd(III) to Tb(III) in (Gd,Yb,Tb)PO_4 Nanocrystals

6.1 Introduction

Understanding the photophysical properties of luminescent nanomaterials is essential to exploit any of their utmost performances or parameters for the desired applications. In this chapter we will explore the down-shifting photoluminescence properties of (Gd,Yb,Tb)PO_4 nanocrystalsis[1]. The nanocrystals are synthesized *via* hydrothermal route at 150 ^{o}C followed by post calcination at 900 ^{o}C for 3 hrs. Characterizations including morphology and phase identifications are performed. Energy-transfer from Gd^{3+} to Tb^{3+} is witnessed by the detailed analyses of the photoluminescence properties such as excited-state lifetimes, emission quantum yields, and emission and excitation spectra. Absolute-emission quantum yields up to 42% are obtained by exciting within the $^6I_{7/2-17/2}$ (Gd^{3+}) manifold at 272 nm. The room temperature emission spectrum is dominated by the $^5D_4 \rightarrow {}^7F_5$ (Tb^{3+}) transition at 543 nm, with a long decay-time (3.95 - 5.50 ms) and exhibiting a rise-time component. The $^5D_3 \rightarrow {}^7F_6$ (Tb^{3+}) rise-time (0.078 ms) and the $^6P_{7/2} \rightarrow {}^8S_{7/2}$ (Gd^{3+}) decay-time (0.103 ms) are of the same order, supporting the Gd^{3+} to Tb^{3+} energy-transfer process. A remarkably longer lifetime of 2.29 ms was measured at 11 K for the $^6P_{7/2} \rightarrow {}^8S_{7/2}$ (Gd^{3+}) emission upon excitation at 272 nm, while the emission spectrum at 11 K is dominated by the $^6P_{7/2} \rightarrow {}^8S_{7/2}$ transition line, showing that the Gd^{3+} to Tb^{3+} energy-transfer process is mainly phonon-assisted with an efficiency of $\sim$95% at room temperature. The Gd^{3+} to Tb^{3+} energy-transfer is governed by the exchange mechanism with rates between 10^2 and 10^3 s^{-1}, depending on the energy mismatch condition between the $^6I_{7/2}$ and $^6P_{7/2}$ levels of Gd^{3+} and the Tb^{3+} $^5I_7$, $^5F_{2,3}$ and $^5H_{5,6,7}$ manifolds and the radial overlap integral values. The calculation of energy-transfer rates and the corresponding analysis were performed in collaboration with Prof. Oscar Malta (Recife, Brazil).

[1] **M. L. Debasu**, D. Ananias, J. Rocha, O. L. Malta, L. D. Carlos, Energy-transfer from Gd(III) to Tb(III) in (Gd,Yb,Tb)PO_4 Nanocrystals, *Phys. Chem. Chem. Phys.*, 2013, 15, 15565-15571.

6.2 Rare earth orthophosphates

Rare earth orthophosphate ($REPO_4$) may be found in the following forms: monoclinic (monazite-type), tetragonal (xenotime-type), hexagonal, orthorhombic and weinschenkite-type [153]. The hydrated orthophosphates, $REPO_4 \cdot nH_2O$, are usually found either in hexagonal or tetragonal forms. All the light lanthanide phosphates (typically from La to Gd) crystallize in monazite-type monoclinic form (space group P1-21/n1) while the heavier ones (from Tb to Lu) adopt xenotime-type tetragonal (zircon-type) structure (I41/amd) [154, 155]. The monazite and xenotime mineral ores are indeed the most ubiquitous rare earth natural compounds.

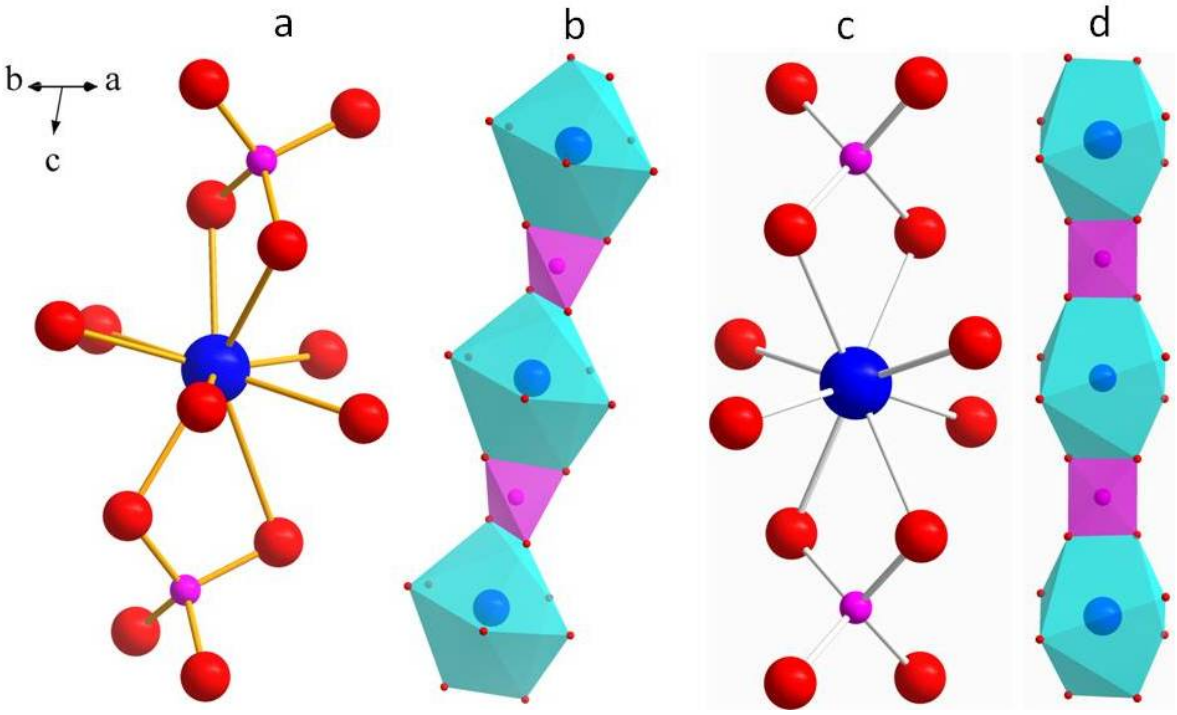

Figure 6.1: Nine-fold coordinations of Gd atom in monoclinic (a) and tetragonal (c) $GdPO_4$. Polyhedral representation for monoclinic (b) and tetragonal (d) $GdPO_4$. Blue, red and pink balls stand for Gd, O and P atoms, respectively.

A complete set of high-precision structure refinements and coordination geometry descriptions for natural and synthetic monazite- and xenotime-type rare earth orthophosphates were given by Ni et al. [154]. As illustrated in Figures 6.1a,c [156, 157], the structural arrangement of monazite is based on the nine-fold coordination of the metal cation, i.e., REO_9 polyhedron (Figures 6.1a,b), whereas in xenotime the cation is eight-fold coordination in a REO_8 polyhedron (Figures 6.1c,d). Clearly, the metal cation in the monazite has an extra oxygen atom relative to the xenotime (Figures 6.1a,c). Furthermore, there are two and nine unique metal-oxygen bond distances in xenotime and monazite, respectively. In both structures, the phosphate tetrahedrons are isolated with respect to a given $REO_{x=9\ or\ 8}$ polyhedron. The polyhedron-tetrahedron chains (Figures 6.1b,d) in the two structures show that infinite chains are formed along [110]

direction by sharing phosphate tetrahedral edges with metal polyhedral edges.

Lehmann et al. [158] reported a complete series of Ln-phosphate nanoparticles (except promethium) while Kijkowska et al. [159] investigated the crystal structure and infrared spectroscopic properties of Ln phosphates. The effect of the synthesis conditions, such as calcination time and temperature, dopant-ion concentration and surface modification, on the emission properties of Ln^{3+}-containing orthophosphates were reported: down-shifting emission of Eu^{3+} [160, 161] and Tb^{3+} [162–164] in $GdPO_4$ nanoparticles, up-conversion emission of Er^{3+} and Tm^{3+} in $YbPO_4$ [165, 166] and quantum-cutting emission of Yb^{3+}/Tb^{3+} in YPO_4 [38] and Tb^{3+} in $GdPO_4$ [167]. White-light emitting nanophosphors were recently reported, based on $GdPO_4$ doped with Eu^{3+}, Tb^{3+} and Dy^{3+} [168].

In this chapter the hydrothermal synthesis and the down-shifting photoluminescence properties (emission spectra, excitation spectra, emission decay curves, lifetimes, quantum yields and Gd^{3+}-to-Tb^{3+} energy-transfer processes) of monoclinic (Gd,Yb,Tb)PO_4 nanocrystals are reported. Upon UV light excitation, the nanocrystals exhibit intense Tb^{3+} intra-$4f^8$-$4f^8$ emission lines and large $^5D_4$ (Tb^{3+}) lifetimes (4.31 - 5.50 ms) at room temperature, in air. Energy-transfer from Gd^{3+} to Tb^{3+} is evidenced and the origin of the rising component in the $^5D_{3,4}$ (Tb^{3+}) emission-decay curves rationalized. High Tb^{3+} absolute-emission quantum yields of up to 42% are reported, unprecedented in this type of host nanocrystal (*ca.* 50 nm size) for Tb^{3+} excited at 272 nm. In chapter 7, the up-conversion emission and relaxivity properties of the nanocrystals will be assessed for applications in bioimaging.

6.3 Synthesis of (Gd,Yb,Tb)PO_4 nanocrystals

(Gd,Yb,Tb)PO_4 nanocrystals were synthesized by a hydrothermal route at 150 ^{o}C following a modified procedure described in Ref. [169]. Three types of crystalline phases, hexagonal, monazite-type monoclinic and xenotime-type tetragonal structures, were obtained mainly by varying the Yb^{3+}/Gd^{3+} content and the calcination temperature while keeping other parameters unchanged. A schematic diagram of the synthesis procedure for the nanocrystals is presented in Figure 6.2. In a typical synthesis of

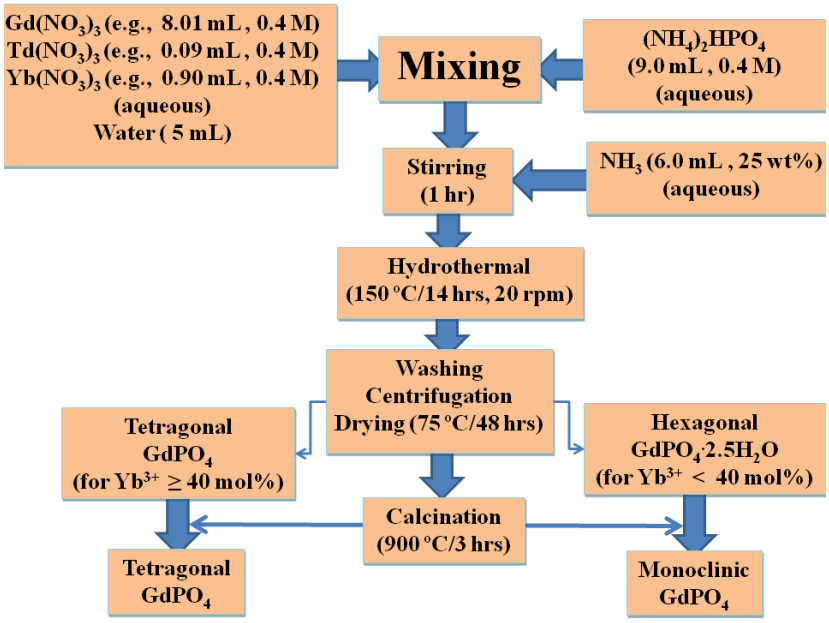

Figure 6.2: A schematic representation of hydrothermal synthesis of monoclinic and tetragonal (Gd,Yb,Tb)PO_4 nanocrystals.

monoclinic $Gd_{0.89}Yb_{0.10}Tb_{0.01}PO_4$, aqueous solutions of $Gd(NO_3)_3$ (8.01 mL, 0.4 M), $Yb(NO_3)_3$ (0.90 mL, 0.4 M) and $Tb(NO_3)_3$(0.09 mL, 0.4 M) were mixed with distilled water (5.00 mL) in a Teflon-lined autoclave (inner volume 42 mL). To this mixture, aqueous solution of $(NH_4)_2HPO_4$ (9.00 mL, 0.4 M) was added, followed by drop-wise addition of NH_3 (6.00 mL, 25 wt%). After one hour of magnetic stirring of the milky solution at room temperature, the autoclave was heated to 150 ^{o}C for 14 hours under rotation (20 rpm). The autoclave was then rapidly cooled in tap water; the white precipitate was washed several times with distilled water and ethanol, and finally dried in air at 75 ^{o}C for 2 days, yielding a hydrated powder, (Gd,Yb,Tb)$PO_4 \cdot 2.5H_2O$. This powder was ground in an agate mortar and pestle to a relatively fine powder, a few milligrams of which were calcined under ambient pressure at 300, 500, 700, 900 and 1200 ^{o}C for 3 hours, with heating and cooling rates of 2 and 5 ^{o}C/min, respectively. Samples with different contents of Yb^{3+} (1.0 - 70.0 mol%) and Tb^{3+} (0.50 - 30.0 mol%) were prepared in a similar procedure, by changing only the molar ratio of Gd^{3+}, Yb^{3+} and Tb^{3+}.

6.4 Composition, structure, morphology, and vibrational spectra

Elemental analysis

ICP-OES revealed that the nominal relative composition of 89.00 mol% Gd^{3+}, 10.00 mol% Yb^{3+} and 1.00 mol% Tb^{3+} in the starting materials translated into, respectively, 88.12, 10.92 and 0.96 mol% in the final (Gd,Yb,Tb)PO_4 nanocrystals obtained after calcination at 900 ^{o}C for 3 hours, denoted here as $Gd_{0.88}Yb_{0.11}Tb_{0.01}PO_4$. Similarly, the 89.50 mol% Gd^{3+}, 10.00 mol% Yb^{3+} and 0.50 mol% Tb^{3+} nominal contents were found to be 88.40, 10.96 and 0.64 mol%, respectively.

Powder X-ray diffraction (PXRD)

PXRD patterns of (Gd,Yb,Tb)PO_4 nanocrystals, as-synthesized and after calcination, are shown in Figure 6.3. Prior to calcination and up to 500 ^{o}C (Figure 6.3a), the samples give broad reflections indexed to the hexagonal samarium phosphate hydrate ($SmPO_4{\cdot}2.5H_2O$) phase, space group $P6_222$ (PDF-00-027-0583), thus indicating the formation of the hydrated hexagonal (Gd,Yb,Tb)$PO_4{\cdot}2.5H_2O$ phase. Upon calcination between 700 and 1200 ^{o}C a monazite-type monoclinic $GdPO_4$ phase, space group P1-21/n1 (PDF-01-083-0657), forms (Figure 6.3b). This is in accord with the thermal decomposition of rare-earth phosphates reported previously [170]. No other phases are detected and the results are in good agreement with those reported for analogous materials [159, 163, 169, 171, 172]. The diffraction peaks sharpen upon raising the calcination temperature above 700 ^{o}C, indicating an increase in the crystal size (Figure 6.3c). The Scherrer equation (appendix A, Equation A.2) yields average particle sizes of 5, 7, 35, 50 and 140 nm for as-synthesized and after calcinations at 500, 700, 900 and 1200 ^{o}C, respectively. Increasing the Yb^{3+} content, e.g., 40 and 70 mol%, results in a xenotime-type tetragonal $YbPO_4$ phase with space group I41/amd (PDF-01-083-0662), which maintains same phase after calcination at 900 and 1200 ^{o}C for 3 hrs (Figure 6.3d). As was discussed before, the crystal structure of $LnPO_4$ depends on the ionic radius of the Ln^{3+} ion: the monazite-type phase preferentially incorporates the light lanthanides (La to Gd), whereas the xenotime-type phase accommodates the heavy lanthanides (Tb to Lu) [155]. Accordingly, increasing the Yb^{3+}/Gd^{3+} molar ratio favors the formation of the tetragonal phase. In this thesis, unless otherwise stated, the photoluminescent study is presented only for the monoclinic (Gd,Yb,Tb)PO_4 nanocrystals, namely, $Gd_{0.895}Yb_{0.10}Tb_{0.005}PO_4$, $Gd_{0.87}Yb_{0.10}Tb_{0.03}PO_4$, $Gd_{0.85}Yb_{0.10}Tb_{0.05}PO_4$, and $Gd_{0.95}Tb_{0.05}PO_4$, obtained after calcination of the as-synthesized hexagonal phase at 900 ^{o}C for 3 hrs.

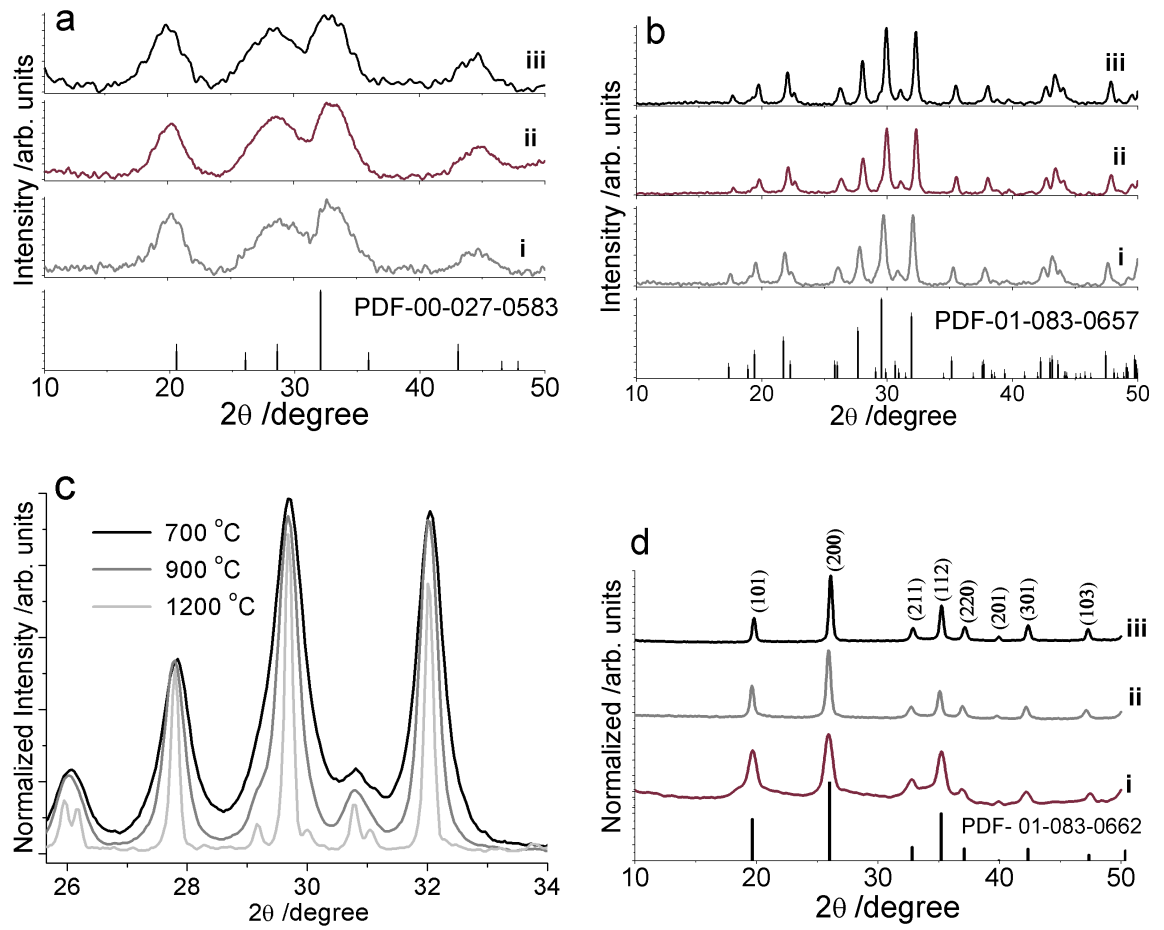

Figure 6.3: PXRD patterns of (a) as-synthesized hexagonal $Gd_{0.90-x}Yb_{0.10}Tb_xPO_4{\cdot}2.5H_2O$ nanocrystals with x = 0.005 (i), x = 0.03 (ii) and x = 0.05 (iii); (b) the corresponding monoclinic $Gd_{0.90-x}Yb_{0.10}Tb_xPO_4$ phase obtained after calcination of the as-synthesized nanocrystals at 900 ^{o}C for 3 hrs; (c) monoclinic $Gd_{0.87}Yb_{0.10}Tb_{0.03}PO_4$ nanocrystals calcined at three distinct temperatures; (d) tetragonal $Gd_{0.49}Yb_{0.50}Tb_{0.01}PO_4$ nanocrystals, (i) as-synthesized, (ii) calcined at 900 ^{o}C/3 hrs and (iii) calcined at 1200 ^{o}C/3 hrs. The vertical lines in each figure represent the diffraction patters of the reference PDF database.

Transmission electron microscopy (TEM)

Represent TEM images of the as-synthesized hexagonal and monoclinic nanocrystals are presented in Figure 6.4 along with the identification of the orientations of the planes for the later. Similar images could not be obtained for the as-synthesized samples because they were not stable in the electron beam (Figure 6.4a). TEM images clearly show that particle size increases with increasing calcination temperature, in accord with the PXRD evidence (Figure 6.4d).

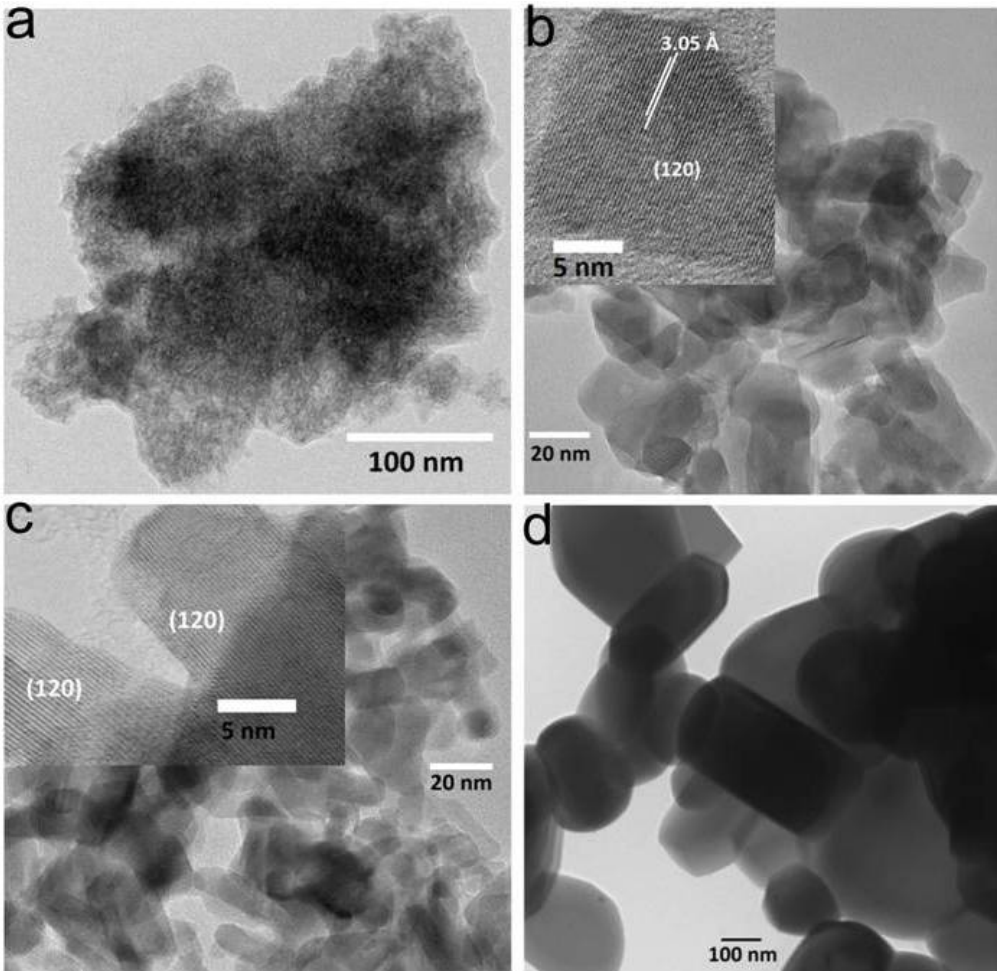

Figure 6.4: TEM images of a) as-synthesized hexagonal phase $Gd_{0.85}Yb_{0.10}Tb_{0.05}PO_4{\cdot}2.5H_2O$ nanocrystals, b) monoclinic $Gd_{0.85}Yb_{0.10}Tb_{0.05}PO_4$ nanocrystals, obtained after calcination at 900 $^oC/3$ hrs, c) monoclinic $Gd_{0.87}Yb_{0.10}Tb_{0.03}PO_4$ nanocrystals, calcination 900 $^oC/3$ hrs, and d) monoclinic $Gd_{0.87}Yb_{0.10}Tb_{0.03}PO_4$ microcrystals, calcination 1200 $^oC/3$ hrs. The insets in (b) and (c) are magnified images showing the crystallographic planes and interplanar distance between two adjacent planes.

Vibrational spectra

Fourier transform infrared spectroscopy (FTIR) revealed some vibrational modes of the nanocrystals (Figure 6.5). The broad band around 3454 cm^{-1} is attributed to the water -OH stretching vibration while the band centered at 1640 cm^{-1} is the corresponding bending vibration. However, the appearance of these peaks at 3454 and 1640 cm^{-1} with relatively weak intensities after calcination at 900 ^oC should be attributed to the adsorbed water molecules on the surface of the nanoparticles during the measurements or storage period of the samples. The peaks at 1076, 624 and 536 cm^{-1} correspond to P-O stretching, O=P-O bending, and O-P-O bending modes, respectively [159, 170, 173]. For the calcined samples, an additional peak around 574 cm^{-1} ascribed to the O-P-O stretching mode was detected, indicating the presence of phase transformation

[159, 170].

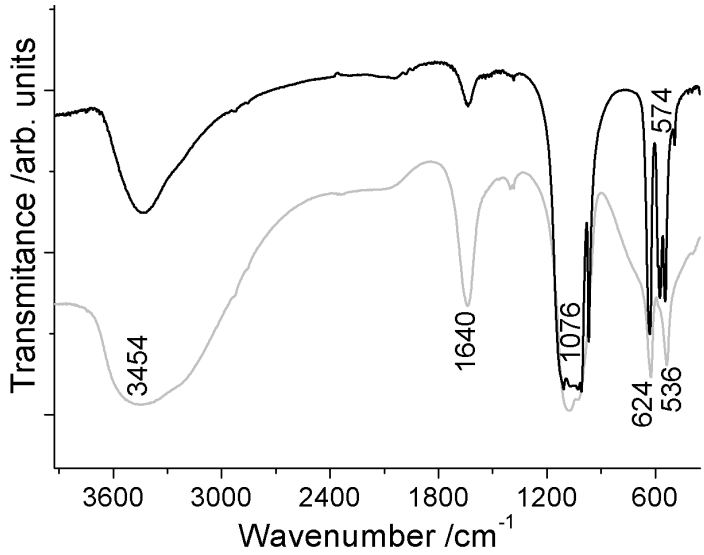

Figure 6.5: FTIR spectra of as-synthesized hexagonal $Gd_{0.87}Yb_{0.10}Tb_{0.03}PO_4{\cdot}2.5H_2O$ nanocrystals (gray line) and monoclinic $Gd_{0.87}Yb_{0.10}Tb_{0.03}PO_4$ nanocrystals (black) obtained after calcination at 900 $^oC/3$ hrs.

6.5 Emission and excitation spectra

The steady-state emission and excitation spectra of the nanocrystals are shown in Figure 6.6. The latter were acquired by monitoring the $^5D_4 \rightarrow {}^7F_5$ (Tb^{3+}) emission at 543 nm. The sharp excitation lines between *ca.* 272 and 278 nm, and 300 and 311 nm are assigned to the $^8S_{7/2} \rightarrow {}^6I_{7/2-17/2}$ and $^6P_{7/2-3/2}$ intra-$4f^7$-$4f^7$ transitions of Gd^{3+}, respectively, while the relatively weak peaks between *ca.* 312 and 500 nm are ascribed to the $^7F_6 \rightarrow {}^5D_{4-0}$, $^5G_{6-2}$, $^5L_{10-6}$, $^5H_7$, intra-$4f^8$-$4f^8$ transitions of Tb^{3+} (inset in Figure 6.6a) [174]. The $^7F_6 \rightarrow {}^5I_8$ and $^7F_6 \rightarrow {}^5H_5$ lines of Tb^{3+} are also discerned centered at *ca.* 283 and 294 nm, respectively (Figure 6.6a). The presence of intense Gd^{3+} transition

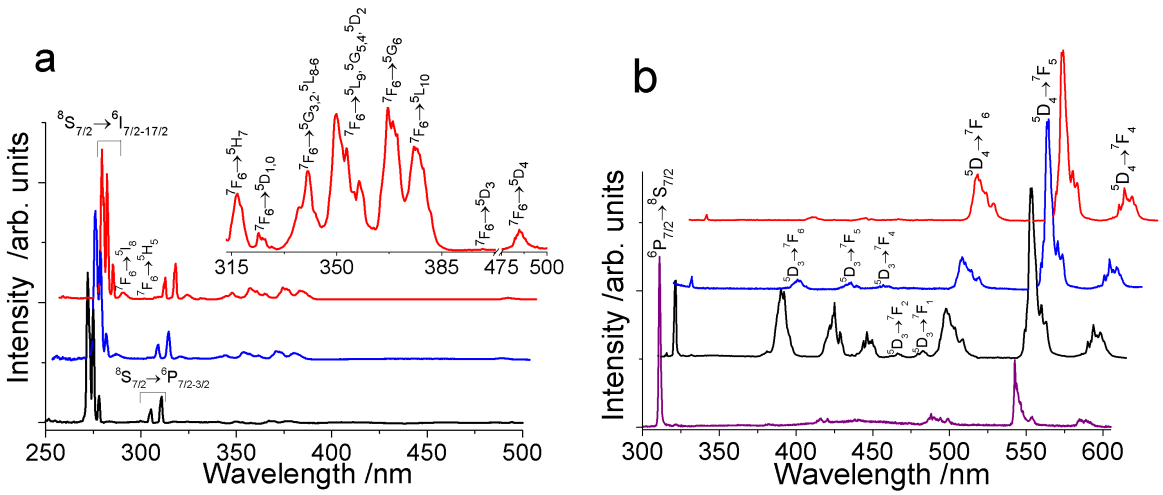

Figure 6.6: Room-temperature excitation spectra monitoring the emission at 543 nm (a) and emission spectra exciting at 272 nm (b) of monoclinic (Gd,Yb,Tb)PO_4 nanocrystals; $Gd_{0.85}Yb_{0.10}Tb_{0.05}PO_4$ (red line), $Gd_{0.87}Yb_{0.10}Tb_{0.03}PO_4$ (blue line), $Gd_{0.895}Yb_{0.10}Tb_{0.005}PO_4$ (black line); the emission spectrum (purple line) in (b) is recorded at 11 K for $Gd_{0.895}Yb_{0.10}Tb_{0.005}PO_4$ excited at 272 nm. The inset in (a) shows a zoom (×12) of the intra-$4f^8$-$4f^8$ transition lines of Tb^{3+} between 312 and 500 nm.

lines in the excitation spectra (Figure 6.6a), while monitoring the $^5D_4 \rightarrow {}^7F_5$ emission of Tb^{3+}, points out Gd^{3+} to Tb^{3+} energy-transfer. The most intense emission from the Tb^{3+} energy levels is, thus, obtained by exciting at 272 nm, corresponding to the strongest peak in the excitation spectra. The $^6P_{7/2} \rightarrow {}^8S_{7/2}$ (Gd^{3+}) and $^5D_{4,3} \rightarrow {}^7F_{6-0}$ (Tb^{3+}) emissions are observed under excitation at 272 nm on the $^8S_{7/2} \rightarrow {}^6I_{7/2-17/2}$ transition, while the green Tb^{3+} emission at 543 nm is dominant at room temperature, irrespective of the Tb^{3+} and Yb^{3+} content (Figure 6.6b).

The strong decrease in the intensity of the $^6P_{7/2} \rightarrow {}^8S_{7/2}$ emission at 311 nm while increasing the Tb^{3+} concentration (in fact, at the expense of a relative decrease in the Gd^{3+} content) suggests increasing Gd^{3+} to Tb^{3+} transfer process [39, 175]. Excitation at 272, 275, 305, 311, 367 and 377 nm does not change the position of the $^5D_{3,4} \rightarrow {}^7F_{0-6}$ emission peaks (Figure 6.7), indicating the presence of a single Tb^{3+} site. As will be discussed, this is further supported by both the single-exponential characteristics of the emission decay curves and the time-resolved emission spectra, which exhibit the same

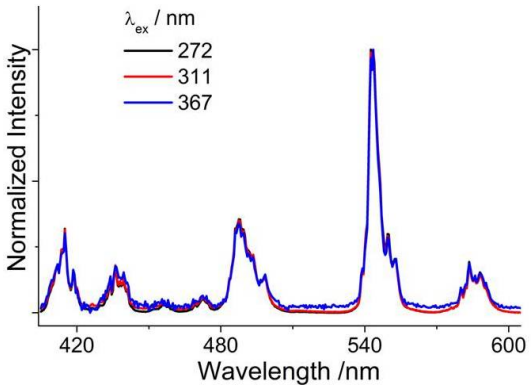

Figure 6.7: Room-temperature emission spectra of $Gd_{0.895}Yb_{0.10}Tb_{0.005}PO_4$ nanocrystals excited at different wavelengths.

position of Tb^{3+} emission lines for initial delays between 0.01 and 0.30 ms. Sousa et al. [176] also noted a single Eu^{3+} site in monoclinic (La,Eu)PO_4. For comparison, the emission spectrum was recorded at 11 K for the $Gd_{0.895}Yb_{0.10}Tb_{0.005}PO_4$ sample excited at 272 nm. As expected, the $^6P_{7/2}\rightarrow{}^8S_{7/2}$ (Gd^{3+}) transition line is much stronger and dominates the emission spectrum at room temperature (Figure 6.6b, purple line). This is due to the fact that energy-transfer from Gd^{3+} to Tb^{3+} is reduced upon decreasing the temperature, indicating that the energy-transfer is mediated by phonons of the host nanocrystal.

6.6 Emission decay curves, energy-transfer and lifetimes

As shown in Figure 6.8, for $Gd_{0.895}Yb_{0.10}Tb_{0.005}PO_4$, the emission decay curve of the $^6P_{7/2}\rightarrow{}^8S_{7/2}$ transition at 311 nm is well described by a single-exponential. The $^5D_{4,3}\rightarrow{}^7F_5$ emission decay curves, however, exhibit a rise-time component when exciting at 272 nm in the $^6I_{7/2-17/2}$ Gd^{3+} manifold (Figure 6.8b,d), whereas the direct excitation on the $^7F_6\rightarrow{}^5D_3,{}^5G_6,{}^5L_{10}$ Tb^{3+} transitions (e.g., at 367 nm) results in a single-exponential decay curve (inset in Figure 6.8), with a rise-time much shorter than the millisecond scale, in agreement with the previous report by Han et al. [39] The rise-time is, therefore, attributed to Gd^{3+}-to-Tb^{3+} energy-transfer followed by non-radiative decays within the Tb^{3+} energy levels (Figure 6.9). This phenomenon is analogous to the rise-time of the $^5D_0(C_2)$ emission decay curves of Eu^{3+} in cubic Gd_2O_3 nanorods (chapter 3) and similar fitting procedures were employed to estimate the rise-time and decay-time. Accordingly, for a single-exponential:

$$i = i_0 exp(\frac{-t}{\tau_d}) + i_c \tag{6.1}$$

where i and i_0 are the intensities of the emitting level at time t and $t = 0$, respectively, τ_d is the decay-time of the emitting level, and i_c is the background constant. Similarly,

for a rising component followed by a single-exponential:

$$I = [I_0 + I_1(1 - exp(\frac{-t}{\tau_r}))]exp(\frac{-t}{\tau_d}) + I_c \tag{6.2}$$

where I and I_0 are, respectively, the intensities of the emitting lower-level at time t and $t = 0$; I_1 is the intensity at $t = 0$ of the upper level feeding the emitting lower-level; τ_r and τ_d are, respectively, the rise-time and the decay-time of the emitting lower-level; I_c is the background constant.

The calculated lifetimes for the different samples using the above equations are summarized in Table 6.1 along with the measured emission quantum yields. Additional emission decay curves are presented in Figure 6.10.

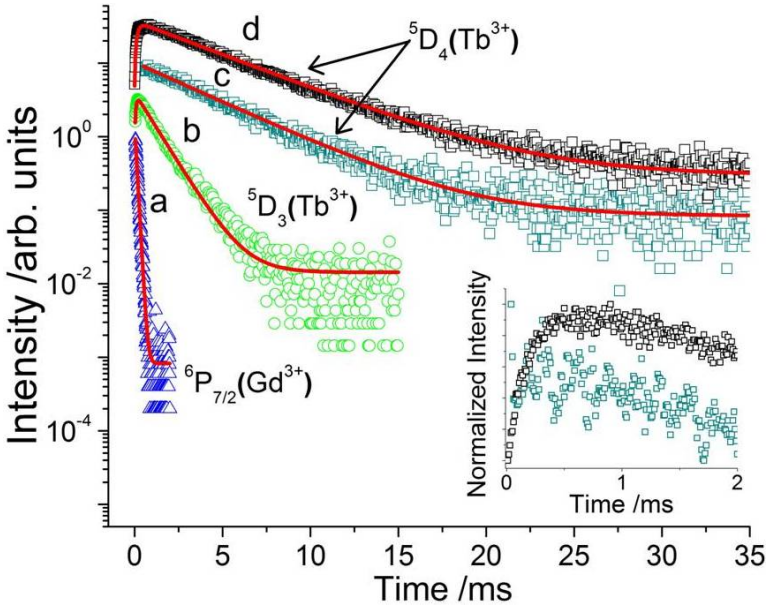

Figure 6.8: Room-temperature emission decay curves of $Gd_{0.895}Yb_{0.10}Tb_{0.005}PO_4$ nanocrystals: monitoring the (a) $^6P_{7/2}\rightarrow{}^8S_{7/2}$, (b) $^5D_3\rightarrow{}^7F_6$ and (d) $^5D_4\rightarrow{}^7F_5$ emissions while exciting at 272 nm, and (c) monitoring the $^5D_4\rightarrow{}^7F_5$ emission and exciting at 367 nm; the symbols represent the experimental data while the solid lines are the fitting curves with $R^2 > 0.997$. The inset shows the magnified decay curves (c) and (d) of the $^5D_4\rightarrow{}^7F_5$ emission exciting at 367 and 272 nm, respectively.

Further evidence of Gd^{3+} to Tb^{3+} energy-transfer comes from the emission decay curves of the $^6P_{7/2}\rightarrow{}^8S_{7/2}$, $^5D_3\rightarrow{}^7F_6$ and $^5D_4\rightarrow{}^7F_5$ transition lines (Figure 6.8). Under excitation at 272 nm the $^6P_{7/2}$ decay-time (0.103 ms) and $^5D_3$ rise-time (0.078 ms) of $Gd_{0.895}Yb_{0.10}Tb_{0.005}PO_4$ are close (Table 6.1), indicating that the $^5D_3$ rise-time is indeed controlled by the Gd^{3+} to Tb^{3+} energy-transfer. In a similar study, the $^5D_3$ rise-time was also observed in $LiGdY(PO_3)_4$:Tb^{3+} under excitation at 273 nm [39].

To better understand the observed Gd^{3+} to Tb^{3+} energy-transfer mechanism and the $^6P_{7/2}$, $^5D_3$ and $^5D_4$ emission decay curves, a schematic representation of the partial

energy level diagram and the possible energy-transfer pathways is presented in Figure 6.9. Gd^{3+} to Tb^{3+} non-radiative energy-transfer can occur either through the electric multipolar or the exchange mechanism. The corresponding selection rules governing transitions between J and J' levels are $J + J \geq \lambda \geq |J - J'|$ ($\lambda = 2, 4, 6$), for the former case, where λ is the rank of the unit irreducible tensor operator $U^{(\lambda)}$, and $J = 0, 1$ for the exchange mechanism. In both cases $J' = J = 0$ is excluded unless weak J-mixing effects are considered [177, 178]. According to these selection rules and energy resonance conditions, the $^6I_{7/2}$ and $^6P_{7/2}$ levels of Gd^{3+} and the Tb^{3+} $^5I_7$, $^5F_{2,3}$ and $^5H_{5,6,7}$ manifolds may be involved in the two mechanisms. The transfer rates through the multipolar mechanism depend on the squared reduced matrix elements of the $U^{(\lambda)}$ ($\lambda = 2, 4, 6$) operators between initial and final states of both donor and acceptor ions. From the well-known Tables given by Carnall et al. [174] their values for the Tb^{3+} ion, involving the acceptor levels of interest here, are vanishing or at least smaller than 10^{-4}. We, then, focus our discussion on the exchange mechanism.

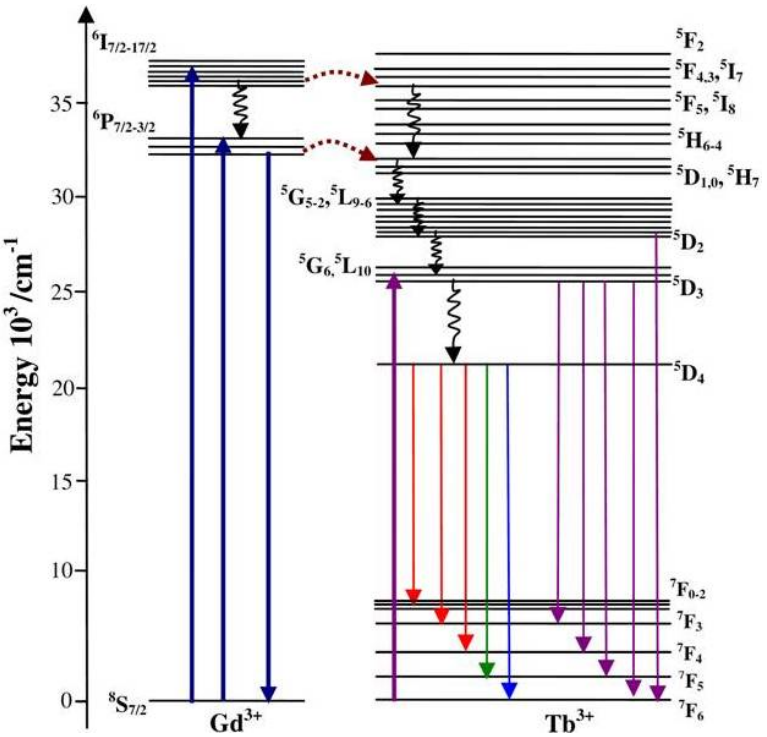

Figure 6.9: Partial energy-levels diagram showing the most probable energy-transfer pathways, non-radiative decays and emission lines in the Gd^{3+}/Tb^{3+} system, the energy levels are assigned using the barycenters of the energy values tabulated by Carnall et al. [174].

According to the model developed by Malta [177], energy-transfer rates between donor (D) and acceptor (A) by the exchange mechanism may be expressed by the isotropic component of the exchange interaction as (it is worth mentioning that in the case of ligand-to-metal intramolecular energy-transfer in coordination compounds, this isotropic term vanishes):

$$W_{ex} = \frac{2\pi}{\hbar}[\frac{e^2}{R}\langle 4f_D|4f_A\rangle]F \tag{6.3}$$

where R is the $D-A$ distance, $\langle 4f_D|4f_A\rangle$ is the radial overlap integral between the 4f subshells of the lanthanide ions, and the temperature dependent factor F contains a sum over Franck-Condon factors and the energy mismatch conditions ($D-A$ spectral overlap) [31]. For resonant or quasi-resonant energy transfer, the spectral overlap factor can be written as [23, 179]:

$$\begin{aligned} F = & \frac{\ln 2}{\sqrt{\pi}} \frac{1}{\hbar^2 \gamma_D \gamma_A} [[(\frac{1}{\hbar\gamma_A})^2 + (\frac{1}{\hbar\gamma_D})^2] \ln 2]^{-\frac{1}{2}} \\ & \times exp[\frac{1}{4} \frac{(\frac{2\Delta}{(\hbar\gamma_D)^2} \ln 2)^2}{[(\frac{1}{\hbar\gamma_A})^2 + (\frac{1}{\hbar\gamma_D})^2] \ln 2} - (\frac{\Delta}{\hbar\gamma_D})^2 \ln 2] \end{aligned} \tag{6.4}$$

where γ_D and γ_A represent band widths at half-height and Δ is the difference between the donor and acceptor transition energies involved in the energy-transfer process. This factor is extremely sensitive to these quantities.

Our interpretation of the role of energy-transfer from Gd^{3+} to Tb^{3+} is as follows. Multiphonon relaxation between relatively close excited 4f levels is usually quite fast in inorganic materials (decay rates typically of the order of 104 s^{-1}). The population channels of the Tb^{3+} $^5D_3$ and $^5D_4$ levels through excitation of the Gd^{3+} ion are composed by Gd^{3+}-to-Tb^{3+} energy-transfer and subsequent multiphonon relaxation towards these levels. These composed channels are governed by the slower steps, which in our case are assigned to the energy-transfer processes. This explains the rise-times observed in the transient curves shown in Figure 6.8, while under direct excitation in the Tb^{3+} ion no rise-time is observed in the time scale used in our measurements. Energy-transfer rates should be, then, smaller than 104 s^{-1}, as in fact corroborated by the rise-time values here observed.

As shown in Figure 6.5, the host nanocrystal exhibits vibrational modes centered at 1076, 624 and 574/536 cm^{-1} ascribed to P-O stretching, O=P-O bending and O-P-O bending modes, respectively. Therefore, it is conceivable that these phonons might play a significant role in the energy-transfer processes. The phonon-assisted Gd^{3+} to Tb^{3+} energy-transfer is indeed ascertained from the emission spectrum at 11 K, where the dominant $^5D_4 \rightarrow {}^7F_5$ line at room temperature is suppressed by the $^6P_{7/2} \rightarrow {}^8S_{7/2}$ emission (Figure 6.6b) due to the restriction of electron-phonon interaction and/or lattice vibration at low temperature. As a result, a remarkably longer decay-time of 2.29 ms was measured for the $^6P_{7/2} \rightarrow {}^8S_{7/2}$ emission at 11 K, when compared to its room temperature counterpart (0.103 ms), Table 6.1. In a similar study, phonon-assisted Gd^{3+}-to-Tb^{3+} energy-transfer in borate glasses was reported by Reisfeld et al. [180]. Figure 6.10a shows the emission decay curve of the $^6P_{7/2} \rightarrow {}^8S_{7/2}$ (Gd^{3+}) emission at 11 K. The Gd^{3+}-to-Tb^{3+} energy-transfer efficiency, η, is given by [39, 180]:

$$\eta = 1 - \frac{\tau}{\tau_o} \tag{6.5}$$

where τ and τ_o denote the lifetime of the $^6P_{7/2} \rightarrow {}^8S_{7/2}$ emission in the presence and absence of Yb^{3+}/Tb^{3+}, respectively. Assuming that the 2.29 ms at 11 K is close to the intrinsic $^6P_{7/2} \rightarrow {}^8S_{7/2}$ lifetime, i.e., $\tau_o = 2.29$ ms, and $\tau = 0.103$ ms, then, the Gd^{3+}-to-

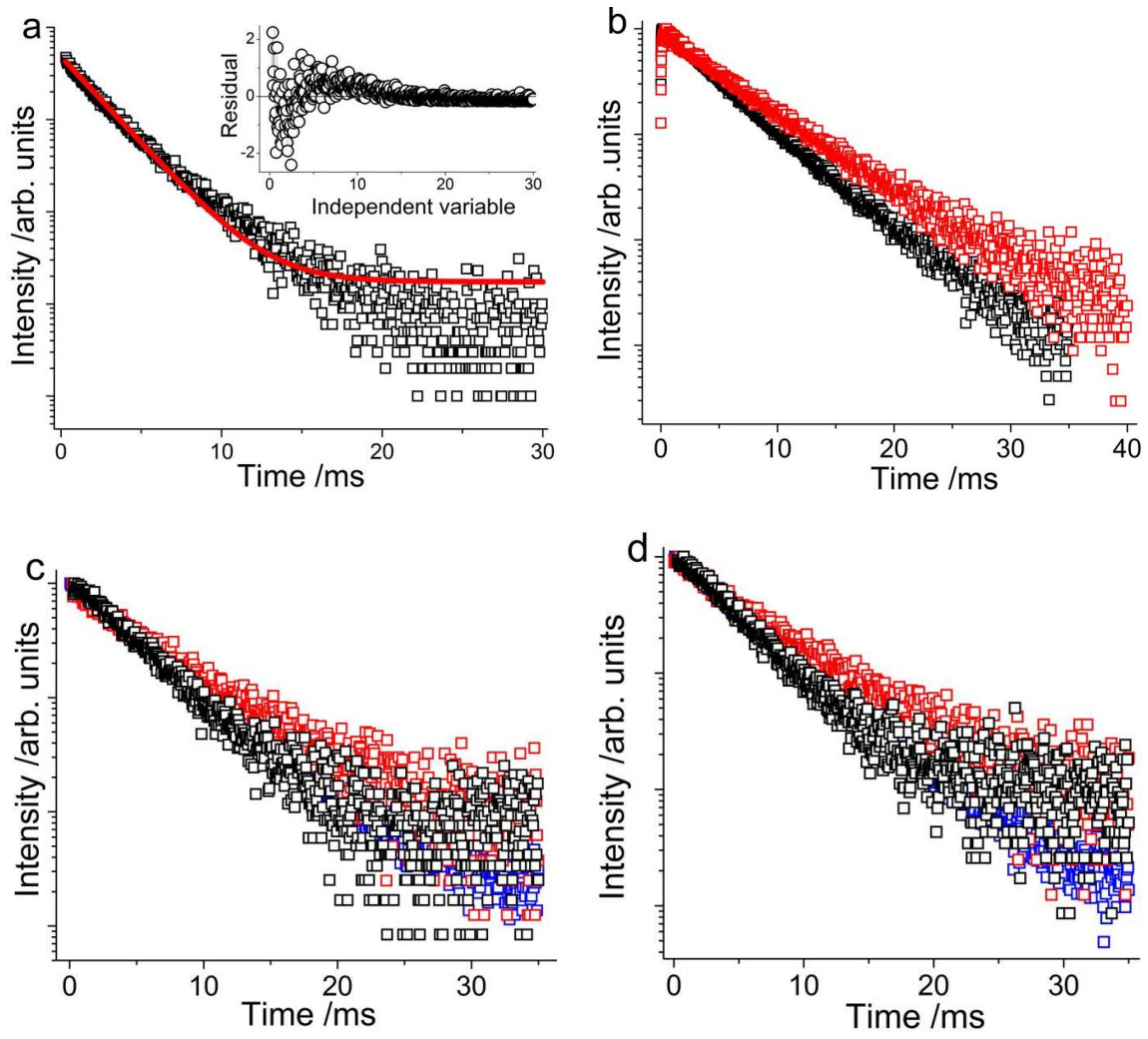

Figure 6.10: a) Emission decay curve of $Gd_{0.895}Yb_{0.10}Tb_{0.005}PO_4$ nanocrystals at 11 K monitoring the emission at 311 nm of the $^6P_{7/2} \rightarrow {}^8S_{7/2}$ (Gd^{3+}) transition and exciting at 272 nm; the solid line is the fitting curve ($R^2 > 0.996$) and the inset shows the residual *vs.* independent variable. b-d) Room-temperature emission decay curves of the nanocrystals: b) monitoring the $^5D_4 \rightarrow {}^7F_5$ (Tb^{3+}) emissions while exciting at 272 nm for $Gd_{0.87}Yb_{0.10}Tb_{0.03}PO_4$ (red squares) and $Gd_{0.85}Yb_{0.10}Tb_{0.05}PO_4$ (black); (c) and (d) monitoring the $^5D_4 \rightarrow {}^7F_5$ (Tb^{3+}) emissions while exciting at 377 and 367 nm, respectively, for $Gd_{0.895}Yb_{0.10}Tb_{0.005}PO_4$ (black), $Gd_{0.87}Yb_{0.10}Tb_{0.03}PO_4$ (red) and $Gd_{0.85}Yb_{0.10}Tb_{0.05}PO_4$ (blue).

Tb^{3+} energy transfer efficiency at room temperature is *ca.* 95% relative to the one at 11 K. Hou et al. [175] measured $\tau_o = 2.72$ ms in $Ba_3Gd(PO_3)_3$ and calculated η up to 97%.

In the estimations of the transfer rates using Equations 6.3 and 6.4, the phonon-assisted energy-transfer from Gd^{3+} to Tb^{3+} may be simulated by tuning the value of the energy mismatch condition. For $\Delta = 100$ cm^{-1} and assuming $\gamma_D = \gamma_A = 120$ cm^{-1} (values estimated from the emission spectra) and $R = 3.99$ Å [157], we get values of transfer rates of ∼8500 s^{-1}, ∼3500 s^{-1} and ∼1000 s^{-1} for values of the radial overlap integral $\langle 4f_D|4f_A\rangle = 0.00025$, 0.0002 and 0.00015, respectively (values that are compatible with

the theoretical overlap integral calculation made in Ref [179]. for a distance $R = 3.99$ Å). For a radial overlap equal to 0.0001 the transfer rate falls to $\sim$200 s^{-1}, a value that is of the same order of magnitude as estimated for the transfer rate through the exchange mechanism between Yb^{3+} ions separated by 4 Å [31].

The inverse of these Gd^{3+} to Tb^{3+} transfer rate values cannot be assumed as the rise-times of Tb^{3+} emitting levels, once the energy-transfer does not occur directly to them, though they constitute the governing step of the population channels of these levels. We note that since the energy of the $^5H_6$ level (not well-discerned in Figure 6.6a) is higher than that of the $^6P_{7/2}$ level (Figure 6.9), the corresponding energy-transfer rate should be calculated by multiplying the direct transfer rate by the Boltzmann factor, exp(-ΔE/kT), where ΔE is the energy difference between these levels, *ca.* 800 cm^{-1} [174], k the Boltzmann constant and T the room temperature. A negligible transfer rate is then estimated.

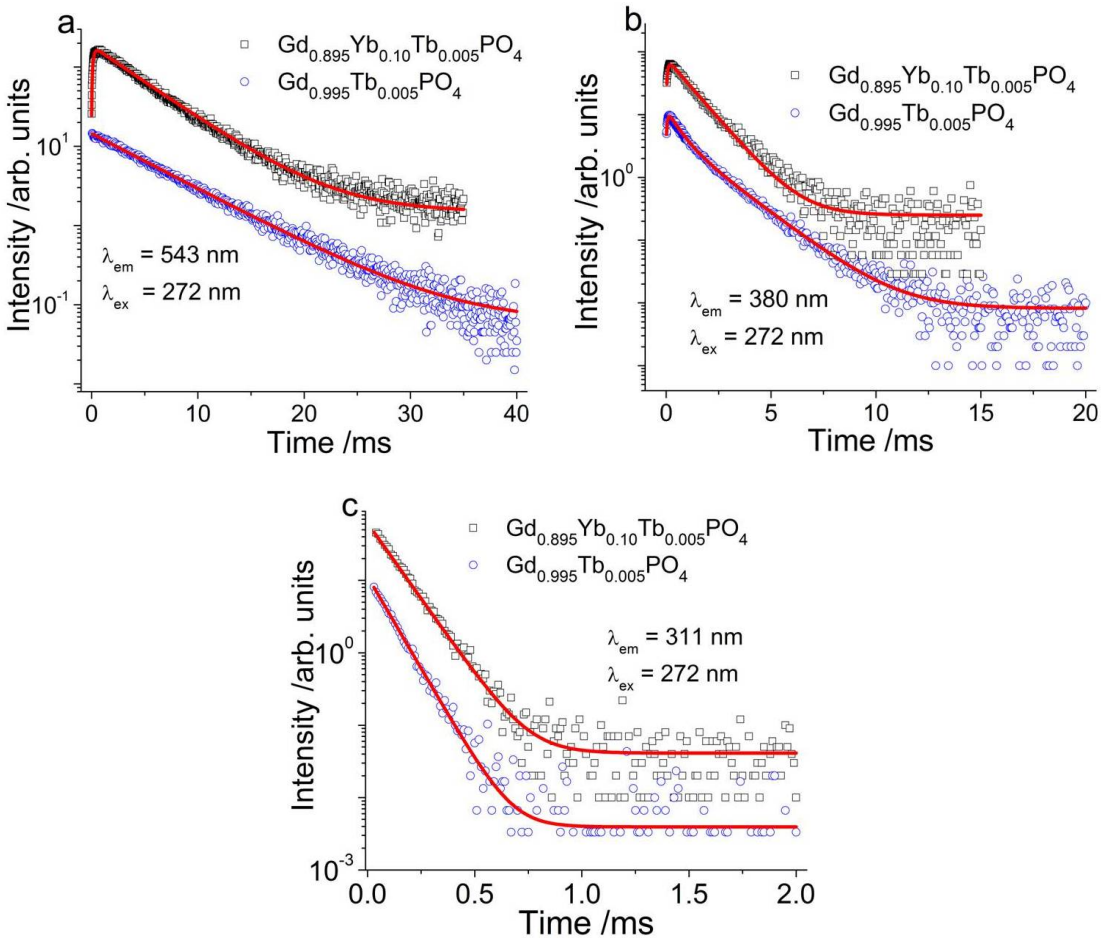

Figure 6.11: Room-temperature emission decay curves of (Gd,Tb)PO_4 nanocrystals with and without Yb^{3+}: monitoring the emissions at a) 543 nm, b) 380 nm and c) 311 nm while exciting at 272 nm. The symbols represent the experimental data while the solid lines are the fitting curves.

As presented in Table 6.1, the estimated $^5D_4$ decay-times are between 4.31 and 5.50 ms for (Gd,Tb,Yb)PO_4 samples excited at 272 nm. In similar studies, decay-times ranging from 3.50 to 7.10 ms were reported for the $^5D_4 \rightarrow {}^7F_5$ transition of Tb^{3+} in analogous $GdPO_4$ [162] and (Gd,Yb)PO_4 [181] nanocrystals, and the rise-time was also observed for low contents of Tb^{3+} in other host materials under excitation at 273 nm [182, 183]. In contrast to the $^5D_4$ decay-time, the rise-time component is shortened at high Tb^{3+} content from 0.160 ms (for 0.5 mol%) to 0.031 ms (for 5.0 mol%), Table 6.1. This is attributed to the energy migration over the $^5D_3$ levels of Tb^{3+} or to defect sites, such as the nanoparticle's surface [39, 165, 184]. This means, for instance, on increasing the Tb^{3+} concentration, the cross-relaxation within $^5D_3 \rightarrow {}^5D_4$ becomes faster due to energy migration over the donor levels and/or concentration quenching [39, 184], thus shortening the $^5D_{3,4}$ rise-times (Table 6.1).

Table 6.1: Room-temperature absolute-emission quantum yields and lifetimes of (Gd,Yb,Tb)PO_4 nanocrystals excited at distinct excitation wavelengths; **A**, **B**, **C**, and **D** represent for $Gd_{0.895}Yb_{0.10}Tb_{0.005}PO_4$, $Gd_{0.87}Yb_{0.10}Tb_{0.03}PO_4$, $Gd_{0.85}Yb_{0.10}Tb_{0.05}PO_4$, and $Gd_{0.95}Tb_{0.05}PO_4$, respectively.

Materials	Excitation λ (nm)	Quantum Yield	$^6P_{7/2} \rightarrow {}^8S_{7/2}$ (Gd^{3+})	$^5D_3 \rightarrow {}^7F_6$ (Tb^{3+})		$^5D_4 \rightarrow {}^7F_5$ (Tb^{3+})	
			τ_d (ms)	τ_r (ms)	τ_d (ms)	τ_r (ms)	τ_d (ms)
A	272	0.37	0.103±0.001 2.29±0.011[a]	0.078±0.002	1.120±0.007	0.160±0.003	4.71±0.021
	367	< 0.01	...	...	...	....	3.95±0.030
	377	< 0.01	...	...	...	...	3.99±0.031
B	272	0.34	0.030±0.038	...	0.031±0.038	0.076±0.002	5.50±0.038
	367	0.07	...	...	...	...	5.27±0.036
	377	0.08	...	...	...	...	5.27±0.036
C	272	0.42	0.024±0.001	...	0.157±0.003	0.031±0.001	4.31±0.011
	367	0.27	...	...	...	...	4.26±0.010
	377	0.35	...	...	...	...	4.43±0.010
D	272	0.20	0.085±0.001	0.064 ±0.003	0.422±0.041	...	6.25±0.021
	367	0.03	...	...	...	...	...
	377	0.03	...	...	...	...	...

[a] At 11 K.

6.7 Absolute-emission quantum yields

The room-temperature absolute-emission quantum yields measured at different excitation wavelengths are presented in Table 6.1. Exciting $Gd_{0.895}Yb_{0.10}Tb_{0.005}PO_4$ on the $^6I_{7/2-17/2}$ manifold at 272 nm gives the largest quantum yield (37%) whereas the direct excitation into the Tb^{3+} levels affords the lowest quantum yields (< 1%), Table 6.1. For $Gd_{0.85}Yb_{0.10}Tb_{0.05}PO_4$, however, a larger quantum yield of 42% is measured exciting at 272 nm. Direct excitation of the Tb^{3+} levels results in a relatively large quantum yield when the Tb^{3+} content is increased, giving quantum yields of 27 and 35% for $Gd_{0.85}Yb_{0.10}Tb_{0.05}PO_4$ excited at 367 and 377 nm, respectively, (*cf.* < 1% for $Gd_{0.895}Yb_{0.10}Tb_{0.005}PO_4$ at same excitation wavelengths), Table 6.1. These results are in agreement with the excitation spectra (Figure 6.6a), in which the relative intensity of the Tb^{3+} intra-$4f^8$-$4f^8$ transitions at high (5 mol%) Tb^{3+} content is higher, and with the emission spectra (Figure 6.6b), showing that the intensity of the $^6P_{7/2}\rightarrow{}^8S_{7/2}$ transition at 311 nm decreases on increasing the Tb^{3+} content due to the additional Tb^{3+} ions involved in receiving energy from the excited-states of Gd^{3+} ions, as discussed above. Therefore, the high quantum yields achieved in these nanocrystals by exciting at 272 nm are accounted for by the efficient Gd^{3+} to Tb^{3+} energy-transfer that has a significant contribution to the Tb^{3+} emission lines. Absolute-emission quantum yields of Tb^{3+} in analogous nanocrystals through indirect excitation have not been reported in the literature and comparison with the present emission quantum yield values cannot be made. However, it should be noted that emission quantum yield up to 80% was reported for Tb^{3+} in tetragonal YPO_4 nanoparticles (average size 117 nm) upon direct excitation at 351 nm [185]. Energy-transfer from Gd^{3+} to Tb^{3+} was noted at room-temperature in $Ba_3Gd(PO_4)_3$:Tb^{3+} phosphors upon increasing the Tb^{3+} concentration from 1 to 50% which reduces the decay-time of the $^6P_{7/2}\rightarrow{}^8S_{7/2}$ (Gd^{3+}) emission from 2.36 to 0.07 ms, respectively, while exciting at 274 nm [175].

The results discussed so far clearly show that Gd^{3+} is an efficient sensitizer for the strong green emission of Tb^{3+} in (Gd,Yb)PO_4 nanocrystals under UV light excitation. Indeed, a higher quantum-cutting efficiency of Tb^{3+} was demonstrated for Gd^{3+} containing $Ca_6Ln_2Na_2(PO_4)_6F_2$ phosphors, as compared to materials without Gd^{3+} [182].

For comparison, the lifetimes, quantum yields, emission decay curves, and emission and excitation spectra of $Gd_{0.995}Tb_{0.005}PO_4$ nanocrystals (without Yb^{3+}) are presented in Table 6.1 and Figure 6.11. In this sample, a relatively longer $^5D_4$ (Tb^{3+}) decay-time (6.21 ms) without a rise-time component, shorter $^5D_3$ (Tb^{3+}) rise-time (0.064 ms) and $^6P_{7/2}$ (Gd^{3+}) decay-time (0.085 ms), and lower emission quantum yield (20%) were noted when compared to those of the $Gd_{0.895}Yb_{0.10}Tb_{0.005}PO_4$ sample excited at 272 nm (Table 6.1 and Figure 6.11). Here, it is important to note that the presence of Yb^{3+} may influence the Tb^{3+} emission [181]. For instance, the shorter $^5D_4$ (Tb^{3+}) decay-time (4.71 ms) of $Gd_{0.895}Yb_{0.10}Tb_{0.005}PO_4$ is likely due to the presence of Tb^{3+}-to-Yb^{3+} energy-transfer. In this regard, both the excitation spectra of $Gd_{0.85}Yb_{0.10}Tb_{0.05}PO_4$ measured monitoring the Yb^{3+} emission at 1031.5 nm, and near infrared emission spectra under 272 and 377 nm excitations, show the occurrence of Gd^{3+}-to-Yb^{3+} and Tb^{3+}-to-Yb^{3+} energy transfers (Figure 6.12).

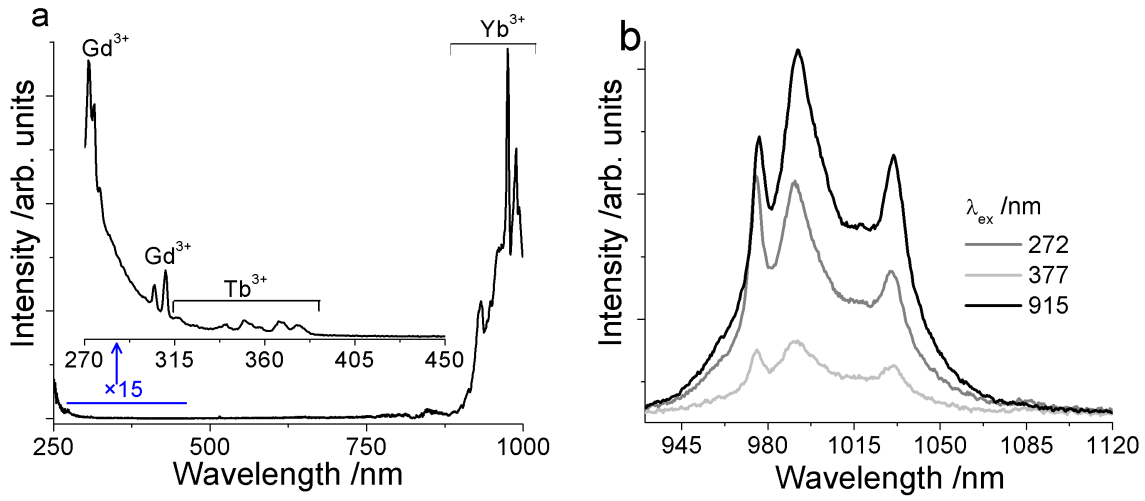

Figure 6.12: Room-temperature excitation and near infrared emission spectra of Yb^{3+} in monoclinic $Gd_{0.85}Yb_{0.10}Tb_{0.05}PO_4$ nanocrystals: a) monitoring the emission at 1031.5 nm and b) exciting at distinct wavelengths that correspond to the peaks in the excitation spectra, showing in the region of the $^2F_{7/2}\rightarrow{}^2F_{5/2}$ (Yb^{3+}) transition. The inset in a) magnifies the spectral region of the $^8S_{7/2}\rightarrow{}^6P_{7/2-3/2}$, $^6I_{7/2-17/2}$ (Gd^{3+}) and $^7F_6\rightarrow{}^5D_{1-2}$, $^5G_{6-2}$, $^5L_{10-6}$, $^5H_7$ (Tb^{3+}) transition lines and the spectrum was recorded with wider emission slits for acquiring better signal.

6.8 Summary and conclusion

Monoclinic (Gd,Yb,Tb)PO_4 nanocrystals were prepared *via* hydrothermal method at 150 ^{o}C followed by post calcination at 900 ^{o}C for 3 hrs. The materials were characterized by PXRD, TEM, FTIR, and PL spectroscopy. The nanocrystal's size increases from *ca.* 5 to 50 nm on rising the calcination temperature up to 900 ^{o}C.

The down-shifting PL properties (emission decay curves, lifetime, quantum yields and energy-transfer processes) of the nanocrystals were investigated in detail. As such, Gd^{3+}-Tb^{3+} energy-transfer is revealed by the emission and excitation spectra and transient decay curves. The room-temperature emission spectrum is dominated by the $^5D_4\rightarrow{}^7F_5$ (Tb^{3+}) transition at 543 nm, which has a long decay-time (4.31 - 5.50 ms) and exhibits a rise-time (0.031 - 0.160 ms) component. Emission quantum yields up to 42% were obtained under excitation at 272 nm. The emission intensity and decay-time of the $^6P_{7/2}\rightarrow{}^8S_{7/2}$ (Gd^{3+}) transition increases remarkably at 11 K, relatively to the room temperature counterparts. Thus, Gd^{3+} is an efficient sensitizer at room temperature (efficiency of ∼95%) for the Tb^{3+} visible light emission *via* the downshift process upon excitation at 272 nm on the $^6I_{7/2-17/2}$ Gd^{3+} manifold.

Chapter 7

(Gd,Yb,Tb)PO_4 Up-conversion Nanocrystals for Bimodal Luminescence-MR Imaging

7.1 Introduction

Photon up-conversion materials, able to change low-energy (e.g., infrared) incident photons into high-energy (e.g., visible) photons, are rapidly emerging as potential candidates for optical imaging agents in biomedicine. In particular, infrared light excitation (in the so-called biological window) has deeper tissue penetration depth than UV-visible light excitation, providing efficient excitation of the nanomaterial probes located deep in biological media without significant attenuation of the original excitation energy. This enables high-resolution deep-tissue optical imaging while avoiding also cell damage and the background fluorescence observed under UV-visible excitation. Furthermore, additional functional properties, e.g., magnetic resonance (MR) imaging, may be obtained from the same optical imaging agents by the rational design of materials synthesis.

In this chapter, the up-conversion emission and magnetic resonance relaxivity properties of (Gd,Yb,Tb)PO_4 nanocrystals synthesized with the procedure described in chapter 6 will be presented and their application in bimodal, luminescence-MR, imaging will be assessed. These materials exhibit ultraviolet, blue and green up-conversion emission lines upon excitation with a 980 nm continuous wave (CW) laser diode. The dependance of the up-conversion emission on Yb^{3+}/Tb^{3+} concentrations and the emission mechanisms are discussed. The intensity of the blue-emission band at 479 nm, ascribed to the simultaneous cooperative emission of a pair of excited Yb^{3+} ions, depends on the Yb^{3+}/Tb^{3+} concentration ratio, calcination temperature and particle size. Strong green up-conversion emission of Tb^{3+} is observed at 543 nm for the $^5D_4 \rightarrow {}^7F_5$ transition. Relaxometry measurements reveal that the nanocrystals are efficient T_2-weighted (negative) contrast agents which, combined with visible-light emission generated by infrared excitation, affords them considerable potential for being used in bimodal imaging[1]. The relaxometry measurements and analysis in this chapter were carried out in collaborations with Prof. Carlos Geraldes (Coimbra, Portugal).

[1] **M. L. Debasu**, D. Ananias, S. L. C. Pinho, C. F. G. C. Geraldes, L. D. Carlos, J. Rocha, (Gd,Yb,Tb)PO_4 up-conversion nanocrystals for bimodal luminescence-MR imaging, *Nanoscale*, 2012, 4, 5297-15303.

7.2 Basic principle of MRI

Magnetic resonance imaging (MRI) uses contrast materials known as contrast agents (CAs) for the enhancement of images of tissues and structures inside a body. 'Contrast' refers to the difference in signal intensities between two adjacent regions of an image. In MRI, the enhancement of the image signal is through the interactions between the contrast agent, e.g., Gd^{3+}, and neighboring water protons (^1H), induced by an external magnetic field and a radio frequency (RF) pulse. Figure 7.1, illustrates the basic principle of MRI [186]. The spins of the hydrogen nuclei tend to align parallel to the external magnetic field $\mathbf{B}_o$, *via* the precession of spins in a cone-shaped fashion under a specified frequency known as the Larmor frequency ω_o, which depends on the magnitude of $\mathbf{B}_o$, Figure 7.1a. Introducing a RF pulse in resonance with ω_o changes the alignment of

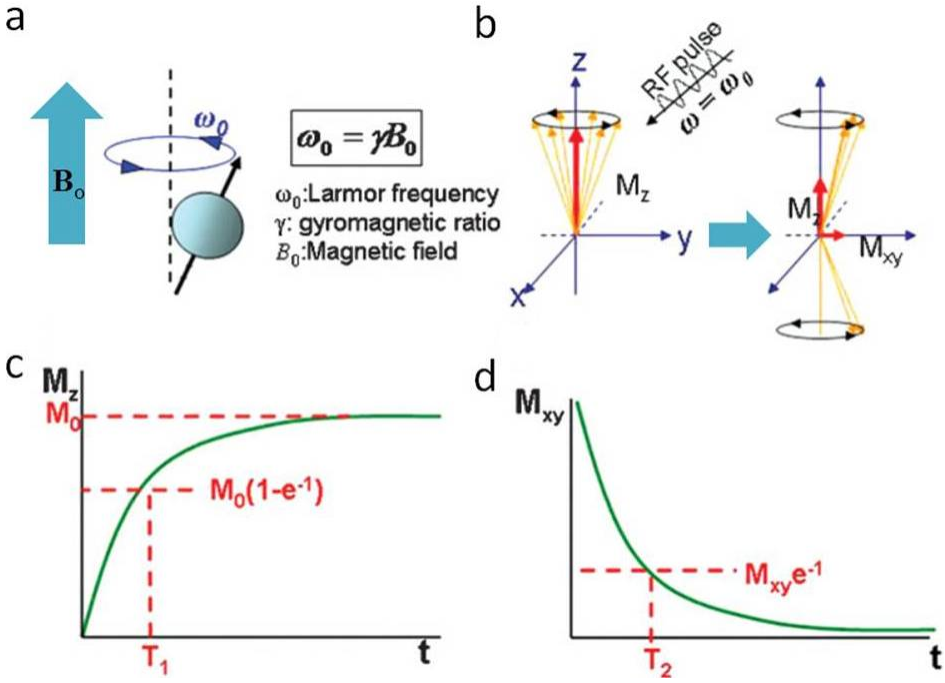

Figure 7.1: Principle of magnetic resonance imaging. a) Spins align parallel or antiparallel to the magnetic field and precess under Larmor frequency (ω_o). b) After induction of RF pulse, magnetization of spins changes. Excited spins take relaxation process of c) T_1 relaxation and d) T_2 relaxation [186].

the nuclei from a longitudinal to a perpendicular (or transverse) axis with respect to $\mathbf{B}_o$. After the disappearance of the RF pulse, the nuclei recover back to their original state (Figure 7.1b). The recovery process is called *relaxation* which is classified into two types: longitudinal or spin-lattice (T_1) relaxation time and transverse or spin-spin (T_2) relaxation time. T_1 relaxation time refers to the recovery of the net magnetization (M_z) to the initial state (Figure 7.1c) while T_2 relaxation is the time taken for the disappearance of the induced magnetization (M_{xy}) *via* spin-dephasing (Figure 7.1d).

The efficiency of a CA is evaluated by relaxivity r_i ($i = 1, 2$) defined by the water

proton relaxation rate enhancement per mM of CA concentration, $[CA]$:

$$\frac{1}{T_i(measured)} = \frac{1}{T_i(water)} + r_i[CA] \tag{7.1}$$

where $T_i(measured)$ is the measured solvent relaxation rate, $T_i(water)$ is the relaxation rate of water proton in the absence of the CA. The value of r_i can be readily determined from the slope of $[CA]$ *vs.* $\frac{1}{T_i}$ curve. The ratio between these relaxivities (i.e., r_2/r_1) is considered as a defining parameter indicating whether a CA can be employed as a T_1-weighted (positive) or T_2-weighted (negative) imaging [186–188].

7.3 $GdPO_4$ materials for bioimaging

Ln^{3+}-containing inorganic nanoparticles have received much attention in the biomedical applications [189, 190] because of their robust multifunctional properties, integrating different diagnostic modes in a single platform such as MR and optical imagings as well as temperature sensing as discussed in chapter 5. For instance, novel Tb^{3+} or Eu^{3+} doped Fe_3O_4@YPO_4 multifunctional spherical particles exhibiting magnetic, fluorescent, drug-loading and potential radiotherapeutic properties were reported by Wang et al [166]. $EuPO_4$ and $TbPO_4$ nanorods are novel fluorescent bio-labels and alternatives to the conventional organic dyes, as shown by tests in human umbilical vein endothelial cells and renal carcinoma cells [191]. Recent examples of Ln-phosphate bioprobes for combined optical and MR imaging include (Gd,Ln)PO_4 nanorods (Ln = Yb, Er, Ce,Tb, and Tb) [192] and (Gd,Eu)PO_4 nanoparticles [193]. Importantly, nanoparticles displaying both MR properties and infrared-activated up-conversion emissions are of particular interest for the biomedical community because they allow the implementation of dual imaging methodologies, optical and MR imagings [194]. Optical imaging using organic dyes, quantum dots and Ln^{3+}-doped materials presents excellent sensitivity and spatial resolution but lacks penetration depth and anatomic detail in thick tissues [195–197]. MRI does not suffer from these limitations, while it is limited by sensitivity and spatial resolution [198, 199]. The light-penetration depth of living tissues strongly depends on the wavelength [200]; under 600 nm, tissue absorption dominates, leading to a small penetration depth and limited spatial resolution of the optical images [195, 197]. For wavelengths in the range 650 - 1450 nm, the absorption coefficient of tissues is small [194] and, thus, excitation with near-infrared light increases the light-penetration depth to over 1 mm [197, 201, 202], enabling high-resolution deep-tissue optical imaging, while avoiding also cell damage and the background fluorescence observed under UV-visible excitation.

Gd^{3+} has been an ideal contrast agent for MRI since it has large number of unpaired electrons with a total spin $S = 7/2$ and large magnetic moment ∼7.94. Indeed, several Gd^{3+}-based CAs were clinically approved for MRI [186, 203–205], and $GdPO_4$ and Gd_2O_3 nanoparticles are among the next generation MRI CAs [186]. Hifumi et al. reported, for instance, a positive (T_1-weighted) MRI CA for dextran-coated $GdPO_4$ nanoparticles, with a low r_2 to r_1 relaxivity ratio similar to ratio of the clinically em-

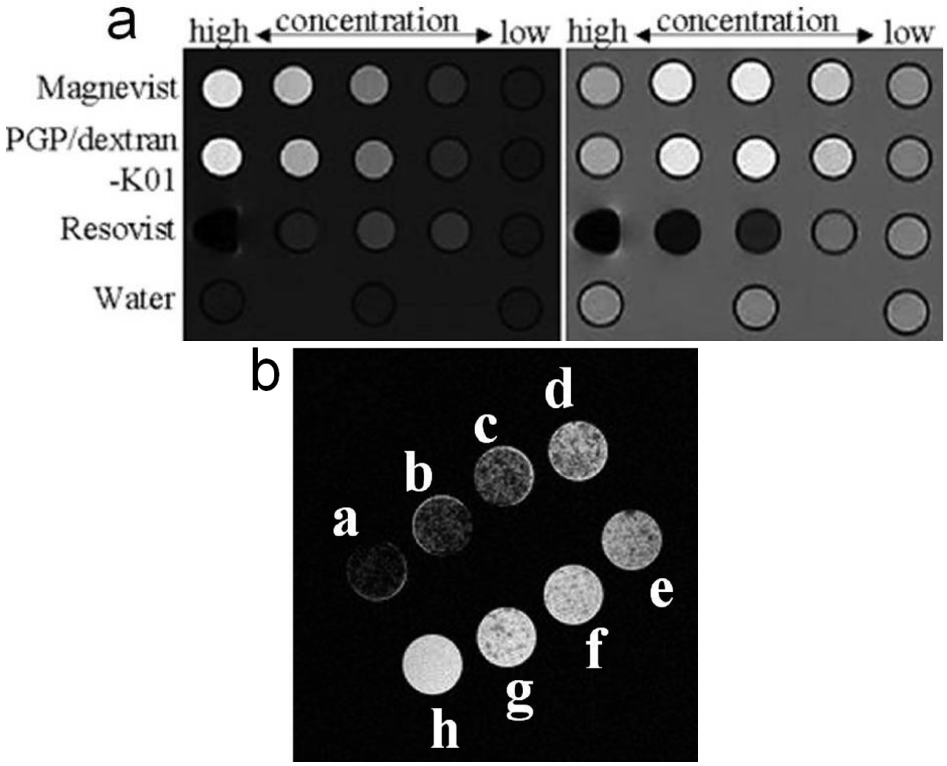

Figure 7.2: a) T_1-weighted (left) and T_2-weighted (right) MR images of various concentrations of CAs and water. First row: Magnevist (from the left) 5.0, 1.0, 0.5, 0.1, 0.01 mM. Second row: PGP/dextran-K01 (from the left) 2.2, 1.1, 0.5, 0.2, 0.04 mM of Gd^{3+}. Third row: Resovist (from the left) 5.0, 1.0, 0.5, 0.1, 0.01 mM of Fe^{3+}. Fourth row: water [187]. b) T_2 weighted images of successive dilutions of $GdPO_4$ nanoparticle-DNA in agarose (in sequence, from a to h: 2, 1.5, 1, 0.5, 0.25, 0.12, 0.06 mM, and pure agarose) [188].

ployed CA Magnevist® [187], Figure 7.2a. Similarly, luminescent (Gd,Eu)PO_4 and (Gd,Tb)PO_4 nanorods were reported as T_1-weighted MRI CAs [192]. On the other hand, DNA surface modified $GdPO_4$ nanoparticles exhibited efficient T_2-weighted (negative) MRI contrast properties as was confirmed by the high r_2/r_1 value of 60.9 [188], Figure 7.2b.

Here, the UV-visible up-conversion emission of (Gd,Yb,Tb)PO_4 nanocrystals is reported as well as the potential of these materials as bimodal, photoluminescence/magnetic resonance, imaging agents is evaluated. We show that the relative intensity of the blue and green emissions of Yb^{3+} and Tb^{3+}, respectively, is tuned by varying the concentration of these ions. As a result, a strong blue cooperative emission due to a pair of Yb^{3+} ions is observed for 10 - 30 mol% Yb^{3+} and 0.5 - 1.0 mol% Tb^{3+} in monoclinic $GdPO_4$ nanocrystals. For the first time, $GdPO_4$ is shown to be an ideal host for tuning the Yb^{3+}-Yb^{3+} pair and Tb^{3+} up-conversion emissions, achieved *via* a cooperative energy-transfer process (CET). The laser excitation-power dependence and energy-transfer mechanisms of the up-conversion emission of the nanocrystals are investigated in detail.

Results and Discussion

7.4 Up-conversion emission spectra

The up-conversion emission spectra of monoclinic (Gd,Yb,Tb)PO_4 nanocrystals (obtained *via* calcination at 900 ^oC for 3 hours) were recorded in the range 300 to 720 nm, upon excitation at 980 nm with a CW laser diode. Figure 7.3a shows representative up-conversion emission spectra, recorded with a pump power density on the sample *ca.* 270 W cm^{-1}. The peaks at 351, 380, 415, 436, 456, 472, 488, 543, 584, 621 and 648 nm are assigned to the $^5L_9 \rightarrow {}^7F_6$ and $^5D_{3,4} \rightarrow {}^7F_{J=2-6}$ intra-$4f^8$-$4f^8$ transitions of Tb^{3+} [132, 206, 207]. A schematic representation of the partial energy levels for Yb^{3+}/Tb^{3+} system and the most probable energy-transfer (ET) mechanisms are shown in Figure 7.3b. The relatively broad blue emission band at 479 nm (depicted by the asterisk) is ascribed to the cooperative up-conversion emission of Yb^{3+} ions [132, 208–210]. The weak emission peak at 522 nm is also due to the cooperative emission of a pair of Yb^{3+} ions [211, 212]. Such cooperative emission from Yb^{3+} ions, often observed as a broad band due to the various combinations of the $^2F_{5/2}$ Stark levels, was reported for other host materials [30, 209–211, 213]. Nakazawa et al. [212] were the first to report a broad and weak green emission band at 497 nm from a pair of excited Yb^{3+} ions in $YbPO_4$. Adam et al. [132] observed a blue emission at 478 nm from fluorophosphate glasses containing only Yb^{3+} and attributed it to the cooperative emission of Yb^{3+} ions.

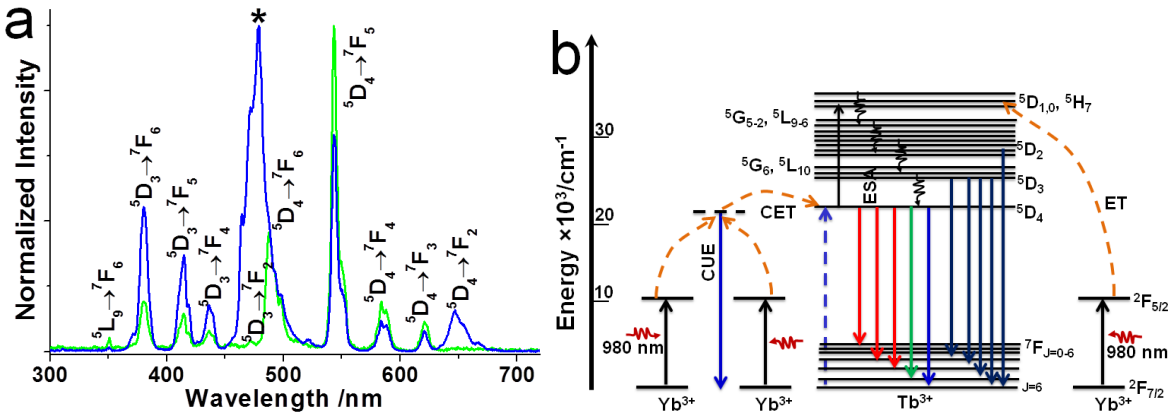

Figure 7.3: a) Up-conversion emission spectra of (Gd,Yb,Tb)PO_4 nanocrystals excited at *ca.* 270 W cm^{-1}, with a 980 nm CW laser diode: $Gd_{0.98}Yb_{0.01}Tb_{0.01}PO_4$ (green line) and $Gd_{0.89}Yb_{0.10}Tb_{0.01}PO_4$ (blue line); b) schematic representation of the partial energy levels and most probable energy-transfer (ET) pathways for Yb^{3+}/Tb^{3+} up-conversion emission. CUE denotes cooperative up-conversion emission.

7.5 Effect of Yb^{3+}/Tb^{3+} concentration ratio

The relative intensities between the cooperative up-conversion emission of Yb^{3+} ions and the $^5D_{3,4} \rightarrow {}^7F_{J=2-6}$ transitions of Tb^{3+} are strongly dependent on the Yb^{3+}/Tb^{3+} contents as shown in Figure 7.4. Intense and dominant blue cooperative up-conversion emission by the pair of Yb^{3+}/Yb^{3+} ions was observed for samples with low Tb^{3+} (0.5 - 1.0 mol%) and high Yb^{3+} (10.0 - 30.0 mol%) concentrations (Figure 7.4). For relatively high contents of Tb^{3+} (3.0 - 8.0 mol%) and Yb^{3+} (10.0 - 30.0 mol%), however, only the $^5D_{3,4} \rightarrow {}^7F_{J=2-6}$ transitions of Tb^{3+} with a dominant green emission band at 543 nm were detected (Figures 7.4a,b). This implies that the cooperative interaction of the two Yb^{3+} ions is influenced by the content of both Tb^{3+} and Yb^{3+}. As shown in Figures

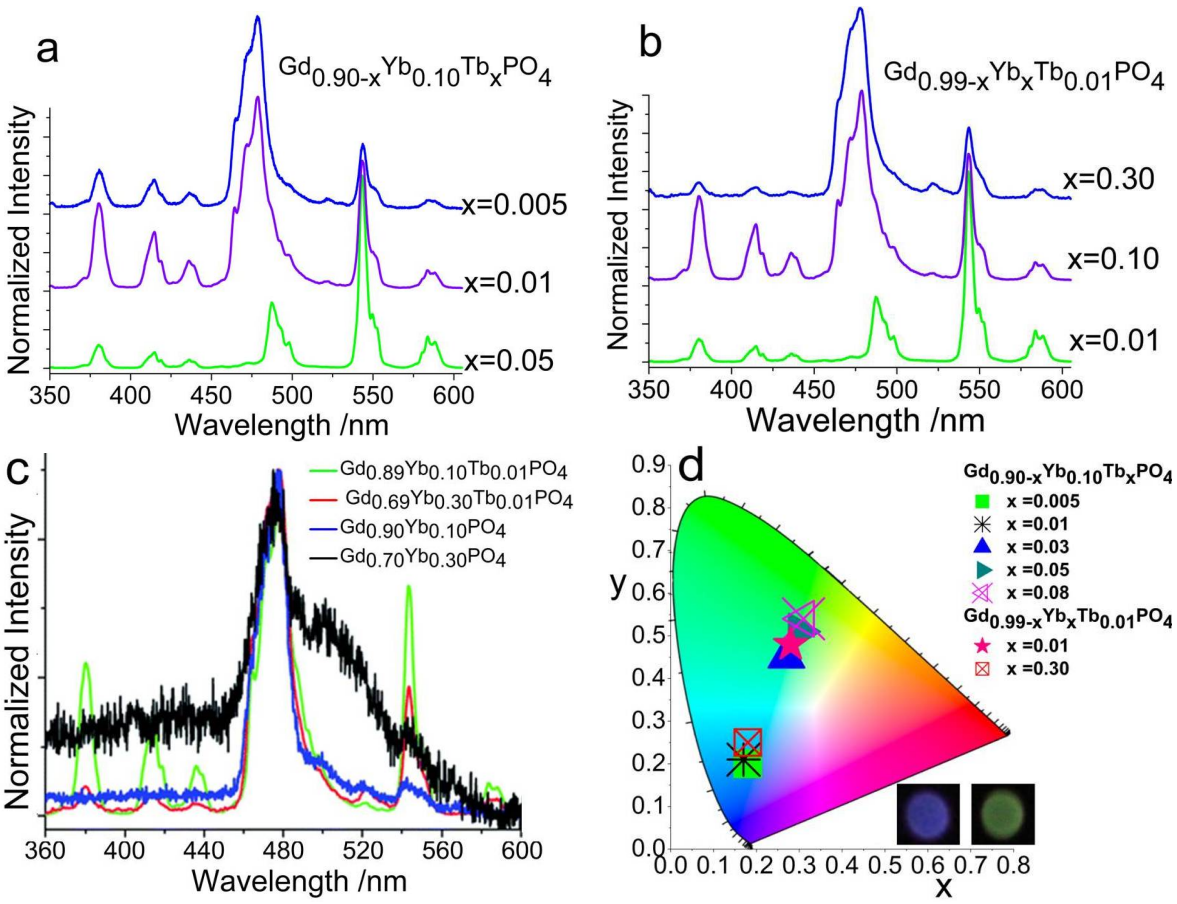

Figure 7.4: Effect of the Yb^{3+} and Tb^{3+} concentration on the up-conversion emission of (Gd,Yb,Tb)PO_4 nanocrystals excited at *ca.* 270 W cm^{-1}, with a 980 nm CW laser diode: a) up-conversion emission spectra for a fixed Yb^{3+} content; b) up-conversion emission spectra for a fixed Tb^{3+} content; c) up-conversion emission spectra with and without Tb^{3+}; d) CIE 1931 chromaticity diagram for the up-conversion emissions. The insets in (d) are digital photographs of blue and green up-conversion emissions of $Gd_{0.895}Yb_{0.10}Tb_{0.005}PO_4$ and $Gd_{0.85}Yb_{0.10}Tb_{0.05}PO_4$ nanocrystals, respectively.

7.4a,b, it is evident that the $^5D_4 \rightarrow {}^7F_5(Tb^{3+})$ emission intensity is weaker when the intensity of the blue emission at 479 nm is stronger, indicating either that the efficiency

of energy-transfer *via* CET decreases due to the Yb^{3+}/Yb^{3+} cooperative emission or that the number of Yb^{3+}/Yb^{3+} pairs active in the cooperative emission increases. In other words, when all available pairs of Yb^{3+} ions transfer their energy to the Tb^{3+} ions the $^5D_{3,4} \rightarrow {}^7F_{J=2-6}$ up-conversion emissions of Tb^{3+} are observed, whereas the cooperative emission from Yb^{3+} ions is hardly detected. In general, the cooperative emission requires close proximity of the interacting ions [30, 89, 211, 214] and, thus, changing the Tb^{3+} or Yb^{3+} concentration changes the average shortest distance between two Yb^{3+} ions, which in turn affects the interaction process. In monoclinic $GdPO_4$, the shortest Gd^{3+}-Gd^{3+} distance is *ca.* 3.99 Å and for each Gd^{3+} there are two closest neighbors of other Gd^{3+} ions located at such distance [157], Figure 7.5. Assuming that the doping of Ln^{3+} in $GdPO_4$ nanocrystals is homogenous, the probability of finding a pair of Yb^{3+} ions within the shortest distance may be influenced by the relative content of Ln^{3+} ions in the crystals. This would explain the variation between the blue and green up-conversion emission intensities with small changes in the Yb^{3+}/Tb^{3+} content, Figure 7.4. For instance, a broad cooperative up-conversion emission band is also

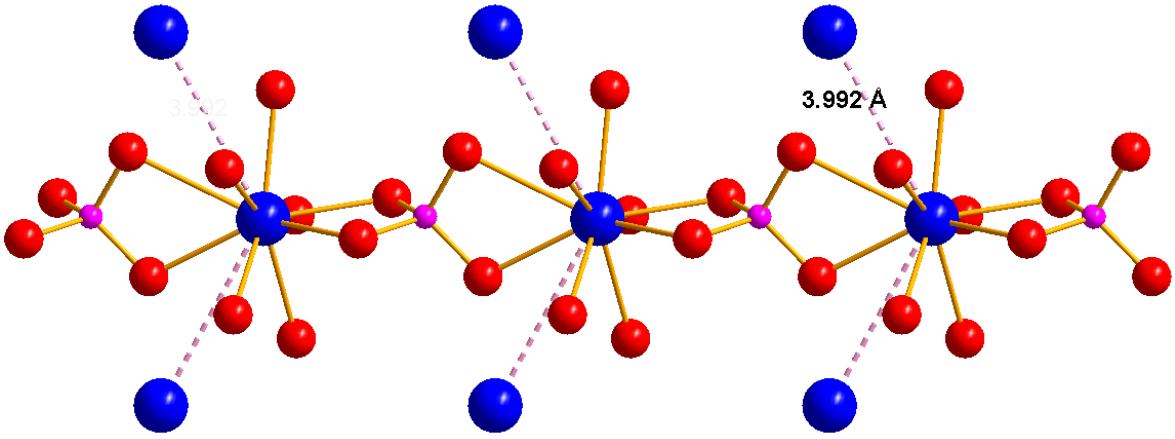

Figure 7.5: Atomic arrangement of monoclinic $GdPO_4$ along the [-100] direction and the nearest-neighbour Gd^{3+}-Gd^{3+} distance (broken lines); blue, red, and pink balls represent Gd, O and P atoms, respectively.

detected for the nanocrystals containing Yb^{3+} (30.0 mol%) but without Tb^{3+}, Figure 7.4c. Such emission, however, is hardly seen by the naked eye and the intensity for this sample is poor as compared to the corresponding emission intensity of the sample with 1.0 mol% Tb^{3+} (Figure 7.4c), clearly showing that the cooperative process for a pair of Yb^{3+} ions can be modified by the Tb^{3+} content. Similarly, for the sample without Tb^{3+} changing only the Yb^{3+} content to, e.g., 10.0 mol%, results in more intense emission band at 479 nm than that of the 30.0 mol% Yb^{3+} (Figure 7.4c). In other words, there is an optimal Yb^{3+} and Tb^{3+} content for the observation of cooperative emission from two excited Yb^{3+} ions in $GdPO_4$ host, since the critical interatomic distance between two Yb^{3+} ions, which are active in the cooperative emission, is certainly influenced by the ratio of the Ln^{3+} ions (Ln^{3+} = Gd^{3+}, Yb^{3+} and/or Tb^{3+}). The Yb^{3+}/Yb^{3+} cooperative emission is also strongly dependent on the calcination temperature (Figure 7.7). As demonstrated by Adam et al. [132], the cooperative emission of Yb^{3+} ions

in fluorophosphate glasses changes when varying the Yb^{3+}/Tb^{3+} concentration ratio. Furthermore, it was noted that the Yb^{3+}/Yb^{3+} pairs broke up and the cooperative emission disappeared after the incorporation of Na^{+} ions in Yb^{3+}-doped CaF_2 laser host [215]. Another evidence supporting the presence of Yb^{3+}/Yb^{3+} cooperative effect may be drawn from the down-shift emission spectra displaying only the $^6P_J \rightarrow {}^8S_{7/2}$ (Gd^{3+}) and $^5D_{3,4} \rightarrow {}^7F_{J=0-6}$ (Tb^{3+}) intra-4f-4f transitions irrespective of the ratio of Yb^{3+}/Tb^{3+} content; no emission band at 479 nm is detected (Figure 6.6b, chapter 6). The results show that the Yb^{3+}/Tb^{3+} up-conversion emission in $GdPO_4$ may be tuned in the UV-visible region by varying the Yb^{3+} and Tb^{3+} concentration and that $GdPO_4$ is a suitable host for such emission, offering the formation of Yb^{3+}-Yb^{3+} pairs for the blue and for the $^5D_{3,4} \rightarrow {}^7F_{J=2-6}$ emissions of Yb^{3+}/Yb^{3+} and Tb^{3+}, respectively.

7.6 Up-conversion mechanism

The up-conversion emission intensity I and the pump power P are related by $I \approx P^n$, where n is the number of photons involved in the former process. Figure 7.6 shows double-logarithmic plots for the integrated intensity of the different up-conversion emission bands against the excitation pump power (Equation 5.5, chapter 5). Irrespective of the Yb^{3+} and/or Tb^{3+} content of the nanocrystals, a quadratic dependence of the up-conversion emission intensity on the pump-power and slopes of *ca.* 2 are obtained, indicating that two photons are involved in the up-conversion process, Figures 7.6a-b. As expected, at high pump power the slope decreases and the data points follow a nearly horizontal line (plateau) attributed to the saturation of the excited $^7F_{5/2}$ (Yb^{3+}) levels [132].

The up-conversion mechanisms responsible for the emission lines may be discussed based on the energy matches in the Yb^{3+}/Tb^{3+} system and the observed pump power dependence of such emissions. The most common up-conversion mechanisms include ground state absorption (GSA), excited state absorption (ESA), energy-transfer up-conversion (ETU), photon avalanche (PA) and cooperative energy-transfer (CET), section 1.7.2 in chapter 1. A comprehensive review of these up-conversion mechanisms and energy-transfer processes in various materials was presented by Auzel [30]. It was shown that CET is less efficient than ESA or ETU because it is a second-order process [30,38,89]. In the present study, however, the CET process involving two simultaneously excited Yb^{3+} ions (Figure 7.3b) is the dominant mechanism for all observed up-conversion emissions because: i) there is no energy level between the $^7F_{5/2}(Yb^{3+})$ and $^5D_4(Tb^{3+})$ levels for the ESA/ETU process, and ii) the energy gap between the $^5D_4$ and $^7F_5$ levels of Tb^{3+} is nearly twice the energy gap between the $^7F_{5/2}$ and $^7F_{7/2}$ levels of Yb^{3+}, making CET the most likely process [30, 89, 211, 216–218]. Moreover, PA can not be responsible for the up-conversion emission because there is no real excited state above the $^7F_{5/2}(Yb^{3+})$ level resonant with the laser frequency and no pump power threshold was observed. Therefore, under the 980 nm laser diode excitation, the Yb^{3+} ions are excited from the ground $^7F_{7/2}$ level to the multiplets of the upper $^7F_{5/2}$ level (Figure 7.3b). Then, two simultaneously excited Yb^{3+} ions may form a virtual excited state from which energy is transferred via a cooperative process to a single

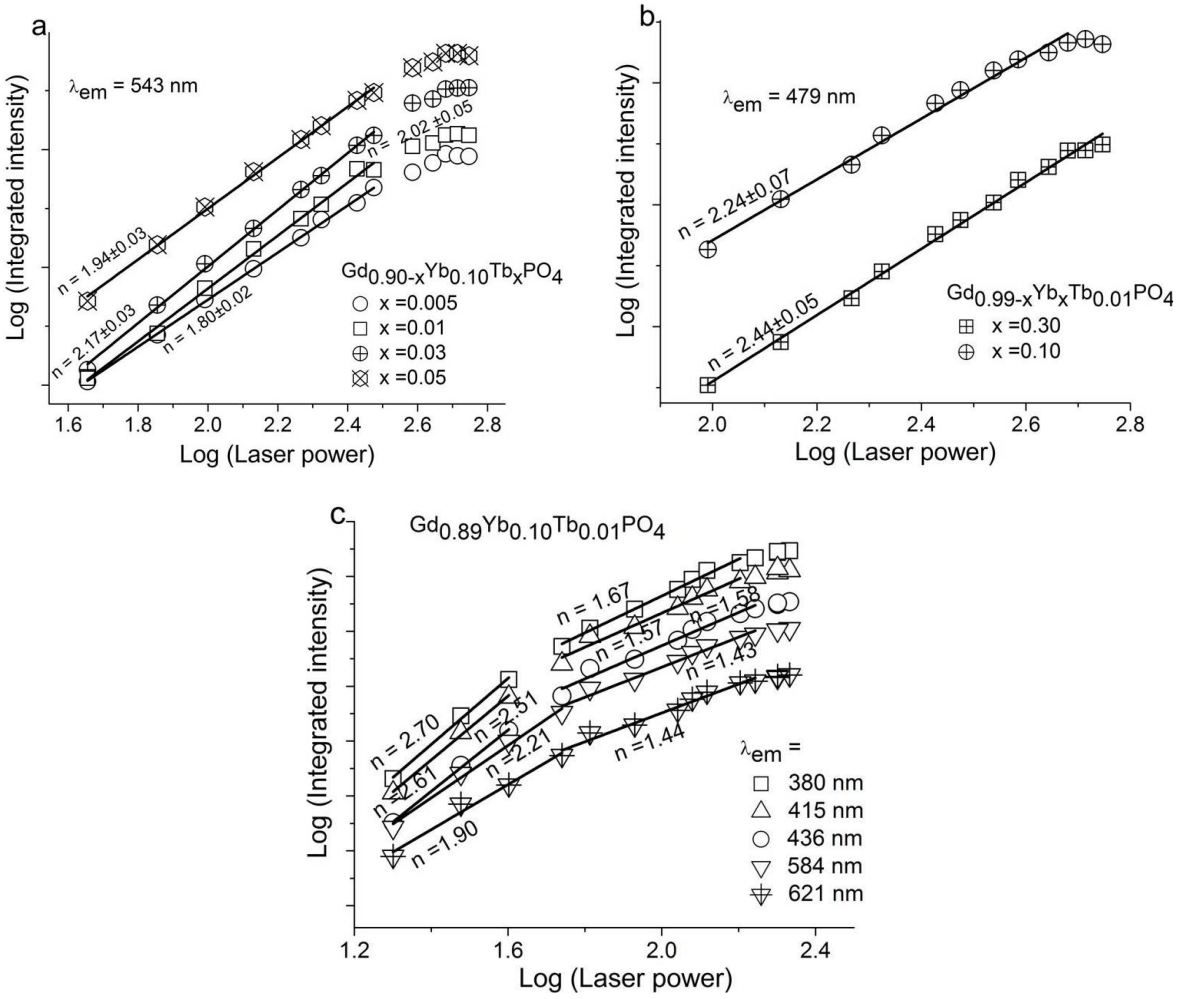

Figure 7.6: Pump power (W cm^{-1}) dependence of (Gd,Yb,Tb)PO_4 nanocrystals: a) green emission band at 543 nm for $Gd_{0.90-x}Yb_{0.10}Tb_xPO_4$, x = 0.005-0.05; b) blue co-operative up-conversion emission (CUE) band at 479 nm for $Gd_{0.89}Yb_{0.10}Tb_{0.01}PO_4$ and $Gd_{0.69}Yb_{0.30}Tb_{0.01}PO_4$; c) emission bands centered at 380, 415, 436, 584 and 621 nm for $Gd_{0.89}Yb_{0.10}Tb_{0.01}PO_4$. The solid lines denote the linear fits for the experimental data represented by the symbols.

Tb^{3+}, leading to the population of the upper $^5D_4(Tb^{3+})$ level, followed by a series of radiative up-conversion emissions at 649, 621, 584, 543 and 487 nm ascribed to the $^5D_4 \rightarrow {}^7F_{J=2-6}$ transitions [207, 216, 219, 220]. In a similar process, the energy of the virtual coupled Yb^{3+}/Yb^{3+} state may be emitted radiatively to the ground state of coupled Yb^{3+} ions (Figure 7.3b), accountable for the relatively broad blue emission at 479 nm. All these up-conversion mechanisms require two photons, in accord with the number of photons derived from the $I \approx P^n$ plots (Figure 7.6). On the other hand, the $^5D_1$ level may be further populated either *via* ESA or energy-transfer (ET) from a single excited Yb^{3+} not involved in CET (Figure 7.3b) [208, 216, 219]. Then, non-radiative inter-level relaxations from the $^5D_1$ levels to the emitting $^5D_3$ level leads to the blue-ultraviolet up-conversion emission bands at 472, 457, 436, 415 and 380 nm, ascribed to the $^5D_3 \rightarrow {}^7F_{J=2-6}$ transitions. These processes (Figure 7.3b) require three

photons and the slopes estimated from the double-log plots in the low pump power region are *ca.* 2.5 to 2.7 (Figure 7.6c), indicating that three photons involved in the ultraviolet up-conversion emission bands of Tb^{3+}.

7.7 Effect of calcination temperature

Raising the calcination temperature above 900 ^{o}C (e.g., 1200 ^{o}C) significantly enhances the up-conversion emission intensities of all samples (visible to the naked eye even at relatively low pump power). This is mainly due to the changing particle size because at low calcination temperature the nanoparticles are smaller, having a relatively high surface-to-volume ratio, with most emitting ions on the surface and subjected to non-radiative mechanisms. Consequently, no up-conversion emission was observed for the samples calcined at 300, 500 and 700 ^{o}C for 3 hours. A strong blue cooperative up-conversion emission of Yb^{3+} was observed after the samples were calcined at 900 ^{o}C and for 10 - 30 mol% Yb^{3+}/0.5 - 1.0 mol% Tb^{3+}. Therefore it should be noted that the cooperative emission is strongly dependent on the calcination temperature and concentration of Yb^{3+}/Tb^{3+}. As shown in Figure 7.7, additional transition lines that could be attributed to the cooperative emission of coupled Yb^{3+}/Yb^{3+} appeared for the sample calcined at 1200 ^{o}C, in contrast to those calcined at 900 ^{o}C. As mentioned, at

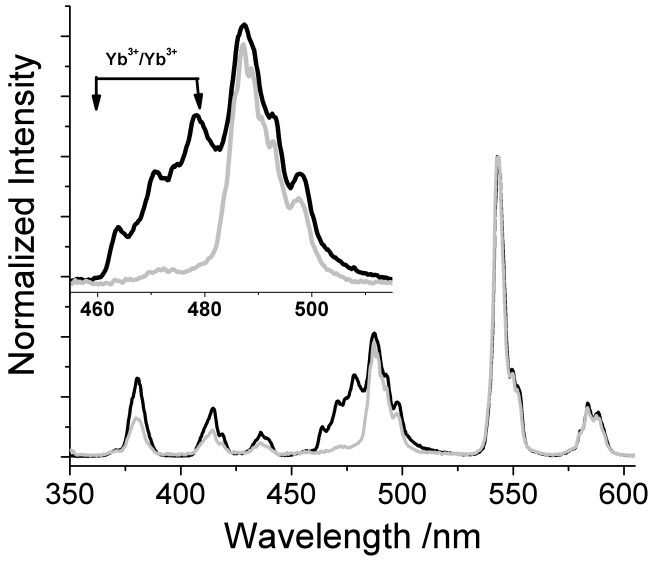

Figure 7.7: Dependence of the up-conversion emission spectra of monoclinic $Gd_{0.85}Yb_{0.10}Tb_{0.05}PO_4$ nanocrystals on the calcination temperature: at 900 ^{o}C/3 hrs (gray line) and at 1200 ^{o}C/3 hrs (black), excited with a 980 nm CW laser diode.

high calcination temperatures the particle size was increased (Figures 6.3a-c, chapter 6) which, in turn, may decrease the non-radiative channels that are strong in the smaller particles. Moreover, increasing the particle size may modify the Yb^{3+}-Yb^{3+} pair interaction and thus create favorable conditions to form a pair of excited Yb^{3+}

ions active for the cooperative emission [214, 221]. The cooperative emissions are thus more likely to be efficient in bigger particles.

7.8 Relaxation measurements

Table 7.1 shows the water ^{1}H relaxivity values (r_1 and r_2) [187, 222] and the r_2/r_1 values, measured at 20 MHz and 25 ^{0}C and 37 ^{0}C, for clear dispersions of the $GdPO_4$, $Gd_{0.85}Yb_{0.10}Tb_{0.05}PO_4$, $Gd_{0.87}Yb_{0.10}Tb_{0.03}PO_4$ and $GdPO_4$, $Gd_{0.87}Yb_{0.10}Tb_{0.03}PO_4$ @Dextran nanoparticles in water. The relaxivities were obtained from the observed linear dependence of the r_i ($r_i = 1/T_i$, $i = 1$, 2) relaxation rates on the concentration of the Gd^{3+} ions in the samples (Equation 7.1), using at least five independent measurements at concentrations between 0 and 5 mM.

Dextran-coated (Gd,Yb,Tb)PO_4 nanocrystals were prepared as follows [187]. After heat treatment of the as-synthesized hexagonal phase at 900 ^{o}C for 3 hours (Figure 6.2, chapter 6), the obtained powder of monoclinic (Gd,Yb,Tb)PO_4 nanocrystals (25 mg) was dispersed in distilled water under stirring and sonication for 20 minutes. The pH of the dispersion was adjusted to 12.5 with aqueous NaOH (1 M). Dextran (400 mg) was then dissolved in the dispersion and the solution was refluxed at 150 ^{o}C for 2 hours under magnetic stirring. Finally, excess dextran and any supernatant were discarded by five cycles of redispersion and centrifugation at 6000 rpm for 10 minutes.

Table 7.1: Water ^{1}H relaxivities, r_1, r_2, and r_2/r_1, for aqueous suspensions of $GdPO_4$ (**A**), $Gd_{0.85}Yb_{0.10}Tb_{0.05}PO_4$ (**B**), $Gd_{0.87}Yb_{0.10}Tb_{0.03}PO_4$ (**C**), and $Gd_{0.87}Yb_{0.10}Tb_{0.03}PO_4$@Dextran (**D**), compared with those reported in the literature for $GdPO_4$@dextran-K01 (**E**), SiO_2-PEG@$GdPO_4$:Eu (**F**), and $GdPO_4$ (**G**).

Materials	r_1 ($s^{-1}mM^{-1}$)		r_2 ($s^{-1}mM^{-1}$)		r_2/r_1		Ref.
	25 ^{o}C	37 ^{o}C	25 ^{o}C	37 ^{o}C	25 ^{o}C	37 ^{o}C	
A	0.21±0.01	0.27±0.01	4.54±0.01	4.34±0.01	21.6	16.0	This work[a]
B	0.29±0.01	0.29±0.01	3.34±0.05	3.49±0.01	11.5	11.8	This work[a]
C	0.25±0.05	0.24±0.01	2.98±0.01	3.20±0.01	11.9	13.6	This work[a]
D	0.14±0.01	0.24±0.01	3.09±0.01	3.20±0.01	22.2	13.6	This work[a]
E	...	13.9	...	15.0	...	1.1	[187][b]
F	1.60	...	30.60	...	19.10	...	[223][c]
G	1.68	...	48.34	...	28.77	...	[224][d]

[a]Measured at 0.47 T (20 MHz).
[b]Measured at 40 ^{o}C, 0.47 T (20 MHz).
[c]Measured at 3 T (127.7 MHz).
[d]Measured at 1.9 T (90 MHz).

The r_1 values are quite low for all samples studied, with larger r_2 values. The value of the r_2/r_1 parameter is larger than 2, indicating that the materials are effective contrast agents for T_2-weighted (negative contrast) imaging. There are significant differences relatively to the relaxivity data reported for analogous $GdPO_4$ materials (Table 7.1 [187, 223, 224], in particular to those reported by Hifumi et al. [187], which have large r_1 and r_2 values and a r_2/r_1 ratio close to one, corresponding to a dominant T_1 -weighted (positive contrast) mechanism. This is attributed to the different crystal structures of these two samples because in Ref. [187]. the relaxivity was measured for hydrated $GdPO_4$ coated with dextran and the coordination of structural water molecules to Gd^{3+} in hydrated $GdPO_4$ considerably enhances the relaxivity through inner- and outer-sphere relaxation mechanisms. We have observed that hydrated hexagonal $GdPO_4$ does not exhibit up-conversion emission unless it is calcined at 900 ^{o}C. At this temperature, however, the material transforms into an anhydrous monoclinic phase, leading to an outer-sphere relaxation mechanism. It is interesting to note that SiO_2-PEG@$GdPO_4$:Eu nanoparticles obtained by assembly of layered gadolinium hydroxide doped with Eu^{3+} ions on the surface of silica spheres and annealed at high temperatures, leading to nanosized $GdPO_4$:Eu, also have very low r_1 relaxivities and a high r_2/r_1 ratio [223]. Thus, the high temperature treatment of the particles seems to be responsible for the non-availability of water molecules in the nanoparticle capable of exchanging efficiently with the bulk water, leading to inefficient T_1-relaxation [225]. Furthermore, owning to the requirements for up-conversion, dextran coating was performed after the sample was calcined at 900 ^{o}C and may not be as effective as the coating procedures employed before [187]. The r_1 values increase slightly with increasing temperature, suggesting that the T_1-relaxation process is limited by slow-to-intermediate water exchange. The r_2 values are ten times larger than the r_1 values, indicating that the T_2-relaxation process also has a strong outer-sphere contribution from field inhomogeneities created by the magnetized particles that the water ^{1}H experience as they diffuse nearby and which increase with the square of the external magnetic field strength. As these nanocrystals showed low r_1 and high r_2 values giving r_2/r_1 values larger than 2, they may be classified as T_2-weighted imaging (negative) contrast agents.

In vitro toxicity studies have not been performed. However, no significant leaching [187] (*ca.* 1.41 μM) of Gd^{3+} from the nanoparticles has been observed in a 2 mM aqueous dispersion of the nanoparticles stored at 4 ^{o}C for a week, Figure 7.8.

7.8.1 Leaching test

Leaching of Gd^{3+} from the nanocrystals was tested following the procedures described in Refs. [187, 226]. Briefly, a buffer solution (500 mL, pH = 5.81) was prepared using acetic acid and aqueous NaOH (1 M). Xylenol orange (3.42 g) was dissolved in the buffer solution (250 mL) and the solution was then stored at a freezing temperature for one week. Furthermore, an aqueous dispersion of (Gd,Yb,Tb)PO_4 nanocrystals (10 mM) in the buffer solution was stored at 4 ^{o}C for a week. A calibration curve was built with Gd^{3+} solutions (0 - 70 μM), prepared with the buffer solution and dissolving Gd_2O_3 with nitric acid (HNO_3, 65 wt%). Soon after thawing the frozen xylenol orange

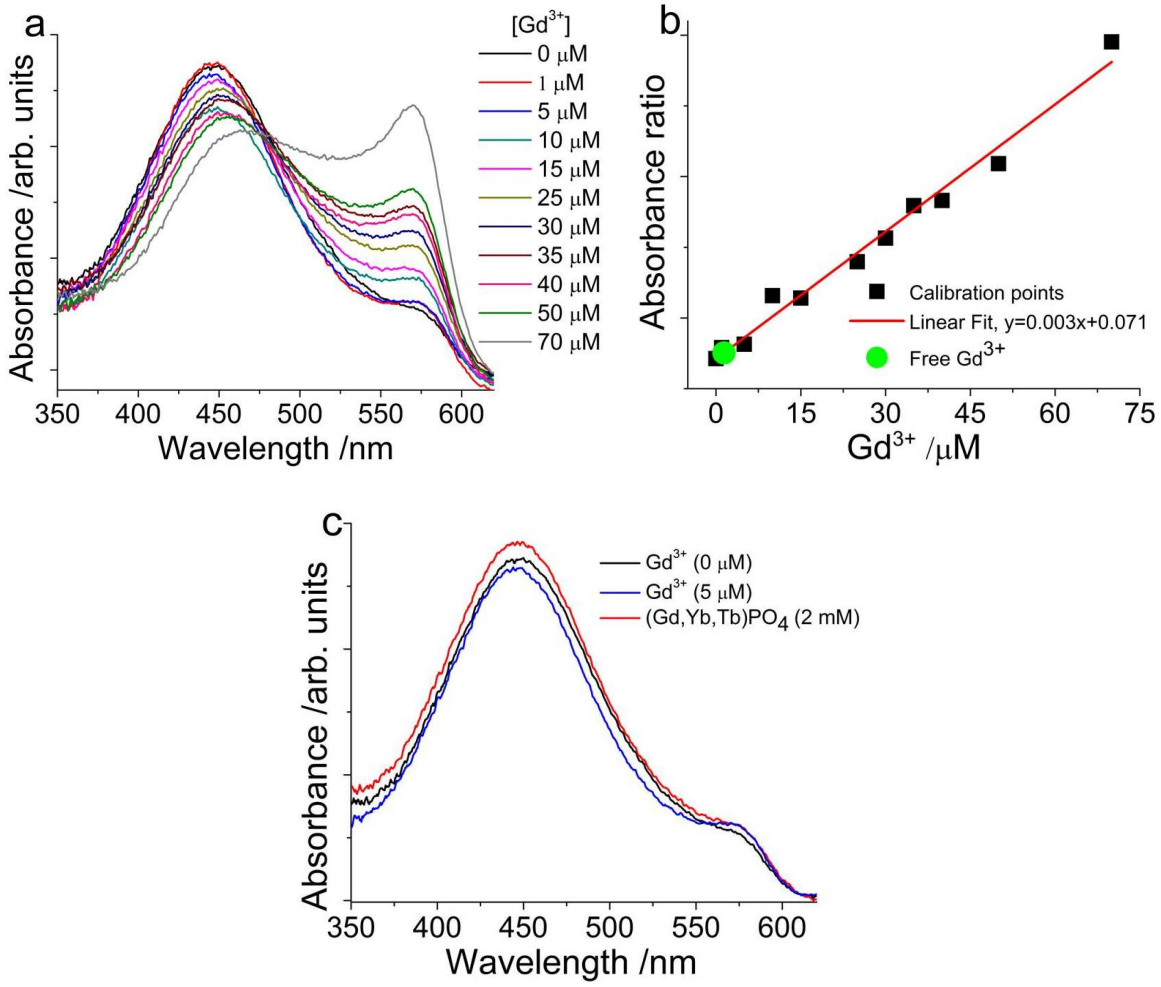

Figure 7.8: a) UV-visible absorption spectra of xylenol orange solution (18 μM) containing different amount of free Gd^{3+} (0 - 70 μM), b) the corresponding calibration curve (black squares) and the amount of free Gd^{3+} in aqueous dispersion of $Gd_{0.87}Yb_{0.10}Tb_{0.03}PO_4$ (2 mM) stored at 4 ^oC for a week (green circle) and c) comparison of UV-visible absorption spectra of xylenol orange solution (18 μM) without free Gd^{3+} (0 μM), with Gd^{3+} (5 μM) and with $Gd_{0.87}Yb_{0.10}Tb_{0.03}PO_4$ (2 mM).

solution, UV-visible absorption spectra were collected for a series of solutions, each containing mixture of xylenol orange (1.5 mL, pH = 5.81, 18 μM,) and Gd^{3+} (0.15 mL, pH = 5.81, 0 - 70 μM) solutions. The calibration curve was determined from the plot of the Gd^{3+} concentration *vs.* the ratio between the integrated intensity of the absorption bands at 573 and 433 nm, Figure 7.8. Finally, the absorption spectrum of a solution containing xylenol orange solution (1.5 mL, pH = 5.81, 18 μM,) and dispersion of (Gd,Yb,Tb)PO_4 nanocrystals (0.15 mL, pH = 5.81, 2 mM,) was measured under the same experimental conditions used for the calibration curve data and the amount of free Gd^{3+} was then readily estimated from the curve (Figure 7.8).

7.9 Summary and conclusion

In this chapter, the up-conversion emission and relaxivity properties of (Gd,Yb,Tb)PO_4 nanocrystals were investigated and their application for bimodal imaging was evaluated. $GdPO_4$ was shown to be an excellent host for the tunable Yb^{3+}/Tb^{3+} up-conversion emission in which Yb^{3+} acts as sensitizer for the UV-visible up-conversion emission of Tb^{3+}, and a strong blue light emitter *via* the Yb^{3+}-Yb^{3+} cooperative luminescence. The relaxivity data indicate that the studied nanocrystals are quite efficient as T_2-weighted (negative) contrast imaging agents as they have high r_2/r_1 values. The use of infrared light excitation for visible light emission coupled with the relaxivity properties affords the material's potential as bimodal contrast agents. These materials are of great interest in biomedicine and nanophotonics.

Chapter 8

Conclusions and Outlook

Advance in novel Ln^{3+}-based functional luminescent nanomaterials for numerous applications such as in biomedicine and optics largely relies on the better understanding and tuning of the Ln^{3+} optical properties as well as on the rational design of material synthesis. In this context, Ln^{3+}-doped oxide and phosphate nanoparticles, namely, $(Gd,Eu)_2O_3$ and $(Gd,Yb,Er)_2O_3$ nanorods, and $(Gd,Yb,Tb)PO_4$ nanocrystals were synthesized and their photoluminescence properties (emission and excitation spectra, excited-sate lifetimes, energy-transfer process among many others) and applications (e.g., smart coatings, temperature sensing, and bimodal imaging) were explored in my four year PhD project. Since summary and conclusion were briefly presented at the end of each chapter, the present chapter shall focus on the concluding remarks and feasible outlook based on the results obtained.

In chapter 3, energy transfer between C_2 and S_6 sites of Eu^{3+} in cubic $(Gd,Eu)_2O_3$ nanorods has been investigated and the contribution of the inter-site energy-transfer mechanisms to the $^5D_0(C_2)$ rise time is ruled out, being the direct $^5D_1(C_2)$ to $^5D_0(C_2)$ relaxation (inter-level energy transfer) the only responsible path for the rise time effect. Furthermore, the longer $^5D_0(C_2)$ decay time observed for the nanorods (relatively to decay time for the bulk counterparts) in air is mainly due to the small filling factor of the nanorods and the change in the effective-refractive index of the milieu surrounding the Eu^{3+} ions. It has been shown that $(Gd,Eu)_2O_3$ nanorods have potential applications for photoactive smart coatings based on polymeric matrices *via* UV-curing process as presented in chapter 4.

The work presented in chapter 5 is a recent breakthrough in the development of a single nanoplatform integrating heaters (gold nanoparticle) and thermometers ($(Gd,Yb,Er)_2O_3$ nanorods) and measuring a wide range of temperatures up to 2000 K. In general, the use of the relative emission intensity between two closely-spaced Ln^{3+} energy states as a temperature-sensitive parameter, known as fluorescence intensity ratio (FIR) or ratiometric method, is a rapidly emerging strategy for non-contact, self-referenced, accurate and non-invasive optical measurement of temperature at the nanoscale. This approach is particularly suited for precise control of tissue temperature in local hyperthermia, the treatment of cancer with heat. In the field of thermo-plasmonics there is also an increasing demand to measure and regulate the surface-temperature of metal nanoparticles for applications in biomedicine and the FIR method is shown to be very promising.

Chapter 6 was devoted to the down-shifting photoluminescence properties of mono-

clinic (Gd,Yb,Tb)PO_4 nanocrystals while their potentials for bimodal imaging applications (luminescence and magnetic resonance) were evaluated in chapter 7. The next step is therefore to push the border towards designing multifunctional nanoprobes integrating several functionalities (heat generation, temperature sensing, light emission and magnetic resonance relaxivity), using metal nanoparticles (Au, Ag, and Cu) and different Ln^{3+} hosting materials such as fluorides, oxides and phosphates. This thesis may open up the following exciting topics for further investigations including (i) developing multiplexing nanocomposites based on Ln^{3+}-host and metal nanoparticles fulfilling current and future demands in biomedical applications, e.g., combining heat generation and self-referenced temperature sensing for *in vitro/in vivo* controlled local hyperthermia as well as for bioimaging; (ii) understanding the photophysical properties of the nanocomposites; and (iii) investigating the heating mechanisms in these systems. Items (i) and (ii) have not yet been addressed in detail in Aveiro or elsewhere [227]. Similarly, (iii) one is not fully understood and the first heat-transfer measurements at atomic-scale junctions (e.g., Au-Au junction) was demonstrated only very recently [228]. The following general strategies may be employed towards addressing the above objectives.

- Prepare size- and shape-controlled metal (Au, Ag, and Cu) nanostructures including spherical nanoparticles and nanorods in order to optimize their plasmonic properties. In parallel, size- and shape-controlled Ln^{3+}-oxide (fluoride or phosphate) nanoparticles (Ln^{3+} = Eu^{3+}, Tm^{3+}, Er^{3+}, Pr^{3+}, Nd^{3+}, Yb^{3+}/Er^{3+}, Yb^{3+}/Tm^{3+}, Yb^{3+}/Er^{3+},Tm^{3+}) will be prepared for efficient down-shifting and/or up-conversion emissions *via* tuning the Ln^{3+} concentration, the nanoparticle size / shape and the surface coatings. The synthesis methods include wet-chemical and/or hydrothermal routes. The prepared metal nanostructures will be subsequently anchored at the oxide nanocrystals surface to produce metal-oxide nanocomposite. The challenge here is to obtain the individually optimized photophysical properties in the nanocomposite or to improve them in the final materials of interest. This procedure may include the rational surface modifications of the oxide nanoparticles, e.g., with suitable polyelectrolytes that will serve as spacers covalently linked to the metal and oxide particles, silica coating, and core-shell prepartion. Alternatively, the metal nanoparticles will be grown *in situ* on the surface of pre-made oxide nanoparticles. In general, the final metal-oxide nanocomposites must fulfill the following requirements: efficient heat generation and Ln^{3+} up-conversion emission under low-power laser excitation in biological and aqueous media as well as good MR relaxivity properties. The desired contrast agent in the composites can be obtained by incorporating paramagnetic Ln^{3+} ions, e.g., Gd^{3+}, during the synthesis. Either T_1-weighted (positive) or T_2-weighted (negative) imaging will be measured depending on the values of the ratio r_2/r_1.

- Study the photoluminescence properties of the prepared metal-oxide nanocomposites with other complementary characterization techniques such as TEM, UV-Vis-NIR absorption, PXRD and FTIR. In particular, characterize the absorption, emission and excitation spectra; analyze the Ln^{3+} emission responses to the changes made on shape, size and concentration of metal nanoparticles; identify key responsive parameters combining optimal Ln^{3+} emission, temperature sensing

and magnetic resonance properties. Furthermore, the mechanism of efficient heat generation has been elusive in different host materials supporting metal nanoparticles (e.g., Au and Ag) under non-resonance laser excitation (with respect to the localized surface plasmon resonance band) and in chapter 5 we have pointed out that this issue deserves further investigation. The melting temperature of the metal nanostructures may be determined using the Ln^{3+} emissions; no precedent to this approach has been reported. In addition, the Ln^{3+} up-conversion emission may be boosted by incorporating transition metals such Mo, Mn and Fe into the nanocomposite as recently observed in Ln^{3+}-doped $NaYF_4$ materials [229, 230]. However, little is known about the mechanism responsible for the increased efficiency of the Ln^{3+} emission and hence there is much to explore in this aspect as well. Here, a challenge also exists in controlling and understanding the crystal growth of the host matrix when substituting a Ln^{3+} with ions of bigger/smaller radii. From future point of view on the supply of Ln elements, it is also important to note that using less expensive transition metals should be an alternative approach. Another objective under this target is to evaluate the MR relaxivity properties of the composites for MRI contrast agent applications.

- Fabricate a multimodal bioprobe. The bioprobe will display heat generation for hyperthermia, Ln^{3+} emissions for temperature sensing and optical and MR imaging. In the current clinical trials of local hyperthermia therapy, precise control of temperature in the tumor site and the surrounding healthy tissue is challenging as the temperature is mainly controlled by the conventional methods, for instance, by placing thermocouples or fiber optical thermometers into the tumor. A novel approach is required to overcome this challenge. Hence, combination of metal nanostructures known for plasmonic-induced efficient heat generation and ratiometric temperature sensors based on the Ln^{3+} emission is an ideal alternative, integrating heaters and thermometers in a single probe. This probe may be selectively administered to a tumor cell and excited with infrared light. Upon excitation, the metal particles generate heat (40 - 45 ^{o}C) enough to kill the tumor cell while the Ln^{3+} emission is used to monitor the local temperature, thereby permitting the control of the temperature of the surrounding healthy tissues. In this regard, it is promising to develop optical nanocontraception methods based on hyperthermia. For instance, Li et al. [231] recently demonstrated male contraception using gold nanorods injected into the testes of mice and excited with infrared laser at 808 nm, resulting in short-lived and permanent male infertility as the temperature raised up to 45 ^{o}C. As was mentioned, Ln-oxide/metal nanocomposites also offer exceptional opportunities to exploit the Ln^{3+} luminescence and MR properties for bimodal imaging purposes. Here, it is important to note that infrared light irradiation (the so-called biological window) has deeper tissue penetration depth than UV-visible light excitation, providing efficient excitation of the nanoprobe located deep in biological media without significant attenuation of the original excitation energy. This enables high-resolution deep-tissue optical imaging while avoiding also cell damage and the background fluorescence observed under UV-visible excitation. The rational design of nanomaterials combining metal and Ln^{3+}-doped oxide nanostructures will thus allow the simultaneous assessment of multifunctional properties from a

single probe.

Appendices

Appendix A

Characterization Techniques

A.1 UV-Vis-NIR Absorption

Light beam is attenuated after passing through a material. The intensity of the incident I_o light beam and the thickness x traveled by the beam through the material are given by Lambert-Beer law:

$$I = I_o exp(-\alpha(\nu)x) \tag{A.1}$$

where $\alpha(\nu)$ is the absorption coefficient of the material at frequency ν of the light beam, assuming negligible scattering. The absorption cross-section $\sigma(\nu)$ and the number density N of absorbing species are related to $\alpha(\nu)$ by $\int \alpha(\nu)d\nu = \sigma N$. Furthermore, it can be shown that $\alpha(\nu)$ is related to the oscillator strength of the optical transition [43,44].

Absorption spectra for aqueous suspensions of powder samples were recorded at room-temperature using a Lambda 950 UV-Vis-NIR spectrophotometer (PerkinElmer) with a 150 mm diameter Spectralon integrating sphere and a Jasco V-560 UV-VIS spectrophotometer. Quartz cells (10 mm optical path length) were used.

A.2 Absolute emission quantum yields

The absolute-emission quantum yields were measured at room temperature using a quantum yield measurement system C9920-02 from Hamamatsu with a 150 W Xenon lamp coupled to a monochromator for wavelength discrimination, an integrating sphere as sample chamber and a multi channel analyzer for signal detection. Three measurements were made for each sample and their average value is reported. The method is accurate to within 10%.

A.3 Powder X-ray diffraction

Powder X-ray diffraction patterns were collected on a Philips X'Pert MPD Powder X-ray diffractometer (CuK_α radiation at 1.5406 Å) in the 2θ range between 5 - 50^o, step scan modes 0.02 - 0.04^o and acquisition time 50 - 60 s per step.

The average size of the nanocrystals was estimated from the Scherrer equation [232]:

$$D = \frac{K\lambda}{B\cos\theta} \tag{A.2}$$

where D is the size of the nanocrystal, K the Scherrer constant (for spherical crystal $K = 0.94$), λ the X-ray wavelength, B the full-width-at-half-maximum of the diffraction peak (in radian), θ the diffraction angle.

A.4 Electron microscopy

The morphology of the samples was analyzed on a Hitachi SU-70 scanning electron microscopy (SEM), a Hitachi H-9000 transmission electron microscopy (TEM) operated at 300 kV and/or a Jeol JEM-2200FS TEM operated at 200 kV. Powder of nanoparticles were well dispersed in ethanol or distilled water under sonication and carbon film or holey carbon film on 300 square mesh copper grids were immersed in the dispersion of the nanoparticles (or a drop of the dispersion was put on the grids). The grids were then dried in air.

A.5 Elemental analysis

The relative percentage of the Ln^{3+} in the materials was determined by inductively coupled plasma optical emission spectroscopy (ICP-OES-Activa-M, Horiba Jobin Yvon). Powder sample (*ca.* 30 mg) was well dissolved in HNO_3 (2 mL, 65 wt%) to prepare 100 mL of aqueous solution containing the Ln^{3+}. ICP-OES analysis was then made on a fraction of the solution.

A.6 Fourier transform infrared spectroscopy

Fourier transformation infrared (FTIR) spectra were recorded in the range of 400-4000 cm^{-1} on a Mattison 7000 FTIR Spectrometer. A powder of nanocrystals was mixed with potassium bromide (KBr) and pressed into thin transparent pellet with a hydraulic press for the infrared spectra measurements.

A.7 Relaxometry

^{1}H longitudinal and transverse relaxation times (T_1 and T_2 respectively) of aqueous suspensions of nanoparticles were measured at 20 MHz (B0 = 0.47 T) on a Bruker Minispec mq20 relaxometer, at 25 and 37 ^{o}C. T_1 values were measured using the inversion recovery pulse sequence and T_2 values with the Carr-Purcell-Meiboom-Gill pulse sequence. The time interval between two consecutive refocusing pulses (τCP) in the

train of 180^o pulses applied was 1.6 ms. All the experimental values were corrected for the diamagnetic contributions using Milli-Q water under the same conditions.

A.8 Zeta potential

Zeta potential was measured using a Zetasizer Nano ZS instrument (Malvern). Powder samples were well dispersed in water or ethanol under sonication for the measurements.

Appendix B

TEM Images, Emission Spectra, and Calculated Temperature: NRs-AuNPs

B.1 TEM images

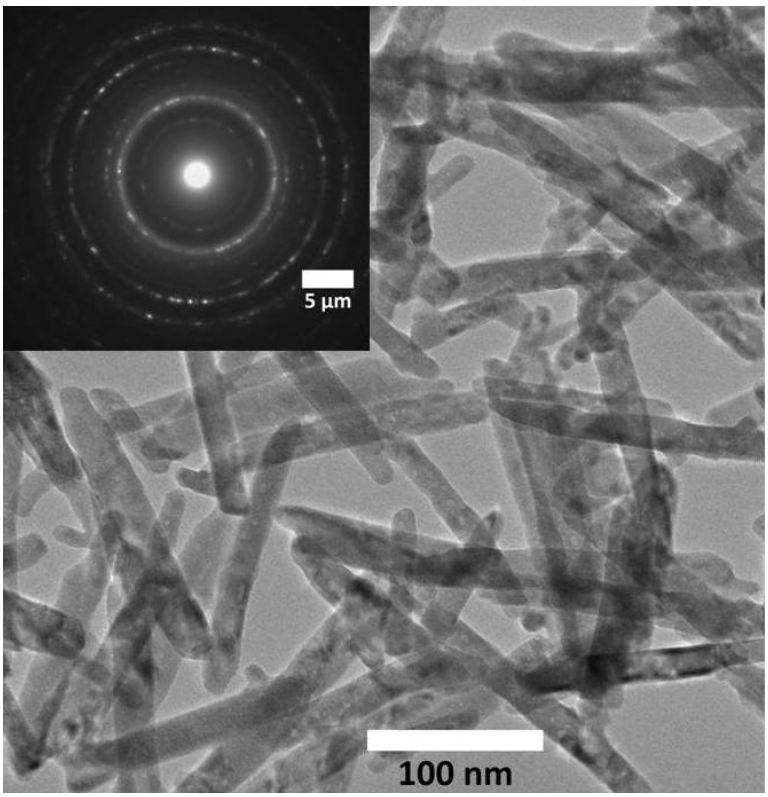

Figure B.1: TEM image of bare $(Gd,Yb,Er)_2O_3$ nanorods synthesized *via* wet-chemical route; the inset is the electron diffraction pattern of the nanorods.

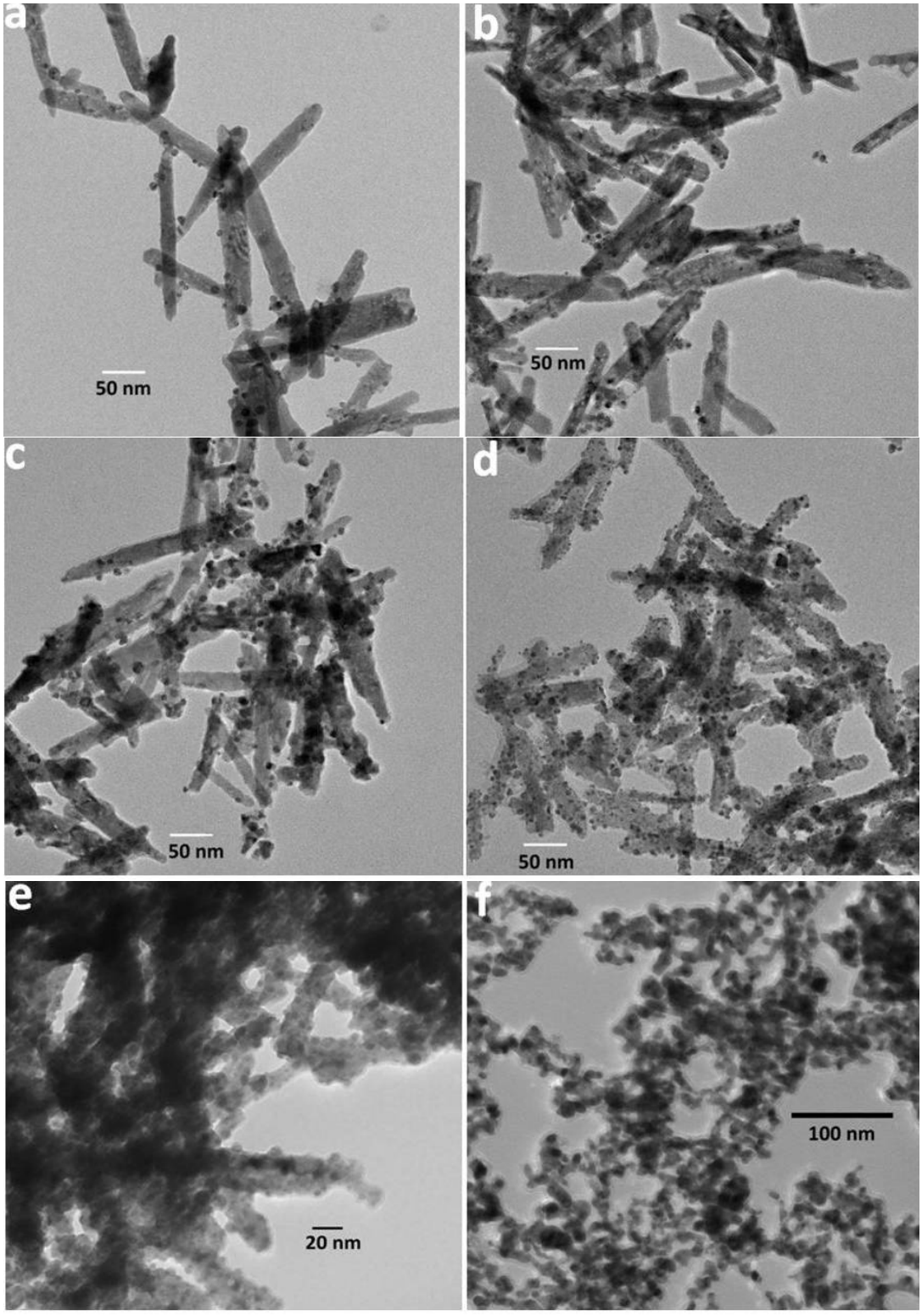

Figure B.2: TEM images of $(Gd,Yb,Er)_2O_3$ NRs-AuNPs-C: a) C = 1.25, b) 2.5, c) 12.5, d) 25.0, e) 37.5 and f) 250.0.

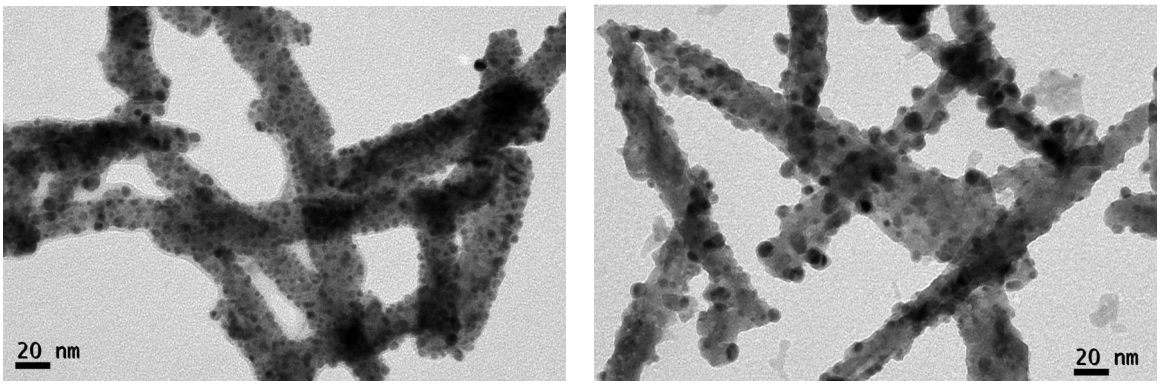

Figure B.3: TEM images of $(Gd,Eu)_2O_3$ NRs-AuNPs (left) and $(Gd,Yb,Tm)_2O_3$ NRs-AuNPs (right), prepared *via* the *in situ* reduction procedure.

B.2 Emission spectra and calculated temperature

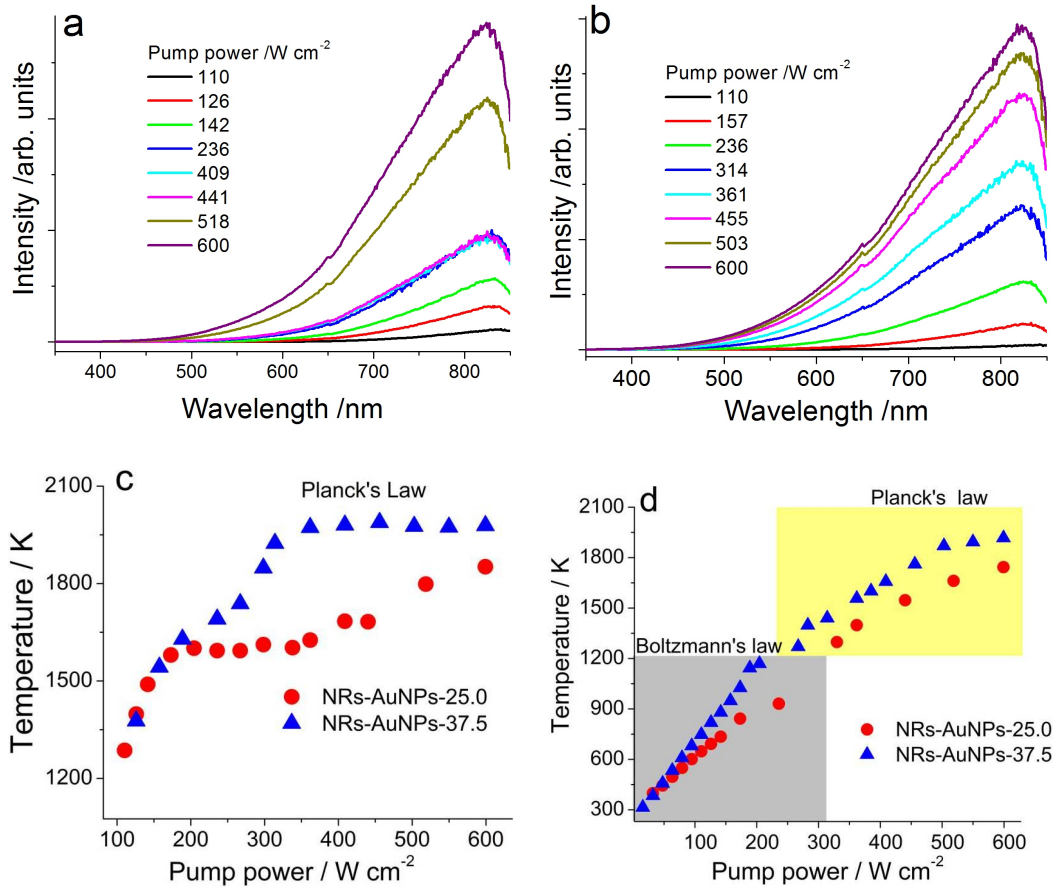

Figure B.4: Emission spectra of $(Gd,Yb,Er)_2O_3$ NRs-AuNPs-C in the first cycle irradiation under a 980 nm CW laser diode (a) C = 25.0 and (b) C = 37.5. Calculated local temperature *vs.* pump power in the first cycle irradiation (c) C = 25.0 and in the second cycle irradiation (d) C = 37.5.

Appendix C

Synthesis of Spherical Gold Nanoparticles (AuNPs)

Citrate stabilized spherical AuNPs were synthesized using the standard Turkevich method [233]. Briefly, aqueous solution of $HAuCl_4$ (1.935 mL, 0.1292 M) was mixed with Milli-Q water (500 mL) in a 1000-mL-flask. The mixture was heated to boiling under magnetic stirring. Then, warm Milli-Q water (50 mL) containing 1 wt% trisodium citrate dehydrate was rapidly poured into the boiling $HAuCl_4$ solution under strong magnetic stirring. After few minutes, the transparent solution changed into deep red and was allowed to boil for additional 20 minutes. TEM images revealed that the prepared AuNPs are spherical and visible-NIR absorption spectrum of the citrate stabilized AuNPs in water showed that the localized surface plasmon resonance (LSPR) band is centered at 519 nm and the average diameter of the nanoparticles is *ca.* 15 nm, Figure C.1.

C.1 Pre-made AuNPs supported on NRs

The measured zeta potential (surface charge) of the calcined NRs dispersed in Milli-Q water at pH ∼7 was +32.5 mV, Figure C.2. For better attachment of the pre-made AuNPs, the NRs were first coated with a negatively charged polyelectrolyte and then with a positively charged polyelectrolyte as follows [234]:

- NRs powder (15 mg) was dispersed in Milli-Q water (5 mL) and, then, aqueous solution of NaCl (50 mL, 0.5 M) containing a negative polyelectrolyte, (poly(styrenesulfonate)-PSS, 1 mg/mL) was added to the NR dispersion under sonication and the solution was allowed for 20 minutes for the adsorption of the PSS onto the NRs. The non-adsorbed PSS was removed by 3 cycles of centrifugation at 7000 rpm for 7 minutes. The zeta potential of the $(Gd_{0.95}Yb_{0.03}Er_{0.02})_2O_3$NRs@PSS dispersion in water was -15.7 mV.

- PSS modified NRs were dispersed in Milli-Q water (2 mL). Then, NaCl aqueous solution (50 mL, 0.5 M) containing a positively charged polyelectrolyte, (poly(allylamine hydrochloride)-PAH, 1mg/mL), was added to that dispersion under sonication. Excess PAH was removed by three cycles of centrifugation and redispersion. The zeta potential of $(Gd_{0.95}Yb_{0.03}Er_{0.02})_2O_3$NRs@PSS@PAH dispersed in water was +51.0 mV.

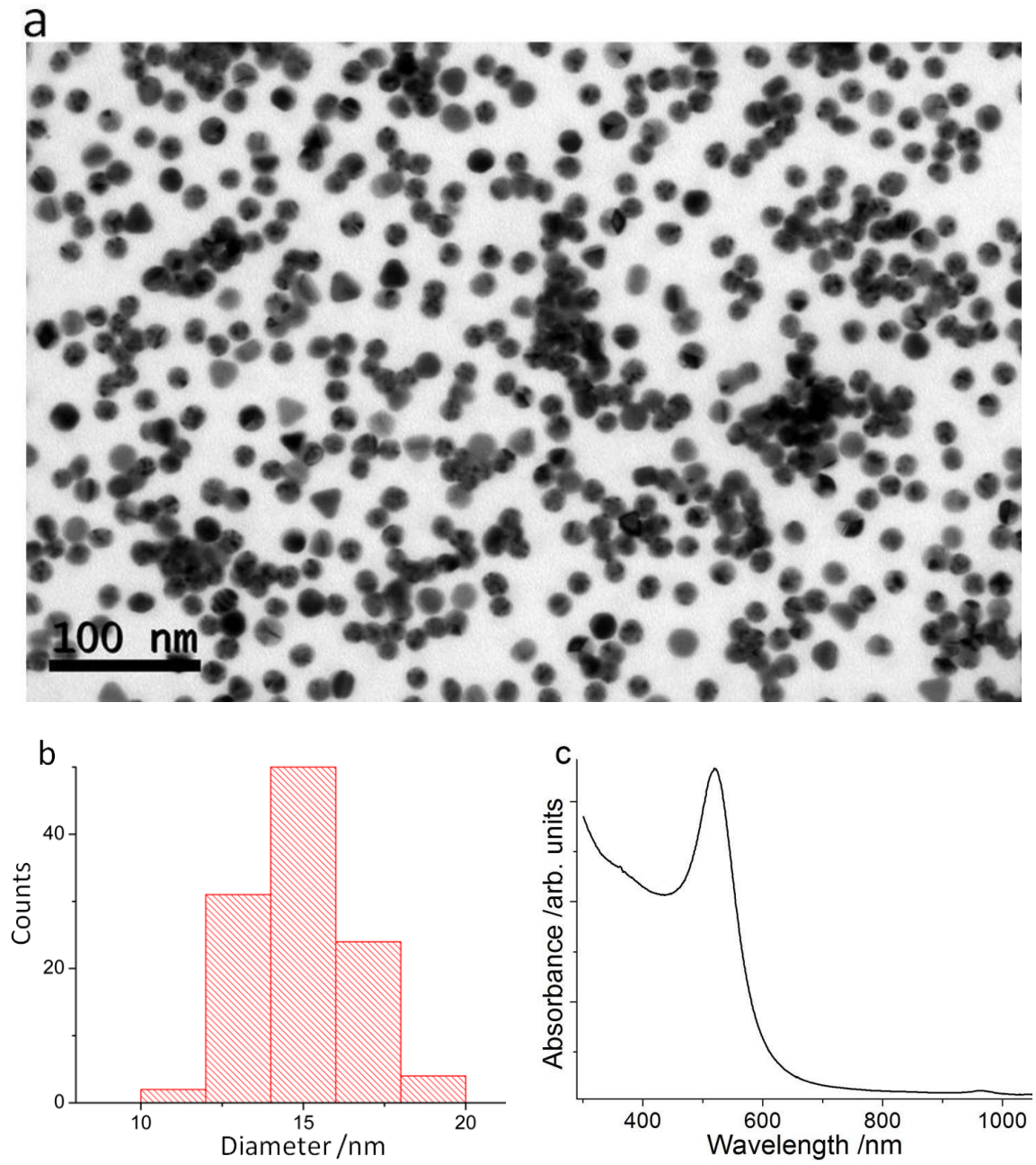

Figure C.1: a) TEM image, b) size distribution and c) absorption spectrum of citrate stabilized spherical AuNPs.

- $(Gd_{0.95}Yb_{0.03}Er_{0.02})_2O_3$NRs@PSS@PAH (6 mg) was dispersed in water and citrate stabilized AuNPs (10 mL, 0.5 mM) was added to the dispersion dropwise under sonication and shaking. The AuNPs were allowed for adsorption onto the modified surface of NRs for 10 minutes. The non-adsorbed AuNPs were removed by centrifugation at 7000 rpm for 10 minutes. This process was repeated 3 times, affording $(Gd_{0.95}Yb_{0.03}Er_{0.02})_2O_3$NRs@PSS@PAH@AuNPs, Figure C.3. Powder samples were obtained after drying the later at 60 ^{o}C.

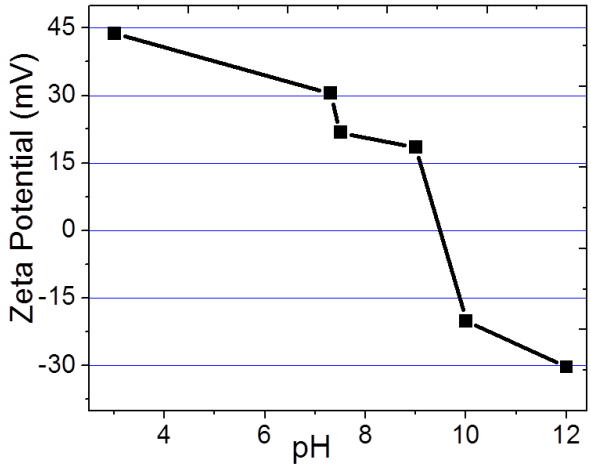

Figure C.2: pH *vs.* zeta potential for $(Gd,Eu)_2O_3$ NRs dispersed in Milli-Q water.

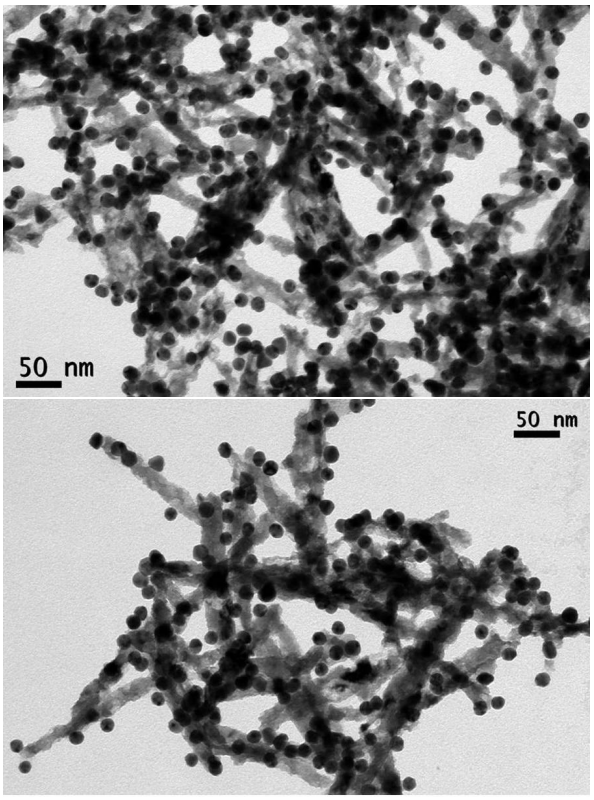

Figure C.3: TEM images of pre-made AuNPs supported on the NRs: $(Gd,Eu)_2O_3$ NRs@PSS@PAH-AuNPs (top) and $(Gd,Yb,Er)_2O_3$ NRs@PSS@PAH@AuNPs (bottom).

Appendix D

Blackbody Radiation

A heated object emits electromagnetic radiation when it has a temperature above absolute zero. We might have experience of observing light from red-hot and white-hot objects such as an element on an electric stove, a glowing metal and a lava flow. Incandescent electric lamps in which electrical current flowing through a thin filament of tungsten metal heats it until it glows white-hot are indeed the most common sources of light. Emission of light from these sources is caused by temperature or heat, a marked difference from luminescence which can be caused by any form of mechanisms other than heating as discussed in chapter 2.

A good absorber of an incident irradiation is also a good emitter. However, an object that perfectly absorbs and emits electromagnetic energy does not exist in nature. An idealized physical body that absorbs all incident electromagnetic radiation, regardless of frequency or angle of incidence is called a blackbody. A blackbody radiation (also known as thermal radiation) is the emission of electromagnetic radiation by such a blackbody in thermal equilibrium (at a constant temperature) and the radiation depends solely on the temperature of the body. In order to better understand this concept, consider a blackbody radiation in a cavity heated to temperature T. The radiated energy can be considered to be produced by standing waves known as cavity modes and thus any electromagnetic wave inside the cavity must vanish at the walls of the cavity. Rayleigh and Jeans showed that the number of modes $n(\nu)$ per unit frequency per unit volume in such a cavity is given by [44, 49]:

$$n(\nu) = \frac{8\pi\nu^2}{c^3} = \frac{8\pi}{\lambda^4} \tag{D.1}$$

where ν are λ are the frequency and wavelength of the mode, respectively; c is the speed of light.

According to Rayleigh and Jeans, the probability of occupying any given mode is equal for all modes and each mode continually emits or absorbs radiation with an average energy of kT. Using Equation D.1, the blackbody radiation energy density $\rho(\nu)$ as a function of temperature is:

$$\rho(\nu) = \frac{8\pi\nu^2}{c^3} kT \tag{D.2}$$

This law, formulated by Rayleigh and Jeans, is invalid at higher frequencies, resulting in the so-called UV catastrophe. In 1990, however, this problem was resolved when Max Planck announced his famous law, Planck's law of blackbody radiation. Instead of the classical approach, Planck assumed that each mode of the radiation field can only emit

or absorb energy in discrete (quantized) units of hv and the Bose-Einstein distribution predicts that the average energy per mode to be the energy of the mode times the probability of that mode being occupied, i.e., $h\nu/(exp(\frac{h\nu}{kT}) - 1)$. From Equation D.2, Planck's law of blackbody radiation that precisely predicts the intensity radiated at any given frequency (wavelength) for any given temperature is therefore given by:

$$\rho(\nu, T) = \frac{8\pi h\nu^3}{c^3} \frac{1}{(exp(\frac{h\nu}{kT}) - 1)} \tag{D.3}$$

Alternatively, the spectral radiance I is given by:

$$I(\lambda, T) = \frac{2\pi hc}{\lambda^5} \frac{1}{(exp(\frac{h\nu}{kT}) - 1)} \tag{D.4}$$

It can be noted from Planck's law that the spectrum of a blackbody radiation is determined by the temperature alone not by the body's shape or composition. In other words, the blackbody radiation from different bodies at a given temperature shows the same spectral shape. Radiation from the sun (T = 6000 K) and from a tungsten filament lamp (T = 2800 K) are good examples of real body radiations with spectral distributions close to that of blackbody distribution.

The total energy flux P_{total} (W m^{-2}) integrated over a blackbody spectrum gives the Stefan-Boltzmann law:

$$P_{total} = \sigma T^4 \tag{D.5}$$

where $\sigma = 5.67\times10^{-8}$ W m^{-2} K^{-4} is the Stefan-Boltzmann constant and T is the temperature in Kelvin. The blackbody radiation from a physical body can be characterized by its emissivity, ϵ, which corresponds to the fraction of the ideal blackbody spectrum energy that a real body actually emits ($\epsilon = 1$ in the ideal case). Therefore, for real body, the Stefan-Boltzmann law is modified by:

$$P_{total} = \epsilon\sigma T^4 \tag{D.6}$$

Applications: A blackbody radiator is used to define color temperature of a light source, i.e., the color temperature of a light source is given by the absolute temperature of an ideal blackbody radiator that has the same color or hue as that of the light source.

Furthermore, the fact that every object above absolute zero emits blackbody radiation may find various practical applications. For example, the human body at a temperature of about 312 K emits a large amount of infrared radiation centered about a wavelength of 10 μm [49]. This has enabled to design a non-contact thermometer that precisely measures the body temperature using the IR radiation emitted from the eardrum inside the ear which may represents the body's core temperature and then calculating the body temperature from the radiation. Similarly, passive infrared detectors, that are commercially available for security purposes, e.g., in residential and commercial places, use the blackbody emission from people/objects to detect their presence/motion.

Appendix E

Color and Color Coordinates

The human eye in the retina has light sensitive photoreceptors known as cones and rods. The spectral region (380 - 780 nm) of light in which the eye is sensitive is called visible light. However, the sensitivity of the eye within this spectral region varies with the wavelength of light. As a result, the response of the eye to visible light is commonly described by tristimulus values based on the three types of color-sensitive cones of the eye, corresponding roughly to the red, green, and blue sensitive detectors. The red, green and blue colors constitute the three primary colors of an additive mixture color model where a color can be specified with a mixing ratio of two of the three primary colors. Therefore, the human eye can, in principle, perceive colors of different wavelengths. The spectral response efficiency of the eye, however, varies with individuals depending on, for instance, environmental and physiological conditions and thus the same color may be differently perceived. In addition, due to the distribution of cones in the eye, the tristimulus values depend on the observer's field of view. To avoid the effects of such parameters and to represent an average human's chromatic response, the CIE (Commission Internationale de l'Eclairage) standard observer was first established in 1931 based on a 2° field of view. The CIE defined a set of three color-matching functions denoted by $\overline{x}(\lambda)$, $\overline{y}(\lambda)$, and $\overline{z}(\lambda)$, over the entire visible range as shown in Figure E.1; where λ is the wavelength in nm. Accordingly, the CIE tristimulus values X, Y, and Z for a color with a spectral power distribution $I(\lambda)$ are given by:

$$\begin{aligned} X &= \int_{380}^{780} I(\lambda)\overline{x}(\lambda)d\lambda \\ Y &= \int_{380}^{780} I(\lambda)\overline{y}(\lambda)d\lambda \\ Z &= \int_{380}^{780} I(\lambda)\overline{z}(\lambda)d\lambda \end{aligned} \tag{E.1}$$

The chromaticity coordinates x and y of the CIE 1931 color system are calculated from the following relations:

$$\begin{aligned} x &= \frac{X}{X+Y+Z} \\ y &= \frac{Y}{X+Y+Z} \\ z &= \frac{Z}{X+Y+Z} \end{aligned} \tag{E.2}$$

These CIE chromaticity coordinates correspond to the mixing ratio of the primary colors and only the two coordinates x and y are sufficient to represent the mapping of

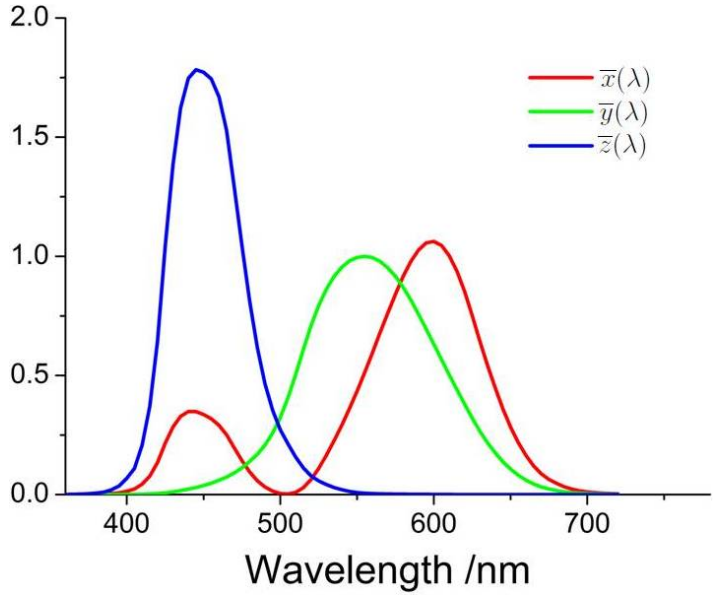

Figure E.1: The CIE (1931) 2° standard observer color-matching functions.

any color in a chromaticity diagram. In other words, the mixture ratio of the three primary colors can be determined by any two of the three coordinates since the sum of the them gives 1, i.e., x + y + z = 1. The center of the diagram color point is called an achromatic point (1/3,1/3). Therefore, the CIE 1931 color system specifies any color of the light source in terms of the two chromaticity coordinates (x, y) and a brightness parameter Y.

It is important to note that the 2° standard observer discussed above is suitable for fields smaller than 4°. In 1964, the CIE also defined an additional standard observer based on a 10° field of view; this is referred to as the 10° Supplementary Standard Observer suitable for a larger circular field of view greater than 4°. Furthermore, to improve the specification accuracy of the CIE 1931 color system, other systems such as the CIE UCS 1960 (Uniform Chromaticity Scale) and the CIE ULCS 1976 (Uniform Lightness Chromaticness Scale) were introduced. These systems are indeed modified color systems in which their chromaticity coordinates can be derived from the CIE 1931 color coordinates. For instance, the CIE UCS 1960 chromaticity coordinates u and v are given in terms of the CIE 1931 coordinates as:

$$\begin{aligned} u &= \frac{4x}{-2x + 12y + 3} \\ v &= \frac{4y}{-2x + 12y + 3} \end{aligned} \tag{E.3}$$

Alternatively, u and v can also be obtained from X, Y and Z of the CIE 1931 color system using the relations:

$$\begin{aligned} u &= \frac{4X}{X + 15Y + 3Z} \\ v &= \frac{6Y}{X + 15Y + 3Z} \end{aligned} \tag{E.4}$$

In 1976, the CIE introduced new coordinates u' and v' as an improvement to the UCS system. These coordinates can be obtained from the relations:

$$\begin{aligned} u' &= u \\ v' &= 1.5v \end{aligned} \tag{E.5}$$

Bibliography

[1] `http://www.iupac.org/fileadmin/user_upload/news/IUPAC_Periodic_Table-1Jun12.pdf`. [Online; accessed in December 2012].

[2] Brian M. Walsh. Judd-Ofelt theory: principles and practices. In Di Bartolo Baldassare and Forte Ottavio, editors, *Advances in Spectroscopy for Lasers and Sensing*. Springer Netherlands, 2006.

[3] V. S. Sastri, J.-C. G. Bunzli, V. R. Rao, G. V. S. Rayudu, and J. R. Perumareddi. *Modern Aspects of Rare Earths and Their Complexes*. Elsevier B.V, The Netherlands, 2003.

[4] A. J. Freeman and R. E. Watson. Theoretical Investigation of Some Magnetic and Spectroscopic Properties of Rare-Earth Ions. *Phys. Rev.*, 127(1):2058–2075, 1962.

[5] Igor I. Sobelman, editor. *Atomic Spectra and Radiative Transitions*. Springer-Verlag, 1992.

[6] B. W. Wybourne. *Spectroscopic Properties of Rare Earths*. John Wiley Sons, Inc, New York, 1965.

[7] J.-C. G.. Bünzli and S. Eliseeva. *Basics of Lanthanide Photophysics, in Lanthanide Luminescence:Photophysical, Analytical and Biological Aspects*. Springer, Verlag Berlin Heidelberg, 2011.

[8] K. Ogasawara, S. Watanabe, H. Toyoshima, and M. G. Brik. *First-Principles Calculations of $4f^N \rightarrow 4f^{N-1}5d$ Transition Spectra,in Handbook on the Physics and Chemistry of Rare Earths*, volume 37. Elsevier B.V, North-Holland, 2007.

[9] O. L. Malta and Luís D. Carlos. Intensities of $4f - 4f$ transitions in glass materials. *Quím. Nova*, 26:889–895, 2003.

[10] M. Fox. *Optical Properties of Soilids*. Oxford University Press, New York, 2001.

[11] K. Binnemans and C. Gorller-Walrand. Application of the Eu^{3+} Ion for Site Symmetry Determination. *J. Rare Earth*, 14(3):173–180, 1996.

[12] Qiang Ju, Yongsheng Liu, Renfu Li, Liqin Liu, Wenqin Luo, and Xueyuan Chen. Optical Spectroscopy of Eu^{3+}-Doped BaFCl Nanocrystals. *J. Phys. Chem. C*, 113(6):2309–2315, 2009.

[13] S. Hüfner. *Optical Spectra of Transparent Rare Earth Compounds*. Academic Press, Inc, New York, 1978.

[14] Guokui Liu and Xueyuan Chen. Spectroscopic properties of lanthanides in nanomaterials. In K. A. Gschneidner Jr., J.-C. G. Bünzli, and V. K. Pecharsky, editors, *Handbook on the Physics and Chemistry of Rare Earths*. Elsevier B.V., 2007.

[15] G. W. Burdick and M. F. Reid. $4f^n$-$4f^{n-1}5d$ Transitions. In K. A. Gschneidner Jr., J.-C. G. Bünzli, and V. K. Pecharsky, editors, *Handbook on the Physics and Chemistry of Rare Earths*. Elsevier B.V., 2007.

[16] L. Smentek and B. W. Wybourne. *Optical Spectroscopy of Lanthanides: Magnetic and Hyperfine Interactions*. CRC Press, Boca Raton, Florida, 2007.

[17] D. R. Bates. *Atomic and Molecular Processe*. Academic Press, New York, 1962.

[18] P. Dorenbos. The $4f^n \leftrightarrow 4f^{n-1}5d$ transitions of the trivalent lanthanides in halogenides and chalcogenides. *J. Lumin.*, 91(1-2):91–106, 2000.

[19] R. T. Wegh and A. Meijerink. Spin-allowed and spin-forbidden $4f^n \leftrightarrow 4f^{n-1}5d$ transitions for heavy lanthanides in fluoride hosts. *Phys. Rev. B*, 60:10820–10830, 1999.

[20] R. T. Wegh, H. Donker, and A. Meijerink. Spin-allowed and spin-forbidden fd emission from Er^{3+} and $LiYF_4$. *Phys. Rev. B*, 57:2025–2028, 1998.

[21] P. Dorenbos. Lanthanide charge transfer energies and related luminescence, charge carrier trapping, and redox phenomena. *J. Allo. Comp.*, 488(2):568–573, 2009.

[22] L van Pieterson and A Meijerink. Charge transfer luminescence of Yb^{3+} in orthophosphates. *J. Allo. Comp.*, 300-301(0):426 – 429, 2000.

[23] W. M. Faustino, O. L. Malta, and G. F. de Sa. Intramolecular energy transfer through charge transfer state in lanthanide compounds: A theoretical approach. *J. Chem. Phys.*, 122(5):054109, 2005.

[24] Andreas H. Krumpel, Philippe Boutinaud, Erik van der Kolk, and Pieter Dorenbos. Charge transfer transitions in the transition metal oxides ABO_4:Ln^{3+} and APO_4:Ln^{3+} (A=La, Gd, Y, Lu, Sc; B=V, Nb, Ta; Ln=lanthanide). *J. Lumin.*, 130(8):1357–1365, 2010.

[25] S. Comby and J.-C.G. Bünzli. *Lanthanide Near-Infrared Luminescence in Molecular Probes and Devices, in Handbook on the Physics and Chemistry of Rare Earths*. Elsevier B.V., North-Holland, 2007.

[26] L. Pidol, B. Viana, A. Galtayries, and P. Dorenbos. Energy levels of lanthanide ions in a $Lu_2Si_2O_7$ host. *Phys. Rev. B*, 72:125110, 2005.

[27] P. Dorenbos. Systematic behaviour in trivalent lanthanide charge transfer energies. *J. Phys.: Condens. Matter*, 15(49):8417, 2003.

[28] C. W. Struck and W. H. Fonger. Role of the charge-transfer states in feeding and thermally emptying the ^5D states of Eu^{3+} in yttrium and lanthanum oxysulfides. *J. Lumin.*, 1-2(0):456–469, 1970.

[29] T. Igarashi, M. Ihara, T. Kusunoki, K. Ohno, T. Isobe, and M. Senna. Relationship between optical properties and crystallinity of nanometer Y_2O_3:Eu phosphor. *Appl. Phys. Lett.*, 76(12):1549–1551, 2000.

[30] François Auzel. Upconversion and Anti-Stokes Processes with f and d Ions in Solids. *Chem. Rev.*, 104(1):139–174, 2004.

[31] O. L. Malta. Mechanisms of non-radiative energy transfer involving lanthanide ions revisited. *J. Non-Cryst. Solids*, 354(42-44):4770–4776, 2008.

[32] G. Blasse and B. C. Grabmaier. *Luminescent Materials.* Springer Berlin Heidelberg, 1994.

[33] T. Förster. *Intermolecular energy migration and fluorescence, in Biological Physics.* American Institute of Physics, New York, 1993.

[34] T. Förster. Zwischenmolekulare Energiewanderung und Fluoreszenz. *Ann. Phys.*, 437(1-2):55–75, 1948.

[35] D. L. Dexter. A Theory of Sensitized Luminescence in Solids. *J. Chem. Phys.*, 21(5):836–850, 1953.

[36] D. L. Dexter and James H. Schulman. Theory of Concentration Quenching in Inorganic Phosphors. *J. Chem. Phys.*, 22(6):1063–1070, 1954.

[37] R. M. Clegg. *Förster resonance energy transfer-FRET what is it, why do it, and how it's done, in Laboratory Techniques in Biochemistry and Molecular Biology.* Elsevier, Academic Press,Burlington, 2009.

[38] P. Vergeer, T. J. H. Vlugt, M. H. F. Kox, M. I. den Hertog, J. P. J. M. van der Eerden, and A. Meijerink. Quantum cutting by cooperative energy transfer in $Yb_xY_{1-x}PO_4$:Tb^{3+}. *Phys. Rev. B*, 71:014119, 2005.

[39] Bing Han, Hongbin Liang, Yan Huang, Ye Tao, and Qiang Su. Vacuum Ultraviolet-Visible Spectroscopic Properties of Tb^{3+} in Li(Y,Gd)$(PO_3)_4$: Tunable Emission, Quantum Cutting, and Energy Transfer. *J. Phys. Chem. C*, 114(14):6770–6777, 2010.

[40] M. F. Joubert. Photon avalanche upconversion in rare earth laser materials. *Opt. Mater.*, 11(2-3):181–203, 1999.

[41] M. F. Joubert, S. Guy, and B. Jacquier. Model of the photon-avalanche effect. *Phys. Rev. B*, 48:10031–10037, 1993.

[42] B. Henderson. *Optical Spectroscopy of Inorganic Solids.* Oxford University Press, 1989.

[43] D. R Vij, editor. *Luminescence of solids.* Plenum Press, New York, 1998.

[44] J. García Solé, L. E. Bausá, and D. Jaque. *An Introduction to the Optical Spectroscopy of Inorganic Solids.* John Wiley and Sons Ltd, West Sussex, England, 2005.

[45] D. Lumb Michael, editor. *Luminescence spectroscopy.* Academic Press, 1978.

[46] T. D. S. Hamilton, I. H. Munro, and G. Walker. Luminescence Instrumentation. In D. Lumb Michael, editor, *Luminescence spectroscopy.* Academic Press, 1978.

[47] M. Yen William, Shionoya Shigeo, and Yamamoto Hajime. *Measurements of Phosphor Properties.* CRC Press, Taylor and Francis Group, LLC, Boca Raton, FL, 2007.

[48] `http://www.hamamatsu.com/us/en/index.html?&glossary_id=13186819`. [Online; accessed in November 2012].

[49] Mark Csele. *Fundamentals of light sources and lasers.* John Wiley and Sons, Inc., Hoboken, New Jersey, 2004.

[50] Christopher Palmer. *Diffraction Grating Handbook.* Richardson Grating Laboratory, Thermo RGL, New York, 2005.

[51] `http://www.horiba.com/scientific/products/optics-tutorial/diffraction-gratings/`. [Online; accessed in Juanuary 2013].

[52] `http://www.genlabsystems.com/jarrell_ash/gratings.html`. [Online; accessed in November 2013].

[53] `http://learn.hamamatsu.com/articles/photomultipliers.html`. [Online; accessed in Fabruary 2013].

[54] `http://www.sales.hamamatsu.com/assets/applications/ETD/pmt_handbook/pmt_handbook_applications.pdf`. [Online; accessed in Fabruary 2013].

[55] *FL3-2 Triax 320 Installation, Horiba Jobin Yvon*. University of Aveiro, 2004.

[56] Nishioka Takuya, Fukui Kôichi, and Matsumoto Kazuko. *Lanthanide chelates as luminescent labels in biomedical analyses; in Handbook on the Physics and Chemistry of Rare Earths*. Elsevier B.V., North-Holland, 2007.

[57] Andreia G. Macedo. *Lanthanide Oxide Nanotubes and Nanorods: Synthesis, Processing, Luminescence and Catalytic Properties*. PhD Dissertation, University of Aveiro, 2010.

[58] Andreia G. Macedo, Rute A. S. Ferreira, Duarte Ananias, Mário S. Reis, Vitor S. Amaral, Luís D. Carlos, and João Rocha. Effects of Phonon Confinement on Anomalous Thermalization, Energy Transfer, and Upconversion in Ln^{3+}-Doped Gd_2O_3 Nanotubes. *Adv. Funct. Mater.*, 20(4):624–634, 2010.

[59] Liqin Liu, En Ma, Renfu Li, Guokui Liu, and Xueyuan Chen. Effects of phonon confinement on the luminescence dynamics of Eu^{3+} in Gd_2O_3 nanotubes. *Nanotechnology*, 18(1):015403, 2007.

[60] M. Buijs, A. Meyerink, and G. Blasse. Energy transfer between Eu^{3+} ions in a lattice with two different crystallographic sites: Y_2O_3:Eu^{3+}, Gd_2O_3:Eu^{3+} and Eu_2O_3. *J. Lumin.*, 37(1):9–20, 1987.

[61] Liqin Liu, En Ma, Renfu Li, and Xueyuan Chen. Preparation, Characterization and Spectroscopy of Eu^{3+} in Gd_2O_3 Nanorods. *J. Nanosci. Nanotechnol.*, 8(3):1398–1403, 2008.

[62] W. O. Gordon, J. A. Carter, and B. M. Tissue. Long-lifetime luminescence of lanthanide-doped gadolinium oxide nanoparticles for immunoassays. *J. Lumin.*, 108(1-4):339–342, 2004.

[63] Liqin Liu and Xueyuan Chen. Energy levels, fluorescence lifetime and Judd-ofelt parameters of Eu^{3+} in Gd_2O_3 nanocrystals. *Nanotechnology*, 18(25):255704, 2007.

[64] A. M. Pires, M. F. Santos, M. R. Davolos, and E. B. Stucchi. The effect of Eu^{3+} ion doping concentration in Gd_2O_3 fine spherical particles. *J. Alloys Compd.*, 344(1-2):276 – 279, 2002.

[65] Yanhong Li and Guangyan Hong. Synthesis and luminescence properties of nanocrystalline Gd_2O_3:Eu^{3+} by combustion process. *J. Lumin.*, 124(2):297–301, 2007.

[66] Guang Jia, Kai Liu, Yuhua Zheng, Yanhua Song, Mei Yang, and Hongpeng You. Highly Uniform $Gd(OH)_3$ and Gd_2O_3:Eu^{3+} Nanotubes: Facile Synthesis and Luminescence Properties. *J. Phys. Chem. C*, 113(15):6050–6055, 2009.

[67] Jihun Choi, Teng-Kuan Tseng, Mark Davidson, and Paul H. Holloway. Enhanced photoluminescence from Gd_2O_3:Eu^{3+} nanocores with a Y_2O_3 thin shell. *J. Mater. Chem.*, 21(9):3113–3118, 2011.

[68] Matvei Zinkevich. Thermodynamics of rare earth sesquioxides. *Prog. Mater. Sci.*, 52(4):597–647, 2007.

[69] Gin-ya Adachi and Nobuhito Imanaka. The Binary Rare Earth Oxides. *Chem. Rev.*, 98(4):1479–1514, 1998.

[70] F. X. Zhang, M. Lang, J. W. Wang, U. Becker, and R. C. Ewing. Structural phase transitions of cubic Gd_2O_3 at high pressures. *Phys. Rev. B*, 78:064114, 2008.

[71] Henry R. Hoekstra and Karl A. Gingerich. High-Pressure B-Type Polymorphs of Some Rare-Earth Sesquioxides. *Science*, 146(3648):1163–1164, 1964.

[72] C. R. Stanek, K. J. McClellan, B. P. Uberuaga, K. E. Sickafus, M. R. Levy, and R. W. Grimes. Determining the site preference of trivalent dopants in bixbyite sesquioxides by atomic-scale simulations. *Phys. Rev. B*, 75:134101, 2007.

[73] N. Hirosaki, S. Ogata, and C. Kocer. Ab initio calculation of the crystal structure of the lanthanide Ln_2O_3 sesquioxides. *J. Allo. Comp.*, 351(1-2):31–34, 2003.

[74] Mikaela Nichkova, Dosi Dosev, Shirley J. Gee, Bruce D. Hammock, and Ian M. Kennedy. Microarray Immunoassay for Phenoxybenzoic Acid Using Polymer Encapsulated Eu:Gd_2O_3 Nanoparticles as Fluorescent Labels. *Anal. Chem.*, 77(21):6864–6873, 2005.

[75] Mikaela Nichkova, Dosi Dosev, Richard Perron, ShirleyJ. Gee, BruceD. Hammock, and Ian M. Kennedy. Eu^{3+}-doped Gd_2O_3 nanoparticles as reporters for optical detection and visualization of antibodies patterned by microcontact printing. *Anal. Bioanal. Chem.*, 384(3):631–637, 2006.

[76] Gautom Kumar Das, Boon Chin Heng, Sui-Choon Ng, Tim White, Joachim Say Chye Loo, Loyola D'Silva, Parasuraman Padmanabhan, Kishore K. Bhakoo, Subramanian Tamil Selvan, and Timothy Thatt Yang Tan. Gadolinium Oxide Ultranarrow Nanorods as Multimodal Contrast Agents for Optical and Magnetic Resonance Imaging. *Langmuir*, 26(11):8959–8965, 2010.

[77] Eva Hemmer, Hiroyuki Takeshita, Tomoyoshi Yamano, Takanori Fujiki, Yvonne Kohl, Karin Löw, Nallusamy Venkatachalam, Hiroshi Hyodo, Hidehiro Kishimoto, and Kohei Soga. In vitro and in vivo investigations of upconversion and NIR emitting Gd_2O_3:Yb^{3+}, Er^{3+} nanostructures for biomedical applications. *J. Mater. Sci.: Mater. Med.*, 23(10):2399–2412, 2012.

[78] Eva Hemmer, Tomoyoshi Yamano, Hidehiro Kishimoto, Nallusamy Venkatachalam, Hiroshi Hyodo, and Kohei Soga. Cytotoxic aspects of gadolinium oxide nanostructures for up-conversion and NIR bioimaging. *Acta Biomaterialia*, 9(1):4734–4743, 2013.

[79] Zhen Liu, Fang Pu, Sa Huang, Qinghai Yuan, Jinsong Ren, and Xiaogang Qu. Long-circulating Gd_2O_3:Yb^{3+},Er^{3+} up-conversion nanoprobes as high-performance contrast agents for multi-modality imaging. *Biomaterials*, 34(6):1712–1721, 2013.

[80] Liangjun Zhou, Zhanjun Gu, Xiaoxiao Liu, Wenyan Yin, Gan Tian, Liang Yan, Shan Jin, Wenlu Ren, Gengmei Xing, Wei Li, Xueling Chang, Zhongbo Hu, and Yuliang Zhao. Size-tunable synthesis of lanthanide-doped Gd_2O_3 nanoparticles and their applications for optical and magnetic resonance imaging. *J. Mater. Chem.*, 22:966–974, 2012.

[81] J. Heber, K. H. Hellwege, U. Köbler, and H. Murmann. Energy levels and interaction between Eu^{3+}-ions at lattice sites of symmetry C_2 and symmetry C_{3i} in Y_2O_3. *Zeitschrift für Physik*, 237(3):189–204, 1970.

[82] R. M. Ranson, E. Evangelou, and C. B. Thomas. Modeling the fluorescent lifetime of Y_2O_3:Eu. *Appl. Phys. Lett.*, 72(21):2663–2664, 1998.

[83] Xue Bai, Hongwei Song, Lixin Yu, Linmei Yang, Zhongxin Liu, Guohui Pan, Shaozhe Lu, Xingguang Ren, Yanqiang Lei, and Libo Fan. Luminescent Properties of Pure Cubic Phase Y_2O_3/Eu^{3+} Nanotubes/Nanowires Prepared by a Hydrothermal Method. *J. Phys. Chem. B.*

[84] M. D. Chambers and D. R. Clarke. Doped Oxides for High-Temperature Luminescence and Lifetime Thermometry. *Annu. Rev. Mater. Res.*, 39(1):325–359, 2009.

[85] M. Buijs and G. Blasse. Energy migration in a two-dimensional Eu^{3+} compound: $EuMgAl_{11}O_{19}$. *J. Sol. Stat. Chem.*, 71(2):296–304, 1987.

[86] Jun Yang, Chunxia Li, Ziyong Cheng, Xiaoming Zhang, Zewei Quan, Cuimiao Zhang, and Jun Lin. Size-Tailored Synthesis and Luminescent Properties of One-Dimensional Gd_2O_3:Eu^{3+} Nanorods and Microrods. *J. Phys. Chem. C*, 111(49):18148–18154, 2007.

[87] Bipin Bihari, Hergen Eilers, and Brian M. Tissue. Spectra and dynamics of monoclinic Eu_2O_3 and Eu^{3+}:Y_2O_3 nanocrystals. *J. Lumin.*, 75(1):1–10, 1997.

[88] L. A. Riseberg and H. W. Moos. Multiphonon Orbit-Lattice Relaxation of Excited States of Rare-Earth Ions in Crystals. *Phys. Rev.*, 174:429–438, 1968.

[89] Toru Miyakawa and D. L. Dexter. Phonon Sidebands, Multiphonon Relaxation of Excited States, and Phonon-Assisted Energy Transfer between Ions in Solids. *Phys. Rev. B*, 1:2961–2969, 1970.

[90] E. Zych. Concentration dependence of energy transfer between Eu^{3+} ions occupying two symmetry sites in Lu_2O_3. *J. Phys.: Condens. Matter*, 14(22):5637, 2002.

[91] R. B. Hunt and R. G. Pappalardo. Fast excited-state relaxation of Eu-Eu pairs in commercial Y_2O_3:Eu^{3+} phosphors. *J. Lumin.*, 34(3):133–146, 1985.

[92] R. S. Meltzer, S. P. Feofilov, B. Tissue, and H. B. Yuan. Dependence of fluorescence lifetimes of Y_2O_3:Eu^{3+} nanoparticles on the surrounding medium. *Phys. Rev. B*, 60:R14012–R14015, 1999.

[93] Hannes Schniepp and Vahid Sandoghdar. Spontaneous Emission of Europium Ions Embedded in Dielectric Nanospheres. *Phys. Rev. Lett.*, 89:257403, 2002.

[94] Ksenia Dolgaleva, Robert W. Boyd, and Peter W. Milonni. Influence of local-field effects on the radiative lifetime of liquid suspensions of Nd:YAG nanoparticles. *J. Opt. Soc. Am. B*, 24(3):516–521, 2007.

[95] Sander F. Wuister, Celso de Mello Donega, and Andries Meijerink. Local-field effects on the spontaneous emission rate of CdTe and CdSe quantum dots in dielectric media. *J. Chem. Phys.*, 121(9):4310–4315, 2004.

[96] R. S. Meltzer, W. M. Yen, Hairong Zheng, S. P. Feofilov, M. J. Dejneka, B. Tissue, and H. B. Yuan. Effect of the matrix on the radiative lifetimes of rare earth doped nanoparticles embedded in matrices. *J. Lumin.*, 94-95(0):217–220, 2001.

[97] Titipun Thongtem, Anukorn Phuruangrat, Dong Jin Ham, Jae Sung Lee, and Somchai Thongtem. Controlled Gd_2O_3 nanorods and nanotubes by the annealing of $Gd(OH)_3$ nanorod and nanotube precursors and self-templates produced by a microwave-assisted hydrothermal process. *CrystEngComm*, 12:2962–2966, 2010.

[98] Asit B. Panda, Garry Glaspell, and M. Samy El-Shall. Microwave Synthesis and Optical Properties of Uniform Nanorods and Nanoplates of Rare Earth Oxides. *J. Phys. Chem. C*, 111(5):1861–1864, 2007.

[99] O. Gallot-lavalléea, G. Teyssedre, C. Laurent, and S. Rowe. Identification of photoluminescence features of an epoxy resin based on components features and curing effects. *Polymer*, 46(8):2722–2731, 2005.

[100] P. Dorenbos. The Eu^{3+} charge transfer energy and the relation with the band gap of compounds. *J. Lumin.*, 111(1-2):89–104, 2005.

[101] Manon P. Oude Wolbers, Frank C. J. M. van Veggel, Bianca H. M. Snellink-Ruël, Johannes W. Hofstraat, Frank A. J. Geurts, and David N. Reinhoudt. Novel Preorganized Hemispherands To Encapsulate Rare Earth Ions: Shielding and Ligand Deuteration for Prolonged Lifetimes of Excited Eu^{3+} Ions. *J. Am. Chem. Soc.*, 119(1):138–144, 1997.

[102] Carlos D. S. Brites, Patricia P. Lima, Nuno J. O. Silva, Angel Millán, Vitor S. Amaral, Fernando Palacio, and Luís D. Carlos. A Luminescent Molecular Thermometer for Long-Term Absolute Temperature Measurements at the Nanoscale. *Adv. Mater.*, 22(40):4499–4504, 2010.

[103] Jon S. Donner, Sebastian A. Thompson, Mark P. Kreuzer, Guillaume Baffou, and Romain Quidant. Mapping Intracellular Temperature Using Green Fluorescent Protein. *Nano Lett.*, 12(4):2107–2111, 2012.

[104] Oktay Yarimaga, Sumi Lee, Dae-Young Ham, Ji-Min Choi, Soon Gyu Kwon, Maesoon Im, Sungho Kim, Jong-Man Kim, and Yang-Kyu Choi. Thermofluorescent Conjugated Polymer Sensors for Nano- and Microscale Temperature Monitoring. *Macromol. Chem. Phys.*, 212(12):1211–1220, 2011.

[105] Carlos D. S. Brites. *Self-Referencing Thermometry in the Nanoscale*. PhD Dissertation, University of Aveiro, 2012.

[106] Carlos D. S. Brites, Patricia P. Lima, Nuno J. O. Silva, Angel Millan, Vitor S. Amaral, Fernando Palacio, and Luis D. Carlos. Thermometry at the nanoscale. *Nanoscale*, 4(16):4799–4829, 2012.

[107] Lorenz H. Fischer, Gregory S. Harms, and Otto S. Wolfbeis. Upconverting Nanoparticles for Nanoscale Thermometry. *Angew. Chem. Int. Ed.*, 50(20):4546–4551, 2011.

[108] Daniel Jaque and Fiorenzo Vetrone. Luminescence nanothermometry. *Nanoscale*, 4:4301–4326, 2012.

[109] Zachary J. Coppens, Wei Li, D. Greg Walker, and Jason G. Valentine. Probing and Controlling Photothermal Heat Generation in Plasmonic Nanostructures. *Nano Lett.*, 13(3):1023–1028, 2013.

[110] Fiorenzo Vetrone, Rafik Naccache, Alicia Zamarrón, Angeles Juarranz de la Fuente, Francisco Sanz-Rodríguez, Laura Martinez Maestro, Emma Martãn Rodriguez, Daniel Jaque, José García Solé, and John A. Capobianco. Temperature Sensing Using Fluorescent Nanothermometers. *ACS Nano*, 4(6):3254–3258, 2010.

[111] Hideo Kusama, Ojars J. Sovers, and Taisuke Yoshioka. Line Shift Method for Phosphor Temperature Measurements. *Jpn. J. Appl. Phys.*, 15(12):2349–2358, 1976.

[112] Sunil Kumar Singh, Kaushal Kumar, and S. B. Rai. Er^{3+}/Yb^{3+} codoped Gd_2O_3 nanophosphor for optical thermometry. *Sensor Actuat. A-Phys.*, 149(1):16–20, 2009.

[113] Harry A. Atwater and Albert Polman. Plasmonics for improved photovoltaic devices. *Nat. Mater.*, 9(3):1476–1122, 2010.

[114] Alexander O. Govorov and Hugh H. Richardson. Generating heat with metal nanoparticles. *Nano Today*, 2(1):30–38, 2007.

[115] Guillaume Baffou and Romain Quidant. Thermo-plasmonics: using metallic nanostructures as nano-sources of heat. *Laser Photonics Rev.*, 7(2):171–187, 2013.

[116] Yue Bing Zheng, Brian Kiraly, Paul S. Weiss, and Tony Jun Huang. Molecular plasmonics for biology and nanomedicine. *Nanomedicine*, 7(5):751–770, 2012.

[117] Z. Qin and J. C. Bischof. Thermophysical and biological responses of gold nanoparticle laser heating. *Chem. Soc. Rev.*, 41(3):1191–1217, 2012.

[118] Huang-Chiao Huang, Kaushal Rege, and Jeffrey J. Heys. Spatiotemporal Temperature Distribution and Cancer Cell Death in Response to Extracellular Hyperthermia Induced by Gold Nanorods. *ACS Nano*, 4(5):2892–2900, 2010.

[119] Michael T. Carlson, Andrew J. Green, and Hugh H. Richardson. Superheating Water by CW Excitation of Gold Nanodots. *Nano Lett.*, 12(3):1534–1537, 2012.

[120] M. Maestro Laura, Haro Patricia, M.C. Iglesias-de la Cruz, Sanz-Rodríguez Francisco, Juarranz Ángeles, García Solé José, and Jaque Daniel. Fluorescent Nano-thermometers provide controlled Plasmonic Mediated Intracellular Hyperthermia. *Nanomedicine*, 8(3):379–388, 2012.

[121] Michael T. Carlson, Aurangzeb Khan, and Hugh H. Richardson. Local Temperature Determination of Optically Excited Nanoparticles and Nanodots. *Nano Lett.*, 11(3):1061–1069, 2011.

[122] Michael T. Carlson, Andrew J. Green, Aurangzeb Khan, and Hugh H. Richardson. Optical Measurement of Thermal Conductivity and Absorption Cross-Section of Gold Nanowires. *J. Phys. Chem. C*, 116(15):8798–8803, 2012.

[123] Kenji Setoura, Daniel Werner, and Shuichi Hashimoto. Optical Scattering Spectral Thermometry and Refractometry of a Single Gold Nanoparticle under CW Laser Excitation. *J. Phys. Chem. C*, 116(29):15458–15466, 2012.

[124] Uéslen Rocha, Carlos Jacinto da Silva, Wagner Ferreira Silva, Ilde Guedes, Antonio Benayas, Laura Martínez Maestro, Mónica Acosta Elias, Enrico Bovero, Frank C. J. M. van Veggel, José Antonio García Solé, and Daniel Jaque. Subtissue Thermal Sensing Based on Neodymium-Doped LaF_3 Nanoparticles. *ACS Nano*, 7(2):1188–1199, 2013.

[125] A. K. Singh, S. Singh, D. Kumar, D. K. Rai, S. B. Rai, and K. Kumar. Light-into-heat conversion in La_2O_3:Er^{3+}-Yb^{3+} phosphor: an incandescent emission. *Opt. Lett.*, 37(5):776–778, 2012.

[126] S. Redmond, S. C. Rand, X. L. Ruan, and M. Kaviany. Multiple scattering and nonlinear thermal emission of Yb^{3+}, Er^{3+}:Y_2O_3 nanopowders. *J. Appl. Phys.*, 95(8):4069–4077, 2004.

[127] Jiwei Wang and Peter A. Tanner. Upconversion for White Light Generation by a Single Compound. *J. Am. Chem. Soc.*, 132(3):947–949, 2010.

[128] W. Strek, L. Marciniak, A. Bednarkiewicz, A. Lukowiak, R. Wiglusz, and D. Hreniak. White emission of lithium ytterbium tetraphosphate nanocrystals. *Opt. Express*, 19(15):14083–14092, 2011.

[129] Wen Xu, Boting Chen, Wei Yu, Yongsheng Zhu, Tong Liu, Sai Xu, Xiaolei Min, Xue Bai, and Hongwei Song. The up-conversion luminescent properties and silver-modified luminescent enhancement of YVO_4:Yb^{3+},Er^{3+} NPs. *Dalton Trans.*, 41(43):13525–13532, 2012.

[130] Zhi Han Lim, Andrielle Lee, Yanwu Zhu, Kim-Yong Lim, and Chorng-Haur Sow. Sustained laser induced incandescence in carbon nanotubes for rapid localized heating. *Appl. Phys. Lett.*, 94(7):073106, 2009.

[131] P. Roura, J. Costa, Miguel M. López-de, B. Garrido, J. Fort, J. R. Morante, and E. Bertran. Black-body emission from nanostructured materials. *J. Lumin.*, 80(1-4):519–522, 1998.

[132] J. L. Adam, N. Duhamel-Henry, and J. Y. Allain. Blue and green up-conversion in (Yb^{3+}, Tb^{3+}) co-doped fluorophosphate glasses. *J. Non-Cryst. Solids*, 213-214(0):245–250, 1997.

[133] J. Pérez-Juste, B. Rodríguez-González, P. Mulvaney, and L. M. Liz-Marzán. Optical control and patterning of gold-nanorod-poly(vinyl alcohol) nanocomposite films. *Adv. Funct. Mater.*, 15(7):1065–1071, 2005.

[134] Ekaterina Y. Lukianova-Hleb, Lindsey J. E. Anderson, Seunghyun Lee, Jason H. Hafner, and Dmitri O. Lapotko. Hot plasmonic interactions: a new look at the photothermal efficacy of gold nanoparticles. *Phys. Chem. Chem. Phys.*, 12(38):12237–12244, 2010.

[135] Alexander O. Govorov and Hugh H. Richardson. Generating heat with metal nanoparticles. *Nano Today*, 2(1):30–38, 2007.

[136] Marta G. Cerruti, Marc Sauthier, Donovan Leonard, Dage Liu, Gerard Duscher, Daniel L. Feldheim, and Stefan Franzen. Gold and Silica-Coated Gold Nanoparticles as Thermographic Labels for DNA Detection. *Anal. Chem.*, 78(10):3282–3288, 2006.

[137] Yanqiang Lei, Hongwei Song, Linmei Yang, Lixin Yu, Zhongxin Liu, Guohui Pan, Xue Bai, and Libo Fan. Upconversion luminescence, intensity saturation effect, and thermal effect in Gd_2O_2:Er^{3+},Yb^{3+} nanowires. *J. Chem. Phys.*, 123(17):174710, 2005.

[138] Tomokatsu Hayakawa, Masahiko Hayakawa, and Masayuki Nogami. Estimation of the fs laser spot temperature inside TeO_2-ZnO-Nb_2O_5 glass by using up-conversion green fluorescence of Er^{3+} ions. *J. Allo. Comp.*, 451(1-2):77–80, 2008.

[139] V. K. Tikhomirov, K. Driesen, V. D. Rodriguez, P. Gredin, M. Mortier, and V. V. Moshchalkov. Optical nanoheater based on the Yb^{3+}-Er^{3+} co-doped nanoparticles. *Opt. Express*, 17(14):11794–11798, 2009.

[140] S. K. Singh, K. Kumar, and S. B. Rai. Diode laser pumped Gd_2O_3:Er^{3+}/Yb^{3+} phosphor as optical nano-heater. *Appl. Phys. B-Lasers O.*, 100(3):443–446, 2010.

[141] Xin Wang, Xianggui Kong, Yi Yu, Yajuan Sun, and Hong Zhang. Effect of Annealing on Upconversion Luminescence of ZnO:Er^{3+} Nanocrystals and High Thermal Sensitivity. *J. Phys. Chem. C*, 111(41):15119–15124, 2007.

[142] Michael R. Beversluis, Alexandre Bouhelier, and Lukas Novotny. Continuum generation from single gold nanostructures through near-field mediated intraband transitions. *Phys. Rev. B*, 68:115433, 2003.

[143] Zhenping Guan, Lakshminarayana Polavarapu, and Qing-Hua Xu. Enhanced Two-Photon Emission in Coupled Metal Nanoparticles Induced by Conjugated Polymers. *Langmuir*, 26(23):18020–18023, 2010.

[144] Tiberiu-Dan Onuta, Matthias Waegele, Christopher C. DuFort, William L. Schaich, and Bogdan Dragnea. Optical Field Enhancement at Cusps between Adjacent Nanoapertures. *Nano Lett.*, 7(3):557–564, 2007.

[145] Haifeng Wang, Terry B. Huff, Daniel A. Zweifel, Wei He, Philip S. Low, Alexander Wei, and Ji-Xin Cheng. *Invitro* and *invivo* two-photon luminescence imaging of single gold nanorods. *PNAS*, 102(44):15752–15756, 2005.

[146] P. Mühlschlegel, H.-J. Eisler, O. J. F. Martin, B. Hecht, and D. W. Pohl. Resonant Optical Antennas. *Science*, 308(5728):1607–1609, 2005.

[147] Hongshang Peng, Matthias I. J. Stich, Jiangbo Yu, Li-ning Sun, Lorenz H. Fischer, and Otto S. Wolfbeis. Luminescent Europium(III) Nanoparticles for Sensing and Imaging of Temperature in the Physiological Range. *Adv. Mater.*, 22(6):716–719, 2010.

[148] Seid Sadat, Aaron Tan, Yi Jie Chua, and Pramod Reddy. Nanoscale Thermometry Using Point Contact Thermocouples. *Nano Lett.*, 10(7):2613–2617, 2010.

[149] Bin Dong, Baosheng Cao, Yangyang He, Zhuang Liu, Zhipeng Li, and Zhiqing Feng. Temperature Sensing and In Vivo Imaging by Molybdenum Sensitized Visible Upconversion Luminescence of Rare-Earth Oxides. *Adv. Mater.*, 24(15):1987–1993, 2012.

[150] B. Dong, D. P. Liu, X. J. Wang, T. Yang, S. M. Miao, and C. R. Li. Optical thermometry through infrared excited green upconversion emissions in Er^{3+}-Yb^{3+} codoped Al_2O_3. *Appl. Phys. Lett.*, 90(18):181117, 2007.

[151] Lionel Aigouy, Elika Saidi, Loic Lalouat, Jessica Labeguerie-Egea, Michel Mortier, Peter Low, and Christian Bergaud. AC thermal imaging of a microwire with a fluorescent nanocrystal: Influence of the near field on the thermal contrast. *J. Appl. Phys.*, 106(7):074301, 2009.

[152] Marcio A. R. C. Alencar, Glauco S. Maciel, Cid B. de Araujo, and Amitava Patra. Er^{3+}-doped $BaTiO_3$ nanocrystals for thermometry: Influence of nanoenvironment on the sensitivity of a fluorescence based temperature sensor. *Appl. Phys. Lett.*, 84(23):4753–4755, 2004.

[153] H. Assaaoudi, A. Ennaciri, A. Rulmont, and M. Harcharras. Gadolinium orthophosphate weinschenkite type and phase change in rare earth orthophosphates. *Phase Transit.*, 72(1):1–13, 2000.

[154] Ni Yunxiang, M. Hughes John, and N. Mariano Anthony. Crystal chemistry of the monazite and xenotime structures. *Am. Mineral.*, 80:21–26, 1995.

[155] Nicolas Clavier, Renaud Podor, and Nicolas Dacheux. Crystal chemistry of the monazite structure. *J. Eur. Ceram. Soc.*, 31(6):941–976, 2011.

[156] R. Rustad James. Density functional calculations of the enthalpies of formation of rare-earth orthophosphates. *Am. Mineral.*, 97:791–799, 2012.

[157] D.F. Mullica, David A. Grossie, and L.A. Boatner. Coordination geometry and structural determinations of $SmPO_4$, $EuPO_4$ and $GdPO_4$. *Inorg. Chim. Acta*, 109(2):105–110, 1985.

[158] O. Lehmann, H. Meyssamy, K. Kömpe, H. Schnablegger, and M. Haase. Synthesis, Growth, and Er^{3+} Luminescence of Lanthanide Phosphate Nanoparticles. *J. Phys. Chem. B*, 107(30):7449–7453, 2003.

[159] R. Kijkowska, E. Cholewka, and B. Duszak. X-ray diffraction and Ir-absorption characteristics of lanthanide orthophosphates obtained by crystallisation from phosphoric acid solution. *J. Mater. Sci.*, 38(2):223–228, 2003.

[160] N. Yaiphaba, R. S. Ningthoujam, N. Shanta Singh, R. K. Vatsa, and N. Rajmuhon Singh. Probing of inversion symmetry site in Eu^{3+}-doped $GdPO_4$ by luminescence study: Concentration and annealing effect. *J. Lumin.*, 130(1):174–180, 2010.

[161] Lixin Yu, Dianchao Li, Mingxin Yue, Jie Yao, and Shaozhe Lu. Dependence of morphology and photoluminescent properties of $GdPO_4$:Eu^{3+} nanostructures on synthesis condition. *Chem. Phys.*, 326(2-3):478–482, 2006.

[162] Ningombam Yaiphaba, Raghumani Singh Ningthoujam, Nongmaithem Rajmuhon Singh, and Rajesh Kumar Vatsa. Luminescence Properties of Redispersible Tb^{3+}-Doped $GdPO_4$ Nanoparticles Prepared by an Ethylene Glycol Route. *Eur. J. Inorg. Chem.*, 2010(18):2682–2687, 2010.

[163] Lixin Yu, Dianchao Li, and Mingxin Yue. Fabrication and characterization of the photoluminescent properties of Tb^{3+} doped one-dimensional $GdPO_4$ nanorods. *Mater. lett.*, 61(22):4374–4376, 2007.

[164] Yuhua Wang, Chunfang Wu, and Jie Wei. Hydrothermal synthesis and luminescent properties of $LnPO_4$:Tb,Bi (Ln=La,Gd) phosphors under UV-VUV excitation. *J. Lumin.*, 126(2):503–507, 2007.

[165] Stephan Heer, Olaf Lehmann, Markus Haase, and Hans-Ulrich Güdel. Blue, Green, and Red Upconversion Emission from Lanthanide-Doped $LuPO_4$ and $YbPO_4$ Nanocrystals in a Transparent Colloidal Solution. *Angew. Chem. Int. Ed.*, 42(27):3179–3182, 2003.

[166] SunHyung Lee, Katsuya Teshima, Shoko Mori, Morinobu Endo, and Shuji Oishi. Selective Growth of Upconverting $YbPO_4$:Ln (Ln = Er or Tm) Crystals in a Micro Reaction Cell. *Cryst. Growth. Des.*, 10(4):1693–1698, 2010.

[167] Deyin Wang and Nobuhiro Kodama. Visible quantum cutting through downconversion in $GdPO_4$:Tb^{3+} and $Sr_3Gd(PO_4)_3$:Tb^{3+}. *J. Solid State Chem.*, 182(8):2219 – 2224, 2009.

[168] Ana I. Becerro, Sonia Rodríguez-Liviano, Alberto J. Fernández-Carrión, and Manuel Ocaña. A Novel 3D Architecture of $GdPO_4$ Nanophosphors: Multicolored and White Light Emission. *Cryst. Growth Des.*, 13(2):526–535, 2013.

[169] Yue-Ping Fang, An-Wu Xu, Rui-Qi Song, Hua-Xin Zhang, Li-Ping You, Jimmy C. Yu, and Han-Qin Liu. Systematic Synthesis and Characterization of Single-Crystal Lanthanide Orthophosphate Nanowires. *J. Am. Chem. Soc.*, 125(51):16025–16034, 2003.

[170] R. Kijkowska. Thermal decomposition of lanthanide orthophosphates synthesized through crystallisation from phosphoric acid solution. *Thermochim. Acta*, 404(1-2):81–88, 2003.

[171] Songzhu Lin, Xiangting Dong, Ruokun Jia, and Yanlin Yuan. Controllable synthesis and luminescence property of $LnPO_4$ (Ln = La, Gd, Y) nanocrystals. *J. Mater. Sci.-Mater. Electron.*, 21(1):38–44, 2010.

[172] Yunxiang Ni, J. M. Hughes, and A. N. Mariano. Crystal chemistry of the monazite and xenotime structures. *Am. Mineral.*, 80(1-2):21–26, 1995.

[173] Heng Wang, Guangshe Li, Xiangfeng Guan, and Liping Li. Synthesis and conductivity of $GdPO_4$ nanorods: Impacts of particle size and Ca^{2+} doping. *J. Alloys Compd.*, 509(10):4160–4166, 2011.

[174] W. T. Carnall, H. Crosswhite, and H. M. Crosswhite. *Energy level structure and transition probabilities in the spectra of the trivalent lanthanides in LaF_3*. Argonne National Laboratory, 1968.

[175] Dejian Hou, Hongbin Liang, Mubiao Xie, Xuemei Ding, Jiuping Zhong, Qiang Su, Ye Tao, Yan Huang, and Zhenhua Gao. Bright green-emitting, energy transfer and quantum cutting of $Ba_3Ln(PO_4)_3$:Tb^{3+} (Ln = La, Gd) under VUV-UV excitation. *Opt. Express*, 19(12):11071–11083, 2011.

[176] Paulo C. de Sousa Filho and Osvaldo A. Serra. Reverse Microemulsion Synthesis, Structure, and Luminescence of Nanosized $REPO_4$:Ln^{3+} (RE = La, Y, Gd, or Yb, and Ln = Eu, Tm, or Er). *J. Phys. Chem. C*, 115(3):636–646, 2011.

[177] O.L Malta. Ligand-Rare-earth ion energy transfer in coordination compounds. A theoretical approach. *J. Lumin.*, 71(3):229–236, 1997.

[178] O. L. Malta and F. R. Goncalves e Silva. A theoretical approach to intramolecular energy transfer and emission quantum yields in coordination compounds of rare earth ions. *Spectrochim. Acta A*, 54(11):1593–1599, 1998.

[179] Sónía S. Nobre, Patrícia P. Lima, Luís Mafra, Rute A. Sá Ferreira, Ricardo O. Freire, Lianshe Fu, Uwe Pischel, Verónica de Zea Bermudez, Oscar L. Malta, and Luís D. Carlos. Energy Transfer and Emission Quantum Yields of Organic-Inorganic Hybrids Lacking Metal Activator Centers. *J. Phys. Chem. C*, 111(8):3275–3284, 2007.

[180] Renata Reisfeld, Esther Greenberg, Rance Velapoldi, and Baruch Barnett. Luminescence Quantum Efficiency of Gd and Tb in Borate Glasses and the Mechanism of Energy Transfer between Them. *J. Chem. Phys.*, 56(4):1698–1705, 1972.

[181] Tomasz Grzyb, Aleksandra Gruszeczka, Rafal J. Wiglusz, Zbigniew Sniadecki, Bogdan Idzikowski, and Stefan Lis. Multifunctionality of $GdPO_4$:Yb^{3+},Tb^{3+} nanocrystals - luminescence and magnetic behaviour. *J. Mater. Chem.*, 22(43):22989–22997, 2012.

[182] Mubiao Xie, Ye Tao, Yan Huang, Hongbin Liang, and Qiang Su. The Quantum Cutting of Tb^{3+} in $Ca_6Ln_2Na_2(PO_2)_6F_2$ (Ln = Gd, La) under VUV-UV Excitation: with and without Gd^{3+}. *Inorg. Chem.*, 49(24):11317–11324, 2010.

[183] Yu-Chun Li, Yen-Hwei Chang, Yee-Shin Chang, Yi-Jing Lin, and Chih-Hao Laing. Luminescence and Energy Transfer Properties of Gd^{3+} and Tb^{3+} in $LaAlGe_2O_7$. *J. Phys. Chem. C*, 111(28):10682–10688, 2007.

[184] Mengistie L. Debasu, D. Ananias, Andreia G. Macedo, J. Rocha, and Luis D. Carlos. Emission-Decay Curves, Energy-Transfer and Effective-Refractive Index in Gd_2O_3:Eu^{3+} Nanorods. *J. Phys. Chem. C*, 115(31):15297–15303, 2011.

[185] Sonia Rodriguez-Liviano, Francisco J. Aparicio, Teresa C. Rojas, Ana B. Hungría, Lidia E. Chinchilla, and Manuel Ocaña. Microwave-Assisted Synthesis and Luminescence of Mesoporous RE-Doped YPO_4 (RE = Eu, Ce, Tb, and Ce + Tb) Nanophosphors with Lenticular Shape. *Cryst. Growth Des.*, 12(2):635–645, 2012.

[186] Hyon Bin Na, In Chan Song, and Taeghwan Hyeon. Inorganic Nanoparticles for MRI Contrast Agents. *Adv. Mater.*, 21(21):2133–2148, 2009.

[187] Hiroki Hifumi, Seiichi Yamaoka, Akihiro Tanimoto, Daniel Citterio, and Koji Suzuki. Gadolinium-Based Hybrid Nanoparticles as a Positive MR Contrast Agent. *J. Am. Chem. Soc.*, 128(47):15090–15091, 2006.

[188] Matthieu F. Dumont, Celine Baligand, Yichen Li, Elisabeth S. Knowles, Mark W. Meisel, Glenn A. Walter, and Daniel R. Talham. DNA Surface Modified Gadolinium Phosphate Nanoparticles as MRI Contrast Agents. *Bioconjugate Chem.*, 23(5):951–957, 2012.

[189] Yong I. Park, Hyung Min Kim, Jeong Hyun Kim, Kyung Chul Moon, Byeongjun Yoo, Kang Taek Lee, Nohyun Lee, Yoonseok Choi, Wooram Park, Daishun Ling, Kun Na, Woo Kyung Moon, Seung Hong Choi, Hong Seok Park, Soo-Young Yoon, Yung Doug Suh, Sung Ho Lee, and Taeghwan Hyeon. Theranostic Probe Based on Lanthanide-Doped Nanoparticles for Simultaneous In Vivo Dual-Modal Imaging and Photodynamic Therapy. *Adv. Mater.*, 24(42):5755–5761, 2012.

[190] Datao Tu, Yongsheng Liu, Haomiao Zhu, and Xueyuan Chen. Optical/Magnetic Multimodal Bioprobes Based on Lanthanide-Doped Inorganic Nanocrystals. *Chem. Eur. J.*, 19(18):5516–5527, 2013.

[191] Chitta Patra, Resham Bhattacharya, Sujata Patra, Sujit Basu, Priyabrata Mukherjee, and Debabrata Mukhopadhyay. Inorganic phosphate nanorods are a novel fluorescent label in cell biology. *J. Nanobiotechnology*, 4(1):11, 2006.

[192] Wenlu Ren, Gan Tian, Liangjun Zhou, Wenyan Yin, Liang Yan, Shan Jin, Yan Zu, Shoujian Li, Zhanjun Gu, and Yuliang Zhao. Lanthanide ion-doped $GdPO_4$ nanorods with dual-modal bio-optical and magnetic resonance imaging properties. *Nanoscale*, 4:3754–3760, 2012.

[193] Sonia Rodriguez-Liviano, Ana I. Becerro, David Alcántara, Valeria Grazú, Jesus M. de la Fuente, and Manuel Ocaña. Synthesis and Properties of Multifunctional Tetragonal Eu:$GdPO_4$ Nanocubes for Optical and Magnetic Resonance Imaging Applications. *Inorg. Chem.*, 52(2):647–654, 2013.

[194] Vikram J. Pansare, Shahram Hejazi, William J. Faenza, and Robert K. Prudhomme. Review of Long-Wavelength Optical and NIR Imaging Materials: Contrast Agents, Fluorophores, and Multifunctional Nano Carriers. *Chem. Mater.*, 24(5):812–827, 2012.

[195] K Licha. *Contrast Agents for Optical Imaging, in Contrast Agents II Optical, Ultrasound, X-Ray and Radiopharmaceutical Imaging*, volume 222. Springer, Berlin, Heidelberg, 1986.

[196] Rajiv Kumar, Marcin Nyk, Tymish Y. Ohulchanskyy, Christopher A. Flask, and Paras N. Prasad. Combined Optical and MR Bioimaging Using Rare Earth Ion Doped $NaYF_4$ Nanocrystals. *Adv, Funct. Mater.*, 19:853–859, 2009.

[197] L. M. Maestro, J. E. Ramirez-Hernandez, N. Bogdan, J. A. Capobianco, F. Vetrone, J. Garcia Sole, and D. Jaque. Deep tissue bio-imaging using two-photon excited CdTe fluorescent quantum dots working within the biological window. *Nanoscale*, 4:298–302, 2012.

[198] M.-F. Penet, M. Mikhaylova, C. Li, B. Krishnamachary, K. Glunde, A. P. Pathak, and Z. M. Bhujwalla. Applications of molecular MRI and optical imaging in cancer. *Future. Med. Chem.*, 2(6):975–988, 2010.

[199] Timothy A Larson, James Bankson, Jesse Aaron, and Konstantin Sokolov. Hybrid plasmonic magnetic nanoparticles as molecular specific agents for MRI/optical imaging and photothermal therapy of cancer cells. *Nanotechnology*, 18(32):325101, 2007.

[200] San Wan, John A. Parrish, R. Rox Anderson, and Michael Madden. Transmittance of Nonionizing Radiation in Human Tissues Photochem. *Photochem. Photobiol.*, 34(6):679–681, 1981.

[201] Ning-Ning Dong, Marco Pedroni, Fabio Piccinelli, Giamaica Conti, Andrea Sbarbati, Juan Enrique Ramírez-Hernández, Laura Martínez Maestro, Maria Carmen Iglesias-de la Cruz, Francisco Sanz-Rodriguez, Angeles Juarranz, Feng Chen, Fiorenzo Vetrone, John A. Capobianco, José García Solé, Marco Bettinelli, Daniel Jaque, and Adolfo Speghini. NIR-to-NIR Two-Photon Excited CaF_2:Tm^{3+},Yb^{3+} Nanoparticles: Multifunctional Nanoprobes for Highly Penetrating Fluorescence Bio-Imaging. *ACS Nano*, 5(11):8665–8671, 2011.

[202] Qiuqiang Zhan, Jun Qian, Huijuan Liang, Gabriel Somesfalean, Dan Wang, Sailing He, Zhiguo Zhang, and Stefan Andersson-Engels. Using 915 nm Laser Excited Tm^{3+}/Er^{3+}/Ho^{3+} -Doped $NaYbF_4$ Upconversion Nanoparticles for in Vitro and Deeper in Vivo Bioimaging without Overheating Irradiation. *ACS Nano*, 5(5):3744–3757, 2011.

[203] Peter Caravan, Jeffrey J. Ellison, Thomas J. McMurry, and Randall B. Lauffer. Gadolinium(III) Chelates as MRI Contrast Agents: Structure, Dynamics, and Applications. *Chem. Rev.*, 99(9):2293–2352, 1999.

[204] Eric J. Werner, Ankona Datta, Christoph J. Jocher, and Kenneth N. Raymond. High-Relaxivity MRI Contrast Agents: Where Coordination Chemistry Meets Medical Imaging. *Angew. Chem. Int. Ed.*, 47(45):8568–8580, 2008.

[205] Peter Caravan. Strategies for increasing the sensitivity of gadolinium based MRI contrast agents. *Chem. Soc. Rev.*, 35:512–523, 2006.

[206] Daqin Chen, Yunlong Yu, Yuansheng Wang, Ping Huang, and Fangyi Weng. Cooperative Energy Transfer Up-Conversion and Quantum Cutting Down-Conversion in Yb^{3+}:TbF_3 Nanocrystals Embedded Glass Ceramics. *J. Phys. Chem. C*, 113(16):6406–6410, 2009.

[207] Tatsuya Yamashita and Yasutake Ohishi. Cooperative energy transfer between and ions co-doped in borosilicate glass. *J. Non-Cryst. Solids*, 354(17):1883–1890, 2008.

[208] B. Lai, J. Wang, and Q. Su. Ultraviolet and visible upconversion emission in Tb^{3+}/Yb^{3+} co-doped fluorophosphate glasses. *Appl. Phys. B*, 98(1):41–47, 2010.

[209] Xiaobo Chen and Zengfu Song. Strong cooperative upconversion luminescence of ytterbium doped oxyfluoride nanophase vitroceramics. *Solid State Commun.*, 136(6):313–317, 2005.

[210] G. S. Maciel, A. Biswas, R. Kapoor, and P. N. Prasad. Blue cooperative upconversion in Yb^{3+}-doped multicomponent sol-gel-processed silica glass for three-dimensional display. *Appl. Phys. Lett.*, 76(15):1978–1980, 2000.

[211] G. M. Salley, R. Valiente, and H. U. Güdel. Cooperative Yb^{3+}-Tb^{3+} dimer excitations and upconversion in $Cs_3Tb_2Br_9$:Yb^{3+}. *Phys. Rev. B*, 67:134111, 2003.

[212] Eiichiro Nakazawa and Shigeo Shionoya. Cooperative Luminescence in $YbPO_4$. *Phys. Rev. Lett.*, 25:1710–1712, 1970.

[213] Georges Boulon. Why so deep research on Yb^{3+}-doped optical inorganic materials? *J. Alloys Compd.*, 451(1-2):1–11, 2008.

[214] G. Boulon and V. Lupei. Energy transfer and cooperative processes in Yb^{3+}-doped cubic sesquioxide laser ceramics and crystals. *J. Lumin.*, 125(1-2):45–54, 2007.

[215] S. Hraiech and A. Jouini and K. Jin Kim and Y. Guyot and C. Goutaudier and A. Yoshikawa and M. Trabelsi-Ayadi and G. Boulon. Breakage of Yb^{3+} pairs by Na^+ in Yb^{3+}-doped CaF_2 laser host. *Ann. Phys. Fr.*, 32:59–61, 2007.

[216] R. K. Verma, D. K. Rai, and S. B. Rai. Investigation of structural properties and its effect on optical properties: Yb^{3+}/Tb^{3+} codoped in aluminum silicate glass. *J. Alloys Compd.*, 509(18):5591–5595, 2011.

[217] G. M. Salley, R. Valiente, and H. U. Guedel. Luminescence upconversion mechanisms in $Yb^{3+}-Tb^{3+}$ systems. *J. Lumin.*, 94-95(0):305–309, 2001.

[218] F. W. Ostermayer and L. G. Van Uitert. Cooperative Energy Transfer from Yb^{3+} to Tb^{3+} in YF_3. *Phys. Rev. B*, 1:4208–4212, 1970.

[219] Sri Sivakumar and Frank C. J. M. van Veggel. Red, Green, and Blue Light Through Cooperative Up-Conversion in Sol-Gel Thin Films Made With $Yb_{0.80}La_{0.15}Tb_{0.05}F_3$ and $Yb_{0.80}La_{0.15}Eu_{0.05}F_3$ Nanoparticles. *J. Display Technol.*, 3(2):176–183, 2007.

[220] W. J. Zhang, Q. J. Chen, Q. Qian, Q. Y. Zhang, and Z. H. Jiang. Cooperative energy transfer in Tb^{3+} /Yb^{3+} - and Nd^{3+} /Yb^{3+} /Tb^{3+} -codoped oxyfluoride glasses. *Physica B: Condens. Matter*, 405(4):1062 – 1066, 2010.

[221] J. Amami, D. Hreniak, Y. Guyot, R. Pazik, C. Goutaudier, G. Boulon, M. Ayadi, and W. Strek. Second harmonic generation and Yb^{3+} cooperative emission used as structural probes in size-driven cubic-tetragonal phase transition in $BaTiO_3$ sol-gel nanocrystals. *J. Lumin.*, 119-120(0):383–387, 2006.

[222] Sonia L. C. Pinho, Giovannia A. Pereira, Pierre Voisin, Jinane Kassem, Véronique Bouchaud, Laetitia Etienne, Joop A. Peters, Luis Carlos, Stéphane Mornet, Carlos F. G. C. Geraldes, João Rocha, and Marie-Hélène Delville. Fine Tuning of the Relaxometry of γ-Fe_2O_3@SiO_2 Nanoparticles by Tweaking the Silica Coating Thickness. *ACS Nano*, 4(9):5339–5349, 2010.

[223] Young-su Yoon, Byung-Il Lee, Kyung Sig Lee, Hyejung Heo, Jung Hee Lee, Song-Ho Byeon, and In Su Lee. Fabrication of a silica sphere with fluorescent and MR contrasting $GdPO_4$ nanoparticles from layered gadolinium hydroxide. *Chem. Commun.*, 46:3654–3656, 2010.

[224] I. Coroiu. Relaxivities of different superparamagnetic particles for application in NMR tomography. *J. Magn. Magn. Mater.*, 201(1-3):449–452, 1999.

[225] Giovannia A. Pereira, Joop A. Peters, Filipe A. Almeida Paz, João Rocha, and Carlos F. G. C. Geraldes. Evaluation of $Ln(H_2cmp)(H_2O)$ Metal Organic Framework Materials for Potential Application as Magnetic Resonance Imaging Contrast Agents. *Inorg. Chem.*, 49(6):2969–2974, 2010.

[226] Alessandro Barge, Giancarlo Cravotto, Eliana Gianolio, and Franco Fedeli. How to determine free Gd and free ligand in solution of Gd chelates. A technical note. *Contrast Med. Mol. Imaging*, 1(5):184–188, 2006.

[227] G. Kucsko, P. C. Maurer, N. Y. Yao, M. Kubo, H. J. Noh, P. K. Lo, H. Park, and M. D. Lukin. Nanometre-scale thermometry in a living cell. *Nature*, 500(7460):54–58, 2013.

[228] Woochul Lee, Kyeongtae Kim, Wonho Jeong, Linda Angela Zotti, Fabian Pauly, Juan Carlos Cuevas, and Pramod Reddy. Heat dissipation in atomic-scale junctions. *Nature*, 498(7453):209–212, 2013.

[229] Gan Tian, Zhanjun Gu, Liangjun Zhou, Wenyan Yin, Xiaoxiao Liu, Liang Yan, Shan Jin, Wenlu Ren, Gengmei Xing, Shoujian Li, and Yuliang Zhao. Mn^{2+} Dopant-Controlled Synthesis of $NaYF_4$:Yb/Er Upconversion Nanoparticles for in vivo Imaging and Drug Delivery. *Adv. Mater.*, 29(9):1226–1231, 2012.

[230] Parthiban Ramasamy, Prakash Chandra, Seog Woo Rhee, and Jinkwon Kim. Enhanced upconversion luminescence in $NaGdF_4$:Yb,Er nanocrystals by Fe^{3+} doping and their application in bioimaging. *Nanoscale*, 5(18):8711–8717, 2013.

[231] Wen-qing Li, Chun-yang Sun, Feng Wang, Yu-cai Wang, Yi-wen Zhai, Meng Liang, Wen-jing Liu, Zhi-min Liu, Jun Wang, and Fei Sun. Achieving a New Controllable Male Contraception by the Photothermal Effect of Gold Nanorods. *Nano Lett.*, 13(6):2477–2484, 2013.

[232] A. L. Patterson. The Scherrer Formula for X-Ray Particle Size Determination. *Phys. Rev.*, 56:978–982, 1939.

[233] John Turkevich, Peter Cooper Stevenson, and James Hillier. A study of the nucleation and growth processes in the synthesis of colloidal gold. *Discuss. Faraday Soc.*, 11:55–75, 1951.

[234] Isabel Pastoriza-Santos, Daniel Gomez, Jorge Perez-Juste, Luis M. Liz-Marzan, and Paul Mulvaney. Optical properties of metal nanoparticle coated silica spheres: a simple effective medium approach. *Phys. Chem. Chem. Phys.*, 6(21):5056–5060, 2004.